UNIVERSITY OF CAPE TOWN

IYUNIVESITHI YASEKAPA • UNIVERSITEIT VAN KAAPSTAD

Numerical simulation of friction welding processes: An arbitrary Lagrangian-Eulerian approach

by

Maien Mohamed Osman Hamed

Thesis Presented for the Degree of

DOCTOR OF PHILOSOPHY

in the Department of Mechanical Engineering

UNIVERSITY OF CAPE TOWN

January 2022

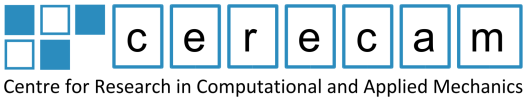

Abstract

The development and implementation of a finite strain thermo-viscoplasticity solver with thermomechanical friction contact for numerical simulation of friction welding processes are described. A finite strain associative coupled thermoplasticity model is used, which is suited for the large deformations characteristic of friction welding processes, and which resolves the viscoplastic deformations in the thermomechanically affected zone as well as the elastic stresses in the parent material. To prevent the large deformations from causing large distortions and degrading the simulation accuracy, an arbitrary Lagrangian-Eulerian (ALE) formulation for coupled finite strain thermoplasticity is developed and incorporated into the solver, in which the motion of the reference configuration is represented incrementally in terms of a reference velocity field. Thus, the deformation from the material configuration is required neither explicitly in terms of a deformation field, nor implicitly in terms of the deformation gradient. The solver is implemented using the deal.II library and programmed for distributed memory parallel computing architectures, which reduces simulation run times and enables simulations with larger meshes than would fit on a single computer. The interprocess communications required in such a distributed memory parallel implementation of the ALE formulation and the thermomechanical friction contact are described and implemented. The axisymmetric solver implementation is validated with benchmark problems and used to simulate a direct drive friction welding process.

Declaration

I **Maien Mohamed Osman Hamed** hereby declare that this thesis represents (except where otherwise acknowledged) entirely my own original work both in concept and execution.

Signature: Signed by candidate Date: January 11, 2022

Acknowledgements

I begin by offering my sincere thanks and heartfelt gratitude to my supervisor, Professor Daya Reddy, and to my co-supervisor, Dr. Andrew McBride, for their teaching and guidance. I am grateful for the opportunity to attend the CISM advanced school in Advanced Finite Element Technologies, and the many seminars and workshops that exposed me and my fellow CERECAM students to many interesting and relevant topics. I am thankful for the many times they offered just the right idea or pointed me to the exact reference I needed to read whenever I got stuck during my research.

I would like to thank my CERECAM colleagues. Through your friendship and the many discussions and activities that we shared, my time in Cape Town and on campus was wonderful, and is a source of many of my fondly cherished memories.

The deal.II library was a great resource to have during this research. I am grateful for the welcoming community behind it. When I needed a feature in my research that the library had not yet offered, I found encouragement and guidance towards implementing it. My thanks go to Professor Wolfgang Bangerth who pointed me towards the relevant parts of the code that needed to be extended and who reviewed most of my changes before they were merged, and to Prof. Dr. Martin Kronbichler and Professor Timo Heister who also reviewed and gave me valuable feedback on my pull requests.

I am thankful to my parents and to my brothers and sisters for their love, support, and continual encouragement. The chat group and weekly video group calls have been a

much needed emotional respite. I am thankful to YuanYuan (Cindy) for her love and for supporting and believing in me, and to Rowan, for coming into our life and giving it meaning.

I am grateful for the financial support, which I received in 2014 and 2015, through the NRF grant holder bursary and CERECAM scholarship.

Contents

List of Figures

List of Tables

Part I

Background and Literature Review

1 Introduction

Friction welding is a family of solid-state joining processes where friction is used to generate the heat necessary for welding. Friction welds are formed in three stages. In the first stage, mechanical friction at the contact surface between the workpieces and the tool, if one is present, produces heat, raising the temperature around the interface. In the second stage, the combined effect of the elevated temperature and compressive and shear stresses plasticises the material in the vicinity of the friction region. In the third stage, the frictional force is removed and a forging force is maintained so that the plasticised material solidifies in the presence of compressive stress to form the weld.

The family of friction welding processes includes friction stir welding (FSW) [1], linear friction welding (LFW)[2], and rotary friction welding (RFW) [3, 4]. In rotary friction welding (Figure 1.1), under which processes such as friction stud welding and friction hydro-pillar welding can be grouped, a rotationally symmetric workpiece is spun around its axis and pressed against the second workpiece, which is kept stationary. This heats and plasticises the material around the friction surface. To complete the weld, rotation is stopped and a forging force is applied and maintained until the newly formed joint has solidified. Linear friction welding (Figure 1.2) is a similar process, the difference being that the relative motion is reciprocating instead of rotational. In friction stir welding, the weld is formed by rotating and translating a non-consumable tool at the interface between the workpieces being welded (Figure 1.3). At the beginning of the weld, the profiled pin is inserted between the abutting work pieces, displacing some of the material

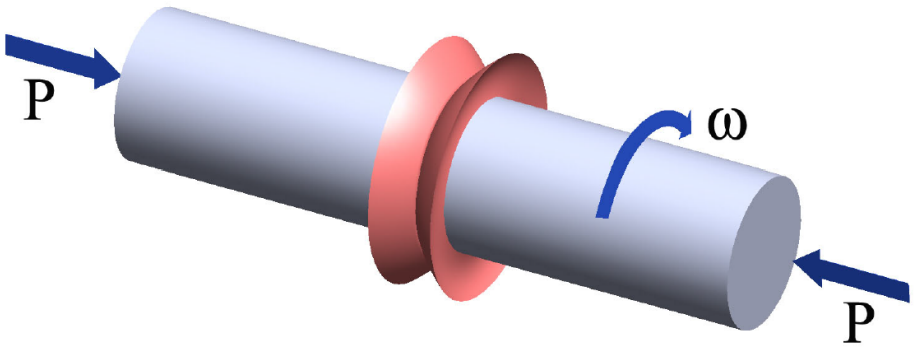

Figure 1.1: Rotary friction welding [5]

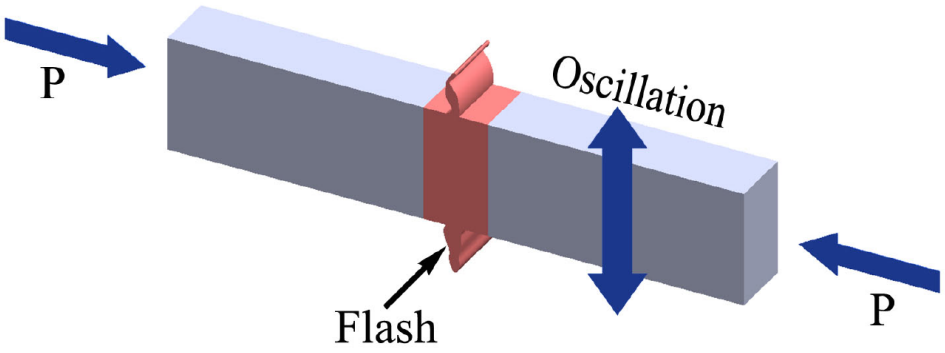

Figure 1.2: Linear friction welding [6]

around the weld interface, until the shoulder touches the outer surface of the work pieces on the opposite side of the backing bar. As the tool rotates, the heat generated around the weld interface from friction with the tool shoulder and viscoplastic dissipation in the material around the pin causes the material to plasticise. The tool is then traversed forward, and the weld is formed behind it as the plasticised and stirred material cools down.

There is a wide interest in numerical simulation of friction welding processes. Numerical simulation is a useful tool for reducing the high cost and time requirements of friction welding process development for new applications. For instance, simulation can be used as an engineering aid for selection of welding parameters such as rotational and traversal

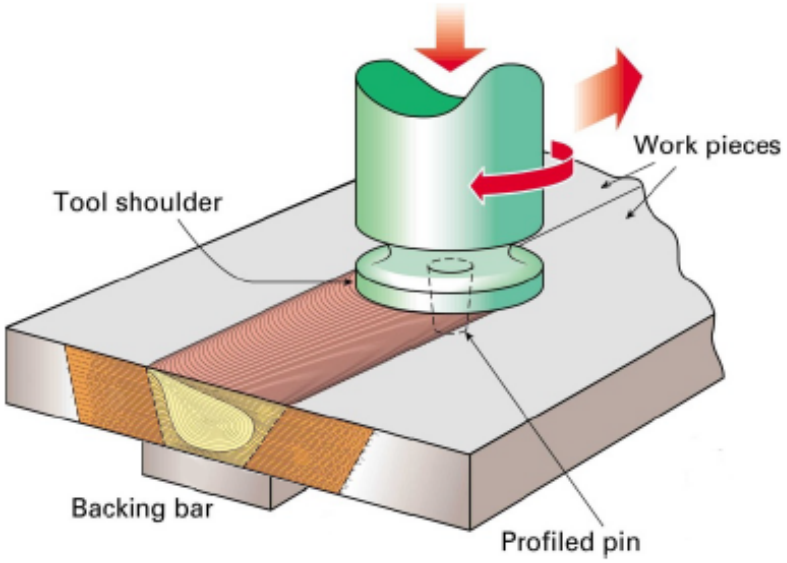

Figure 1.3: Friction stir welding [7]

speeds and forging forces. Simulation is also useful in the development of friction welding machinery and tooling. Friction stir welding tool design, for instance, can benefit from rapid iteration using numerical simulation. Furthermore, besides the practical interest in simulation of the processes, there is also an interest in the insight that can be gained from studying the complex material behaviour that characterises friction welding processes. These processes involve tight coupling between thermal and mechanical effects such as frictional and viscoplastic work heating and temperature dependent material properties.

Numerical simulation of friction stir welding has been subject to much research, of which reviews were carried out by He, Gu and Ball [8] and by Neto and Neto [9]. Linear and rotary friction welding have also been subject to some numerical simulation research, albeit not as extensive as that on FSW. For instance, a finite element model of linear friction welding of titanium blocks was presented by Vairis and Frost [10], a process model of rotary friction welding of aluminium alloys using a finite difference method was reported by Frigaard, Grong and Midling [11], and the Johnson-Cook thermo-viscoplastic model was used to model rotary friction welding [5] and linear friction welding [6]. A literature review of strategies for numerical simulation of linear friction welding was

conducted by Buffa and Fratini [12].

An aspect of friction welding processes that is qualitatively understood but remains to be addressed in the literature of numerical simulation of these processes is the interaction between viscoplastic stresses and frictional forces in the thermomechanically affected zone (TMAZ). One of the main advantages of friction welding processes is that they are solid state processes, in which no significant melting occurs [13, 14]. While evidence of melting was observed in some studies on welding of dissimilar materials [15, 16], it is localised and transient. The generally accepted reason for the absence of melting is that as the temperature increases, the resulting decrease in yield strength of material in the TMAZ due to thermal softening decreases shear stresses and, as a result, frictional forces across the weld interface. As a consequence, the rate of heat generation due to friction is reduced, which causes the temperature to remain below the melting point. This effect is highly nonlinear, and it plays an important role in the resulting weld quality.

The challenges in numerical simulation of the interaction between frictional contact forces and viscoplastic stresses stem from the large deformations undergone by the material in the TMAZ, and the large range of strain rate values. The physics of the process is appropriately represented with a finite strain coupled thermoplasticity model, with thermomechanical frictional contact. The extent of deformations in the TMAZ would result in excessive mesh distortions during the numerical simulation, which necessitates frequent remeshing or adopting an arbitrary Lagrangian-Eulerian (ALE) formulation [8, 12]. The two main formulations of ALE for finite strain plasticity in the literature [17, 18] are not suited for addressing these challenges. The limitation resides in two features shared by these formulations. First, they both rely on keeping track of the deformation from the initial material configuration, either explicitly by representing the initial material configuration as a variable, or implicitly by keeping track of the deformation gradient. The extent of deformations in the TMAZ at the end of the weld precludes keeping track of the initial material configuration. Second, both formulations rely on a split step approach, which comprises a Lagrangian step where the deformed

configuration is computed with a vanishing convective velocity, and an Eulerian step where the mesh is updated keeping the deformation fixed. The large range of deformation rate values within the weld makes it such that updating the deformation in a Lagrangian step without excessive mesh distortion would require a very small time step, which may increase the required simulation time to prohibitive durations.

The aim of this work is to develop and implement a numerical simulation of friction welding, modelling the workpieces as deformable finite strain thermo-viscoplastic materials undergoing thermomechanical frictional contact. To address the challenges outlined above, a novel arbitrary Lagrangian-Eulerian formulation for finite strain plasticity is developed in which the motion is represented in terms of an intermediate reference configuration by a combination of the deformation and the reference velocity. The deformation from the material configuration is required neither explicitly by representing the material configuration field, nor implicitly by tracking the deformation gradient. Instead, the material configuration is only referenced in terms of the reference velocity, so that excessive deformation in the TMAZ does not cause numerical difficulties. Also, the stresses are resolved by simultaneously updating the deformation and the reference velocity, so that the number of time steps required to simulate the weld remains reasonably small, preventing excessive computational expense. The finite strain plasticity and the finite deformation thermomechanical frictional contact formulations are extended by including the contribution of the reference velocity, and the resulting consistent tangent moduli are computed in order to preserve the convergence order when a Newton-Raphson method is used.

While the mathematical derivations of the arbitrary Lagrangian-Eulerian approach are presented for general three-dimensional geometries, the implemented solver uses axisymmetric elements to exploit the rotational symmetry in RFW processes. The reference motion is therefore decomposed into an in-plane component and a circumferential component. In this implementation, the in-plane component of the motion is described in terms of both the reference velocity as well as the deformation from the reference config-

uration, while the circumferential component of the motion is described entirely in terms of the reference velocity. Thus, both in-plane and torsional effects are captured while the reference and current configuration meshes remain entirely on the axisymmetry plane.

The developed model is implemented in C++ leveraging deal.II [19], and can run in distributed memory parallel computing systems. deal.II is an object-oriented library that enables rapid development of numerical simulation codes by providing classes that compute element degrees of freedom and element shape functions, and that support linking of local and global degrees of freedom, linear system assembly, and integration with linear solvers [19]. As part of this work, the deal.II library was extended by incrementing the highest available order of spatial derivatives of the element shape functions [20]. This was necessary for representing the consistent tangent moduli of the tangential contact contributions.

This thesis is composed of four parts. The first part, which comprises the present Chapter and Chapter 2, is concerned with the literature of friction welding processes and related theoretical, experimental, and computational research. The second part deals with the mathematical model of the process. It is composed of Chapter 3 on the kinematics of large deformations, finite strains and multi-body frictional contact, Chapter 4 on the constitutive models of coupled thermomechanical finite strain plastic deformation and frictional contact, and Chapter 5 on the balance equations and weak formulations. The third part concerns the formulation, implementation and solution of the resulting finite element model. It consists of Chapter 6 and Chapter 7. The fourth part is on the results of the developed model. Chapter 8 presents simulations of benchmark problems and Chapter 9 presents simulations of a friction welding process. Chapter 10 concludes the thesis and discusses the findings.

2 Literature Review

2.1 Friction Welding Processes

Though friction welding processes have been used for several decades [1–4, 21], they remain an active area of research, of which several literature reviews have been published [13, 14, 22–27].

Much of the literature has focused on application of friction welding to weld a variety of materials [28–41], and on characterisation of metallurgical and mechanical properties of the welds [42–50].

Thermodynamic behaviour of the material plays a central role during friction welding, and has been subject to much research [51–56]. Some authors have developed analytical models of the temperature field during friction welding [57, 58]. Others have developed numerical models of temperature evolution during friction welding, with the heat source power obtained experimentally [59], or approximated from material and process parameters [60, 61]. Balasubramanian, Li, Stotler *et al.* [62] combined these approaches by estimating the friction coefficient from experimentally measured temperature profiles.

Thermomechanical deformation and material flow in friction welding have also been the subject of several analytical and experimental studies [63–65]. However, as detailed in the following section, much of the research on thermomechanical material response in friction welding has been by means of numerical simulation.

Friction is central to friction welding processes, and several researchers have studied friction models [66–69]. Wang, Li, Xiong *et al.* [70] experimentally studied the transition from sliding friction to viscoplastic deformation at the interface in RFW.

2.2 Numerical Simulation of Friction Welding

He, Gu and Ball [8] reviewed the literature of numerical simulation of FSW, and Buffa and Fratini reviewed the literature of numerical simulation of LFW [12]. The review by Maalekian [22] includes a section on the literature of numerical simulation of LFW and RFW.

Many of the early numerical models of RFW were based on CFD models. Moal and Massoni [71] developed a coupled thermomechanical model of inertial friction welding (IFW), where the material was modelled by an incompressible temperature-dependent viscoplastic Norton–Hoff law. Bendzsak, North and Li [72] developed a numerical model for the steady-state flow in friction welding by using the Navier-Stokes equations with a non-Newtonian viscosity governed by the shear stress, the pressure, and the temperature. D'Alvise, Massoni and Walløe [73] developed a numerical model to simulate IFW of dissimilar materials, which consisted of a viscous flow model coupled with friction contact and thermal models. A 3D rigid viscoplastic simulation of direct drive friction welding was carried out by Zhang, Zhang, Liu *et al.* [74]. Schmicker, Naumenko and Strackeljan [75] developed a numerical simulation of direct drive friction welding using a modified Carreau fluid constitutive model.

Fu, Duan and Du [76] performed a finite element simulation of inertia friction welding of a 36CrNiMo4 steel tube using the DEFORM software. Xu, Jing, Han *et al.* [77] performed numerical simulation of FHPP on Abaqus, in which they studied the influence of the geometry of the hole and stud on the resulting weld. They used a finite strain elasto–viscoplastic material model in which the temperature- and strain rate-dependent

properties were interpolated from experimentally determined values. Landell, Kanan, Luis Fernando *et al.* [78] also performed numerical simulation of FHPP using Abaqus, in which they placed tracer particles near the contact interface to resolve material flow in the radial and axial directions.

2.3 Numerical Simulation of Thermo-viscoplasticity

Coupled thermoplasticity is an important subject of numerical simulation, and has been subject to much research [79–81]. Simo and Miehe [82] formulated a model for numerical simulation of coupled thermoplasticity at finite strains that has been extensively used in simulation of metal forming [83–96]. They introduced the plastic entropy as an independent internal variable which represents the plastic configurational entropy that arises from dislocation and defect movement, and they employed an operator split to construct a product formula algorithm such that the model can be solved in a split-step procedure. Further development of the model was subsequently carried out in several works [97, 98].

2.4 Numerical Simulation of Thermomechanical Contact

Thermomechanical frictional contact plays a central role in friction welding processes, and without taking it into account, a numerical simulation of material flow in these processes would be incomplete. Several researchers have studied numerical simulation of frictional contact. Formulations for finite-element solution of large deformation frictional contact were presented by Wriggers, Vu Van and Stein [99] and by Laursen and Simo [100]. For improved numerical properties of the discretised systems, Simo and Laursen introduced an augmented Lagrangian treatment of the formulation [101], and

used it for algorithmically symmetrizing the resulting linear systems [102]. These formulations have been used for coupled finite element simulation of thermomechanical frictional contact [103, 104].

2.5 Arbitrary Lagrangian-Eulerian Methods

Arbitrary-Lagrangian-Eulerian (ALE) formulations are based on representing motion in terms of a reference configuration whose motion may be arbitrarily prescribed [105]. Since they appeared several decades ago for modelling fluid dynamics and fluid-structure interaction [106, 107], ALE methods have been the subject of much research [108–116].

The use of ALE methods for solid mechanics applications has also been of much interest [117–119]. In particular, ALE formulations for finite strain elastoplasticity have been presented. Rodriguez-Ferran, Perez-Foguet and Huerta [17] developed an ALE method for finite strain plasticity. Armero and Love [18] presented a method that tracks, in terms of the reference configuration, both the deformed configuration as well as the material configuration. Both these approaches [17, 18] are performed in a split-step procedure: a fully Lagrangian step where the convective velocity is set to zero, followed by an advection step where fields are remapped according to an incremental mesh motion.

There does not appear to be in the literature an ALE formulation for finite strain thermoplasticity where the deformation is updated in the presence of a nonzero convective velocity, or without computing the deformation gradient from the initial material configuration being required.

Part II

Mathematical Models

3 Kinematics

This Chapter describes the kinematics of deformation and multibody frictional contact between multiple bodies undergoing finite strains. Section 3.1 describes the configurations of a deformable body and the representation of scalar, vector, and tensor fields defined on one. In Section 3.2, the strain measures of finite strain plasticity are described. Section 3.3 details the kinematics of multibody frictional contact.

3.1 Configurations and Fields of a Deformable Body

The approach taken is to consider two deformable bodies involved in a friction welding process and assign one as the contactor and the other as the target. We identify them throughout by superscripts con and tar, respectively. They are denoted in the material configuration by $\Omega_0^{\mathcal{B}} \subset \mathbb{R}^3$, $\mathcal{B} \in \{\text{con}, \text{tar}\}$. Physical properties of these bodies are modelled as functions of space and time. In particular, the motion at any time t is given for $\boldsymbol{X}_0 \in \Omega_0^{\mathcal{B}}$ as a continuous function $\boldsymbol{x} = \boldsymbol{\varphi}_0(\boldsymbol{X}_0, t)$ that is invertible with respect to the first parameter. It maps the material configuration $\Omega_0^{\mathcal{B}}$ to the deformed configuration $\tilde{\Omega}^{\mathcal{B}} \coloneqq \{\boldsymbol{x} = \boldsymbol{\varphi}_0(\boldsymbol{X}_0, t) | \boldsymbol{X}_0 \in \Omega_0^{\mathcal{B}}\}$. The latter is also referred to as the current (spatial) configuration. Invertibility of the motion means that the function $\boldsymbol{\varphi}_0^{-1}$ exists such that $\boldsymbol{X}_0 = \boldsymbol{\varphi}_0^{-1}(\boldsymbol{\varphi}_0(\boldsymbol{X}_0, t), t)$ and $\boldsymbol{x} = \boldsymbol{\varphi}_0\left(\boldsymbol{\varphi}_0^{-1}(\boldsymbol{x}, t), t\right)$ at any time t and for any $\boldsymbol{X}_0 \in \Omega_0^{\mathcal{B}}$ and any $\boldsymbol{x} \in \tilde{\Omega}^{\mathcal{B}}$. Consequently, a scalar or tensor field $q \coloneqq q_0(\boldsymbol{X}_0, t)$ can also be given

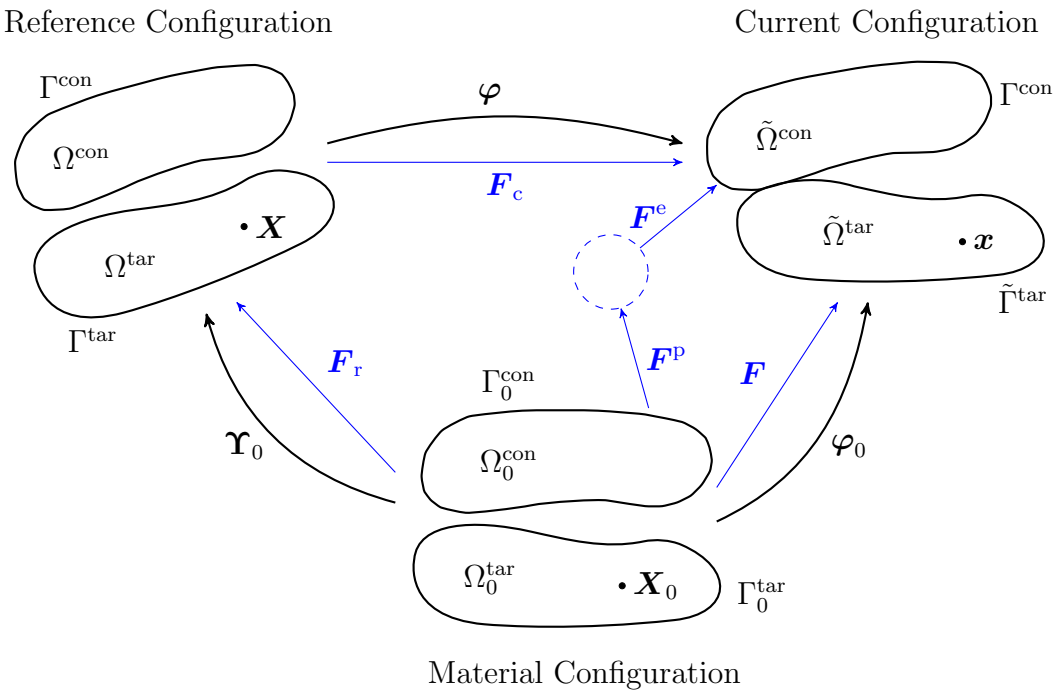

Figure 3.1: Configurations of contacting bodies

as a function of the deformed configuration as $q = \tilde{q}(\boldsymbol{x}, t) = q_0(\boldsymbol{\varphi}_0^{-1}(\boldsymbol{x}, t), t)$. The spatial and material gradients of a scalar field q are denoted, respectively, by

$$\nabla q \coloneqq \operatorname{grad} q \coloneqq \frac{\partial \tilde{q}}{\partial \boldsymbol{x}}\,, \tag{3.1.1}$$

and

$$\operatorname{Grad}_0 q \coloneqq \frac{\partial q_0}{\partial \boldsymbol{X}_0}. \tag{3.1.2}$$

The first and second partial time derivatives of the motion at a fixed material point are, respectively, the material velocity

$$\boldsymbol{v} \coloneqq \dot{\boldsymbol{x}} \coloneqq \frac{\partial}{\partial t}\boldsymbol{\varphi}_0(\boldsymbol{X}_0, t)\,, \tag{3.1.3}$$

and the acceleration

$$\boldsymbol{a} \coloneqq \ddot{\boldsymbol{x}} \coloneqq \frac{\partial^2}{\partial t^2}\boldsymbol{\varphi}_0(\boldsymbol{X}_0, t)\,. \tag{3.1.4}$$

In general, we adopt the notations

$$\dot{q} \coloneqq \frac{\mathrm{D}q}{\mathrm{D}t} \coloneqq \frac{\partial q_0}{\partial t}\,, \tag{3.1.5}$$

to denote the material time derivative for a scalar field q. It is given in the current configuration by

$$\begin{aligned}\dot{\tilde{q}}(\boldsymbol{x},t) &= \frac{\partial}{\partial t}\tilde{q}(\boldsymbol{x},t) + \frac{\partial}{\partial \boldsymbol{x}}\tilde{q}(\boldsymbol{x},t)\cdot\frac{\partial}{\partial t}\boldsymbol{\varphi}_0(\boldsymbol{X}_0,t)\Big|_{\boldsymbol{X}_0=\boldsymbol{\varphi}_0^{-1}(\boldsymbol{x},t)} \\ &= \left(\frac{\partial\tilde{q}}{\partial t} + \left(\frac{\partial\tilde{q}}{\partial\boldsymbol{x}}\right)\cdot\boldsymbol{v}\right)\Big|_{(\boldsymbol{x},t)}\,.\end{aligned} \tag{3.1.6}$$

Similarly, for a tensor field $\boldsymbol{q}$, the total time derivative is given in the current configuration by

$$\dot{\tilde{\boldsymbol{q}}}(\boldsymbol{x},t) = \left(\frac{\partial\tilde{\boldsymbol{q}}}{\partial t} + \left(\frac{\partial\tilde{\boldsymbol{q}}}{\partial\boldsymbol{x}}\right)\boldsymbol{v}\right)\Big|_{(\boldsymbol{x},t)}\,. \tag{3.1.7}$$

The local deformation state from the material configuration is described by the deformation gradient

$$\boldsymbol{F} = \frac{\partial\boldsymbol{\varphi}_0}{\partial\boldsymbol{X}_0}\,. \tag{3.1.8}$$

Continuity and material impenetrability conditions require throughout the motion that the Jacobian determinant J of the deformation gradient be strictly positive: that is,

$$J \coloneqq \det(\boldsymbol{F}) > 0\,. \tag{3.1.9}$$

The classical descriptions of motion correspond to representing fields by functions given in either the material configuration or the current configuration. The Lagrangian description of motion corresponds to representing fields as functions in the material configuration. This description is suitable for solid mechanics problems for which there is a readily identifiable material (undeformed) configuration. It has the advantages of the simple form of the material time derivative, and that all variables are functions of the

initial position and time. In the Eulerian description of motion, fields are represented as functions of the current configuration. This description is appropriate for fluid mechanics problems where the domain remains fixed in time, and stress and pressure are functions of the velocity and velocity gradients; total deformations are not needed.

For some classes of problems, such as fluid-structure interaction and metal forming processes involving severe deformations, difficulties arise with both the Eulerian and Lagrangian descriptions of motion. These classes of problems have two difficulties in common. First, the deformation is so severe that keeping track of the initial material configuration is impractical. Second, they involve moving boundaries, such that the motion cannot be represented as a function of position in the deformed configuration.

The arbitrary Lagrangian-Eulerian (ALE) description is a tradeoff that enables both representing a domain with moving boundaries as well as limiting distortions in the resulting discretisation grids. Fields are given as functions of position in an arbitrary reference configuration $\Omega^{\mathcal{B}}$ given by the reference motion $\boldsymbol{\Upsilon}_0 \colon \Omega_0^{\mathcal{B}} \times \mathbb{R}^+ \to \mathbb{R}^3$, which is continuous and invertible with respect to the first parameter, as $\Omega^{\mathcal{B}} \coloneqq \{\boldsymbol{X} = \boldsymbol{\Upsilon}_0(\boldsymbol{X}_0, t) | \boldsymbol{X}_0 \in \Omega_0^{\mathcal{B}}\}$.

The motion is given in the reference configuration by $\boldsymbol{x} = \boldsymbol{\varphi}(\boldsymbol{X}, t) \coloneqq \boldsymbol{\varphi}_0(\boldsymbol{\Upsilon}_0^{-1}(\boldsymbol{X}, t), t)$. Similarly, any scalar or tensor field $q = q_0(\boldsymbol{X}_0, t)$ is given in the reference configuration by $q = q(\boldsymbol{X}, t) = q_0(\boldsymbol{\Upsilon}_0^{-1}(\boldsymbol{X}, t), t)$. The gradient of a scalar field q and the gradient and divergence of a tensor field $\boldsymbol{q}$ in the reference configuration are denoted, respectively, by

$$\operatorname{Grad} q \coloneqq \frac{\partial}{\partial \boldsymbol{X}} q(\boldsymbol{X}, t)\,, \tag{3.1.10}$$

$$\operatorname{Grad} \boldsymbol{q} \coloneqq \frac{\partial}{\partial \boldsymbol{X}} \boldsymbol{q}(\boldsymbol{X}, t)\,, \tag{3.1.11}$$

$$\operatorname{Div} \boldsymbol{q} \coloneqq (\operatorname{Grad} \boldsymbol{q}) : \mathbf{1}. \tag{3.1.12}$$

In particular, the gradient of the motion $\boldsymbol{\varphi}$ in the reference configuration is denoted by

$$\boldsymbol{F}_{\mathrm{c}} \coloneqq \frac{\partial}{\partial \boldsymbol{X}} \boldsymbol{\varphi}(\boldsymbol{X}, t) = \operatorname{Grad} \boldsymbol{\varphi}\,, \tag{3.1.13}$$

where the subscript c refers to the current configuration.

It is related to the deformation gradient (3.1.8), through the chain rule, by

$$\begin{aligned}\boldsymbol{F} &= \left(\frac{\partial \boldsymbol{\varphi}}{\partial \boldsymbol{X}}\right)\left(\frac{\partial \boldsymbol{\Upsilon}_0}{\partial \boldsymbol{X}_0}\right) \\ &= \boldsymbol{F}_{\mathrm{c}}\,\mathrm{Grad}_0\,\boldsymbol{\Upsilon}_0\,,\end{aligned} \tag{3.1.14}$$

so that by defining the reference motion gradient

$$\boldsymbol{F}_{\mathrm{r}} \coloneqq \mathrm{Grad}_0\,\boldsymbol{\Upsilon}_0\,, \tag{3.1.15}$$

the deformation gradient can be decomposed as

$$\boldsymbol{F} = \boldsymbol{F}_{\mathrm{c}}\boldsymbol{F}_{\mathrm{r}}\,. \tag{3.1.16}$$

Thus, by defining the reference motion Jacobian as

$$J_{\mathrm{r}} = \det \boldsymbol{F}_{\mathrm{r}}\,, \tag{3.1.17}$$

The determinant of the deformation gradient is

$$J = J_{\mathrm{r}}\,\det \boldsymbol{F}_{\mathrm{c}}\,. \tag{3.1.18}$$

Gradients in the reference and current configurations are related, through the chain rule, by

$$\frac{\partial\,\tilde{\bullet}}{\partial \boldsymbol{x}} = \frac{\partial\,\bullet}{\partial \boldsymbol{X}}\left(\frac{\partial \boldsymbol{x}}{\partial \boldsymbol{X}}\right)^{-1}\,, \tag{3.1.19}$$

that is

$$\nabla\,\bullet = (\mathrm{Grad}\,\bullet)\,\boldsymbol{F}_{\mathrm{c}}^{-1}\,. \tag{3.1.20}$$

The material time derivative of the reference motion is the reference velocity

$$\boldsymbol{V} \coloneqq \frac{\partial}{\partial t}\boldsymbol{\Upsilon}_0(\boldsymbol{X}_0, t). \tag{3.1.21}$$

It gives the material time derivative in the reference configuration of a scalar field $q(\boldsymbol{X},t) = q_0(\boldsymbol{X}_0,t)$ in a form analogous to that in the current configuration in (3.1.6) as

$$\begin{aligned}\dot{q}(\boldsymbol{X},t) &\coloneqq \frac{\partial}{\partial t} q_0(\boldsymbol{X}_0,t)\Big|_{\boldsymbol{X}_0=\boldsymbol{\Upsilon}_0^{-1}(\boldsymbol{X},t)} \\ &= \left(\frac{\partial q}{\partial t} + (\operatorname{Grad} q)\cdot\boldsymbol{V}\right)\Big|_{(\boldsymbol{X},t)} . \end{aligned} \tag{3.1.22}$$

Similarly, for a tensor field $\boldsymbol{q}$, the total time derivative in the reference configuration is

$$\dot{\boldsymbol{q}}(\boldsymbol{X},t) = \left(\frac{\partial \boldsymbol{q}}{\partial t} + (\operatorname{Grad} \boldsymbol{q})\boldsymbol{V}\right)\Big|_{(\boldsymbol{X},t)} . \tag{3.1.23}$$

The velocity is then given in the reference configuration by

$$\begin{aligned}\boldsymbol{v} &= \frac{\partial \boldsymbol{\varphi}}{\partial t} + (\operatorname{Grad} \boldsymbol{\varphi})\boldsymbol{V} \\ &= \frac{\partial \boldsymbol{\varphi}}{\partial t} + \boldsymbol{F}_{\mathrm{c}}\boldsymbol{V} . \end{aligned} \tag{3.1.24}$$

The acceleration $\boldsymbol{a}$, which is the material time derivative of the velocity $\boldsymbol{v}$, is given from equations (3.1.22) and (3.1.24) by

$$\begin{aligned} a_i &= \frac{\partial}{\partial t}\left(\frac{\partial \varphi_i}{\partial t} + \varphi_{i,j}V_j\right) + \frac{\partial}{\partial X_j}\left(\frac{\partial \varphi_i}{\partial t} + \varphi_{i,k}V_k\right)V_j \\ &= \frac{\partial^2 \varphi_i}{\partial t^2} + \frac{\partial \varphi_{i,j}}{\partial t}V_j + \varphi_{i,j}\frac{\partial V_j}{\partial t} + \left(\frac{\partial}{\partial X_j}\frac{\partial \varphi_i}{\partial t}\right)V_j + \varphi_{i,jk}V_jV_k + \varphi_{i,j}V_{j,k}V_k \\ &= \frac{\partial^2 \varphi_i}{\partial t^2} + 2\frac{\partial \varphi_{i,j}}{\partial t}V_j + \varphi_{i,j}\left(\frac{\partial V_j}{\partial t} + V_{j,k}V_k\right) + \varphi_{i,jk}V_jV_k . \end{aligned} \tag{3.1.25}$$

In coordinate-free form,

$$\boldsymbol{a} = \frac{\partial^2 \boldsymbol{\varphi}}{\partial t^2} + 2\left(\frac{\partial \boldsymbol{F}_{\mathrm{c}}}{\partial t}\right)\boldsymbol{V} + \boldsymbol{F}_{\mathrm{c}}\left(\frac{\partial \boldsymbol{V}}{\partial t} + (\operatorname{Grad}\boldsymbol{V})\,\boldsymbol{V}\right) + ((\operatorname{Grad}\boldsymbol{F}_{\mathrm{c}})\,\boldsymbol{V})\,\boldsymbol{V} , \tag{3.1.26}$$

where $\frac{\partial \boldsymbol{F}_{\mathrm{c}}}{\partial t} = \frac{\partial}{\partial t}\operatorname{Grad}\boldsymbol{\varphi}$.

Equation (3.1.22) also relates the spatial and temporal derivatives of the material configuration by noting that

$$\begin{aligned}\frac{\mathrm{D}\boldsymbol{X}_0}{\mathrm{D}t} &= \frac{\partial \boldsymbol{\Upsilon}_0^{-1}}{\partial t} + \left(\frac{\partial \boldsymbol{\Upsilon}_0^{-1}}{\partial \boldsymbol{X}}\right)\boldsymbol{V} \\ &= \boldsymbol{0} , \end{aligned} \tag{3.1.27}$$

which gives

$$\frac{\partial \boldsymbol{\Upsilon}_0^{-1}}{\partial t} = -\boldsymbol{F}_{\mathrm{r}}^{-1}\boldsymbol{V}\,. \tag{3.1.28}$$

Notations of fields in the three configurations are summarised in Table 3.1.

The gradient in the reference configuration of the reference velocity is an important variable which we denote by

$$\boldsymbol{L} \coloneqq \mathrm{Grad}\ \boldsymbol{V}\,, \tag{3.1.29}$$

and whose symmetric and skew symmetric parts we denote by

$$\boldsymbol{D} = \frac{1}{2}\left(\boldsymbol{L} + \boldsymbol{L}^{\mathrm{t}}\right)\,, \tag{3.1.30}$$

$$\boldsymbol{W} = \frac{1}{2}\left(\boldsymbol{L} - \boldsymbol{L}^{\mathrm{t}}\right)\,. \tag{3.1.31}$$

It can be obtained in terms of $\boldsymbol{F}_{\mathrm{r}}$ as

$$\begin{aligned} L_{ij} &= \frac{\partial V_i}{\partial X_j} \\ &= \frac{\partial V_{0_i}}{\partial X_{0_k}} \left(\frac{\partial \Upsilon_{0_j}}{\partial X_{0_k}}\right)^{-1} \\ &= \left[\frac{\partial}{\partial X_{0_k}}\left(\frac{\partial \Upsilon_{0_i}}{\partial t}\right)\right] \left(\frac{\partial \Upsilon_{0_j}}{\partial X_{0_k}}\right)^{-1} \\ &= \left[\frac{\partial}{\partial t}\left(\frac{\partial \Upsilon_{0_i}}{\partial X_{0_k}}\right)\right] \left(\frac{\partial \Upsilon_{0_j}}{\partial X_{0_k}}\right)^{-1}\,, \end{aligned} \tag{3.1.32}$$

which, in coordinate-free form, reads

$$\begin{aligned} \boldsymbol{L} &= \left[\frac{\partial}{\partial t}\left(\frac{\partial \boldsymbol{\Upsilon}_0}{\partial \boldsymbol{X}_0}\right)\right] \left(\frac{\partial \boldsymbol{\Upsilon}_0}{\partial \boldsymbol{X}_0}\right)^{-1} \\ &= \dot{\boldsymbol{F}}_{\mathrm{r}}\boldsymbol{F}_{\mathrm{r}}^{-1}\,. \end{aligned} \tag{3.1.33}$$

Table 3.1: Notations in material, reference, and current configurations

	Material configuration	Reference configuration	Current configuration
motion $\boldsymbol{x}$	$\boldsymbol{\varphi}_0(\boldsymbol{X}_0, t)$	$\boldsymbol{\varphi}(\boldsymbol{X}, t)$	$\boldsymbol{x}$
reference motion $\boldsymbol{X}$	$\boldsymbol{\Upsilon}_0(\boldsymbol{X}_0, t)$	$\boldsymbol{X}$	$\boldsymbol{\varphi}^{-1}(\boldsymbol{x}, t)$
material point $\boldsymbol{X}_0$	$\boldsymbol{X}_0$	$\boldsymbol{\Upsilon}_0^{-1}(\boldsymbol{X}, t)$	$\boldsymbol{\varphi}_0^{-1}(\boldsymbol{x}, t)$
velocity $\boldsymbol{v}$	$\frac{\partial}{\partial t}\boldsymbol{\varphi}_0(\boldsymbol{X}_0, t)$	$\frac{\partial}{\partial t}\boldsymbol{\varphi}(\boldsymbol{X}, t) + \left(\frac{\partial}{\partial \boldsymbol{X}}\boldsymbol{\varphi}(\boldsymbol{X}, t)\right)\boldsymbol{V}$	$\tilde{\boldsymbol{v}}(\boldsymbol{x}, t)$
reference velocity $\boldsymbol{V}$	$\frac{\partial}{\partial t}\boldsymbol{\Upsilon}_0(\boldsymbol{X}_0, t)$	$\boldsymbol{V}(\boldsymbol{X}, t)$	$\frac{\partial}{\partial t}\boldsymbol{\varphi}^{-1}(\boldsymbol{x}, t) + \left(\frac{\partial}{\partial \boldsymbol{x}}\boldsymbol{\varphi}^{-1}(\boldsymbol{x}, t)\right)\boldsymbol{v}$
acceleration $\boldsymbol{a}$	$\frac{\partial^2}{\partial t^2}\boldsymbol{\varphi}_0(\boldsymbol{X}_0, t)$	equation (3.1.26)	$\frac{\partial}{\partial t}\tilde{\boldsymbol{v}}(\boldsymbol{x}, t) + \left(\frac{\partial}{\partial \boldsymbol{x}}\tilde{\boldsymbol{v}}(\boldsymbol{x}, t)\right)\boldsymbol{v}$
a field q	$q_0(\boldsymbol{X}_0, t)$	$q(\boldsymbol{X}, t)$	$\tilde{q}(\boldsymbol{x}, t)$
$\dot{q}$	$\frac{\partial}{\partial t}q_0(\boldsymbol{X}_0, t)$	$\frac{\partial}{\partial t}q(\boldsymbol{X}, t) + \left(\frac{\partial}{\partial \boldsymbol{X}}q(\boldsymbol{X}, t)\right) \cdot \boldsymbol{V}$	$\frac{\partial}{\partial t}\tilde{q}(\boldsymbol{x}, t) + \left(\frac{\partial}{\partial \boldsymbol{x}}\tilde{q}(\boldsymbol{x}, t)\right) \cdot \boldsymbol{v}$
$\mathrm{Grad}_0\, q$	$\frac{\partial}{\partial \boldsymbol{X}_0}q_0(\boldsymbol{X}_0, t)$	$\frac{\partial}{\partial \boldsymbol{X}}q(\boldsymbol{X}, t)\left(\frac{\partial}{\partial \boldsymbol{X}}\boldsymbol{\Upsilon}_0^{-1}(\boldsymbol{X}, t)\right)^{-1}$	$\frac{\partial}{\partial \boldsymbol{x}}\tilde{q}(\boldsymbol{x}, t)\left(\frac{\partial}{\partial \boldsymbol{x}}\boldsymbol{\varphi}_0^{-1}(\boldsymbol{x}, t)\right)^{-1}$
$\mathrm{Grad}\, q$	$\frac{\partial}{\partial \boldsymbol{X}_0}q_0(\boldsymbol{X}_0, t)\left(\frac{\partial}{\partial \boldsymbol{X}_0}\boldsymbol{\Upsilon}_0(\boldsymbol{X}_0, t)\right)^{-1}$	$\frac{\partial}{\partial \boldsymbol{X}}q(\boldsymbol{X}, t)$	$\frac{\partial}{\partial \boldsymbol{x}}\tilde{q}(\boldsymbol{x}, t)\left(\frac{\partial}{\partial \boldsymbol{x}}\boldsymbol{\varphi}^{-1}(\boldsymbol{x}, t)\right)^{-1}$
∇q	$\frac{\partial}{\partial \boldsymbol{X}_0}q_0(\boldsymbol{X}_0, t)\left(\frac{\partial}{\partial \boldsymbol{X}_0}\boldsymbol{\varphi}_0(\boldsymbol{X}_0, t)\right)^{-1}$	$\frac{\partial}{\partial \boldsymbol{X}}q(\boldsymbol{X}, t)\left(\frac{\partial}{\partial \boldsymbol{X}}\boldsymbol{\varphi}(\boldsymbol{X}, t)\right)^{-1}$	$\frac{\partial}{\partial \boldsymbol{x}}\tilde{q}(\boldsymbol{x}, t)$

3.1.1 Exponential and Logarithm of a Symmetric Tensor

Let $\boldsymbol{s}$ be a symmetric tensor that has the spectral decomposition $\boldsymbol{s} = \sum \lambda_i \boldsymbol{q}_i \otimes \boldsymbol{q}_i$, where λ_i are the real eigenvalues and $\boldsymbol{q}_i$ are the corresponding orthonormal eigenvectors, i.e. $\boldsymbol{q}_i \cdot \boldsymbol{q}_j = \delta_{ij}$, where δ_{ij} is the Kronecker delta

$$\delta_{ij} = \begin{cases} 1 & \text{if} \quad i = j \\ 0 & \text{otherwise}\,. \end{cases} \tag{3.1.34}$$

Then the exponential of $\boldsymbol{s}$ is given by

$$\exp \boldsymbol{s} = \sum (\exp \lambda_i)\, \boldsymbol{q}_i \otimes \boldsymbol{q}_i\,. \tag{3.1.35}$$

Similarly, if $\boldsymbol{s}$ is positive definite so that its eigenvalues are strictly positive $\lambda_i > 0$, then the logarithm of $\boldsymbol{s}$ is

$$\log \boldsymbol{s} = \sum (\log \lambda_i)\, \boldsymbol{q}_i \otimes \boldsymbol{q}_i\,. \tag{3.1.36}$$

The trace and the determinant of a tensor are both rotation invariant measures. As a result, the trace of a symmetric tensor equals the sum of its eigenvalues, and the determinant of a symmetric tensor equals the product of its eigenvalues

$$\operatorname{tr} \boldsymbol{s} = \sum \lambda_i\,, \tag{3.1.37}$$

$$\det \boldsymbol{s} = \prod \lambda_i\,. \tag{3.1.38}$$

This relates the determinant of a tensor to the trace of its log.

$$\operatorname{tr} (\log \boldsymbol{s}) = \log (\det \boldsymbol{s})\ . \tag{3.1.39}$$

In particular, if a tensor has a unit determinant, then its logarithm is a deviatoric tensor. Similarly,

$$\det (\exp \boldsymbol{s}) = \exp (\operatorname{tr} \boldsymbol{s})\ , \tag{3.1.40}$$

so that, in particular, the exponential of a deviatoric tensor has a unit determinant.

3.2 Strain Measures

The right and left Cauchy-green deformation tensors are defined respectively by

$$\boldsymbol{C} = \boldsymbol{F}^{\mathrm{t}}\boldsymbol{F}\,, \tag{3.2.1}$$

and

$$\boldsymbol{b} = \boldsymbol{F}\boldsymbol{F}^{\mathrm{t}}\,. \tag{3.2.2}$$

The velocity gradient is given by

$$\boldsymbol{l} = \frac{\partial \boldsymbol{v}}{\partial \boldsymbol{x}} = \dot{\boldsymbol{F}}\boldsymbol{F}^{-1}\,. \tag{3.2.3}$$

This can be decomposed into its symmetric and antisymmetric parts, namely, the rate of deformation tensor

$$\boldsymbol{d} = \frac{1}{2}\left(\boldsymbol{l} + \boldsymbol{l}^{\mathrm{t}}\right)\,, \tag{3.2.4}$$

and the spin tensor

$$\boldsymbol{w} = \frac{1}{2}\left(\boldsymbol{l} - \boldsymbol{l}^{\mathrm{t}}\right)\,. \tag{3.2.5}$$

The finite strain plasticity model is based on a multiplicative decomposition of the deformation gradient into an elastic part $\boldsymbol{F}^{\mathrm{e}}$ and a plastic part $\boldsymbol{F}^{\mathrm{p}}$, that is,

$$\boldsymbol{F} = \boldsymbol{F}^{\mathrm{e}}\boldsymbol{F}^{\mathrm{p}}\,. \tag{3.2.6}$$

We define the elastic left Cauchy-Green deformation tensor

$$\boldsymbol{b}^{\mathrm{e}} = \boldsymbol{F}^{\mathrm{e}}\boldsymbol{F}^{\mathrm{e}^{\mathrm{t}}}\,, \tag{3.2.7}$$

and the plastic right Cauchy-Green deformation tensor

$$\boldsymbol{C}^{\mathrm{p}} = \boldsymbol{F}^{\mathrm{p}^{\mathrm{t}}}\boldsymbol{F}^{\mathrm{p}}\,, \tag{3.2.8}$$

and its inverse

$$\boldsymbol{G}^{\mathrm{p}} = \left(\boldsymbol{C}^{\mathrm{p}}\right)^{-1}\,. \tag{3.2.9}$$

These tensors are related by

$$\boldsymbol{b}^{\mathrm{e}} = \boldsymbol{F}\boldsymbol{G}^{\mathrm{p}}\boldsymbol{F}^{\mathrm{t}}\,. \tag{3.2.10}$$

The plastic strain is assumed volume preserving, so that

$$\det(\boldsymbol{F}^{\mathrm{p}}) = 1\,, \tag{3.2.11}$$

and, as a consequence, the deformation Jacobian is given by the determinant of the elastic part of the deformation gradient

$$J = \det \boldsymbol{F} = \det \boldsymbol{F}^{\mathrm{e}}\,. \tag{3.2.12}$$

This gives the volume-preserving part of $\boldsymbol{b}^{\mathrm{e}}$ as

$$\bar{\boldsymbol{b}}^{\mathrm{e}} = J^{-2/3}\,\boldsymbol{b}^{\mathrm{e}}\,, \tag{3.2.13}$$

such that

$$\boldsymbol{b}^{\mathrm{e}} = J^{2/3}\bar{\boldsymbol{b}}^{\mathrm{e}}\,, \tag{3.2.14}$$

$$\det \bar{\boldsymbol{b}}^{\mathrm{e}} = 1\,. \tag{3.2.15}$$

The volume-preserving part of the left Cauchy-Green elastic tensor $\bar{\boldsymbol{b}}^{\mathrm{e}}$ is symmetric positive definite, so that its logarithm $\log \bar{\boldsymbol{b}}^{\mathrm{e}}$ is always well-defined by (3.1.36), and is deviatoric since by (3.2.15) and (3.1.39)

$$\operatorname{tr}\left(\log \bar{\boldsymbol{b}}^{\mathrm{e}}\right) = 0\,. \tag{3.2.16}$$

From (3.2.10), the total time derivative of $\boldsymbol{b}^{\mathrm{e}}$ is given in terms of its Lie derivative, which is defined as

$$\mathscr{L}_v \boldsymbol{b}^{\mathrm{e}} \coloneqq \boldsymbol{F}\dot{\boldsymbol{G}}^{\mathrm{p}}\boldsymbol{F}^{\mathrm{t}}\,, \tag{3.2.17}$$

by

$$\begin{aligned}\dot{\boldsymbol{b}}^{\mathrm{e}} &= \dot{\boldsymbol{F}}\boldsymbol{G}^{\mathrm{p}}\boldsymbol{F}^{\mathrm{t}} + \boldsymbol{F}\boldsymbol{G}^{\mathrm{p}}\dot{\boldsymbol{F}}^{\mathrm{t}} + \boldsymbol{F}\dot{\boldsymbol{G}}^{\mathrm{p}}\boldsymbol{F}^{\mathrm{t}} \\ &= \boldsymbol{l}\boldsymbol{b}^{\mathrm{e}} + \boldsymbol{b}^{\mathrm{e}}\boldsymbol{l}^{\mathrm{t}} + \mathscr{L}_v \boldsymbol{b}^{\mathrm{e}}.\end{aligned} \tag{3.2.18}$$

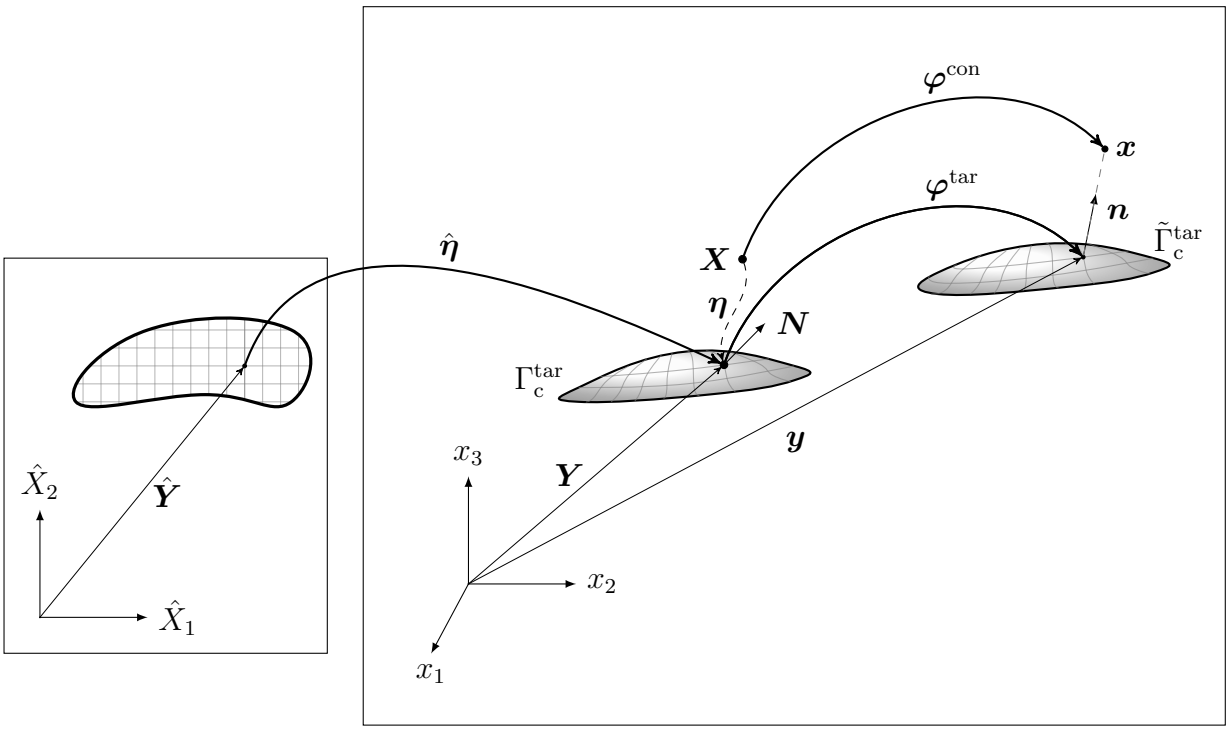

Figure 3.2: Contact target surface configurations

3.3 Multibody Frictional Contact

Frictional contact occurs between two deformable bodies given in the reference configuration by Ω^{con} and $\Omega^{\mathrm{tar}} \subset \mathbb{R}^3$. The subset of the boundary of each body that may potentially come into contact with the other is denoted, in the reference configuration, by $\Gamma_{\mathrm{c}}^{\mathcal{B}} \subseteq \partial\Omega^{\mathcal{B}}$, $\mathcal{B} \in \{\mathrm{con}, \mathrm{tar}\}$. It is expedient to designate one of the bodies as the contactor and the other as the target, and in the following, without loss of generality, these roles are respectively assigned to Ω^{con} and Ω^{tar}.

To avoid ambiguity, functions on the contact surfaces are distinguished by superscripts for the contactor and the target surfaces. In particular, the motion of the contactor surface is given by $\boldsymbol{\varphi}^{\mathrm{con}} \coloneqq \boldsymbol{\varphi}|_{\Gamma_{\mathrm{c}}^{\mathrm{con}}}$, and that of the target surface by $\boldsymbol{\varphi}^{\mathrm{tar}} \coloneqq \boldsymbol{\varphi}|_{\Gamma_{\mathrm{c}}^{\mathrm{tar}}}$.

For each contactor point $\boldsymbol{X} \in \Gamma_{\mathrm{c}}^{\mathrm{con}}$, a corresponding target point $\boldsymbol{Y} = \boldsymbol{\eta}(\boldsymbol{X}, t) \in \Gamma_{\mathrm{c}}^{\mathrm{tar}}$ is considered such that the distance in the current configuration is minimised between the

two points $\boldsymbol{x} = \boldsymbol{\varphi}(\boldsymbol{X}, t)$ and $\boldsymbol{y} = \boldsymbol{\varphi}(\boldsymbol{Y}, t)$. This means that

$$\left\|\boldsymbol{\varphi}^{\mathrm{con}}(\boldsymbol{X}, t) - \boldsymbol{\varphi}^{\mathrm{tar}}(\boldsymbol{\eta}(\boldsymbol{X}, t), t)\right\| \leq \left\|\boldsymbol{\varphi}^{\mathrm{con}}(\boldsymbol{X}, t) - \boldsymbol{\varphi}^{\mathrm{tar}}(\boldsymbol{Y}', t)\right\| \text{ for any } \boldsymbol{Y}' \in \Gamma_{\mathrm{c}}^{\mathrm{tar}} . \tag{3.3.1}$$

The contact geometry is represented in Figure 3.2.

The position $\boldsymbol{y} = \boldsymbol{\varphi}^{\mathrm{tar}}\left(\boldsymbol{\eta}\left(\boldsymbol{X}, t\right), t\right)$ of the target point in the current configuration is not only dependent on the deformation $\boldsymbol{\varphi}^{\mathrm{tar}}$, but also on the position of the target point in the reference configuration $\boldsymbol{Y} = \boldsymbol{\eta}(\boldsymbol{X}, t)$. Thus, its partial time derivative, with the contactor position in the reference configuration $\boldsymbol{X}$ fixed, is given through the chain rule by

$$\frac{\partial}{\partial t}\varphi_i^{\mathrm{tar}}(\boldsymbol{\eta}(\boldsymbol{X}, t), t) = \frac{\partial}{\partial t}\varphi_i^{\mathrm{tar}}(\boldsymbol{Y}, t)\bigg|_{\boldsymbol{Y}=\boldsymbol{\eta}(\boldsymbol{X},t)} + \left[\frac{\partial}{\partial Y_j}\varphi_i^{\mathrm{tar}}\left(\boldsymbol{Y}, t\right)\bigg|_{\boldsymbol{Y}=\boldsymbol{\eta}(\boldsymbol{X},t)}\right]\frac{\partial}{\partial t}\eta_j(\boldsymbol{X}, t) . \tag{3.3.2}$$

This is needed for computing the slip velocity, which will be described in Subsection 3.3.3.

As shown in Figure 3.2, the target surface in the reference configuration $\Gamma_{\mathrm{c}}^{\mathrm{tar}} \subset \mathbb{R}^3$ is parameterised by a region $\hat{\Gamma}^{\mathrm{tar}} \subset \mathbb{R}^2$ through a continuous bijective mapping $\hat{\boldsymbol{\eta}} : \hat{\Gamma}^{\mathrm{tar}} \to \Gamma_{\mathrm{c}}^{\mathrm{tar}}$ such that $\boldsymbol{Y} = \hat{\boldsymbol{\eta}}(\hat{\boldsymbol{Y}})$. Here, $\hat{\boldsymbol{Y}} = \hat{\boldsymbol{Y}}(\boldsymbol{X}, t) \in \hat{\Gamma}^{\mathrm{tar}}$ is given by $\hat{\boldsymbol{Y}}(\boldsymbol{X}, t) = \hat{\boldsymbol{\eta}}^{-1}\left(\boldsymbol{\eta}(\boldsymbol{X}, t)\right)$. Then, by condition (3.3.1), for any $\hat{\boldsymbol{Y}}' \in \hat{\Gamma}^{\mathrm{tar}}$,

$$\frac{1}{2}\left\|\boldsymbol{\varphi}^{\mathrm{con}}(\boldsymbol{X}, t) - \boldsymbol{\varphi}^{\mathrm{tar}}\left(\hat{\boldsymbol{\eta}}\left(\hat{\boldsymbol{Y}}(\boldsymbol{X}, t)\right), t\right)\right\|^2 \leq \frac{1}{2}\left\|\boldsymbol{\varphi}^{\mathrm{con}}(\boldsymbol{X}, t) - \boldsymbol{\varphi}^{\mathrm{tar}}\left(\hat{\boldsymbol{\eta}}\left(\hat{\boldsymbol{Y}}'\right), t\right)\right\|^2 . \tag{3.3.3}$$

This requires that

$$\frac{\partial}{\partial \hat{\boldsymbol{Y}}}\bigg|_{\hat{\boldsymbol{Y}}=\hat{\boldsymbol{Y}}(\boldsymbol{X},t)}\left(\frac{1}{2}\left\|\boldsymbol{\varphi}^{\mathrm{con}}(\boldsymbol{X}, t) - \boldsymbol{\varphi}^{\mathrm{tar}}\left(\hat{\boldsymbol{\eta}}\left(\hat{\boldsymbol{Y}}\right), t\right)\right\|^2\right) = 0 , \tag{3.3.4}$$

which, by the chain rule, gives

$$\left[\boldsymbol{\varphi}^{\mathrm{con}}(\boldsymbol{X}, t) - \boldsymbol{\varphi}^{\mathrm{tar}}\left(\boldsymbol{\eta}(\boldsymbol{X}, t), t\right)\right] \cdot \left\{\left[\frac{\partial}{\partial \boldsymbol{Y}}\bigg|_{\boldsymbol{Y}=\boldsymbol{\eta}(\boldsymbol{X},t)}\boldsymbol{\varphi}^{\mathrm{tar}}(\boldsymbol{Y}, t)\right]\frac{\partial \hat{\boldsymbol{\eta}}}{\partial \hat{\boldsymbol{Y}}}\bigg|_{\hat{\boldsymbol{Y}}=\hat{\boldsymbol{Y}}(\boldsymbol{X},t)}\right\} = \boldsymbol{0} . \tag{3.3.5}$$

For convenience, we define the tensors

$$\boldsymbol{\Xi} = \boldsymbol{\Xi}(\hat{\boldsymbol{Y}}) \coloneqq \frac{\partial \hat{\boldsymbol{\eta}}}{\partial \hat{\boldsymbol{Y}}}\,, \tag{3.3.6}$$

$$\begin{aligned}\boldsymbol{G} = \boldsymbol{G}(\boldsymbol{Y}, t) &\coloneqq \left[\frac{\partial}{\partial \boldsymbol{Y}} \boldsymbol{\varphi}^{\mathrm{tar}}(\boldsymbol{Y}, t)\right] \left.\frac{\partial \hat{\boldsymbol{\eta}}}{\partial \hat{\boldsymbol{Y}}}\right|_{\hat{\boldsymbol{Y}} = \hat{\boldsymbol{\eta}}^{-1}(\boldsymbol{Y})} \\ &= \left[\frac{\partial}{\partial \boldsymbol{Y}} \boldsymbol{\varphi}^{\mathrm{tar}}(\boldsymbol{Y}, t)\right] \boldsymbol{\Xi}\left(\hat{\boldsymbol{\eta}}^{-1}(\boldsymbol{Y})\right)\,. \end{aligned} \tag{3.3.7}$$

In array form,

$$\boldsymbol{\xi}_i \coloneqq \frac{\partial \hat{\boldsymbol{\eta}}}{\partial \hat{Y}_i} \in \mathbb{R}^3\,, \tag{3.3.8}$$

$$\boldsymbol{g}_i \coloneqq \frac{\partial}{\partial \hat{Y}_i}\left(\boldsymbol{\varphi}^{\mathrm{tar}} \circ \hat{\boldsymbol{\eta}}\right) = \left(\operatorname{Grad} \boldsymbol{\varphi}^{\mathrm{tar}}\right) \boldsymbol{\xi}_i \in \mathbb{R}^3\,, \tag{3.3.9}$$

$$\boldsymbol{\Xi} = \begin{bmatrix} | & | \\ \boldsymbol{\xi}_1 & \boldsymbol{\xi}_2 \\ | & | \end{bmatrix} \in \mathbb{R}^{3\times 2}\,, \tag{3.3.10}$$

$$\boldsymbol{G} = \begin{bmatrix} | & | \\ \boldsymbol{g}_1 & \boldsymbol{g}_2 \\ | & | \end{bmatrix} \in \mathbb{R}^{3\times 2}\,. \tag{3.3.11}$$

Thus, equation (3.3.5) becomes

$$\left[\boldsymbol{\varphi}^{\mathrm{con}}(\boldsymbol{X}, t) - \boldsymbol{\varphi}^{\mathrm{tar}}\left(\boldsymbol{\eta}(\boldsymbol{X}, t), t\right)\right] \cdot \boldsymbol{G}\left(\boldsymbol{\eta}(\boldsymbol{X}, t), t\right) = \boldsymbol{0}\,. \tag{3.3.12}$$

For a fixed contactor point $\boldsymbol{X} \in \Gamma_{\mathrm{c}}^{\mathrm{con}}$ and the corresponding target point $\boldsymbol{Y} = \boldsymbol{\eta}(\boldsymbol{X}, t)$, the partial time derivative of $\boldsymbol{\eta}$ can be obtained by differentiation of $\boldsymbol{Y} = \boldsymbol{\eta}\left(\boldsymbol{X}, t\right) = \hat{\boldsymbol{\eta}}\left(\hat{\boldsymbol{Y}}(\boldsymbol{X}, t)\right)$ using the chain rule to get

$$\begin{aligned}\frac{\partial}{\partial t}\boldsymbol{\eta}(\boldsymbol{X}, t) &= \left(\left.\frac{\partial}{\partial \hat{\boldsymbol{Y}}}\hat{\boldsymbol{\eta}}(\hat{\boldsymbol{Y}})\right|_{\hat{\boldsymbol{Y}} = \hat{\boldsymbol{Y}}(\boldsymbol{X}, t)}\right) \frac{\partial}{\partial t}\hat{\boldsymbol{Y}}(\boldsymbol{X}, t) \\ &= \boldsymbol{\Xi}\left(\hat{\boldsymbol{Y}}(\boldsymbol{X}, t)\right) \frac{\partial}{\partial t}\hat{\boldsymbol{Y}}(\boldsymbol{X}, t)\,. \end{aligned} \tag{3.3.13}$$

Thus, equation (3.3.2) becomes

$$\begin{aligned}\frac{\partial}{\partial t}\varphi_i^{\mathrm{tar}}(\boldsymbol{\eta}(\boldsymbol{X},t),t) &= \frac{\partial}{\partial t}\varphi_i^{\mathrm{tar}}(\boldsymbol{Y},t)\Big|_{\boldsymbol{Y}=\boldsymbol{\eta}(\boldsymbol{X},t)} + \left[\frac{\partial}{\partial Y_j}\varphi_i^{\mathrm{tar}}(\boldsymbol{Y},t)\Big|_{\boldsymbol{Y}=\boldsymbol{\eta}(\boldsymbol{X},t)}\right]\Xi_{jk}\left(\hat{\boldsymbol{Y}}(\boldsymbol{X},t)\right)\frac{\partial}{\partial t}\hat{Y}_k(\boldsymbol{X},t)\\ &= \frac{\partial}{\partial t}\varphi_i^{\mathrm{tar}}(\boldsymbol{Y},t)\Big|_{\boldsymbol{Y}=\boldsymbol{\eta}(\boldsymbol{X},t)} + G_{ik}\left(\boldsymbol{\eta}(\boldsymbol{X},t),t\right)\frac{\partial}{\partial t}\hat{Y}_k(\boldsymbol{X},t)\,. \qquad (3.3.14)\end{aligned}$$

In turn, the partial time derivative of $\hat{\boldsymbol{Y}}(\boldsymbol{X},t)$ is obtained as follows. First, the partial time derivative of $\boldsymbol{G}(\boldsymbol{\eta}(\boldsymbol{X},t),t)$ for a fixed contactor point $\boldsymbol{X}\in\Gamma_{\mathrm{c}}^{\mathrm{con}}$ and a target point $\boldsymbol{Y}=\boldsymbol{\eta}(\boldsymbol{X},t)\in\Gamma_{\mathrm{c}}^{\mathrm{tar}}$ is given, using the chain rule, by

$$\begin{aligned}\frac{\partial}{\partial t}G_{ij}\left(\boldsymbol{\eta}(\boldsymbol{X},t),t\right) =& \frac{\partial}{\partial t}\left[\varphi_{i,k}\left(\boldsymbol{\eta}(\boldsymbol{X},t),t\right)\,\Xi_{kj}\left(\hat{\boldsymbol{Y}}(\boldsymbol{X},t)\right)\right]\\ =& \left(\frac{\partial}{\partial t}\left[\varphi_{i,k}\left(\boldsymbol{Y},t\right)\right]\Big|_{\boldsymbol{Y}=\boldsymbol{\eta}(\boldsymbol{X},t)}\right)\Xi_{kj}\left(\hat{\boldsymbol{Y}}(\boldsymbol{X},t)\right)\\ &+\left(\frac{\partial}{\partial \hat{Y}_l}\left[\varphi_{i,k}\left(\hat{\boldsymbol{\eta}}(\hat{\boldsymbol{Y}}),t\right)\,\Xi_{kj}\left(\hat{\boldsymbol{Y}}\right)\right]\Big|_{\hat{\boldsymbol{Y}}=\hat{\boldsymbol{Y}}(\boldsymbol{X},t)}\right)\frac{\partial}{\partial t}\hat{Y}_l\left(\boldsymbol{X},t\right)\\ =& \left(\frac{\partial}{\partial t}\left[\varphi_{i,k}\left(\boldsymbol{Y},t\right)\right]\Big|_{\boldsymbol{Y}=\boldsymbol{\eta}(\boldsymbol{X},t)}\right)\Xi_{kj}\left(\hat{\boldsymbol{Y}}(\boldsymbol{X},t)\right)\\ &+\left(\frac{\partial}{\partial \hat{Y}_l}\left[G_{ij}\left(\hat{\boldsymbol{\eta}}(\hat{\boldsymbol{Y}}),t\right)\right]\Big|_{\hat{\boldsymbol{Y}}=\hat{\boldsymbol{Y}}(\boldsymbol{X},t)}\right)\frac{\partial}{\partial t}\hat{Y}_l\left(\boldsymbol{X},t\right)\,, \qquad (3.3.15)\end{aligned}$$

where

$$\begin{aligned}\frac{\partial}{\partial \hat{Y}_l}G_{ij}\left(\hat{\boldsymbol{\eta}}(\hat{\boldsymbol{Y}}),t\right) =& \varphi_{i,km}\left(\hat{\boldsymbol{\eta}}(\hat{\boldsymbol{Y}}),t\right)\,\Xi_{ml}\left(\hat{\boldsymbol{Y}}\right)\,\Xi_{kj}\left(\hat{\boldsymbol{Y}}\right)\\ &+\varphi_{i,k}\left(\hat{\boldsymbol{\eta}}(\hat{\boldsymbol{Y}}),t\right)\,\hat{\eta}_{k,jl}\left(\hat{\boldsymbol{Y}}\right)\,. \qquad (3.3.16)\end{aligned}$$

Next, differentiating both sides of (3.3.12) making use of (3.3.15) gives

$$\begin{aligned}&\left\{\frac{\partial}{\partial t}\varphi_i^{\mathrm{con}}(\boldsymbol{X},t) - \left[\frac{\partial}{\partial t}\varphi_i^{\mathrm{tar}}(\boldsymbol{Y},t)\right]_{\boldsymbol{Y}=\boldsymbol{\eta}(\boldsymbol{X},t)} - G_{ik}\left(\boldsymbol{\eta}(\boldsymbol{X},t),t\right)\,\frac{\partial}{\partial t}\hat{Y}_k(\boldsymbol{X},t)\right\}G_{ij}(\boldsymbol{\eta}(\boldsymbol{X},t),t)\\ &\quad+\left[\varphi_i^{\mathrm{con}}(\boldsymbol{X},t)-\varphi_i^{\mathrm{tar}}(\boldsymbol{\eta}(\boldsymbol{X},t),t)\right]\left[\left(\frac{\partial}{\partial t}\left[\varphi_{i,k}^{\mathrm{tar}}\left(\boldsymbol{Y},t\right)\right]\Big|_{\boldsymbol{Y}=\boldsymbol{\eta}(\boldsymbol{X},t)}\right)\Xi_{kj}\left(\hat{\boldsymbol{Y}}(\boldsymbol{X},t)\right)\right.\\ &\qquad\left.+\left(\frac{\partial}{\partial \hat{Y}_k}\left[G_{ij}\left(\hat{\boldsymbol{\eta}}(\hat{\boldsymbol{Y}}),t\right)\right]\Big|_{\hat{\boldsymbol{Y}}=\hat{\boldsymbol{Y}}(\boldsymbol{X},t)}\right)\frac{\partial}{\partial t}\hat{Y}_k\left(\boldsymbol{X},t\right)\right] = 0_j\,, \qquad (3.3.17)\end{aligned}$$

so that

$$\frac{\partial}{\partial t}\hat{Y}_k\left(\boldsymbol{X},t\right)=\left[\mathcal{A}_{jk}\left(\boldsymbol{X},t\right)\right]^{-1}\mathcal{V}_j\left(\boldsymbol{X},t\right)\,, \tag{3.3.18}$$

where

$$\begin{aligned}\mathcal{A}_{jk}\left(\boldsymbol{X},t\right)=&\,G_{ij}(\boldsymbol{\eta}(\boldsymbol{X},t),t)\,G_{ik}(\boldsymbol{\eta}(\boldsymbol{X},t),t)\\&-\left[\varphi_i^{\mathrm{con}}(\boldsymbol{X},t)-\varphi_i^{\mathrm{tar}}(\boldsymbol{\eta}(\boldsymbol{X},t),t)\right]\frac{\partial}{\partial\hat{Y}_k}\left[G_{ij}\left(\hat{\boldsymbol{\eta}}(\hat{\boldsymbol{Y}}),t\right)\right]\Big|_{\hat{\boldsymbol{Y}}=\hat{\boldsymbol{Y}}(\boldsymbol{X},t)}\,,\end{aligned} \tag{3.3.19}$$

and

$$\begin{aligned}\mathcal{V}_j\left(\boldsymbol{X},t\right)=&\left[\varphi_i^{\mathrm{con}}(\boldsymbol{X},t)-\varphi_i^{\mathrm{tar}}(\boldsymbol{\eta}(\boldsymbol{X},t),t)\right]\left(\frac{\partial}{\partial t}\left[\varphi_{i,k}^{\mathrm{tar}}\left(\boldsymbol{Y},t\right)\right]\Big|_{\boldsymbol{Y}=\boldsymbol{\eta}(\boldsymbol{X},t)}\right)\Xi_{kj}\left(\hat{\boldsymbol{Y}}(\boldsymbol{X},t)\right)\\&+\left[\frac{\partial}{\partial t}\varphi_i^{\mathrm{con}}(\boldsymbol{X},t)-\frac{\partial}{\partial t}\varphi_i^{\mathrm{tar}}(\boldsymbol{Y},t)\Big|_{\boldsymbol{Y}=\boldsymbol{\eta}(\boldsymbol{X},t)}\right]G_{ij}(\boldsymbol{\eta}(\boldsymbol{X},t),t)\,.\end{aligned} \tag{3.3.20}$$

Here, the gradient $\frac{\partial}{\partial\hat{Y}_k}G_{ij}\left(\hat{\boldsymbol{\eta}}(\hat{\boldsymbol{Y}}),t\right)$ given by (3.3.16) involves the second spatial derivative of the motion. As a result, the third spatial derivative enters into linearisation of the discretised system.

3.3.1 Normal and Tangential Components of Vectors

For a given point $\boldsymbol{Y}\in\ \Gamma_{\mathrm{c}}^{\mathrm{tar}}$ in the reference configuration and a given time t, any vector $\boldsymbol{w}\in\mathbb{R}^3$ can be decomposed into two components: a component $\boldsymbol{w}_{\mathrm{n}}$ which is orthogonal to the target surface in the current configuration $\tilde{\Gamma}_{\mathrm{c}}^{\mathrm{tar}}$ at $\boldsymbol{y}=\boldsymbol{\varphi}^{\mathrm{tar}}(\boldsymbol{Y},t)$, and another component $\boldsymbol{w}_{\mathrm{t}}$ which is tangent to $\tilde{\Gamma}_{\mathrm{c}}^{\mathrm{tar}}$ at $\boldsymbol{y}$, so that

$$\boldsymbol{w}_{\mathrm{n}}+\boldsymbol{w}_{\mathrm{t}}=\boldsymbol{w}\,, \tag{3.3.21}$$

$$(\boldsymbol{n}\otimes\boldsymbol{n})\,\boldsymbol{w}=\boldsymbol{w}_{\mathrm{n}}\,, \tag{3.3.22}$$

$$\boldsymbol{n}\cdot\boldsymbol{w}_{\mathrm{t}}=0\,. \tag{3.3.23}$$

The vectors $\boldsymbol{g}_i=\boldsymbol{g}_i(\boldsymbol{Y},t)$ defined in (3.3.9) form a basis for the plane of vectors tangent to $\tilde{\Gamma}_{\mathrm{c}}^{\mathrm{tar}}$ at $\boldsymbol{y}$, so that the tangential component $\boldsymbol{w}_{\mathrm{t}}$ is given by some $\hat{\boldsymbol{W}}=\begin{bmatrix}\hat{W}_1 & \hat{W}_2\end{bmatrix}^{\mathrm{T}}\in$

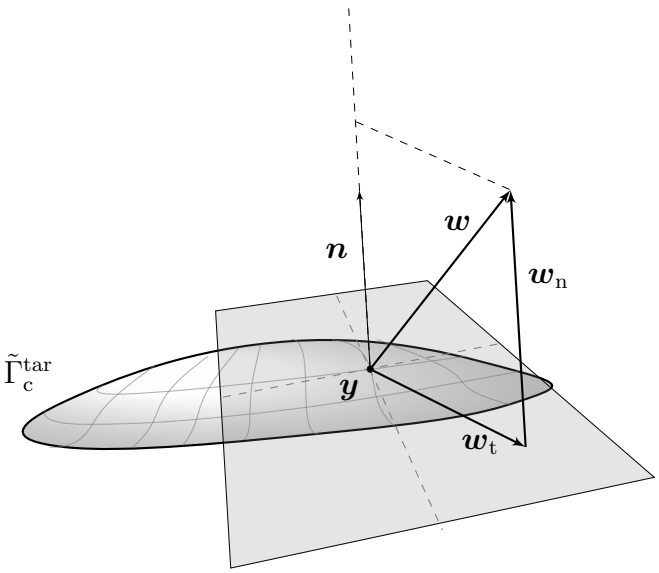

Figure 3.3: Normal and tangential components of a vector

$\mathbb{R}^2$ as $\boldsymbol{w}_\mathrm{t} = \boldsymbol{g}_i \hat{W}_i$. or, in array form,

$$\begin{bmatrix} | \\ \boldsymbol{w}_\mathrm{t} \\ | \end{bmatrix} = \begin{bmatrix} | & | \\ \boldsymbol{g}_1 & \boldsymbol{g}_2 \\ | & | \end{bmatrix} \begin{bmatrix} \hat{W}_1 \\ \hat{W}_2 \end{bmatrix} , \tag{3.3.24}$$

that is

$$\boldsymbol{w}_\mathrm{t} = \boldsymbol{G}\hat{\boldsymbol{W}} . \tag{3.3.25}$$

Furthermore, the vectors $\boldsymbol{g}_i$ are both orthogonal to the normal $\boldsymbol{n}$, so that $\boldsymbol{g}_i \cdot \boldsymbol{n} = 0$. In array form,

$$\begin{bmatrix} — & \boldsymbol{g}_1 & — \\ — & \boldsymbol{g}_2 & — \end{bmatrix} \begin{bmatrix} | \\ \boldsymbol{n} \\ | \end{bmatrix} = \begin{bmatrix} 0 \\ 0 \end{bmatrix} , \tag{3.3.26}$$

that is

$$\boldsymbol{G}^\mathrm{t}\boldsymbol{n} = \boldsymbol{0} . \tag{3.3.27}$$

Thus, pre-multiplying both sides of (3.3.21) by $\boldsymbol{G}^{\mathrm{t}}$ gives

$$\begin{aligned}\boldsymbol{G}^{\mathrm{t}}\boldsymbol{w} &= \boldsymbol{G}^{\mathrm{t}}\left(\boldsymbol{w}_{\mathrm{n}} + \boldsymbol{w}_{\mathrm{t}}\right)\\ &= \left(\boldsymbol{n}\cdot\boldsymbol{w}\right)\boldsymbol{G}^{\mathrm{t}}\boldsymbol{n} + \boldsymbol{G}^{\mathrm{t}}\boldsymbol{w}_{\mathrm{t}}\\ &= \boldsymbol{G}^{\mathrm{t}}\boldsymbol{w}_{\mathrm{t}}\\ &= \boldsymbol{G}^{\mathrm{t}}\boldsymbol{G}\hat{\boldsymbol{W}}\,. \end{aligned} \tag{3.3.28}$$

Since the vectors $\boldsymbol{g}_i$ are linearly independent, the tensor $\left(\boldsymbol{G}^{\mathrm{t}}\boldsymbol{G}\right)_{ij} = \boldsymbol{g}_i\cdot\boldsymbol{g}_j$ is invertible, so that pre-multiplying both sides of (3.3.28) by $\left(\boldsymbol{G}^{\mathrm{t}}\boldsymbol{G}\right)^{-1}$ gives

$$\hat{\boldsymbol{W}} = \left(\boldsymbol{G}^{\mathrm{t}}\boldsymbol{G}\right)^{-1}\boldsymbol{G}^{\mathrm{t}}\boldsymbol{w}\,, \tag{3.3.29}$$

which, by (3.3.25), gives

$$\boldsymbol{w}_{\mathrm{t}} = \boldsymbol{G}\left(\boldsymbol{G}^{\mathrm{t}}\boldsymbol{G}\right)^{-1}\boldsymbol{G}^{\mathrm{t}}\boldsymbol{w}\,. \tag{3.3.30}$$

The rank deficient tensors $\boldsymbol{G}\left(\boldsymbol{G}^{\mathrm{t}}\boldsymbol{G}\right)^{-1}\boldsymbol{G}^{\mathrm{t}}$ and $\boldsymbol{n}\otimes\boldsymbol{n}$ represent projections, respectively, onto the plane tangent to $\tilde{\Gamma}_{\mathrm{c}}^{\mathrm{tar}}$ at $\boldsymbol{y}$, and the line along the unit normal $\boldsymbol{n}$ of $\tilde{\Gamma}_{\mathrm{c}}^{\mathrm{tar}}$ at $\boldsymbol{y}$. Thus, since the two subspaces are orthogonal complements in $\mathbb{R}^3$,

$$\boldsymbol{n}\otimes\boldsymbol{n} + \boldsymbol{G}\left(\boldsymbol{G}^{\mathrm{t}}\boldsymbol{G}\right)^{-1}\boldsymbol{G}^{\mathrm{t}} = \boldsymbol{1}\,, \tag{3.3.31}$$

$$\left(\boldsymbol{n}\otimes\boldsymbol{n}\right)\left(\boldsymbol{G}\left(\boldsymbol{G}^{\mathrm{t}}\boldsymbol{G}\right)^{-1}\boldsymbol{G}^{\mathrm{t}}\right) = \left(\boldsymbol{G}\left(\boldsymbol{G}^{\mathrm{t}}\boldsymbol{G}\right)^{-1}\boldsymbol{G}^{\mathrm{t}}\right)\left(\boldsymbol{n}\otimes\boldsymbol{n}\right) = \boldsymbol{0}\,. \tag{3.3.32}$$

3.3.2 Normal Contact

The primary normal contact constraint is that contactor surface points may not penetrate into the bulk of the target in the current configuration. As a result, for a fixed contactor point $\boldsymbol{X}\in\Gamma_{\mathrm{c}}^{\mathrm{con}}$ given in the current configuration by $\boldsymbol{x} = \boldsymbol{\varphi}^{\mathrm{con}}(\boldsymbol{X},t)$, and a corresponding target point $\boldsymbol{Y} = \boldsymbol{\eta}(\boldsymbol{X},t)\in\Gamma_{\mathrm{c}}^{\mathrm{tar}}$ given in the current configuration by $\boldsymbol{y} = \boldsymbol{\varphi}^{\mathrm{tar}}(\boldsymbol{Y},t)$, with the outward unit normal of the target surface in the current configuration $\boldsymbol{\varphi}^{\mathrm{tar}}(\Gamma_{\mathrm{c}}^{\mathrm{tar}},t)$ at $\boldsymbol{y}$ given by $\boldsymbol{n} = \boldsymbol{n}\left(\boldsymbol{Y},t\right)$, define the penetration g by contactor point $\boldsymbol{x}$ into the current configuration of the target by

$$g(\boldsymbol{X},t) \coloneqq -\left[\boldsymbol{\varphi}^{\mathrm{con}}(\boldsymbol{X},t) - \boldsymbol{\varphi}^{\mathrm{tar}}(\boldsymbol{\eta}(\boldsymbol{X},t),t)\right]\cdot\boldsymbol{n}\left(\boldsymbol{\eta}(\boldsymbol{X},t),t\right)\,. \tag{3.3.33}$$

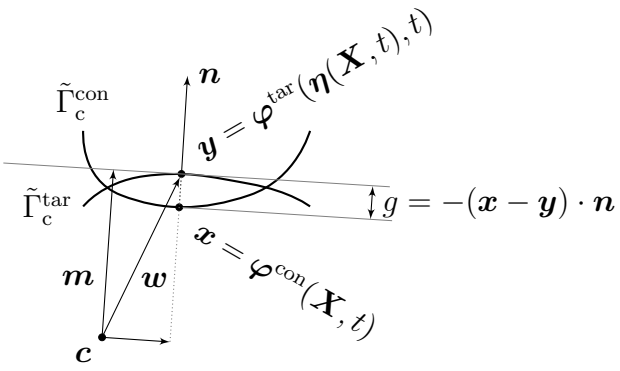

Figure 3.4: Normal contact penetration

We require that g be nonpositive. This is demonstrated in Figure 3.4.

The unit normal $\boldsymbol{n}$ is given in terms of the tensor $\boldsymbol{G}$. If a vector $\boldsymbol{w}$ forms an acute angle with the unit normal, $\boldsymbol{n} \cdot \boldsymbol{w} > 0$, then the projection of $\boldsymbol{w}$ onto the unit normal is in the direction of the unit normal. Such a vector $\boldsymbol{w}$ can be obtained using some point $\boldsymbol{c}$ in the interior of the target deformed configuration Ω^{tar}, as shown in Figure 3.4, by taking $\boldsymbol{w} = \boldsymbol{y} - \boldsymbol{c}$. The normal component $\boldsymbol{m}$ of $\boldsymbol{w}$ has the same direction as the unit normal, so that

$$\boldsymbol{n} = \frac{\boldsymbol{m}}{\|\boldsymbol{m}\|}\,. \tag{3.3.34}$$

It is is given by (3.3.22) and (3.3.31) as

$$\boldsymbol{m} = (\boldsymbol{n} \otimes \boldsymbol{n})\,\boldsymbol{w} = \left(\boldsymbol{1} - \boldsymbol{G}\left(\boldsymbol{G}^{\mathrm{t}}\boldsymbol{G}\right)^{-1}\boldsymbol{G}^{\mathrm{t}}\right)\boldsymbol{w}, \tag{3.3.35}$$

The interior point $\boldsymbol{c}$ is arbitrarily chosen, but remains fixed. Therefore, $\frac{\partial \boldsymbol{c}}{\partial t} = \boldsymbol{0}$, and the partial time derivative $\frac{\partial \boldsymbol{w}}{\partial t}$ of $\boldsymbol{w}$ is equivalent to that of $\boldsymbol{y}$ and is given, from (3.3.14), by

$$\frac{\partial \boldsymbol{w}}{\partial t} = \left.\frac{\partial \boldsymbol{\varphi}^{\mathrm{tar}}}{\partial t}\right|_{\boldsymbol{Y}=\boldsymbol{\eta}(\boldsymbol{X},t)} + \operatorname{Grad}\boldsymbol{\varphi}^{\mathrm{tar}}\frac{\partial \boldsymbol{\eta}}{\partial t}\,.$$

The partial time derivative $\frac{\partial \boldsymbol{n}}{\partial t}$ of the unit normal $\boldsymbol{n}$ is, from (3.3.34),

$$\begin{aligned}
\frac{\partial \boldsymbol{n}}{\partial t} &= \frac{\partial}{\partial t}\frac{\boldsymbol{m}}{\|\boldsymbol{m}\|} \\
&= \frac{1}{\|\boldsymbol{m}\|^2}\left[\|\boldsymbol{m}\|\frac{\partial \boldsymbol{m}}{\partial t} - \left(\frac{\partial}{\partial t}\|\boldsymbol{m}\|\right)\boldsymbol{m}\right] \\
&= \frac{1}{\|\boldsymbol{m}\|^2}\left[\|\boldsymbol{m}\|\frac{\partial \boldsymbol{m}}{\partial t} - \left(\frac{1}{\|\boldsymbol{m}\|}\left(\boldsymbol{m}\cdot\frac{\partial \boldsymbol{m}}{\partial t}\right)\right)\boldsymbol{m}\right] \\
&= \frac{1}{\|\boldsymbol{m}\|}\frac{\partial \boldsymbol{m}}{\partial t} - \left(\frac{\boldsymbol{m}}{\|\boldsymbol{m}\|}\cdot\frac{1}{\|\boldsymbol{m}\|}\frac{\partial \boldsymbol{m}}{\partial t}\right)\frac{\boldsymbol{m}}{\|\boldsymbol{m}\|} \\
&= \frac{1}{\|\boldsymbol{m}\|}\frac{\partial \boldsymbol{m}}{\partial t} - \left(\boldsymbol{n}\cdot\frac{1}{\|\boldsymbol{m}\|}\frac{\partial \boldsymbol{m}}{\partial t}\right)\boldsymbol{n} \\
&= (\mathbf{1}-\boldsymbol{n}\otimes\boldsymbol{n})\left(\frac{1}{\|\boldsymbol{m}\|}\frac{\partial \boldsymbol{m}}{\partial t}\right). \qquad (3.3.36)
\end{aligned}$$

Differentiation of both sides of the identity $\square^{-1}\square = \mathbf{1}$ using the product rule gives $\left(\frac{\partial}{\partial t}\square^{-1}\right)\square + \square^{-1}\left(\frac{\partial}{\partial t}\square\right) = \mathbf{0}$, which, by post-multiplication by $\square^{-1}$, gives the identity

$$\frac{\partial}{\partial t}\square^{-1} = -\square^{-1}\left(\frac{\partial}{\partial t}\square\right)\square^{-1}. \qquad (3.3.37)$$

The partial time derivative $\frac{\partial \boldsymbol{m}}{\partial t}$ of the unnormalised normal $\boldsymbol{m}$ is in turn given, from (3.3.35) and using the product rule, as

$$\begin{aligned}
\frac{\partial m_i}{\partial t} =& \frac{\partial}{\partial t}\left[\left(\delta_{im} - G_{ij}\left(G_{kj}G_{kl}\right)^{-1}G_{ml}\right)w_m\right] \\
=& \left(\delta_{im} - G_{ij}\left(G_{kj}G_{kl}\right)^{-1}G_{ml}\right)\frac{\partial}{\partial t}w_m \\
&+ \left[-\frac{\partial G_{ij}}{\partial t}\left(G_{kj}G_{kl}\right)^{-1}G_{ml} + G_{ij}\left(G_{kj}G_{kl}\right)^{-1}\left(\frac{\partial G_{nl}}{\partial t}G_{np} + G_{nl}\frac{\partial G_{np}}{\partial t}\right)\left(G_{qp}G_{qr}\right)^{-1}G_{mr}\right. \\
&\left. - G_{ij}\left(G_{kj}G_{kl}\right)^{-1}\frac{\partial G^{\mathrm{t}}_{ml}}{\partial t}\right]w_m, \qquad (3.3.38)
\end{aligned}$$

where the identity (3.3.37) was used in the term involving $\left(\boldsymbol{G}^{\mathrm{t}}\boldsymbol{G}\right)^{-1}$. Thus, substitution of (3.3.38) into (3.3.36) gives

$$\begin{aligned}
\frac{\partial \boldsymbol{n}}{\partial t} =& \frac{1}{\|\boldsymbol{m}\|}(\mathbf{1}-\boldsymbol{n}\otimes\boldsymbol{n})\frac{\partial \boldsymbol{m}}{\partial t} \\
=& \frac{1}{\|\boldsymbol{m}\|}(\mathbf{1}-\boldsymbol{n}\otimes\boldsymbol{n})\left(\mathbf{1}-\boldsymbol{G}\left(\boldsymbol{G}^{\mathrm{t}}\boldsymbol{G}\right)^{-1}\boldsymbol{G}^{\mathrm{t}}\right)\frac{\partial \boldsymbol{w}}{\partial t} \\
&+ (\mathbf{1}-\boldsymbol{n}\otimes\boldsymbol{n})\left[-\frac{\partial \boldsymbol{G}}{\partial t}\left(\boldsymbol{G}^{\mathrm{t}}\boldsymbol{G}\right)^{-1}\boldsymbol{G}^{\mathrm{t}} + \boldsymbol{G}\left(\boldsymbol{G}^{\mathrm{t}}\boldsymbol{G}\right)^{-1}\left(\frac{\partial \boldsymbol{G}^{\mathrm{t}}}{\partial t}\boldsymbol{G} + \boldsymbol{G}^{\mathrm{t}}\frac{\partial \boldsymbol{G}}{\partial t}\right)\left(\boldsymbol{G}^{\mathrm{t}}\boldsymbol{G}\right)^{-1}\boldsymbol{G}^{\mathrm{t}}\right. \\
&\left. - \boldsymbol{G}\left(\boldsymbol{G}^{\mathrm{t}}\boldsymbol{G}\right)^{-1}\frac{\partial \boldsymbol{G}^{\mathrm{t}}}{\partial t}\right]\frac{\boldsymbol{w}}{\|\boldsymbol{m}\|}. \qquad (3.3.39)
\end{aligned}$$

The first term vanishes by (3.3.31) and (3.3.32), so that substitution of (3.3.31) gives

$$\begin{aligned}\frac{\partial \boldsymbol{n}}{\partial t} =& \boldsymbol{G}\left(\boldsymbol{G}^{\mathrm{t}}\boldsymbol{G}\right)^{-1}\boldsymbol{G}^{\mathrm{t}}\left[-\frac{\partial \boldsymbol{G}}{\partial t}\left(\boldsymbol{G}^{\mathrm{t}}\boldsymbol{G}\right)^{-1}\boldsymbol{G}^{\mathrm{t}}+\boldsymbol{G}\left(\boldsymbol{G}^{\mathrm{t}}\boldsymbol{G}\right)^{-1}\left(\frac{\partial \boldsymbol{G}^{\mathrm{t}}}{\partial t}\boldsymbol{G}+\boldsymbol{G}^{\mathrm{t}}\frac{\partial \boldsymbol{G}}{\partial t}\right)\left(\boldsymbol{G}^{\mathrm{t}}\boldsymbol{G}\right)^{-1}\boldsymbol{G}^{\mathrm{t}}\right.\\ &\left.-\boldsymbol{G}\left(\boldsymbol{G}^{\mathrm{t}}\boldsymbol{G}\right)^{-1}\frac{\partial \boldsymbol{G}^{\mathrm{t}}}{\partial t}\right]\frac{\boldsymbol{w}}{\|\boldsymbol{m}\|}\\ =& \boldsymbol{G}\left(\boldsymbol{G}^{\mathrm{t}}\boldsymbol{G}\right)^{-1}\frac{\partial \boldsymbol{G}^{\mathrm{t}}}{\partial t}\left[\boldsymbol{G}\left(\boldsymbol{G}^{\mathrm{t}}\boldsymbol{G}\right)^{-1}\boldsymbol{G}^{\mathrm{t}}-1\right]\frac{\boldsymbol{w}}{\|\boldsymbol{m}\|}\\ =& -\left(\boldsymbol{G}\left(\boldsymbol{G}^{\mathrm{t}}\boldsymbol{G}\right)^{-1}\frac{\partial \boldsymbol{G}^{\mathrm{t}}}{\partial t}\right)\frac{\boldsymbol{m}}{\|\boldsymbol{m}\|}\\ =& -\left(\boldsymbol{G}\left(\boldsymbol{G}^{\mathrm{t}}\boldsymbol{G}\right)^{-1}\frac{\partial \boldsymbol{G}^{\mathrm{t}}}{\partial t}\right)\boldsymbol{n}\,. \end{aligned} \tag{3.3.40}$$

3.3.3 Slip Velocity

The contact slip velocity, which is defined as the projection of the difference between the contactor and target velocities onto the plane tangent to the target surface, is given by (3.3.30) as

$$\boldsymbol{v}_s \coloneqq \boldsymbol{G}\left(\boldsymbol{G}^{\mathrm{t}}\boldsymbol{G}\right)^{-1}\boldsymbol{G}^{\mathrm{t}}\left(\boldsymbol{v}^{\mathrm{con}}-\boldsymbol{v}^{\mathrm{tar}}\right)\,, \tag{3.3.41}$$

where the contactor and target velocities are, respectively, given by (3.1.24) as

$$\boldsymbol{v}^{\mathrm{con}} = \frac{\partial \boldsymbol{\varphi}^{\mathrm{con}}}{\partial t} + \left(\operatorname{Grad}\boldsymbol{\varphi}^{\mathrm{con}}\right)\boldsymbol{V}^{\mathrm{con}}\,, \tag{3.3.42}$$

$$\boldsymbol{v}^{\mathrm{tar}} = \frac{\partial \boldsymbol{\varphi}^{\mathrm{tar}}}{\partial t} + \left(\operatorname{Grad}\boldsymbol{\varphi}^{\mathrm{tar}}\right)\boldsymbol{V}^{\mathrm{tar}}\,, \tag{3.3.43}$$

so that

$$\begin{aligned}\boldsymbol{v}_s =& \boldsymbol{G}\left(\boldsymbol{G}^{\mathrm{t}}\boldsymbol{G}\right)^{-1}\boldsymbol{G}^{\mathrm{t}}\left(\frac{\partial \boldsymbol{\varphi}^{\mathrm{con}}}{\partial t}-\left.\frac{\partial \boldsymbol{\varphi}^{\mathrm{tar}}}{\partial t}\right|_{\boldsymbol{Y}=\boldsymbol{\eta}(\boldsymbol{X},t)}\right)\\ &+\boldsymbol{G}\left(\boldsymbol{G}^{\mathrm{t}}\boldsymbol{G}\right)^{-1}\boldsymbol{G}^{\mathrm{t}}\left(\left(\operatorname{Grad}\boldsymbol{\varphi}^{\mathrm{con}}\right)\boldsymbol{V}^{\mathrm{con}}-\left(\operatorname{Grad}\boldsymbol{\varphi}^{\mathrm{tar}}\right)\boldsymbol{V}^{\mathrm{tar}}\right)\,. \end{aligned} \tag{3.3.44}$$

Equation (3.3.17) can be rearranged to give

$$\begin{aligned}\left[\frac{\partial\varphi_i^{\mathrm{con}}}{\partial t}-\left.\frac{\partial\varphi_i^{\mathrm{tar}}}{\partial t}\right|_{\boldsymbol{Y}=\boldsymbol{\eta}(\boldsymbol{X},t)}\right]G_{im}&=G_{im}G_{ik}\frac{\partial\hat{Y}_k}{\partial t}\\&\quad-(x_i-y_i)\left[\left(\left.\frac{\partial\varphi_{i,j}^{\mathrm{tar}}}{\partial t}\right|_{\boldsymbol{Y}=\boldsymbol{\eta}(\boldsymbol{X},t)}\right)\Xi_{jm}+\frac{\partial G_{im}}{\partial Y_j}\Xi_{jk}\frac{\partial\hat{Y}_k}{\partial t}\right]\\&=G_{im}G_{ij}\frac{\partial\hat{Y}_j}{\partial t}-(x_i-y_i)\frac{\partial G_{im}}{\partial t}\,,\end{aligned}\tag{3.3.45}$$

which can be used to express the projection of the partial time derivative of the slip as

$$\begin{aligned}&G_{ij}\left(G_{kj}G_{kl}\right)^{-1}G_{ml}\left(\frac{\partial\varphi_m^{\mathrm{con}}}{\partial t}-\left.\frac{\partial\varphi_m^{\mathrm{tar}}}{\partial t}\right|_{\boldsymbol{Y}=\boldsymbol{\eta}(\boldsymbol{X},t)}\right)\\&\quad=G_{ij}\left(G_{kj}G_{kl}\right)^{-1}\left[G_{ml}G_{mn}\frac{\partial\hat{Y}_n}{\partial t}-(x_m-y_m)\frac{\partial G_{ml}}{\partial t}\right]\\&\quad=G_{ij}\frac{\partial\hat{Y}_j}{\partial t}-G_{ij}\left(G_{kj}G_{kl}\right)^{-1}\frac{\partial G_{ml}}{\partial t}(x_m-y_m)\,.\end{aligned}\tag{3.3.46}$$

Equation (3.3.40), in index form reads

$$\frac{\partial n_i}{\partial t}=-G_{ij}\left(G_{kj}G_{kl}\right)^{-1}\frac{\partial G_{ml}}{\partial t}n_m\,;\tag{3.3.47}$$

using this, along with

$$\begin{aligned}G_{ij}\frac{\partial\hat{Y}_j}{\partial t}&=\varphi_{i,k}\Xi_{kj}\frac{\partial\hat{Y}_j}{\partial t}\\&=\varphi_{i,j}\frac{\partial\eta_j}{\partial t}\,,\end{aligned}\tag{3.3.48}$$

and

$$\left(\varphi_m^{\mathrm{con}}-\varphi_m^{\mathrm{tar}}\right)=-gn_m\,,\tag{3.3.49}$$

gives

$$G_{ij}\left(G_{kj}G_{kl}\right)^{-1}G_{ml}\left(\frac{\partial\varphi_m^{\mathrm{con}}}{\partial t}-\left.\frac{\partial\varphi_m^{\mathrm{tar}}}{\partial t}\right|_{\boldsymbol{Y}=\boldsymbol{\eta}(\boldsymbol{X},t)}\right)=\varphi_{i,j}\frac{\partial\eta_j}{\partial t}-g\frac{\partial n_i}{\partial t}.\tag{3.3.50}$$

Substitution in (3.3.44) then gives the slip velocity

$$\boldsymbol{v}_s=\left(\mathrm{Grad}\,\boldsymbol{\varphi}^{\mathrm{tar}}\right)\frac{\partial\boldsymbol{\eta}}{\partial t}-g\frac{\partial\boldsymbol{n}}{\partial t}+\boldsymbol{G}\left(\boldsymbol{G}^{\mathrm{t}}\boldsymbol{G}\right)^{-1}\boldsymbol{G}^{\mathrm{t}}\left(\left(\mathrm{Grad}\,\boldsymbol{\varphi}^{\mathrm{con}}\right)\boldsymbol{V}^{\mathrm{con}}-\left(\mathrm{Grad}\,\boldsymbol{\varphi}^{\mathrm{tar}}\right)\boldsymbol{V}^{\mathrm{tar}}\right)\,.\tag{3.3.51}$$

4 Constitutive Models

This chapter describes the constitutive models of coupled thermomechanical finite strain plastic deformation and frictional contact. Section 4.1 is about the stress measures in materials undergoing finite strains. Sections 4.2 through 4.4 describe the constitutive models of coupled thermo-viscoplasticity at finite strains. Section 4.5 describes the constraints and constitutive models of thermomechanical frictional contact.

4.1 Stress Measures

This section introduces the stress measures used in this work, which are standard in the continuum mechanics literature. Additional details are available in textbooks on the subject [120, 121]. A body $\mathcal{B}$ given in the material configuration by $\Omega_0^{\mathcal{B}}$, and in the reference configuration, through $\boldsymbol{\Upsilon}_0$ by $\Omega^{\mathcal{B}}$, is deformed under external loads by the motion $\boldsymbol{\varphi}_0$ into $\tilde{\Omega}^{\mathcal{B}}$. The internal forces within the deformed configuration at a point $\boldsymbol{x} \in \tilde{\Omega}^{\mathcal{B}}$ are determined by considering a smooth surface passing through $\boldsymbol{x}$, which divides the body into two parts, and whose normal at $\boldsymbol{x}$ is given by $\boldsymbol{n}$ (Figure 4.1). The forces exerted by one part of the body on the other through a small area element Δa around $\boldsymbol{x}$ are given by an equivalent force $\Delta \boldsymbol{p}$ and an equivalent moment $\Delta \boldsymbol{m}$. The moment $\Delta \boldsymbol{m}$ is assumed to vanish as $\Delta a \to 0$, that is, $\lim_{\Delta a \to 0} \frac{\Delta \boldsymbol{m}}{\Delta a} = 0$, and the internal force $\boldsymbol{t}$ at $\boldsymbol{x}$,

$$\boldsymbol{t}(\boldsymbol{n}) = \lim_{\Delta a \to 0} \frac{\Delta \boldsymbol{p}}{\Delta a}\,, \tag{4.1.1}$$

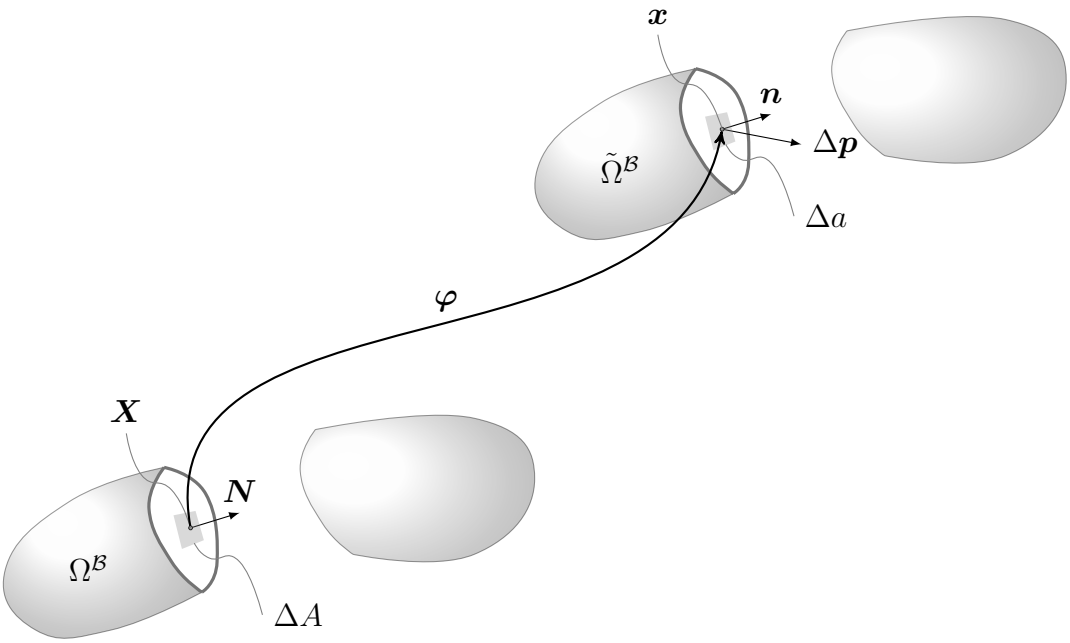

Figure 4.1: Stress

is completely determined by the surface normal $\boldsymbol{n}$ and the Cauchy stress tensor $\boldsymbol{\sigma}$ as

$$\boldsymbol{t} = \boldsymbol{\sigma}\boldsymbol{n}. \tag{4.1.2}$$

The Cauchy stress tensor $\boldsymbol{\sigma}$ is a symmetric tensor due to conservation of angular momentum. It is related to the Kirchhoff stress tensor $\boldsymbol{\tau}$ by

$$\boldsymbol{\tau} = J\boldsymbol{\sigma}. \tag{4.1.3}$$

In the reference configuration, similarly, the equivalent force through an area element ΔA around a point $\boldsymbol{X} \in \Omega^{\mathcal{B}}$, with a unit normal $\boldsymbol{N}$, is given by

$$\boldsymbol{t}_{\mathrm{c}}(\boldsymbol{N}) = \lim_{\Delta A \to 0} \frac{\Delta \boldsymbol{p}}{\Delta A}\,. \tag{4.1.4}$$

It is completely determined by the unit normal $\boldsymbol{N}$ and the first Piola-Kirchhoff stress $\boldsymbol{P}$ as

$$\boldsymbol{t}_{\mathrm{c}} = \boldsymbol{P}\boldsymbol{N}. \tag{4.1.5}$$

A surface $\Gamma \subset \Omega$ in the reference configuration is transformed by the motion $\boldsymbol{\varphi}$ into a surface $\tilde{\Gamma} \subset \tilde{\Omega}$. Under this transformation, an infinitesimal area element $\mathrm{d}A$ at a point $\boldsymbol{X} \in \Gamma$, whose direction is given by a unit normal $\boldsymbol{N}$ is transformed into an infinitesimal areal element $\mathrm{d}a$ at $\boldsymbol{x} = \boldsymbol{\varphi}(\boldsymbol{X}, t)$, whose direction is given by a unit normal $\boldsymbol{n}$. They are related by Nanson's relation:

$$\boldsymbol{n}\,\mathrm{d}a = J\boldsymbol{F}_{\mathrm{c}}^{-\mathrm{t}}\boldsymbol{N}\,\mathrm{d}A\,. \tag{4.1.6}$$

The definitions of internal forces in the reference and current configurations are related by

$$\boldsymbol{t}\mathrm{d}a = \boldsymbol{t}_{\mathrm{c}}\mathrm{d}A\,. \tag{4.1.7}$$

Thus, by substitution of equations (4.1.2) and (4.1.5),

$$\boldsymbol{\sigma}\boldsymbol{n}\mathrm{d}a = \boldsymbol{P}\boldsymbol{N}\mathrm{d}A\,, \tag{4.1.8}$$

and, by Nanson's relation (4.1.6), the two stress tensors are related by

$$\boldsymbol{P} = J\,\boldsymbol{\sigma}\,\boldsymbol{F}_{\mathrm{c}}^{-\mathrm{t}}\,, \tag{4.1.9}$$

which, by (4.1.3), gives

$$\boldsymbol{P} = \boldsymbol{\tau}\,\boldsymbol{F}_{\mathrm{c}}^{-\mathrm{t}}\,. \tag{4.1.10}$$

Nanson's relation (4.1.6) can also be used to relate the unit normals in the reference and current configurations:

$$\begin{aligned}\boldsymbol{n}\,\frac{\mathrm{d}a}{\mathrm{d}A}\,\mathrm{d}a &= J\boldsymbol{F}_{\mathrm{c}}^{-\mathrm{t}}\boldsymbol{N}\,\frac{\mathrm{d}a}{\mathrm{d}A}\,\mathrm{d}A \\ &= J\boldsymbol{F}_{\mathrm{c}}^{-\mathrm{t}}\boldsymbol{N}\,\mathrm{d}a\,,\end{aligned} \tag{4.1.11}$$

so that

$$\left(\frac{1}{J}\,\frac{\mathrm{d}a}{\mathrm{d}A}\right)\boldsymbol{n} = \boldsymbol{F}_{\mathrm{c}}^{-\mathrm{t}}\boldsymbol{N}\,. \tag{4.1.12}$$

The norm of the left-hand side,

$$\left\| \left(\frac{1}{J} \frac{\mathrm{d}a}{\mathrm{d}A} \right) \boldsymbol{n} \right\| = \left(\frac{1}{J} \frac{\mathrm{d}a}{\mathrm{d}A} \right) \|\boldsymbol{n}\| = \frac{1}{J} \frac{\mathrm{d}a}{\mathrm{d}A} \,, \tag{4.1.13}$$

must equal the norm of the left-hand side $\|\boldsymbol{F}_{\mathrm{c}}^{-\mathrm{t}} \boldsymbol{N}\|$, which gives

$$\frac{1}{J} \frac{\mathrm{d}a}{\mathrm{d}A} = \|\boldsymbol{F}_{\mathrm{c}}^{-\mathrm{t}} \boldsymbol{N}\| \,. \tag{4.1.14}$$

Substitution in (4.1.12) gives

$$\boldsymbol{F}_{\mathrm{c}}^{-\mathrm{t}} \boldsymbol{N} = \left\| \boldsymbol{F}_{\mathrm{c}}^{-\mathrm{t}} \boldsymbol{N} \right\| \boldsymbol{n} \,, \tag{4.1.15}$$

which, along with (4.1.9), gives

$$\begin{aligned} \boldsymbol{P} \boldsymbol{N} &= J \, \boldsymbol{\sigma} \, \boldsymbol{F}_{\mathrm{c}}^{-\mathrm{t}} \boldsymbol{N} \\ &= J \, \left\| \boldsymbol{F}_{\mathrm{c}}^{-\mathrm{t}} \boldsymbol{N} \right\| \boldsymbol{\sigma} \, \boldsymbol{n} \,. \end{aligned} \tag{4.1.16}$$

4.2 Reduced Dissipation Inequality and Constitutive Relations

The reduced dissipation inequality and constitutive relations for associative coupled thermoplasticity at finite strains were derived by Simo and Miehe [82] following the procedure presented by Coleman and Noll [122]. The internal energy $e = \hat{e}(\boldsymbol{b}^{\mathrm{e}}, \alpha, \eta^{\mathrm{e}})$ is a function of the elastic deformation $\boldsymbol{b}^{\mathrm{e}}$ defined in (3.2.7), the equivalent plastic strain α, and the elastic entropy $\eta^{\mathrm{e}} \coloneqq \eta - \eta^{\mathrm{p}}$. Here, η^{p} is the plastic entropy proposed by Simo and Miehe [82]. Given the local dissipation inequality

$$\mathcal{D} \coloneqq \theta \dot{\eta} + \boldsymbol{\tau} : \boldsymbol{d} - \dot{e} \geq 0, \tag{4.2.1}$$

and the free energy function $\psi \coloneqq \hat{\psi}(\boldsymbol{b}^{\mathrm{e}}, \alpha, \theta)$, which is related to the internal energy by the Legendre transformation,

$$\hat{\psi}(\boldsymbol{b}^{\mathrm{e}}, \alpha, \theta) \coloneqq \hat{e}(\boldsymbol{b}^{\mathrm{e}}, \alpha, \eta^{\mathrm{e}}) - \eta^{\mathrm{e}} \theta \,, \tag{4.2.2}$$

the reduced dissipation inequality is derived as follows [82]. The total time derivative of the free energy (4.2.2) is

$$\dot{\psi} = \dot{e} - \eta^{\mathrm{e}}\dot{\theta} - \dot{\eta}^{\mathrm{e}}\theta\,, \tag{4.2.3}$$

which, by rearranging and by substitution of $\theta\dot{\eta}^{\mathrm{e}} = \theta\dot{\eta} - \theta\dot{\eta}^{\mathrm{p}}$, gives

$$\theta\dot{\eta} - \dot{e} = \theta\dot{\eta}^{\mathrm{p}} - \dot{\psi} - (\dot{\eta} - \dot{\eta}^{\mathrm{p}})\,\theta\,. \tag{4.2.4}$$

Substitution into (4.2.1) then gives

$$\mathcal{D} = \theta\dot{\eta}^{\mathrm{p}} + \boldsymbol{\tau}\colon \boldsymbol{d} - \dot{\psi} - (\eta - \eta^{\mathrm{p}})\,\dot{\theta} \geq 0\,. \tag{4.2.5}$$

Then, using

$$\begin{aligned}\dot{\psi} \coloneqq \frac{\mathrm{D}}{\mathrm{D}t}\hat{\psi}(\boldsymbol{b}^{\mathrm{e}}, \alpha, \theta) &= \frac{\partial\hat{\psi}}{\partial\boldsymbol{b}^{\mathrm{e}}}\colon \dot{\boldsymbol{b}}^{\mathrm{e}} + \frac{\partial\hat{\psi}}{\partial\alpha}\dot{\alpha} + \frac{\partial\hat{\psi}}{\partial\theta}\dot{\theta} \\ &= \frac{\partial\hat{\psi}}{\partial\boldsymbol{b}^{\mathrm{e}}}\colon \left(\boldsymbol{l}\boldsymbol{b}^{\mathrm{e}} + \boldsymbol{b}^{\mathrm{e}}\boldsymbol{l}^{\mathrm{t}} + \mathscr{L}_v\boldsymbol{b}^{\mathrm{e}}\right) + \frac{\partial\hat{\psi}}{\partial\alpha}\dot{\alpha} + \frac{\partial\hat{\psi}}{\partial\theta}\dot{\theta}\,,\end{aligned} \tag{4.2.6}$$

along with (3.2.18), gives

$$\begin{aligned}\mathcal{D} = \theta\dot{\eta}^{\mathrm{p}} + \boldsymbol{\tau}\colon \boldsymbol{d} - \frac{\partial\hat{\psi}}{\partial\boldsymbol{b}^{\mathrm{e}}}\colon \left(\boldsymbol{l}\boldsymbol{b}^{\mathrm{e}} + \boldsymbol{b}^{\mathrm{e}}\boldsymbol{l}^{\mathrm{t}} + \mathscr{L}_v\boldsymbol{b}^{\mathrm{e}}\right) - \frac{\partial\hat{\psi}}{\partial\alpha}\dot{\alpha} - \left[\frac{\partial\hat{\psi}}{\partial\theta} + (\eta - \eta^{\mathrm{p}})\right]\dot{\theta} \\ \geq 0\,.\end{aligned} \tag{4.2.7}$$

Then, since $\frac{\partial\hat{\psi}}{\partial\boldsymbol{b}^{\mathrm{e}}}\boldsymbol{b}^{\mathrm{e}} = \boldsymbol{b}^{\mathrm{e}}\frac{\partial\hat{\psi}}{\partial\boldsymbol{b}^{\mathrm{e}}}$ due to the isotropy assumption [82],

$$\begin{aligned}\frac{\partial\hat{\psi}}{\partial\boldsymbol{b}^{\mathrm{e}}}\colon \left(\boldsymbol{l}\boldsymbol{b}^{\mathrm{e}} + \boldsymbol{b}^{\mathrm{e}}\boldsymbol{l}^{\mathrm{t}}\right) &= \frac{\partial\hat{\psi}}{\partial\boldsymbol{b}^{\mathrm{e}}}\boldsymbol{b}^{\mathrm{e}}\colon \boldsymbol{l} + \boldsymbol{b}^{\mathrm{e}}\frac{\partial\hat{\psi}}{\partial\boldsymbol{b}^{\mathrm{e}}}\colon \boldsymbol{l}^{\mathrm{t}} \\ &= \frac{\partial\hat{\psi}}{\partial\boldsymbol{b}^{\mathrm{e}}}\boldsymbol{b}^{\mathrm{e}}\colon \left(\boldsymbol{l} + \boldsymbol{l}^{\mathrm{t}}\right) \\ &= 2\frac{\partial\hat{\psi}}{\partial\boldsymbol{b}^{\mathrm{e}}}\boldsymbol{b}^{\mathrm{e}}\colon \boldsymbol{d}\,.\end{aligned} \tag{4.2.8}$$

Thus, (4.2.7) becomes

$$\begin{aligned}\mathcal{D} = \theta\dot{\eta}^{\mathrm{p}} + \left(\boldsymbol{\tau} - 2\frac{\partial\hat{\psi}}{\partial\boldsymbol{b}^{\mathrm{e}}}\boldsymbol{b}^{\mathrm{e}}\right)\colon \boldsymbol{d} - \frac{\partial\hat{\psi}}{\partial\boldsymbol{b}^{\mathrm{e}}}\colon \mathscr{L}_v\boldsymbol{b}^{\mathrm{e}} - \frac{\partial\hat{\psi}}{\partial\alpha}\dot{\alpha} - \left[\frac{\partial\hat{\psi}}{\partial\theta} + (\eta - \eta^{\mathrm{p}})\right]\dot{\theta} \\ \geq 0\,.\end{aligned} \tag{4.2.9}$$

This must hold for all processes, so that

$$\boldsymbol{\tau} = 2\frac{\partial \hat{\psi}}{\partial \boldsymbol{b}^{\mathrm{e}}}\boldsymbol{b}^{\mathrm{e}}\,, \tag{4.2.10}$$

$$\eta = \eta^{\mathrm{p}} - \frac{\partial \hat{\psi}}{\partial \theta}\,. \tag{4.2.11}$$

and therefore, setting $\beta = -\frac{\partial \hat{\psi}}{\partial \alpha}$ gives the reduced dissipation inequality [82]

$$\mathcal{D} = \underbrace{\boldsymbol{\tau} \colon \left[-\frac{1}{2}\left(\mathscr{L}_v \boldsymbol{b}^{\mathrm{e}}\right)\left(\boldsymbol{b}^{\mathrm{e}}\right)^{-1}\right] + \beta\dot{\alpha}}_{\mathcal{D}_{\mathrm{mech}}} + \theta\dot{\eta}^{\mathrm{p}} \geq 0\,. \tag{4.2.12}$$

Equation (4.2.5) then becomes

$$\begin{aligned}\dot{\psi} &= \boldsymbol{\tau} \colon \boldsymbol{d} - \mathcal{D}_{\mathrm{mech}} + \frac{\partial \hat{\psi}}{\partial \theta}\dot{\theta} \\ &= \boldsymbol{\tau} \colon \boldsymbol{d} - \mathcal{D}_{\mathrm{mech}} - \left(\eta - \eta^{\mathrm{p}}\right)\dot{\theta}\,.\end{aligned} \tag{4.2.13}$$

4.3 Finite Strain Thermoplasticity

An applicable constitutive model in this work is the coupled thermomechanical J_2-flow theory for associative thermoplasticity at finite strains presented by Simo and Miehe [82]. The model is based on a multiplicative decomposition of the deformation gradient into its elastic and plastic parts, that is

$$\boldsymbol{F} = \boldsymbol{F}^{\mathrm{e}}\boldsymbol{F}^{\mathrm{p}}\,. \tag{4.3.1}$$

The plastic part $\boldsymbol{F}^{\mathrm{p}}$ takes the material to a locally defined intermediate configuration, and the elastic deformation then maps the intermediate configuration to the final deformed configuration via $\boldsymbol{F}^{\mathrm{e}}$.

In addition, the elastic and thermal behaviour are defined through a free energy function ψ given, in terms of the deformation Jacobian J, the isochoric component of the elastic left Cauchy Green tensor $\bar{\boldsymbol{b}}^{\mathrm{e}}$, the temperature θ, and the equivalent plastic strain α:

$$\psi = \hat{\psi}\left(J, \bar{\boldsymbol{b}}^{\mathrm{e}}, \theta, \alpha\right), \tag{4.3.2}$$

We assume a free energy function of the form

$$\hat{\psi} = \hat{T}(\theta) + \hat{M}(J,\theta) + \hat{U}(J) + \hat{W}(\bar{\boldsymbol{b}}^{\mathrm{e}}) + \hat{K}(\alpha), \tag{4.3.3}$$

with

$$\hat{U}(J) = \kappa\left[\frac{1}{2}\left(J^2-1\right) - \ln J\right] \quad \text{and} \quad \hat{W}(\bar{\boldsymbol{b}}^{\mathrm{e}}) = \int \frac{\mu}{2}\left(\log \bar{\boldsymbol{b}}^{\mathrm{e}}\right)\left(\bar{\boldsymbol{b}}^{\mathrm{e}}\right)^{-1} : \mathrm{d}\bar{\boldsymbol{b}}^{\mathrm{e}}\,, \tag{4.3.4}$$

where μ and κ are the elastic shear and bulk moduli. The Kirchhoff stress tensor $\boldsymbol{\tau} = J\boldsymbol{\sigma}$ is then given by

$$\boldsymbol{\tau} = J\left(\frac{\partial\hat{\psi}}{\partial J}\right)\mathbf{1} + 2\frac{\partial\hat{\psi}}{\partial\bar{\boldsymbol{b}}^{\mathrm{e}}}\bar{\boldsymbol{b}}^{\mathrm{e}}, \tag{4.3.5}$$

$$\hat{W}\left(\bar{\boldsymbol{b}}^{\mathrm{e}}\right) = \int \frac{\mu}{2}\left(\log \bar{\boldsymbol{b}}^{\mathrm{e}}\right)\left(\bar{\boldsymbol{b}}^{\mathrm{e}}\right)^{-1} : \mathrm{d}\bar{\boldsymbol{b}}^{\mathrm{e}}\,, \tag{4.3.6}$$

so that the deviatoric and spherical parts of the stress, respectively $\operatorname{dev}\boldsymbol{\tau}$ and p, are given by

$$\operatorname{dev}\boldsymbol{\tau} = \mu \log \bar{\boldsymbol{b}}^{\mathrm{e}}\,, \tag{4.3.7a}$$

$$p = \kappa\left(J^2-1\right)\,. \tag{4.3.7b}$$

As detailed in [82], along with this stress-strain relationship, a yield criterion

$$\phi = \hat{\phi}(\boldsymbol{\tau},\beta,\theta), \tag{4.3.8}$$

where $\beta = -\hat{K}'(\alpha)$ is an internal variable representing strain hardening, and the reduced dissipation inequality (4.2.12) give rise to the evolution equations through the principle of maximum dissipation. The values of $\boldsymbol{\tau}$, β and θ maximise the dissipation over the thermoelastic domain $\mathbb{E} := \left\{(\boldsymbol{\tau},\beta,\theta) : \hat{\phi}(\boldsymbol{\tau},\beta,\theta) \leq 0\right\}$, so that for any $(\boldsymbol{\tau}^*,\beta^*,\theta^*) \in \mathbb{E}$,

$$(\boldsymbol{\tau}-\boldsymbol{\tau}^*) : \left[-\frac{1}{2}\left(\mathscr{L}_v\boldsymbol{b}^{\mathrm{e}}\right)\left(\boldsymbol{b}^{\mathrm{e}}\right)^{-1}\right] + (\beta-\beta^*)\dot{\alpha} + (\theta-\theta^*)\dot{\eta}^{\mathrm{p}} \geq 0\,. \tag{4.3.9}$$

We consider the case where the thermoelastic domain has a smooth boundary $\hat{\phi} = 0$, so that the evolution equations become

$$\mathscr{L}_v\boldsymbol{b}^{\mathrm{e}} = -2\gamma\left[\partial_{\boldsymbol{\tau}}\hat{\phi}\right]\boldsymbol{b}^{\mathrm{e}}\,, \tag{4.3.10}$$

$$\dot{\alpha} = \gamma\partial_\beta\hat{\phi}\,, \tag{4.3.11}$$

$$\dot{\eta}^{\mathrm{p}} = \gamma\partial_\theta\hat{\phi}\,, \tag{4.3.12}$$

where $\mathscr{L}_v \boldsymbol{b}^{\mathrm{e}} = \boldsymbol{F}\dot{\boldsymbol{G}}^{\mathrm{p}}\boldsymbol{F}^{\mathrm{t}}$ and $\boldsymbol{G}^{\mathrm{p}} = \left[\boldsymbol{F}^{\mathrm{pt}}\boldsymbol{F}^{\mathrm{p}}\right]^{-1}$, and γ, which is a strain rate, is the Lagrange multiplier from the Karush-Kuhn-Tucker (KKT) conditions

$$\phi \leq 0, \quad \gamma \geq 0, \quad \gamma\phi = 0\,. \tag{4.3.13}$$

The evolution equation (4.3.10) is an expression in the current configuration of the plastic flow being normal to the yield surface in stress space in the intermediate configuration [82]. This becomes clear by rewriting the equation in terms of $\boldsymbol{L}^{\mathrm{p}} = \dot{\boldsymbol{F}}^{\mathrm{p}}\boldsymbol{F}^{\mathrm{p}-1}$ and the second Piola-Kirchhoff stress in the intermediate configuration $\boldsymbol{S} = \boldsymbol{F}^{\mathrm{e}-1}\boldsymbol{\tau}\boldsymbol{F}^{\mathrm{e}-\mathrm{t}}$, which gives

$$\mathrm{sym}[\boldsymbol{L}^{\mathrm{p}}] = \gamma\partial_{\boldsymbol{S}}\phi\boldsymbol{C}^{\mathrm{e}}, \tag{4.3.14}$$

where $\boldsymbol{C}^{\mathrm{e}} = \boldsymbol{F}^{\mathrm{et}}\boldsymbol{F}^{\mathrm{e}}$.

The conservation of energy equation (5.1.12) is given in terms of the specific heat c, the dissipation due to mechanical deformation $\mathcal{D}_{\mathrm{mech}}$, the elastic-plastic structural heating $\mathcal{H}$, and the heat flux $\boldsymbol{q}$. These quantities are given by [82]

$$c = \partial^2_{\theta\theta}\psi, \tag{4.3.15a}$$

$$\mathcal{D}_{\mathrm{mech}} = \boldsymbol{\tau} : \left(-\frac{1}{2}(\mathscr{L}_v\boldsymbol{b}^{\mathrm{e}})\boldsymbol{b}^{\mathrm{e}-1}\right) + \beta\dot{\alpha}, \tag{4.3.15b}$$

$$\mathcal{H} = -\theta\partial_\theta\left(\boldsymbol{\tau} : \boldsymbol{d} - \mathcal{D}_{\mathrm{mech}}\right), \tag{4.3.15c}$$

$$\boldsymbol{q} = -k\ \mathrm{grad}\ \theta, \tag{4.3.15d}$$

where k is the thermal conductivity.

4.3.1 Multiplicative Split in the Reference Configuration

We seek a formulation of multiplicative plasticity in the reference configuration where the material configuration $\boldsymbol{\Upsilon}_0^{-1}$ only enters in terms of the reference velocity $\boldsymbol{V}$. We start by defining

$$\boldsymbol{B}^{\mathrm{e}} \coloneqq \boldsymbol{F}_{\mathrm{r}}\boldsymbol{G}^{\mathrm{p}}\boldsymbol{F}_{\mathrm{r}}^{\mathrm{t}}\,, \tag{4.3.16}$$

so that equation (3.2.10) can be written as

$$\begin{aligned} \boldsymbol{b}^{\mathrm{e}} &= \boldsymbol{F}_{\mathrm{c}}\boldsymbol{F}_{\mathrm{r}}\boldsymbol{G}^{\mathrm{p}}\boldsymbol{F}_{\mathrm{r}}^{\mathrm{t}}\boldsymbol{F}_{\mathrm{c}}^{\mathrm{t}} \\ &= \boldsymbol{F}_{\mathrm{c}}\boldsymbol{B}^{\mathrm{e}}\boldsymbol{F}_{\mathrm{c}}^{\mathrm{t}}\,. \end{aligned} \tag{4.3.17}$$

Then, evolution of the elastic strain (3.2.18) can be written as

$$\dot{\boldsymbol{b}}^{\mathrm{e}} = \dot{\boldsymbol{F}}_{\mathrm{c}}\boldsymbol{B}^{\mathrm{e}}\boldsymbol{F}_{\mathrm{c}}^{\mathrm{t}} + \boldsymbol{F}_{\mathrm{c}}\boldsymbol{B}^{\mathrm{e}}\dot{\boldsymbol{F}}_{\mathrm{c}}^{\mathrm{t}} + \boldsymbol{F}_{\mathrm{c}}\dot{\boldsymbol{B}}^{\mathrm{e}}\boldsymbol{F}_{\mathrm{c}}^{\mathrm{t}}\,. \tag{4.3.18}$$

By rearranging equation (3.1.33) as

$$\dot{\boldsymbol{F}}_{\mathrm{r}} = \boldsymbol{L}\boldsymbol{F}_{\mathrm{r}}\,, \tag{4.3.19}$$

the material derivative of $\boldsymbol{B}^{\mathrm{e}}$ is

$$\dot{\boldsymbol{B}}^{\mathrm{e}} = \boldsymbol{L}\boldsymbol{B}^{\mathrm{e}} + \boldsymbol{B}^{\mathrm{e}}\boldsymbol{L}^{\mathrm{t}} + \boldsymbol{F}_{\mathrm{r}}\dot{\boldsymbol{G}}^{\mathrm{p}}\boldsymbol{F}_{\mathrm{r}}^{\mathrm{t}}\,. \tag{4.3.20}$$

This can be substituted in (4.3.18) to give

$$\dot{\boldsymbol{b}}^{\mathrm{e}} = \dot{\boldsymbol{F}}_{\mathrm{c}}\boldsymbol{B}^{\mathrm{e}}\boldsymbol{F}_{\mathrm{c}}^{\mathrm{t}} + \boldsymbol{F}_{\mathrm{c}}\boldsymbol{B}^{\mathrm{e}}\dot{\boldsymbol{F}}_{\mathrm{c}}^{\mathrm{t}} + \boldsymbol{F}_{\mathrm{c}}\left[\boldsymbol{L}\boldsymbol{B}^{\mathrm{e}} + \boldsymbol{B}^{\mathrm{e}}\boldsymbol{L}^{\mathrm{t}}\right]\boldsymbol{F}_{\mathrm{c}}^{\mathrm{t}} + \mathscr{L}_v\boldsymbol{b}^{\mathrm{e}}\,. \tag{4.3.21}$$

Equivalently, using (4.3.17),

$$\dot{\boldsymbol{b}}^{\mathrm{e}} = \left[\dot{\boldsymbol{F}}_{\mathrm{c}}\boldsymbol{F}_{\mathrm{c}}^{-1} + \boldsymbol{F}_{\mathrm{c}}\boldsymbol{L}\boldsymbol{F}_{\mathrm{c}}^{-1}\right]\boldsymbol{b}^{\mathrm{e}} + \boldsymbol{b}^{\mathrm{e}}\left[\dot{\boldsymbol{F}}_{\mathrm{c}}\boldsymbol{F}_{\mathrm{c}}^{-1} + \boldsymbol{F}_{\mathrm{c}}\boldsymbol{L}\boldsymbol{F}_{\mathrm{c}}^{-1}\right]^{\mathrm{t}} + \mathscr{L}_v\boldsymbol{b}^{\mathrm{e}}\,. \tag{4.3.22}$$

4.4 Viscoplastic Behaviour

The effect of viscoplastic strain rate hardening can be introduced by allowing the yield criterion ϕ to attain positive values, which can be interpreted as allowing the stress to take values beyond the elastic range $\phi \leq 0$. A possible way to achieve this is by using a Perzyna-type model or, equivalently, a Duvaut-Lions-type model, as described, for instance, in [123]. In these models, the KKT conditions (4.3.13) are replaced by the constitutive equations

$$\gamma = \begin{cases} \frac{1}{\xi}g(\phi,\theta), & \text{if } \phi > 0\,, \\ 0, & \text{otherwise,} \end{cases} \tag{4.4.1}$$

where ξ is a viscosity parameter and $g(\phi, \theta)$ is a nonnegative function that vanishes if and only if $\phi \leq 0$. This approach to modelling thermo-viscoplastic behaviour of materials during friction welding has been used in several studies [124–126].

An alternative approach is to use constitutive laws that prescribe the viscoplastic yield stress σ^y as a function of the equivalent plastic strain, its rate of change, and the temperature, $\sigma^y = \sigma^y(\alpha, \dot{\alpha}, \theta)$, together with the von Mises yield criterion:

$$\phi = \|\mathrm{dev}\,\boldsymbol{\tau}\| - \sqrt{\frac{2}{3}}\sigma^{\mathrm{y}}(\alpha, \dot{\alpha}, \theta) \leq 0\,. \tag{4.4.2}$$

One of the most commonly used among these constitutive models is the Johnson-Cook model [127], which has been used in several works on simulation of FSW [128–130]. It is an empirical model that represents the effects of strain and strain rate hardening and of thermal softening as the product of three terms:

$$\sigma^{\mathrm{y}} = [A + B(\alpha)^n]\left[1 + C\ln\left(\frac{\dot{\alpha}}{\dot{\varepsilon}_0^{\mathrm{vp}}}\right)\right]\left[1 - \left(\frac{\theta - \theta_0}{\theta_{\mathrm{m}} - \theta_0}\right)^m\right]. \tag{4.4.3}$$

Here A, B, C, m and n are model parameters, θ_0 and θ_{m} are respectively the reference and melting temperatures, and $\dot{\varepsilon}_0^{\mathrm{vp}}$ is the reference strain rate. Several other researchers [131–134] have used the Sheppard-Wright model [135], which defines a temperature compensated strain rate given in terms of an activation energy Q and the gas constant R by

$$Z = \dot{\alpha}\exp\left(\frac{Q}{R\theta}\right), \tag{4.4.4}$$

and relates it to the yield stress by

$$\sigma^{\mathrm{y}} = \frac{1}{C}\sinh^{-1}\left[\left(\frac{Z}{A}\right)^{\frac{1}{n}}\right], \tag{4.4.5}$$

where A, C and n are model parameters.

4.5 Thermomechanical Frictional Contact

4.5.1 Mechanical Contact

The constraint that no penetration may occur and the fact that contact can give rise to compressive forces but not tensile ones are modelled, in terms of the penetration g (3.3.33) and the normal component of the contact force $f_{\mathrm{N}} \coloneqq -\boldsymbol{n} \cdot \boldsymbol{f}_{\mathrm{c}}$, by the complementarity conditions

$$g \leq 0\,, \tag{4.5.1a}$$

$$f_{\mathrm{N}} \geq 0\,, \tag{4.5.1b}$$

$$f_{\mathrm{N}} \cdot g = 0\,. \tag{4.5.1c}$$

In addition to these contact constraints, the stick-slip condition of the tangential contact tractions is given in terms of the tangential component of the contact traction $\boldsymbol{f}_{\mathrm{T}} \coloneqq \boldsymbol{f}_{\mathrm{c}} - (\boldsymbol{n} \cdot \boldsymbol{f}_{\mathrm{c}})\,\boldsymbol{n}$, the stick limit $\Phi\left(\boldsymbol{f}_{\mathrm{T}}, f_{\mathrm{N}}\right)$, and a Lagrange multiplier ν, by the complementarity conditions [136]

$$\Phi\left(\boldsymbol{f}_{\mathrm{T}}, f_{\mathrm{N}}\right) \leq 0\,, \tag{4.5.2a}$$

$$\nu \geq 0\,, \tag{4.5.2b}$$

$$\nu\Phi = 0\,, \tag{4.5.2c}$$

and the evolution law

$$\boldsymbol{v}_{\mathrm{s}} = \nu \frac{\partial \Phi}{\partial \boldsymbol{f}_{\mathrm{T}}}\,, \tag{4.5.3}$$

where the slip velocity $\boldsymbol{v}_{\mathrm{s}}$, given by (3.3.51), is the tangential component of the relative velocity between the contactor and the target in the current configuration.

4.5.2 Thermal Contact

The heat flux through the contact interface is given by [137]

$$q_{\mathrm{hc}} = \hat{h}(t_{\mathrm{N}}, \theta_{\mathrm{G}}) g_{\theta}(\boldsymbol{X}, t) \tag{4.5.4}$$

where $g_\theta(\boldsymbol{X}, t) \coloneqq \theta^{\mathrm{con}}(\boldsymbol{X}, t) - \theta^{\mathrm{tar}}(\boldsymbol{\eta}(\boldsymbol{X}, t), t)$ is the temperature difference across the interface. The heat transfer coefficient $\hat{h}$ is a function of the normal contact force t_{N} and the mean gas temperature, which is given in terms of the relative thermal effusivities $h_\epsilon^{\mathcal{B}}$, $\mathcal{B} \in \{\mathrm{con}, \mathrm{tar}\}$, and the temperatures at the contact interface by

$$\theta_{\mathrm{G}}(\boldsymbol{X}, t) = h_\epsilon^{\mathrm{con}} \theta^{\mathrm{con}}(\boldsymbol{X}, t) + h_\epsilon^{\mathrm{tar}} \theta^{\mathrm{tar}}(\boldsymbol{\eta}(\boldsymbol{X}, t), t)\,. \tag{4.5.5}$$

Frictional heat generation due to tangential slip against frictional forces is modelled as a boundary heat source given by

$$\mathcal{D}_{\mathrm{fric}}^{\mathcal{B}} = h_\epsilon^{\mathcal{B}} \boldsymbol{v}_{\mathrm{s}} \cdot \boldsymbol{f}_{\mathrm{T}}\,, \quad \mathcal{B} \in \{\mathrm{con}, \mathrm{tar}\}\,. \tag{4.5.6}$$

5 Problem Formulation

In this Chapter, the mathematical model of a friction welding process is described by completing the problem formulation based on thermomechanical balance laws as well as the kinematics and constitutive models described in the previous Chapters. In Section 5.1, the thermomechanical initial boundary value problem is described. The mechanical and thermal weak formulations are then derived in Section 5.2. The resulting problem formulation is summarised in Section 5.3.

5.1 Initial Boundary Value Problem

The internal stress state in the material is governed by the momentum balance equation, which is given in the reference configuration by

$$\operatorname{Div} \boldsymbol{P} + \boldsymbol{f}_{\mathrm{b}} = \rho_{\mathrm{m}} \boldsymbol{a} \qquad \text{in } \Omega^{\mathcal{B}}\,, \tag{5.1.1}$$

where $\boldsymbol{f}_{\mathrm{b}}$ is the external force per unit volume in the reference configuration, and ρ_{m} is the mass density per unit volume in the reference configuration.

In addition, boundary conditions are given on subsets of the boundary by

$$\boldsymbol{\varphi}(\boldsymbol{X}, t) = \boldsymbol{\varphi}_{\mathrm{pre}}(\boldsymbol{X}, t) \qquad \text{on } \Gamma^{\mathcal{B}}_{D_\mu} \subset \Gamma^{\mathcal{B}}\,, \tag{5.1.2a}$$

$$\boldsymbol{V}(\boldsymbol{X}, t) = \boldsymbol{V}_{\mathrm{pre}}(\boldsymbol{X}, t) \qquad \text{on } \Gamma^{\mathcal{B}}_{V} \subset \Gamma^{\mathcal{B}}\,, \tag{5.1.2b}$$

$$\boldsymbol{\sigma}\, \boldsymbol{n} = \boldsymbol{f}_s \qquad \text{on } \Gamma^{\mathcal{B}}_{N_\mu} \subset \Gamma^{\mathcal{B}}\,. \tag{5.1.2c}$$

Here, $\Gamma^{\mathcal{B}}_{D_\mu}$ is the subset of $\Gamma^{\mathcal{B}}$ where an essential boundary condition is given on the deformation, $\Gamma^{\mathcal{B}}_{V}$ is the subset where an essential boundary condition on the velocity is given, and $\Gamma^{\mathcal{B}}_{N_\mu}$ is that where a natural boundary condition on the boundary traction is given.

Furthermore, on each contact boundary pair $\Gamma_{\mathrm{c}}^{\mathrm{con}}$ and $\Gamma_{\mathrm{c}}^{\mathrm{tar}}$, contact boundary conditions are given by the contact force $\boldsymbol{f}_{\mathrm{c}}$ as

$$\boldsymbol{\sigma}^{\mathrm{con}}\boldsymbol{n}^{\mathrm{con}} = \boldsymbol{f}_{\mathrm{c}} \qquad \text{on } \Gamma_{\mathrm{c}}^{\mathrm{con}}\,, \tag{5.1.3a}$$

$$\boldsymbol{\sigma}^{\mathrm{tar}}\boldsymbol{n}^{\mathrm{tar}} = -\boldsymbol{f}_{\mathrm{c}} \qquad \text{on } \Gamma_{\mathrm{c}}^{\mathrm{tar}}\,. \tag{5.1.3b}$$

At the initial time t_0, the deformation and reference velocity are given by known fields $\boldsymbol{x}_{\mathrm{initial}}$ and $\boldsymbol{V}_{\mathrm{initial}}$ as

$$\boldsymbol{\varphi}(\boldsymbol{X}, t_0) = \boldsymbol{x}_{\mathrm{initial}}(\boldsymbol{X})\,, \tag{5.1.4a}$$

$$\boldsymbol{V}(\boldsymbol{X}, t_0) = \boldsymbol{V}_{\mathrm{initial}}(\boldsymbol{X})\,. \tag{5.1.4b}$$

The material behaviour is also subject to the local balance of energy [82]

$$-J\,\mathrm{div}\left[\frac{1}{J}\boldsymbol{q}\right] + \mathcal{R}_b = \dot{e} - \boldsymbol{\tau}\colon \boldsymbol{d}\,, \tag{5.1.5}$$

where $\mathcal{R}_b$ is the heat source per unit volume in the reference configuration and e is the internal energy. Substitution of (4.2.1) gives

$$-J\,\mathrm{div}\left[\frac{1}{J}\boldsymbol{q}\right] + \mathcal{R}_b = \theta\dot{\eta} - \mathcal{D} = \theta\,(\dot{\eta} - \dot{\eta}^{\mathrm{p}}) - \mathcal{D}_{\mathrm{mech}}\,. \tag{5.1.6}$$

Taking the total time derivative of (4.2.11) gives

$$\begin{aligned}\dot{\eta} - \dot{\eta}^{\mathrm{p}} &= -\frac{\partial\dot{\psi}}{\partial\theta} \\ &= -\frac{\partial}{\partial\theta}\left(\boldsymbol{\tau}\colon\boldsymbol{d} - \mathcal{D}_{\mathrm{mech}}\right) - \frac{\partial^2\hat{\psi}}{\partial\theta^2}\dot{\theta}\,.\end{aligned} \tag{5.1.7}$$

Then, defining the specific heat capacity c per unit volume in the reference configuration and the elastic-plastic structural heating $\mathcal{H}$ as

$$c = -\theta\frac{\partial^2\hat{\psi}}{\partial\theta^2}\,, \tag{5.1.8}$$

$$\mathcal{H} = -\theta\frac{\partial}{\partial\theta}\left(\boldsymbol{\tau}\colon\boldsymbol{d} - \mathcal{D}_{\mathrm{mech}}\right)\,, \tag{5.1.9}$$

gives

$$\theta\,(\dot{\eta} - \dot{\eta}^{\mathrm{p}}) = c\dot{\theta} + \mathcal{H}\,. \tag{5.1.10}$$

This is substituted in (5.1.6) to give

$$-J\,\mathrm{div}\left[\frac{1}{J}\boldsymbol{q}\right] + \mathcal{R}_b = c\dot{\theta} + \mathcal{H} - \mathcal{D}_{\mathrm{mech}}\,, \tag{5.1.11}$$

which, along with the Piola transformation $J\,\mathrm{div}\left[\frac{1}{J}\boldsymbol{q}\right] = \mathrm{Div}\left(\boldsymbol{F}_{\mathrm{c}}^{-1}\boldsymbol{q}\right)$, gives the temperature evolution equation

$$c\dot{\theta} = (\mathcal{D}_{\mathrm{mech}} - \mathcal{H}) + \left[\mathcal{R}_b - \mathrm{Div}\left(\boldsymbol{F}_{\mathrm{c}}^{-1}\boldsymbol{q}\right)\right] \qquad \text{in } \Omega^{\mathcal{B}}\,. \tag{5.1.12}$$

The boundary conditions are

$$\theta(\boldsymbol{X},t) = \bar{\theta}(\boldsymbol{X},t) \qquad \text{on } \Gamma^{\mathcal{B}}_{D_\theta} \subset \Gamma^{\mathcal{B}}\,, \tag{5.1.13a}$$

$$\boldsymbol{q}\cdot\,\boldsymbol{n} = \mathcal{R}_s \qquad \text{on } \Gamma^{\mathcal{B}}_{N_\theta} \subset \Gamma^{\mathcal{B}}\,, \tag{5.1.13b}$$

where $\Gamma^{\mathcal{B}}_{D_\theta}$ is the subset of the boundary where an essential boundary condition is given on the temperature, and $\Gamma^{\mathcal{B}}_{N_\theta}$ is the subset where a natural boundary condition is given on the boundary heat flux.

In addition, on each contact boundary pair $\Gamma_{\mathrm{c}}^{\mathrm{con}}$ and $\Gamma_{\mathrm{c}}^{\mathrm{tar}}$, thermal contact boundary conditions are given in terms of the contact heat flux q_{hc} and the frictional heat generation $\mathcal{D}^{\mathcal{B}}_{\mathrm{fric}}\,, \mathcal{B} \in \{\mathrm{con}, \mathrm{tar}\}$ by

$$\boldsymbol{q}^{\mathrm{con}}\cdot\boldsymbol{n}^{\mathrm{con}} = \mathcal{D}^{\mathrm{con}}_{\mathrm{fric}} + q_{\mathrm{hc}} \qquad \text{on } \Gamma_{\mathrm{c}}^{\mathrm{con}}\,, \tag{5.1.14a}$$

$$\boldsymbol{q}^{\mathrm{tar}}\cdot\boldsymbol{n}^{\mathrm{tar}} = \mathcal{D}^{\mathrm{tar}}_{\mathrm{fric}} - q_{\mathrm{hc}} \qquad \text{on } \Gamma_{\mathrm{c}}^{\mathrm{tar}}\,. \tag{5.1.14b}$$

The thermal initial condition is given by an initial temperature field $\theta_{\mathrm{initial}}$ as

$$\theta(\boldsymbol{X},t_0) = \theta_{\mathrm{initial}}(\boldsymbol{X})\,. \tag{5.1.15}$$

5.2 Weak Formulations

Taking the inner product of equation (5.1.1) with an arbitrary test function $\delta\boldsymbol{u}$ that is sufficiently smooth and which satisfies the homogeneous form of the essential boundary conditions (5.1.2a) and (5.1.2b), and integrating over the reference configuration $\Omega^{\mathcal{B}}$ gives

$$\int_{\Omega^{\mathcal{B}}} \delta\boldsymbol{u} \cdot \operatorname{Div} \boldsymbol{P} \,\mathrm{d}\Omega + \int_{\Omega^{\mathcal{B}}} \delta\boldsymbol{u} \cdot \boldsymbol{f}_b \,\mathrm{d}\Omega = \int_{\Omega^{\mathcal{B}}} \delta\boldsymbol{u} \cdot \rho_{\mathrm{m}} \boldsymbol{a} \,\mathrm{d}\Omega \,. \tag{5.2.1}$$

Using integration by parts and substitution of (4.1.10) and (4.1.16), the first term becomes

$$\begin{aligned} \int_{\Omega^{\mathcal{B}}} \delta\boldsymbol{u} \cdot \operatorname{Div} \boldsymbol{P} \,\mathrm{d}\Omega &= -\int_{\Omega^{\mathcal{B}}} \operatorname{Grad} \delta\boldsymbol{u} \colon \boldsymbol{P} \,\mathrm{d}\Omega + \int_{\Gamma^{\mathcal{B}}} \delta\boldsymbol{u} \cdot (\boldsymbol{P}\boldsymbol{N}) \,\mathrm{d}\Gamma \\ &= -\int_{\Omega^{\mathcal{B}}} \operatorname{Grad} \delta\boldsymbol{u} \colon \left(\boldsymbol{\tau}\boldsymbol{F}_c^{-\mathrm{t}}\right) \mathrm{d}\Omega + \int_{\Gamma^{\mathcal{B}}} \delta\boldsymbol{u} \cdot \left(J\|\boldsymbol{F}_{\mathrm{c}}^{-\mathrm{t}}\boldsymbol{N}\| \,\boldsymbol{\sigma}\boldsymbol{n}\right) \mathrm{d}\Gamma \,. \end{aligned} \tag{5.2.2}$$

By (3.1.20), we get

$$\begin{aligned} \operatorname{Grad} \delta\boldsymbol{u} \colon \boldsymbol{\tau}\boldsymbol{F}_{\mathrm{c}}^{-\mathrm{t}} &= (\operatorname{Grad} \delta\boldsymbol{u})\, \boldsymbol{F}_{\mathrm{c}}^{-1} \colon \boldsymbol{\tau} \\ &= \nabla\delta\boldsymbol{u} \colon \boldsymbol{\tau} \,, \end{aligned} \tag{5.2.3}$$

so that

$$\int_{\Omega^{\mathcal{B}}} \delta\boldsymbol{u} \cdot \operatorname{Div} \boldsymbol{P} \,\mathrm{d}\Omega = -\int_{\Omega^{\mathcal{B}}} \nabla\delta\boldsymbol{u} \colon \boldsymbol{\tau} \,\mathrm{d}\Omega + \int_{\Gamma^{\mathcal{B}}} \delta\boldsymbol{u} \cdot (\boldsymbol{\sigma}\boldsymbol{n})\, J\|\boldsymbol{F}^{-\mathrm{t}}\boldsymbol{N}\| \,\mathrm{d}\Gamma \,. \tag{5.2.4}$$

Then, defining

$$J_\Gamma \coloneqq \frac{\mathrm{d}\tilde{\Gamma}}{\mathrm{d}\Gamma} = J\|\boldsymbol{F}^{-\mathrm{t}}\boldsymbol{N}\| \,, \tag{5.2.5}$$

and substitution of the surface forces from the boundary conditions (5.1.2c) and (5.1.3) gives

$$\begin{aligned} \int_{\Omega^{\mathcal{B}}} \delta\boldsymbol{u} \cdot \operatorname{Div} \boldsymbol{P} \,\mathrm{d}\Omega = &-\int_{\Omega^{\mathcal{B}}} \nabla\delta\boldsymbol{u} \colon \boldsymbol{\tau} \,\mathrm{d}\Omega + \int_{\Gamma^{\mathcal{B}}_{N_\mu}} \delta\boldsymbol{u} \cdot \boldsymbol{f}_s \, J_\Gamma \,\mathrm{d}\Gamma \\ &+ \int_{\Gamma^{\mathcal{B}}_{\mathrm{c}}} s^{\mathcal{B}} \delta\boldsymbol{u} \cdot \boldsymbol{f}_{\mathrm{c}} \, J_\Gamma \,\mathrm{d}\Gamma \,, \end{aligned} \tag{5.2.6}$$

where the contact surface sign function s^{bod}, $\mathrm{bod} \in \{\mathrm{con}, \mathrm{tar}\}$ is defined as

$$s^{\mathrm{con}} \coloneqq 1\,, \tag{5.2.7a}$$

$$s^{\mathrm{tar}} \coloneqq -1\,. \tag{5.2.7b}$$

By substitution of (5.2.6) and following the convention of integrating the contribution of the target surface on the contactor surface instead [100], equation (5.2.1) becomes

$$\begin{aligned}\int_{\Omega^{\mathcal{B}}} \nabla\delta\boldsymbol{u} \colon \boldsymbol{\tau}\,\mathrm{d}\Omega + \int_{\Omega^{\mathcal{B}}} \delta\boldsymbol{u}\cdot\rho_{\mathrm{m}}\boldsymbol{a}\,\mathrm{d}\Omega - \int_{\Omega^{\mathcal{B}}} \delta\boldsymbol{u}\cdot\boldsymbol{f}_b\,\mathrm{d}\Omega \\ - \int_{\Gamma^{\mathcal{B}}_{N_\mu}} \delta\boldsymbol{u}\cdot\boldsymbol{f}_s\,J_\Gamma\,\mathrm{d}\Gamma - \int_{\Gamma^{\mathrm{con}}_{\mathrm{c}}} s^{\mathcal{B}}\delta\boldsymbol{u}\cdot\boldsymbol{f}_{\mathrm{c}}\,J_\Gamma\,\mathrm{d}\Gamma = 0\,.\end{aligned} \tag{5.2.8}$$

The inertial force term can be expanded by substitution of equation (3.1.26) to obtain

$$\begin{aligned}\int_{\Omega^{\mathcal{B}}} \delta\boldsymbol{u}\cdot\rho_{\mathrm{m}}\boldsymbol{a}\,\mathrm{d}\Omega = \int_{\Omega^{\mathcal{B}}} \delta\boldsymbol{u}\cdot\rho_{\mathrm{m}}\left[\frac{\partial^2\boldsymbol{\varphi}}{\partial t^2} + 2\left(\frac{\partial\boldsymbol{F}_{\mathrm{c}}}{\partial t}\right)\boldsymbol{V} + \boldsymbol{F}_{\mathrm{c}}\left(\frac{\partial\boldsymbol{V}}{\partial t} + (\operatorname{Grad}\boldsymbol{V})\,\boldsymbol{V}\right)\right. \\ \left. + \left((\operatorname{Grad}\boldsymbol{F}_{\mathrm{c}})\,\boldsymbol{V}\right)\boldsymbol{V}\right]\,\mathrm{d}\Omega\,.\end{aligned} \tag{5.2.9}$$

The term involving $\operatorname{Grad}\boldsymbol{F}_{\mathrm{c}}$ can be simplified using integration by parts, to give

$$\begin{aligned}\int_{\Omega^{\mathcal{B}}} \delta\boldsymbol{u}\cdot\rho_{\mathrm{m}}\left((\operatorname{Grad}\boldsymbol{F}_{\mathrm{c}})\,\boldsymbol{V}\right)\boldsymbol{V}\,\mathrm{d}\Omega = &- \int_{\Omega^{\mathcal{B}}} \delta\boldsymbol{u}\cdot\rho_{\mathrm{m}}\left(\boldsymbol{F}_{\mathrm{c}}\left(\operatorname{Grad}\boldsymbol{V}\right)\boldsymbol{V}\right)\,\mathrm{d}\Omega \\ &- \int_{\Omega^{\mathcal{B}}} \left(\delta\boldsymbol{u}\cdot\boldsymbol{F}_{\mathrm{c}}\boldsymbol{V}\right)\left(\rho_{\mathrm{m}}\operatorname{Div}\boldsymbol{V}\right)\,\mathrm{d}\Omega \\ &- \int_{\Omega^{\mathcal{B}}} \left(\delta\boldsymbol{u}\cdot\boldsymbol{F}_{\mathrm{c}}\boldsymbol{V}\right)\left(\operatorname{Grad}\rho_{\mathrm{m}}\cdot\boldsymbol{V}\right)\,\mathrm{d}\Omega \\ &- \int_{\Omega^{\mathcal{B}}} \left(\left(\operatorname{Grad}\delta\boldsymbol{u}\right)\boldsymbol{V}\right)\cdot\rho_{\mathrm{m}}\left(\boldsymbol{F}_{\mathrm{c}}\boldsymbol{V}\right)\,\mathrm{d}\Omega \\ &+ \int_{\Gamma^{\mathcal{B}}} \delta\boldsymbol{u}\cdot\rho_{\mathrm{m}}\left(\boldsymbol{F}_{\mathrm{c}}\boldsymbol{V}\right)\left(\boldsymbol{V}\cdot\boldsymbol{N}\right)\,\mathrm{d}\Gamma\,,\end{aligned} \tag{5.2.10}$$

which by substitution in (5.2.9) yields

$$\begin{aligned}\int_{\Omega^{\mathcal{B}}} \delta\boldsymbol{u}\cdot\rho_{\mathrm{m}}\boldsymbol{a}\,\mathrm{d}\Omega = \int_{\Omega^{\mathcal{B}}} \delta\boldsymbol{u}\cdot\rho_{\mathrm{m}}\left[\frac{\partial^2\boldsymbol{\varphi}}{\partial t^2} + 2\left(\frac{\partial\boldsymbol{F}_{\mathrm{c}}}{\partial t}\right)\boldsymbol{V} + \boldsymbol{F}_{\mathrm{c}}\left(\frac{\partial\boldsymbol{V}}{\partial t}\right)\right]\,\mathrm{d}\Omega \\ - \int_{\Omega^{\mathcal{B}}} \delta\boldsymbol{u}\cdot\operatorname{Div}(\rho_{\mathrm{m}}\boldsymbol{V})\boldsymbol{F}_{\mathrm{c}}\boldsymbol{V}\,\mathrm{d}\Omega - \int_{\Omega^{\mathcal{B}}} \left(\left(\operatorname{Grad}\,\delta\boldsymbol{u}\right)\boldsymbol{V}\right)\cdot\rho_{\mathrm{m}}\left(\boldsymbol{F}_{\mathrm{c}}\boldsymbol{V}\right)\,\mathrm{d}\Omega \\ + \int_{\Gamma^{\mathcal{B}}} \delta\boldsymbol{u}\cdot\rho_{\mathrm{m}}\left(\boldsymbol{F}_{\mathrm{c}}\boldsymbol{V}\right)\left(\boldsymbol{V}\cdot\boldsymbol{N}\right)\,\mathrm{d}\Gamma\,.\end{aligned} \tag{5.2.11}$$

For the thermal balance equation, the weak formulation is derived similarly by first multiplying equation (5.1.12) by an arbitrary test function $\delta\vartheta$ that is sufficiently smooth and which satisfies the homogeneous form of the essential boundary conditions (5.1.13a). Integration over the reference configuration $\Omega^{\mathcal{B}}$ gives

$$\int_{\Omega^{\mathcal{B}}} \delta\vartheta \; c\dot{\theta} \, \mathrm{d}\Omega = \int_{\Omega^{\mathcal{B}}} \delta\vartheta \; \left(\mathcal{D}_{\mathrm{mech}} - \mathcal{H}\right) \, \mathrm{d}\Omega + \int_{\Omega^{\mathcal{B}}} \delta\vartheta \; \left(\mathcal{R}_b - \mathrm{Div}\left(\boldsymbol{F}_{\mathrm{c}}^{-1}\boldsymbol{q}\right)\right) \, \mathrm{d}\Omega \,. \tag{5.2.12}$$

Integration by parts, then, gives

$$\begin{aligned}
-\int_{\Omega^{\mathcal{B}}} \delta\vartheta \; \mathrm{Div}\left(\boldsymbol{F}_{\mathrm{c}}^{-1}\boldsymbol{q}\right) \, \mathrm{d}\Omega &= -\int_{\Omega^{\mathcal{B}}} \delta\vartheta \; \frac{\partial}{\partial X_i} \left(\left(\frac{\partial x_j}{\partial X_i} \right)^{-1} q_j \right) \mathrm{d}\Omega \\
&= \int_{\Omega^{\mathcal{B}}} \left(\frac{\partial}{\partial X_i} \delta\vartheta \right) \left(\left(\frac{\partial x_j}{\partial X_i} \right)^{-1} q_j \right) \mathrm{d}\Omega \\
&\quad - \int_{\Gamma^{\mathcal{B}}} \delta\vartheta \left(\left(\frac{\partial x_j}{\partial X_i} \right)^{-1} q_j \right) N_i \, \mathrm{d}\Gamma \\
&= \int_{\Omega^{\mathcal{B}}} \left(\frac{\partial}{\partial X_i} \delta\vartheta \right) \left(\frac{\partial x_j}{\partial X_i} \right)^{-1} q_j \, \mathrm{d}\Omega \\
&\quad - \int_{\Gamma^{\mathcal{B}}} \delta\vartheta \; q_j \left(\frac{\partial x_j}{\partial X_i} \right)^{-1} N_i \, \mathrm{d}\Gamma \,.
\end{aligned} \tag{5.2.13}$$

By the chain rule and using (4.1.15), this becomes

$$\begin{aligned}
-\int_{\Omega^{\mathcal{B}}} \delta\vartheta \; \mathrm{Div}\left(\boldsymbol{F}_{\mathrm{c}}^{-1}\boldsymbol{q}\right) \, \mathrm{d}\Omega &= \int_{\Omega^{\mathcal{B}}} \left(\frac{\partial}{\partial x_j} \delta\vartheta \right) \, q_j \, \mathrm{d}\Omega \\
&\quad - \int_{\Gamma^{\mathcal{B}}} \delta\vartheta \; q_j \left(\varphi_{j,i}\right)^{-1} N_i \, \mathrm{d}\Gamma \\
&= \int_{\Omega^{\mathcal{B}}} \nabla\delta\vartheta \cdot \boldsymbol{q} \, \mathrm{d}\Omega - \int_{\Gamma^{\mathcal{B}}} \delta\vartheta \; \boldsymbol{q} \cdot \left(\boldsymbol{F}^{-\mathrm{t}}\boldsymbol{N}\right) \, \mathrm{d}\Gamma \\
&= \int_{\Omega^{\mathcal{B}}} \nabla\delta\vartheta \cdot \boldsymbol{q} \, \mathrm{d}\Omega - \int_{\Gamma^{\mathcal{B}}} \delta\vartheta \; \boldsymbol{q} \cdot \boldsymbol{n} \left\| \boldsymbol{F}^{-\mathrm{t}}\boldsymbol{N} \right\| \, \mathrm{d}\Gamma \\
&= \int_{\Omega^{\mathcal{B}}} \nabla\delta\vartheta \cdot \boldsymbol{q} \, \mathrm{d}\Omega - \int_{\Gamma^{\mathcal{B}}} \delta\vartheta \; \boldsymbol{q} \cdot \boldsymbol{n} \, \frac{J_\Gamma}{J} \, \mathrm{d}\Gamma \,.
\end{aligned} \tag{5.2.14}$$

Substitution of the boundary conditions (5.1.13b) and (5.1.14) and using (5.2.7) gives

$$\int_{\Gamma^{\mathcal{B}}} \delta\vartheta \; \boldsymbol{q} \cdot \boldsymbol{n} \, \frac{J_\Gamma}{J} \, \mathrm{d}\Gamma = \int_{\Gamma^{\mathcal{B}}_{N_\theta}} \delta\vartheta \; \mathcal{R}_s \, \frac{J_\Gamma}{J} \, \mathrm{d}\Gamma + \int_{\Gamma^{\mathcal{B}}_{\mathrm{c}}} \delta\vartheta \; \left(\mathcal{D}^{\mathcal{B}}_{\mathrm{fric}} + s^{\mathcal{B}} q_{\mathrm{hc}}\right) \, \frac{J_\Gamma}{J} \, \mathrm{d}\Gamma \,. \tag{5.2.15}$$

Thus, substitution into (5.2.12) and integration of the contact term contribution of the target surface on the contactor surface gives

$$\int_{\Omega^{\mathcal{B}}} \nabla\delta\vartheta \cdot \boldsymbol{q}\, \mathrm{d}\Omega + \int_{\Omega^{\mathcal{B}}} \delta\vartheta\, c\dot{\theta}\, \mathrm{d}\Omega - \int_{\Omega^{\mathcal{B}}} \delta\vartheta\, (\mathcal{R}_b + \mathcal{D}_{\mathrm{mech}} - \mathcal{H})\, \mathrm{d}\Omega \\ - \int_{\Gamma^{\mathcal{B}}_{N_\theta}} \delta\vartheta\, \mathcal{R}_s\, \frac{J_\Gamma}{J}\, \mathrm{d}\Gamma - \int_{\Gamma_{\mathrm{c}}^{\mathrm{con}}} \delta\vartheta\, \left(\mathcal{D}^{\mathcal{B}}_{\mathrm{fric}} + s^{\mathcal{B}} q_{\mathrm{hc}}\right)\, \frac{J_\Gamma}{J}\, \mathrm{d}\Gamma = 0\,. \quad (5.2.16)$$

5.3 Problem Statement

As a summary of the previous sections, the problem statement is as follows:

Problem 5.3.1. *Find the deformation $\boldsymbol{\varphi}$, the reference velocity $\boldsymbol{V}$, and the temperature θ, in functional spaces defined on $\Omega^{\mathcal{B}} \times \mathbb{R}^+$, $i = 1, 2$, such that:*

- *The weak forms (5.2.8) and (5.2.16) are satisfied for all admissible test functions $\delta\vartheta$ and $\delta\boldsymbol{u}$ defined on $\Omega^{\mathcal{B}} \times \mathbb{R}^+$, $i = 1, 2$.*
- *The essential boundary conditions (5.1.2a), (5.1.2b) and (5.1.13a) and the initial conditions (5.1.4) and (5.1.15) are met.*
- *The stress $\boldsymbol{\tau}$ in (5.2.8) is given by (4.3.7) and satisfies the yield criterion (4.4.2), where the elastic left Cauchy-Green deformation tensor $\boldsymbol{b}^{\mathrm{e}}$ is given by (4.3.17) and evolves according to (4.3.10).*
- *The normal and tangential components of the contact force $\boldsymbol{f}_{\mathrm{c}}$ in (5.2.8) are given by (4.5.1) and (4.5.2).*
- *The specific heat capacity c, the mechanical dissipation $\mathcal{D}_{mech}$, the structural heating $\mathcal{H}$, and the heat flux $\boldsymbol{q}$ are given by (4.3.15)*

In the following Chapter, discrete approximations of the problem are developed, together with algorithms for their numerical solution.

Part III

Solution Formulation and Implementation

6 Discretisation and Numerical Solution Procedure

Thermomechanical behaviour during a friction weld is governed by the constitutive models presented in Chapter 4 and the weak formulations in Section 5.2. The exact solutions are fields in infinite dimensional subspaces. They are functions of position in the reference configuration and time. Numerical simulation approximates these solutions on finite dimensional subspaces that have discrete representations amenable to computer solution. This discretisation is conceptually carried out in several stages.

First, time is discretised into N time steps $1, ..., N$, with each time step n corresponding to a time interval $[t_{n-1}, t_n]$. Thus, the continuous problem is converted into a semi-discrete problem, which comprises a sequence of problems, each of which corresponding to a time step n. These problems are solved sequentially, so that in formulating the problem corresponding to time step n, the solution from the previous time step $n-1$ is available. This is carried out by approximating temporal derivatives by finite differences given in terms of the time increment $\Delta t = t_n - t_{n-1}$ and of the values at t_n and t_{n-1}. This is detailed in Section 6.1.

The next stage is operator splitting to decouple the mechanical and thermal problems. The coupled thermomechanical problem corresponding to each time step is approximated by a sequence of three smaller problems: a mechanical one, followed by a thermal one, and finally another mechanical problem. This is detailed in Section 6.2.

To address the contact constraints arising from (4.5.1) and (4.5.2), an augmented Lagrangian approach is followed, in which each of the two mechanical problems within a time step is converted into a sequence of augmented Lagrangian iterations. In each of these augmented Lagrangian iterations, the contact forces are approximated by the sum of penalty terms and the accumulated values from the previous iterations. These iterations continue until the contact constraints are met with sufficient accuracy. This is detailed in Section 6.3.

The outcome of time discretisation and operator splitting is a sequence of discrete-in-time continuous-in-space thermal and mechanical problems, each of which is posed on infinite-dimensional functional subspaces on the reference configuration. In the next stage, these problems are discretised in space using the finite element method, where the approximate solution is sought in finite element subspaces defined on discrete meshes of the domains of the contacting bodies in the reference configuration. This is detailed in Section 6.4.

The resulting nonlinear thermomechanical problem is then linearised using the Newton-Raphson method. This converts each of these problems into a sequence of linear problems, each of which is an iterative step to compute an incremental update towards the solution. This is detailed in Section 6.5.

The stages of formulating the discrete linear problems are represented in Figure 6.1.

6.1 Time Discretisation

For numerical approximation of Problem 5.3.1, we first discretise time into steps $t_1, ..., t_N$, and seek an approximate solution at each time instant t_n. This gives rise to a sequence of problems, one corresponding to each time step. They are to be solved sequentially, so that at each time step, the solution from the previous one is available as input.

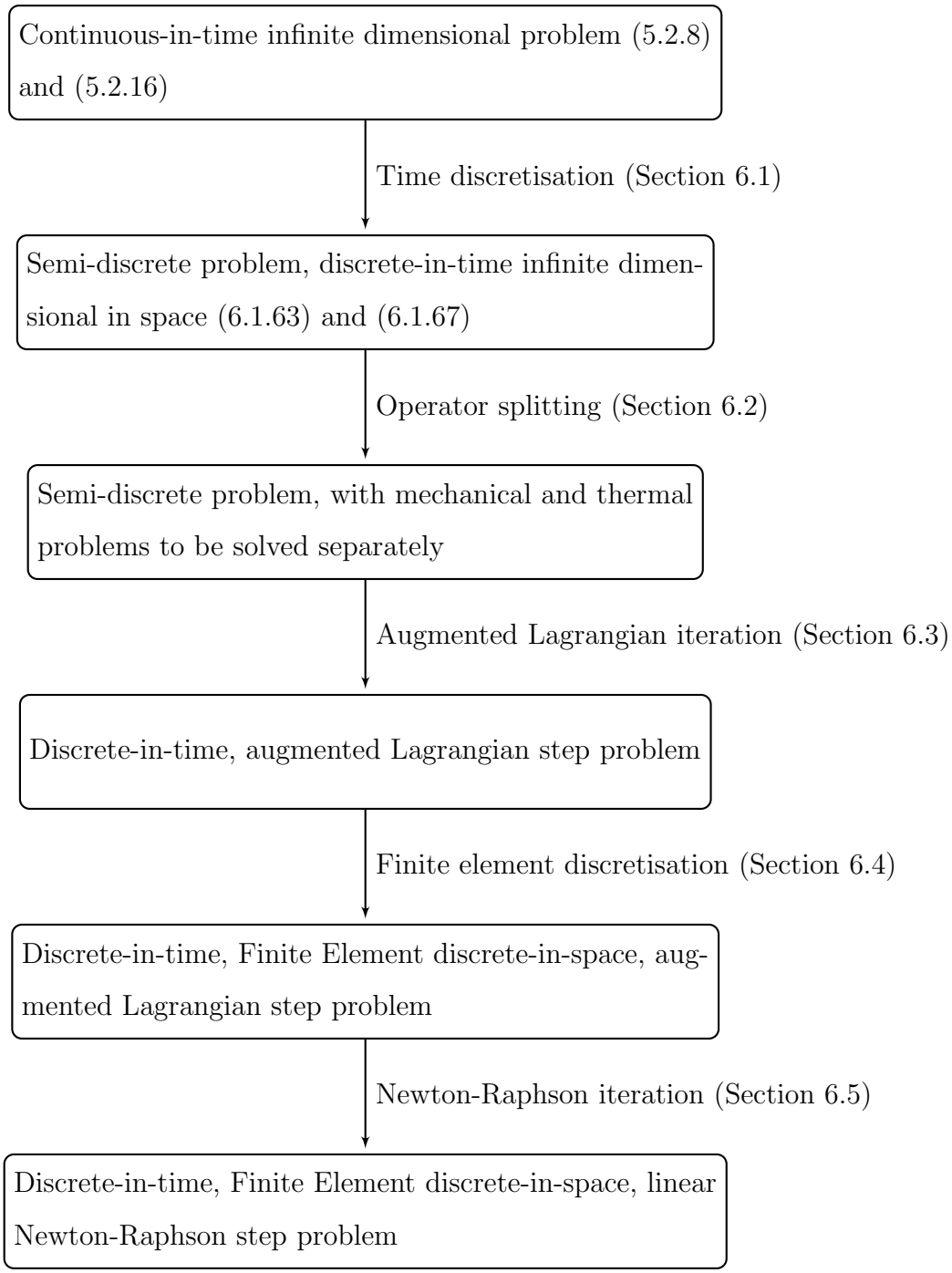

Figure 6.1: Problem approximation steps

The time derivatives are approximated by finite differences. Let the motion from the reference configuration, and its first and second partial time derivatives,

$$\boldsymbol{\varphi}_n \approx \boldsymbol{\varphi}|_{t=t_n} \,, \tag{6.1.1a}$$

$$\left(\frac{\partial \boldsymbol{\varphi}}{\partial t}\right)_n \approx \left(\frac{\partial \boldsymbol{\varphi}}{\partial t}\right)\Big|_{t=t_n} \,, \tag{6.1.1b}$$

$$\left(\frac{\partial^2 \boldsymbol{\varphi}}{\partial t^2}\right)_n \approx \left(\frac{\partial^2 \boldsymbol{\varphi}}{\partial t^2}\right)\Big|_{t=t_n} \,, \tag{6.1.1c}$$

be given from the initial conditions at time step t_1 and, at later time steps t_n, from the solution of the preceding time steps. Then, the updated second and first partial time derivatives at time step t_{n+1} are approximated using the updated motion $\boldsymbol{\varphi}_{n+1}$ through Newmark's method by

$$\left(\frac{\partial^2 \boldsymbol{\varphi}}{\partial t^2}\right)_{n+1} = \frac{1}{\beta \Delta t^2}\left[\boldsymbol{\varphi}_{n+1} - \boldsymbol{\varphi}_n - \Delta t \left(\frac{\partial \boldsymbol{\varphi}}{\partial t}\right)_n\right] - \left(\frac{1}{2\beta} - 1\right)\left(\frac{\partial^2 \boldsymbol{\varphi}}{\partial t^2}\right)_n \,, \tag{6.1.2a}$$

$$\left(\frac{\partial \boldsymbol{\varphi}}{\partial t}\right)_{n+1} = \left(\frac{\partial \boldsymbol{\varphi}}{\partial t}\right)_n + \Delta t \left[(1-\gamma)\left(\frac{\partial^2 \boldsymbol{\varphi}}{\partial t^2}\right)_n + \gamma \left(\frac{\partial^2 \boldsymbol{\varphi}}{\partial t^2}\right)_{n+1}\right] \,, \tag{6.1.2b}$$

where the Newmark parameters β and γ are computed using the generalised-α method [138]:

$$\gamma = \frac{1}{2} - \alpha_\mathrm{m} + \alpha_\mathrm{f} \,, \tag{6.1.3}$$

$$\beta = \frac{1}{4}(1 - \alpha_\mathrm{m} + \alpha_\mathrm{f})^2 \,, \tag{6.1.4}$$

$$\alpha_\mathrm{m} = \frac{2\rho_\infty - 1}{\rho_\infty + 1} \,, \tag{6.1.5}$$

$$\alpha_\mathrm{f} = \frac{\rho_\infty}{\rho_\infty + 1} \,, \tag{6.1.6}$$

$$\rho_\infty \in [0, 1] \,. \tag{6.1.7}$$

The partial time derivative of the reference velocity $\frac{\partial \boldsymbol{V}}{\partial t}$ is approximated in a similar fashion to those of the motion (6.1.2). With the reference velocity and its partial time derivative known at time $t = t_n$,

$$\boldsymbol{V}_n \approx \boldsymbol{V}|_{t=t_n} \,, \tag{6.1.8}$$

$$\left(\frac{\partial \boldsymbol{V}}{\partial t}\right)_n \approx \left(\frac{\partial \boldsymbol{V}}{\partial t}\right)\Big|_{t=t_n} \,, \tag{6.1.9}$$

its updated partial time derivative for a given updated reference velocity $\boldsymbol{V}_{n+1}$ is approximated by

$$\left(\frac{\partial \boldsymbol{V}}{\partial t}\right)_{n+1} = \frac{1}{\gamma \Delta t}\left(\boldsymbol{V}_{n+1} - \boldsymbol{V}_n\right) - \frac{1-\gamma}{\gamma}\left(\frac{\partial \boldsymbol{V}}{\partial t}\right)_n . \tag{6.1.10}$$

The thermal field is treated similarly. For a known temperature at time t_n

$$\theta_n \approx \theta|_{t=t_n} , \tag{6.1.11}$$

the updated partial time derivative of the temperature is approximated by the finite difference

$$\left(\frac{\partial \theta}{\partial t}\right)_{n+1} = \frac{1}{\Delta t}\left(\theta_{n+1} - \theta_n\right) . \tag{6.1.12}$$

Using the generalised midpoints α_{m} (6.1.5) and α_{f} (6.1.6) to define the generalised intermediate values $\bullet_{n+1-\alpha_{\mathrm{m}}}$ and $\bullet_{n+1-\alpha_{\mathrm{f}}}$ as

$$\begin{aligned} \bullet_{n+1-\alpha_{\mathrm{f}}} &= (1-\alpha_{\mathrm{f}})\left(\bullet_n\right) + \alpha_{\mathrm{f}}\left(\bullet_{n+1}\right) \\ \bullet_{n+1-\alpha_{\mathrm{m}}} &= (1-\alpha_{\mathrm{m}})\left(\bullet_n\right) + \alpha_{\mathrm{m}}\left(\bullet_{n+1}\right) , \end{aligned} \tag{6.1.13}$$

6.1.1 Stress Update

The stress $\boldsymbol{\tau}_{n+1}$ is given in terms of the deformation Jacobian J_{n+1} and the volume preserving part $\bar{\boldsymbol{b}}^{\mathrm{e}}_{n+1}$ of the elastic left Cauchy-Green tensor by (4.3.3) and (4.3.5) as

$$\boldsymbol{\tau}_{n+1} = \operatorname{dev} \boldsymbol{\tau}_{n+1} + p_{n+1}\mathbf{1} , \tag{6.1.14}$$

$$p_{n+1} = J_{n+1}\left\{\partial_J\left[\hat{M}(J_{n+1}, \theta_{n+1}) + \hat{U}(J_{n+1})\right]\right\} , \tag{6.1.15}$$

$$\operatorname{dev} \boldsymbol{\tau}_{n+1} = 2 \operatorname{dev}\left\{\left[\partial_{\bar{\boldsymbol{b}}^{\mathrm{e}}} \hat{W}(\bar{\boldsymbol{b}}^{\mathrm{e}}_{n+1})\right] \bar{\boldsymbol{b}}^{\mathrm{e}}_{n+1}\right\} , \tag{6.1.16}$$

where the deformation Jacobian is given in terms of the gradient of the motion in the reference configuration and the reference motion Jacobian by

$$J_{n+1} = \det\left[\operatorname{Grad} \boldsymbol{\varphi}_{n+1}\right] J_{\mathrm{r},n+1} . \tag{6.1.17}$$

The elastic left Cauchy-Green tensor $\boldsymbol{b}^{\mathrm{e}}_{n+1} = J^{2/3}_{n+1}\bar{\boldsymbol{b}}^{\mathrm{e}}_{n+1}$ is given by (3.2.10) as

$$\boldsymbol{b}^{\mathrm{e}}_{n+1} = \boldsymbol{F}_{n+1}\boldsymbol{G}^{\mathrm{p}}_{n+1}\boldsymbol{F}^{\mathrm{t}}_{n+1}\,, \tag{6.1.18}$$

and its volume preserving part is

$$\bar{\boldsymbol{b}}^{\mathrm{e}}_{n+1} = J^{-2/3}_{n+1}\,\boldsymbol{b}^{\mathrm{e}}_{n+1}\,. \tag{6.1.19}$$

The material time derivative of the plastic tensor $\boldsymbol{G}^{\mathrm{p}}_{n+1}$ is given by (3.2.17) as

$$\dot{\boldsymbol{G}}^{\mathrm{p}}_{n+1} = \boldsymbol{F}^{-1}_{n+1}\mathscr{L}_v\boldsymbol{b}^{\mathrm{e}}_{n+1}\boldsymbol{F}^{-\mathrm{t}}_{n+1}\,, \tag{6.1.20}$$

where the Lie derivative $\mathscr{L}_v\boldsymbol{b}^{\mathrm{e}}_{n+1}$ is given by (4.3.10) as

$$\mathscr{L}_v\boldsymbol{b}^{\mathrm{e}}_{n+1} = -2\gamma_{n+1}\left[\partial_{\boldsymbol{\tau}}\hat{\phi}_{n+1}\right]\boldsymbol{b}^{\mathrm{e}}_{n+1}\,. \tag{6.1.21}$$

Here, the consistency parameter γ_{n+1} is governed by the KKT conditions (4.3.13):

$$\phi_{n+1} = \|\mathrm{dev}\,\boldsymbol{\tau}_{n+1}\| - \sqrt{\frac{2}{3}}\sigma^{\mathrm{y}}(\alpha_{n+1}, \dot{\alpha}_{n+1}, \theta_{n+1}) \leq 0\,, \tag{6.1.22a}$$

$$\gamma_{n+1} \geq 0\,, \tag{6.1.22b}$$

$$\gamma_{n+1}\phi_{n+1} = 0\,, \tag{6.1.22c}$$

where the time derivative of the equivalent plastic strain is

$$\dot{\alpha}_{n+1} = \sqrt{\frac{2}{3}}\gamma_{n+1}\,. \tag{6.1.23}$$

Substitution of (6.1.22a) into (6.1.21) gives

$$\mathscr{L}_v\boldsymbol{b}^{\mathrm{e}}_{n+1} = -2\gamma_{n+1}\frac{\mathrm{dev}\,\boldsymbol{\tau}_{n+1}}{\|\mathrm{dev}\,\boldsymbol{\tau}_{n+1}\|}\boldsymbol{b}^{\mathrm{e}}_{n+1}\,. \tag{6.1.24}$$

The KKT conditions (6.1.22) mean that one of two scenarios must hold. Either the consistency parameter γ_{n+1} vanishes, or it is strictly positive and the yield criterion (6.1.22a) is met with equality such that (6.1.22c) holds. To determine which of these scenarios is true, a return mapping approach is used, which comprises a predictor step followed, if

necessary, by a corrector step. In the predictor step, the first scenario is assumed, and a trial solution is computed with the assumption that $\gamma_{n+1}^{\mathrm{trial}} = 0$. In this case,

$$\gamma_{n+1}^{\mathrm{trial}} = 0\,, \tag{6.1.25a}$$

$$\mathscr{L}_v \boldsymbol{b}_{n+1}^{\mathrm{e,trial}} = \boldsymbol{0}\,, \tag{6.1.25b}$$

$$\alpha_{n+1}^{\mathrm{trial}} = \alpha_n\,, \tag{6.1.25c}$$

$$\dot{\alpha}_{n+1}^{\mathrm{trial}} = 0\,, \tag{6.1.25d}$$

$$\phi_{n+1}^{\mathrm{trial}} \coloneqq \left\|\operatorname{dev} \boldsymbol{\tau}_{n+1}^{\mathrm{trial}}\right\| - \sqrt{\frac{2}{3}}\sigma^{\mathrm{y}}(\alpha_n, 0, \theta_{n+1})\,. \tag{6.1.25e}$$

Here, the trial stress deviator $\operatorname{dev} \boldsymbol{\tau}_{n+1}^{\mathrm{trial}}$ is computed using the trial left Cauchy-Green elastic tensor $\boldsymbol{b}_{n+1}^{\mathrm{e,trial}}$, which is given by (3.2.10) as

$$\boldsymbol{b}_{n+1}^{\mathrm{e,trial}} = \boldsymbol{F}_{n+1}\boldsymbol{G}_{n+1}^{\mathrm{p,trial}}\boldsymbol{F}_{n+1}^{\mathrm{t}}\,, \tag{6.1.26}$$

where the material time derivative of the trial value of the plastic tensor $\boldsymbol{G}_{n+1}^{\mathrm{p,trial}}$ vanishes due to (3.2.17) and (6.1.25b)

$$\dot{\boldsymbol{G}}_{n+1}^{\mathrm{p,trial}} = \boldsymbol{F}_{n+1}^{-1}\mathscr{L}_v \boldsymbol{b}_{n+1}^{\mathrm{e,trial}}\boldsymbol{F}_{n+1}^{-\mathrm{t}} = 0\,. \tag{6.1.27}$$

If the trial yield criterion (6.1.25e) is admissible, i.e. $\phi_{n+1}^{\mathrm{trial}} \leq 0$, then the predictor assumption is valid, and the trial values coincide with the solution. Otherwise, the assumption is not valid, and a corrector step is required to ensure that the solution is consistent with the second scenario. Namely, the consistency parameter is strictly positive $\gamma_{n+1} > 0$, and the yield criterion (6.1.22a) is met with equality to satisfy (6.1.22c). This is achieved by using the evolution laws (6.1.21) and (6.1.23) to write the yield criterion (6.1.22a) in terms of the trial values and the consistency parameter γ_{n+1}. To this end, the stress deviator $\operatorname{dev} \boldsymbol{\tau}_{n+1}$ must be computed from its trial value $\operatorname{dev} \boldsymbol{\tau}_{n+1}^{\mathrm{trial}}$ and the consistency parameter γ_{n+1}. This, in turn, requires relating the left Cauchy-Green elastic tensor $\boldsymbol{b}_{n+1}^{\mathrm{e}}$ to its trial value $\boldsymbol{b}_{n+1}^{\mathrm{e,trial}}$ and the consistency parameter γ_{n+1}. Equation (6.1.24) is satisfied if the corrected left Cauchy-Green elastic tensor $\boldsymbol{b}^{\mathrm{e}}$ at a time $t \in (t_n, t_{n+1}]$ relates to its trial value by

$$\boldsymbol{b}^{\mathrm{e}} = \exp\left(-2\gamma_{n+1}\,(t - t_n)\,\frac{\operatorname{dev} \boldsymbol{\tau}_{n+1}}{\|\operatorname{dev} \boldsymbol{\tau}_{n+1}\|}\right)\boldsymbol{b}^{\mathrm{e,trial}}\,, \tag{6.1.28}$$

such that

$$\begin{aligned}
\boldsymbol{G}^{\mathrm{p}} &= \boldsymbol{F}^{-1}\boldsymbol{b}^{\mathrm{e}}\boldsymbol{F}^{-\mathrm{t}} \\
&= \boldsymbol{F}^{-1}\exp\left(-2\gamma_{n+1}\left(t-t_n\right)\frac{\operatorname{dev}\boldsymbol{\tau}_{n+1}}{\|\operatorname{dev}\boldsymbol{\tau}_{n+1}\|}\right)\boldsymbol{b}^{\mathrm{e,trial}}\boldsymbol{F}^{-\mathrm{t}} \\
&= \boldsymbol{F}^{-1}\exp\left(-2\gamma_{n+1}\left(t-t_n\right)\frac{\operatorname{dev}\boldsymbol{\tau}_{n+1}}{\|\operatorname{dev}\boldsymbol{\tau}_{n+1}\|}\right)\boldsymbol{F}\boldsymbol{F}^{-1}\boldsymbol{b}^{\mathrm{e,trial}}\boldsymbol{F}^{-\mathrm{t}} \\
&= \boldsymbol{F}^{-1}\exp\left(-2\gamma_{n+1}\left(t-t_n\right)\frac{\operatorname{dev}\boldsymbol{\tau}_{n+1}}{\|\operatorname{dev}\boldsymbol{\tau}_{n+1}\|}\right)\boldsymbol{F}\boldsymbol{G}^{\mathrm{p,trial}}\,. \qquad (6.1.29)
\end{aligned}$$

Thus,

$$\dot{\boldsymbol{G}}^{\mathrm{p}} = \boldsymbol{F}^{-1}\left(-2\gamma_{n+1}\frac{\operatorname{dev}\boldsymbol{\tau}_{n+1}}{\|\operatorname{dev}\boldsymbol{\tau}_{n+1}\|}\right)\exp\left(-2\gamma_{n+1}\left(t-t_n\right)\frac{\operatorname{dev}\boldsymbol{\tau}_{n+1}}{\|\operatorname{dev}\boldsymbol{\tau}_{n+1}\|}\right)\boldsymbol{F}\boldsymbol{G}^{\mathrm{p,trial}}\,, \qquad (6.1.30)$$

and therefore

$$\begin{aligned}
\mathscr{L}_v\boldsymbol{b}^{\mathrm{e}}_{n+1} &\coloneqq \boldsymbol{F}\dot{\boldsymbol{G}}^{\mathrm{p}}\boldsymbol{F}^{\mathrm{t}} \\
&= -2\gamma_{n+1}\frac{\operatorname{dev}\boldsymbol{\tau}_{n+1}}{\|\operatorname{dev}\boldsymbol{\tau}_{n+1}\|}\,\exp\left(-2\gamma_{n+1}\left(t-t_n\right)\frac{\operatorname{dev}\boldsymbol{\tau}_{n+1}}{\|\operatorname{dev}\boldsymbol{\tau}_{n+1}\|}\right)\boldsymbol{F}\boldsymbol{G}^{\mathrm{p,trial}}\boldsymbol{F}^{\mathrm{t}} \\
&= -2\gamma_{n+1}\frac{\operatorname{dev}\boldsymbol{\tau}_{n+1}}{\|\operatorname{dev}\boldsymbol{\tau}_{n+1}\|}\,\exp\left(-2\gamma_{n+1}\left(t-t_n\right)\frac{\operatorname{dev}\boldsymbol{\tau}_{n+1}}{\|\operatorname{dev}\boldsymbol{\tau}_{n+1}\|}\right)\boldsymbol{b}^{\mathrm{e,trial}} \\
&= -2\gamma_{n+1}\frac{\operatorname{dev}\boldsymbol{\tau}_{n+1}}{\|\operatorname{dev}\boldsymbol{\tau}_{n+1}\|}\,\boldsymbol{b}^{\mathrm{e}}\,. \qquad (6.1.31)
\end{aligned}$$

Multiplication of both sides of (6.1.28) by $J^{-2/3}$ and taking the logarithm gives, at $t = t_{n+1}$,

$$\log\bar{\boldsymbol{b}}^{\mathrm{e}}_{n+1} = \log\bar{\boldsymbol{b}}^{\mathrm{e,trial}}_{n+1} - 2\gamma_{n+1}\Delta t\frac{\operatorname{dev}\boldsymbol{\tau}_{n+1}}{\|\operatorname{dev}\boldsymbol{\tau}_{n+1}\|}\,. \qquad (6.1.32)$$

Multiplication by the shear modulus μ then gives

$$\operatorname{dev}\boldsymbol{\tau}_{n+1} = \operatorname{dev}\boldsymbol{\tau}^{\mathrm{trial}}_{n+1} - 2\mu\Delta\lambda_{n+1}\boldsymbol{n}_{n+1}\,, \qquad (6.1.33)$$

where

$$\operatorname{dev}\boldsymbol{\tau}^{\mathrm{trial}}_{n+1} = \mu\log\bar{\boldsymbol{b}}^{\mathrm{e,trial}}_{n+1}\,, \qquad (6.1.34)$$

$$\Delta\lambda_{n+1} = \gamma_{n+1}\Delta t\,, \qquad (6.1.35)$$

$$\boldsymbol{n}_{n+1} \coloneqq \frac{\operatorname{dev}\boldsymbol{\tau}_{n+1}}{\|\operatorname{dev}\boldsymbol{\tau}_{n+1}\|} = \frac{\operatorname{dev}\boldsymbol{\tau}^{\mathrm{trial}}_{n+1}}{\|\operatorname{dev}\boldsymbol{\tau}^{\mathrm{trial}}_{n+1}\|}\,. \qquad (6.1.36)$$

The yield criterion can be written by substitution of (6.1.25e) into (6.1.22a) as

$$\phi_{n+1} = \left\|\operatorname{dev} \boldsymbol{\tau}_{n+1}^{\text{trial}}\right\| - 2\mu\Delta\lambda_{n+1} - \sqrt{\frac{2}{3}}\sigma^{\text{y}}(\alpha_{n+1}, \dot{\alpha}_{n+1}, \theta_{n+1})\,. \tag{6.1.37}$$

This predictor-corrector approach is summarised in Algorithm 6.1.1.

Algorithm 6.1.1 Predictor-Corrector Approach

if $\phi_{n+1}^{\text{trial}} \coloneqq \left\|\operatorname{dev} \boldsymbol{\tau}_{n+1}^{\text{trial}}\right\| - \sqrt{\frac{2}{3}}\sigma^{\text{y}}(\alpha_n, 0, \theta_{n+1}) \leq 0$ **then**
  $\gamma_{n+1} = \gamma_{n+1}^{\text{trial}} = 0\,,$
  $\mathscr{L}_v \boldsymbol{b}_{n+1}^{\text{e}} = \mathscr{L}_v \boldsymbol{b}_{n+1}^{\text{e,trial}} = \boldsymbol{0}\,,$
  $\dot{\alpha}_{n+1} = \dot{\alpha}_{n+1}^{\text{trial}} = 0\,,$
  $\alpha_{n+1} = \alpha_{n+1}^{\text{trial}} = \alpha_n\,,$
  $\operatorname{dev} \boldsymbol{\tau}_{n+1} = \operatorname{dev} \boldsymbol{\tau}_{n+1}^{\text{trial}}\,.$
else
  $\gamma_{n+1} > 0\,,$
  $\phi_{n+1} = \|\operatorname{dev} \boldsymbol{\tau}_{n+1}\| - \sqrt{\frac{2}{3}}\sigma^{\text{y}}(\alpha_{n+1}, \dot{\alpha}_{n+1}, \theta_{n+1}) = 0\,,$
  $\mathscr{L}_v \boldsymbol{b}_{n+1}^{\text{e}} = -2\gamma_{n+1}\frac{\operatorname{dev} \boldsymbol{\tau}_{n+1}}{\|\operatorname{dev} \boldsymbol{\tau}_{n+1}\|}\boldsymbol{b}_{n+1}^{\text{e}}\,,$
  $\dot{\alpha}_{n+1} = \sqrt{\frac{2}{3}}\gamma_{n+1}\,,$
  $\alpha_{n+1} = \alpha_n + \sqrt{\frac{2}{3}}\gamma_{n+1}\Delta t\,.$
  $\operatorname{dev} \boldsymbol{\tau}_{n+1} = \operatorname{dev} \boldsymbol{\tau}_{n+1}^{\text{trial}} - 2\mu\gamma_{n+1}\Delta t\, \boldsymbol{n}_{n+1}\,,$
  $\boldsymbol{n}_{n+1} \coloneqq \frac{\operatorname{dev} \boldsymbol{\tau}_{n+1}}{\|\operatorname{dev} \boldsymbol{\tau}_{n+1}\|} = \frac{\operatorname{dev} \boldsymbol{\tau}_{n+1}^{\text{trial}}}{\left\|\operatorname{dev} \boldsymbol{\tau}_{n+1}^{\text{trial}}\right\|}\,.$
end if

The evolution law (6.1.27) means that, for a fixed point $\boldsymbol{X}_0$ in the material configuration, the trial plastic tensor $\boldsymbol{G}_{n+1}^{\text{p,trial}}$ remains unchanged from the previous time step n. This implies that the only change in the plastic deformation at a point $\boldsymbol{X}$ in the reference configuration is due to a change in the reference motion $\boldsymbol{\Upsilon}_0$ such that the material point mapped to $\boldsymbol{X}$ is different from the previous time step. Thus, with the plastic deformation given in the material configuration by $\boldsymbol{G}_0^{\text{p}}|_{\left(\boldsymbol{\Upsilon}^{-1}(\boldsymbol{X},t),t\right)} = \boldsymbol{G}^{\text{p}}|_{(\boldsymbol{X},t)}$, the trial

plastic tensor is $\boldsymbol{G}^{\mathrm{p,trial}}\big|_{(\boldsymbol{X},t_{n+1})} = \boldsymbol{G}_0^p\big|_{\left(\boldsymbol{\Upsilon}^{-1}(\boldsymbol{X},t_{n+1}),t_n\right)}$. To compute this value of $\boldsymbol{G}^{\mathrm{p,trial}}$ and account for the change in $\boldsymbol{b}^e$ due to the reference velocity $\boldsymbol{V}$, it is useful to define a material remapping operator; this is done in the following subsection.

6.1.2 Material Remapping Operator

The predictor-corrector approach of computing the left Cauchy-Green elastic tensor $\boldsymbol{b}^{\mathrm{e}}_{n+1}$ requires evaluation of its trial value $\boldsymbol{b}^{\mathrm{e,trial}}_{n+1}$, which arises from the trial assumptions (6.1.25). The goal of this subsection is to describe the steps necessary to compute this trial value at a given point $\boldsymbol{X}$ in the reference configuration based on the deformation $\boldsymbol{\varphi}_{n+1}$ and reference velocity $\boldsymbol{V}_{n+1}$ fields, and on the value at the previous time step $t = t_n$ and the corresponding point $\boldsymbol{X}_0 = \boldsymbol{\Upsilon}^{-1}(\boldsymbol{X}, t_n)$ in the material configuration.

For a given position $\boldsymbol{X}$ in the reference configuration and a given time t_{n+1}, the elastic deformation $\boldsymbol{b}^e$ is given by (4.3.17) from the deformation gradient $\boldsymbol{F}_{\mathrm{c}}$ and the tensor $\boldsymbol{B}^e$. The motion $\boldsymbol{\varphi}$ is sufficient to determine the deformation gradient $\boldsymbol{F}_{\mathrm{c}}$. Determination of $\boldsymbol{B}^e$ at a time t_{n+1} using a predictor-corrector approach involves assuming that the plastic deformation associated with the material point $\boldsymbol{X}_0 = \boldsymbol{\Upsilon}_0^{-1}(\boldsymbol{X}, t_{n+1})$ remains unchanged from its value at t_n:

$$\boldsymbol{G}_0^{\mathrm{p,trial}}\left(\boldsymbol{X}_0, t_{n+1}\right) = \boldsymbol{G}_0^{\mathrm{p}}\left(\boldsymbol{X}_0, t_n\right) , \tag{6.1.38}$$

which is written in terms of position $\boldsymbol{X} = \boldsymbol{\Upsilon}_0\left(\boldsymbol{X}_0, t_{n+1}\right)$ in the reference configuration as

$$\boldsymbol{G}^{\mathrm{p,trial}}\left(\boldsymbol{X}, t_{n+1}\right) = \boldsymbol{G}_0^{\mathrm{p}}\left(\boldsymbol{\Upsilon}_0^{-1}(\boldsymbol{X}, t_{n+1}), t_n\right) . \tag{6.1.39}$$

As a shorthand, it is useful to define the following operator, which denotes for a position $\boldsymbol{X}$ in the reference configuration and a time t_{n+1} the value of a scalar or tensor field $\square$ at the corresponding material point $\boldsymbol{X}_0 = \boldsymbol{\Upsilon}_0^{-1}(\boldsymbol{X}, t_{n+1})$ and another time t_n. Let $\square$ be any scalar or tensor field given as a function of position in the reference configuration

and time as $\square = \square(\boldsymbol{X}, t)$ and as a function of position in the material configuration and time as $\square = \square_0(\boldsymbol{X}_0, t)$. Then, for a point $\boldsymbol{X}$ in the reference configuration, and two time instants t_n, $t_{n+1} > 0$, material remapping to t_{n+1} is given at $\boldsymbol{X}$ and t_n by

$$\mathcal{M}_{t_n}^{t_{n+1}}\{\square\}\Big|_{\boldsymbol{X}} \coloneqq M(\square, \boldsymbol{X}, t_n, t_{n+1}) \coloneqq \square_0\left(\boldsymbol{\Upsilon}_0^{-1}(\boldsymbol{X}, t_{n+1}), t_n\right) . \tag{6.1.40}$$

Thus, equation (6.1.39) can be written as

$$\boldsymbol{G}^{\mathrm{p,trial}}(\boldsymbol{X}, t_{n+1}) = \mathcal{M}_{t_n}^{t_{n+1}}\{\boldsymbol{G}^{\mathrm{p}}\}\Big|_{\boldsymbol{X}} . \tag{6.1.41}$$

The operator $\mathcal{M}$ is a continuum operator defined on continuous spatial and temporal fields. Its effect is remapping the material configuration such that any point $\boldsymbol{X}_0$ is identified by its position $\boldsymbol{X}$ in the reference configuration at time t_{n+1}: $\boldsymbol{X} = \boldsymbol{\Upsilon}_0(\boldsymbol{X}_0, t_{n+1})$. Position in the reference configuration is itself a valid input to the operator $\mathcal{M}$, since it is given as a function of position in the reference configuration and time by the identity function, and is given as a function of position in the material configuration and time by the reference motion $\boldsymbol{\Upsilon}_0$. Thus,

$$\mathcal{M}_{t_n}^{t_{n+1}}\{\boldsymbol{X}\} = \boldsymbol{\Upsilon}_0\left(\boldsymbol{\Upsilon}_0^{-1}(\boldsymbol{X}, t_{n+1}), t_n\right) . \tag{6.1.42}$$

Substitution of this into $\square(\boldsymbol{X}, t_n) = \square_0(\boldsymbol{\Upsilon}_0^{-1}(\boldsymbol{X}, t_n), t_n)$, gives

$$\begin{aligned}
\square(\mathcal{M}_{t_n}^{t_{n+1}}\{\boldsymbol{X}\}, t_n) &= \square_0(\boldsymbol{\Upsilon}_0^{-1}(\mathcal{M}_{t_n}^{t_{n+1}}\{\boldsymbol{X}\}, t_n), t_n) \\
&= \square_0(\boldsymbol{\Upsilon}_0^{-1}(\boldsymbol{\Upsilon}_0\left(\boldsymbol{\Upsilon}_0^{-1}(\boldsymbol{X}, t_{n+1}), t_n\right), t_n), t_n) \\
&= \square_0\left(\boldsymbol{\Upsilon}_0^{-1}(\boldsymbol{X}, t_{n+1}), t_n\right) ,
\end{aligned} \tag{6.1.43}$$

which, by definition (6.1.40), gives

$$\mathcal{M}_{t_n}^{t_{n+1}}\{\square\}\Big|_{\boldsymbol{X}} = \square\left(\mathcal{M}_{t_n}^{t_{n+1}}\{\boldsymbol{X}\}, t_n\right) . \tag{6.1.44}$$

This obviates the requirement of keeping track of the material configuration for evaluating $\mathcal{M}_{t_n}^{t_{n+1}}\{\square\}\Big|_{\boldsymbol{X}}$, as long as $\mathcal{M}_{t_n}^{t_{n+1}}\{\boldsymbol{X}\}$ is known, which is the position in the reference configuration at time t_n of the material point whose position in the reference configuration at time t_{n+1} is $\boldsymbol{X}$.

Some Properties of the Material Remapping Operator

From definition (6.1.40) it follows that

$$\mathcal{M}_{t_n}^{t_{n+1}}\{p+q\} = \mathcal{M}_{t_n}^{t_{n+1}}\{p\} + \mathcal{M}_{t_n}^{t_{n+1}}\{q\}\,, \tag{6.1.45}$$

$$\mathcal{M}_{t_n}^{t_{n+1}}\{p\,q\} = \left(\mathcal{M}_{t_n}^{t_{n+1}}\{p\}\right)\left(\mathcal{M}_{t_n}^{t_{n+1}}\{q\}\right)\,, \tag{6.1.46}$$

$$\mathcal{M}_{t_n}^{t_{n+1}}\{p^{-1}\} = \left(\mathcal{M}_{t_n}^{t_{n+1}}\{p\}\right)^{-1}\,. \tag{6.1.47}$$

Also, the partial time derivative with respect to time with $\boldsymbol{X}$ and the target time t_{n+1} kept constant is,

$$\begin{aligned}\frac{\partial}{\partial t}\left[\mathcal{M}_t^{t_{n+1}}\{\square\}\Big|_{\boldsymbol{X}}\right] &= \frac{\partial}{\partial t}\left[\square_0\left(\boldsymbol{\Upsilon}_0^{-1}(\boldsymbol{X},t_{n+1}),t\right)\right]\\ &= \mathcal{M}_t^{t_{n+1}}\left\{\frac{\mathrm{D}\square}{\mathrm{D}t}\right\}\Big|_{\boldsymbol{X}}\,.\end{aligned} \tag{6.1.48}$$

In particular, $\frac{\mathrm{D}\boldsymbol{X}}{\mathrm{D}t} = \boldsymbol{V}$ so that

$$\frac{\partial}{\partial t}\left[\mathcal{M}_t^{t_{n+1}}\{\boldsymbol{X}\}\Big|_{\boldsymbol{X}}\right] = \mathcal{M}_t^{t_{n+1}}\left\{\boldsymbol{V}\right\}\Big|_{\boldsymbol{X}}\,, \tag{6.1.49}$$

and therefore, by the fundamental theorem of calculus,

$$\begin{aligned}\boldsymbol{X} = \mathcal{M}_{t_{n+1}}^{t_{n+1}}\{\boldsymbol{X}\} &= \mathcal{M}_{t_n}^{t_{n+1}}\{\boldsymbol{X}\} + \int_{t_n}^{t_{n+1}} \frac{\partial}{\partial\tau}\mathcal{M}_\tau^{t_{n+1}}\left\{\boldsymbol{X}\right\}\,\mathrm{d}\tau\\ &= \mathcal{M}_{t_n}^{t_{n+1}}\{\boldsymbol{X}\} + \int_{t_n}^{t_{n+1}} \mathcal{M}_\tau^{t_{n+1}}\left\{\boldsymbol{V}\right\}\,\mathrm{d}\tau\,.\end{aligned} \tag{6.1.50}$$

By definition (6.1.40) we also have

$$\begin{aligned}\mathrm{Grad}_0\ \mathcal{M}_{t_n}^{t_{n+1}}\{\square\}\Big|_{\boldsymbol{X}} &= \frac{\partial}{\partial\boldsymbol{X}_0}\left[\mathcal{M}_{t_n}^{t_{n+1}}\{\square\}\Big|_{\boldsymbol{X}}\right]\Big|_{\boldsymbol{X}_0=\boldsymbol{\Upsilon}_0^{-1}(\boldsymbol{X},t_{n+1})}\\ &= \frac{\partial}{\partial\boldsymbol{X}_0}\square_0\left(\boldsymbol{\Upsilon}_0^{-1}(\boldsymbol{X},t_{n+1}),t_n\right)\Big|_{\boldsymbol{X}_0=\boldsymbol{\Upsilon}_0^{-1}(\boldsymbol{X},t_{n+1})}\\ &= \frac{\partial}{\partial\boldsymbol{X}_0}\square_0\left(\boldsymbol{X}_0,t_n\right)\Big|_{\boldsymbol{X}_0=\boldsymbol{\Upsilon}_0^{-1}(\boldsymbol{X},t_{n+1})}\\ &= \mathcal{M}_{t_n}^{t_{n+1}}\left\{\mathrm{Grad}_0\,\square|_{\boldsymbol{X}}\right\}\,.\end{aligned} \tag{6.1.51}$$

In particular, since $\boldsymbol{F}_\mathrm{r} = \mathrm{Grad}_0\,\boldsymbol{X}$,

$$\mathcal{M}_{t_n}^{t_{n+1}}\left\{\boldsymbol{F}_\mathrm{r}\right\} = \mathrm{Grad}_0\,\mathcal{M}_{t_n}^{t_{n+1}}\left\{\boldsymbol{X}\right\}\,. \tag{6.1.52}$$

6.1.3 Trial Elastic Deformation Tensor

Let $\boldsymbol{X}$ be the position in the reference configuration at time step $n+1$ of a material point $\boldsymbol{X}_0 = \boldsymbol{\Upsilon}_{0,n+1}^{-1}\big|_{\boldsymbol{X}}$. The trial elastic left Cauchy-Green deformation $\boldsymbol{b}_{n+1}^{\mathrm{e,trial}}\Big|_{\boldsymbol{X}}$ is obtained by assuming that the plastic right Cauchy-Green deformation corresponding to the material point $\boldsymbol{X}_0$ remains unchanged from the previous time step

$$\boldsymbol{G}_{0,n}^{\mathrm{p,trial}}\Big|_{\boldsymbol{X}_0} = \boldsymbol{G}_{0,n}^{\mathrm{p}}\big|_{\boldsymbol{X}_0} \,. \tag{6.1.53}$$

In general, this is different from the plastic deformation at the previous time step at the same position in the reference configuration $\boldsymbol{G}_n^{\mathrm{p}}|_{\boldsymbol{X}}$, because the latter corresponds to a possibly different material point $\boldsymbol{X}_0' = \boldsymbol{\Upsilon}_{0,n}^{-1}\big|_{\boldsymbol{X}}$. An exception is the special case where the reference velocity $\boldsymbol{V}$ is identically zero. To write (6.1.53) in terms of position in the reference configuration, we use the operator $\mathcal{M}_{t_n}^{t_{n+1}}$ to keep the material point fixed:

$$\boldsymbol{G}_{n+1}^{\mathrm{p,trial}}\Big|_{\boldsymbol{X}} = \mathcal{M}_{t_n}^{t_{n+1}}\left\{\boldsymbol{G}^{\mathrm{p}}\right\}\Big|_{\boldsymbol{X}} \,. \tag{6.1.54}$$

Equation (4.3.17) then gives

$$\boldsymbol{b}_{n+1}^{\mathrm{e,trial}} = \boldsymbol{F}_{c_{(n+1)}}\boldsymbol{F}_{\mathrm{r}_{(n+1)}}\left(\mathcal{M}_{t_n}^{t_{n+1}}\left\{\boldsymbol{G}^{\mathrm{p}}\right\}\right)\boldsymbol{F}_{\mathrm{r}_{(n+1)}}^{\mathrm{t}}\boldsymbol{F}_{c_{(n+1)}}^{\mathrm{t}} \,. \tag{6.1.55}$$

The reference motion gradient $\boldsymbol{F}_{\mathrm{r}}$ in (6.1.55) requires keeping track of the material configuration as presented in [18]. There, besides the motion $\boldsymbol{\varphi}$, the material configuration is tracked as an additional variable $\boldsymbol{X}_0 = \boldsymbol{\Upsilon}_0^{-1}(\boldsymbol{X})$, which gives the reference motion gradient as $\boldsymbol{F}_{\mathrm{r}} = \left(\mathrm{Grad}\,\boldsymbol{\Upsilon}_0^{-1}\right)^{-1}$. This is achieved by discretisation of both the motion as well as the material configuration as node variables on a mesh of the reference configuration. Following this approach, however, would limit the total reference motion possible, because large reference motion deformations may cause excessive distortion between the material and reference configurations, causing the mesh of the material configuration to become degenerate.

To avoid this limitation on the reference motion, we seek a representation of $\boldsymbol{b}_{n+1}^{\mathrm{e,trial}}$ where motion of the reference configuration enters only in terms of the reference velocity $\boldsymbol{V}$,

such that the total reference motion $\boldsymbol{\Upsilon}_0$ and the reference motion gradient $\boldsymbol{F}_\mathrm{r}$ are not needed.

Definition (4.3.16) of $\boldsymbol{B}^e$ and equation (6.1.46) give

$$\mathcal{M}_{t_n}^{t_{n+1}}\left\{\boldsymbol{G}^p\right\} = \left(\mathcal{M}_{t_n}^{t_{n+1}}\left\{\boldsymbol{F}_\mathrm{r}^{-1}\right\}\right)\left(\mathcal{M}_{t_n}^{t_{n+1}}\left\{\boldsymbol{B}^e\right\}\right)\left(\mathcal{M}_{t_n}^{t_{n+1}}\left\{\boldsymbol{F}_\mathrm{r}^{-1}\right\}\right)^\mathrm{t}. \tag{6.1.56}$$

Equations (6.1.52) and (6.1.47) then give

$$\begin{aligned}\mathcal{M}_{t_n}^{t_{n+1}}\left\{\boldsymbol{F}_\mathrm{r}^{-1}\right\} &= \left(\mathrm{Grad}_0\,\mathcal{M}_{t_n}^{t_{n+1}}\left\{\boldsymbol{X}\right\}\right)^{-1}\\ &= \boldsymbol{F}_\mathrm{r}^{-1}\boldsymbol{F}_\mathrm{r}\left(\mathrm{Grad}_0\,\mathcal{M}_{t_n}^{t_{n+1}}\left\{\boldsymbol{X}\right\}\right)^{-1}\\ &= \boldsymbol{F}_\mathrm{r}^{-1}\left[\left(\mathrm{Grad}_0\,\mathcal{M}_{t_n}^{t_{n+1}}\left\{\boldsymbol{X}\right\}\right)\boldsymbol{F}_\mathrm{r}^{-1}\right]^{-1}\\ &= \boldsymbol{F}_\mathrm{r}^{-1}\left(\mathrm{Grad}\,\mathcal{M}_{t_n}^{t_{n+1}}\left\{\boldsymbol{X}\right\}\right)^{-1},\end{aligned} \tag{6.1.57}$$

so that equation (6.1.56) becomes

$$\begin{aligned}&\mathcal{M}_{t_n}^{t_{n+1}}\left\{\boldsymbol{G}^p\right\}\\ &\quad= \boldsymbol{F}_\mathrm{r}^{-1}\left(\mathrm{Grad}\,\mathcal{M}_{t_n}^{t_{n+1}}\left\{\boldsymbol{X}\right\}\right)^{-1}\left(\mathcal{M}_{t_n}^{t_{n+1}}\left\{\boldsymbol{B}^e\right\}\right)\left(\mathrm{Grad}\,\mathcal{M}_{t_n}^{t_{n+1}}\left\{\boldsymbol{X}\right\}\right)^{-\mathrm{t}}\boldsymbol{F}_\mathrm{r}^{-\mathrm{t}}.\end{aligned} \tag{6.1.58}$$

Substitution into (6.1.55) then gives

$$\boldsymbol{b}_{n+1}^{\mathrm{e,trial}} = \boldsymbol{F}_{c_{(n+1)}}\boldsymbol{B}_{n+1}^{\mathrm{e,trial}}\boldsymbol{F}_{c_{(n+1)}}^{\mathrm{t}}, \tag{6.1.59}$$

where

$$\boldsymbol{B}_{n+1}^{\mathrm{e,trial}} = \left(\mathrm{Grad}\,\mathcal{M}_{t_n}^{t_{n+1}}\left\{\boldsymbol{X}\right\}\right)^{-1}\left(\mathcal{M}_{t_n}^{t_{n+1}}\left\{\boldsymbol{B}^e\right\}\right)\left(\mathrm{Grad}\,\mathcal{M}_{t_n}^{t_{n+1}}\left\{\boldsymbol{X}\right\}\right)^{-\mathrm{t}}. \tag{6.1.60}$$

With equations (6.1.44) and (6.1.50), this becomes

$$\boldsymbol{B}_{n+1}^{\mathrm{e,trial}} = \left(\mathrm{Grad}\,\hat{\boldsymbol{X}}_{n+1}\right)^{-1}\left(\boldsymbol{B}_n^e|_{\hat{\boldsymbol{X}}_{n+1}}\right)\left(\mathrm{Grad}\,\hat{\boldsymbol{X}}_{n+1}\right)^{-\mathrm{t}}, \tag{6.1.61}$$

$$\hat{\boldsymbol{X}}_{n+1} \coloneqq \mathcal{M}_{t_n}^{t_{n+1}}\left\{\boldsymbol{X}\right\} = \boldsymbol{X} - \int_{t_n}^{t_{n+1}} \mathcal{M}_{\tau}^{t_{n+1}}\left\{\boldsymbol{V}\right\}\,\mathrm{d}\tau\,. \tag{6.1.62}$$

6.1.4 Semi-discrete Problem

The generalised-α method [138] is used to approximate Problem 5.3.1 as follows:

Problem 6.1.1. *For each time step t_{n+1}, given the deformation $\boldsymbol{\varphi}_n$, the reference velocity $\boldsymbol{V}_n^{\mathcal{B}}$, and the temperature θ_n from the previous time step t_n, find the deformation $\boldsymbol{\varphi}_{n+1}$, the reference velocity $\boldsymbol{V}_{n+1}^{\mathcal{B}}$, and the temperature θ_{n+1}, in functional spaces defined on $\bigcup_{i=1}^{2} \Omega^{\mathcal{B}}$, such that for all admissible test functions $\delta\boldsymbol{u}$ defined on $\bigcup_{i=1}^{2} \Omega^{\mathcal{B}}$,*

$$\int_{\Omega^{\mathcal{B}}} \nabla\delta\boldsymbol{u} : \boldsymbol{\tau}_{n+1-\alpha_\mathrm{f}} \,\mathrm{d}\Omega + G_{inertial} - \int_{\Omega^{\mathcal{B}}} \delta\boldsymbol{u} \cdot \boldsymbol{f}_{b(n+1-\alpha_\mathrm{f})} \,\mathrm{d}\Omega \\ - \int_{\Gamma^{\mathcal{B}}_{N_\mu}} \delta\boldsymbol{u} \cdot \boldsymbol{f}_{s(n+1-\alpha_\mathrm{f})} \, J_\Gamma \,\mathrm{d}\Gamma - \int_{\Gamma_\mathrm{c}^{\mathrm{con}}} s^{\mathcal{B}} \delta\boldsymbol{u} \cdot \boldsymbol{f}_{\mathrm{c}(n+1-\alpha_\mathrm{f})} \, J_\Gamma \,\mathrm{d}\Gamma = 0 \,, \tag{6.1.63}$$

where the inertial term $G_{inertial} = \int_{\Omega^{\mathcal{B}}} \delta\boldsymbol{u} \cdot \rho_\mathrm{m} \boldsymbol{a}_{n+1-\alpha_m} \,\mathrm{d}\Omega$ is given from (5.2.11) by

$$G_{inertial} = \int_{\Omega^{\mathcal{B}}} \delta\boldsymbol{u} \cdot \rho_\mathrm{m} \left\{ \left(\frac{\partial^2 \boldsymbol{\varphi}}{\partial t^2} \right)_{n+1-\alpha_\mathrm{m}} + \left[\boldsymbol{F}_\mathrm{c} \left(\frac{\partial \boldsymbol{V}}{\partial t} \right) \right]_{n+1-\alpha_\mathrm{m}} \right\} \,\mathrm{d}\Omega \\ + 2 \int_{\Omega^{\mathcal{B}}} \delta\boldsymbol{u} \cdot \rho_\mathrm{m} \left[\left(\frac{\partial \boldsymbol{F}_\mathrm{c}}{\partial t} \right) \boldsymbol{V} \right]_{n+1-\alpha_\mathrm{f}} \,\mathrm{d}\Omega \tag{6.1.64}$$

$$- \int_{\Omega^{\mathcal{B}}} \delta\boldsymbol{u} \cdot \left[\mathrm{Div}(\rho_\mathrm{m} \boldsymbol{V}) \boldsymbol{F}_\mathrm{c} \boldsymbol{V} \right]_{n+1-\alpha_\mathrm{f}} \,\mathrm{d}\Omega \tag{6.1.65}$$

$$- \int_{\Omega^{\mathcal{B}}} \left[(\mathrm{Grad}\ \delta\boldsymbol{u}) \, \boldsymbol{V}_{n+1-\alpha_\mathrm{f}} \right] \cdot \rho_\mathrm{m} \left(\boldsymbol{F}_\mathrm{c} \boldsymbol{V} \right)_{n+1-\alpha_\mathrm{f}} \,\mathrm{d}\Omega \\ + \int_{\Gamma^{\mathcal{B}}} \delta\boldsymbol{u} \cdot \left[\rho_\mathrm{m} \left(\boldsymbol{F}_\mathrm{c} \boldsymbol{V} \right) \left(\boldsymbol{V} \cdot \boldsymbol{N} \right) \right]_{n+1-\alpha_\mathrm{f}} \,\mathrm{d}\Gamma \,, \tag{6.1.66}$$

and such that for all admissible test functions $\delta\vartheta$ defined on $\bigcup_{i=1}^{2} \Omega^{\mathcal{B}}$,

$$\int_{\Omega^{\mathcal{B}}} \nabla\delta\vartheta \cdot \boldsymbol{q}_{n+1} \,\mathrm{d}\Omega - \int_{\Omega^{\mathcal{B}}} \delta\vartheta \left[\mathcal{R}_{b(n+1)} + \mathcal{D}_{\mathrm{mech}(n+1)} - \mathcal{H}_{n+1} \right] \,\mathrm{d}\Omega \\ + \int_{\Omega^{\mathcal{B}}} \delta\vartheta \, c\dot{\theta}_{n+1} \,\mathrm{d}\Omega - \int_{\Gamma^{\mathcal{B}}_{N_\theta}} \delta\vartheta \, \mathcal{R}_{s(n+1)} \, \frac{J_\Gamma}{J} \,\mathrm{d}\Gamma \\ - \int_{\Gamma_\mathrm{c}^{\mathrm{con}}} \delta\vartheta \, \left(\mathcal{D}_{fric_{(n+1)}} + s^{\mathcal{B}} q_{hc(n+1)} \right) \, \frac{J_\Gamma}{J} \,\mathrm{d}\Gamma = 0 \,. \tag{6.1.67}$$

6.2 Mechanical-Thermal Operator Splitting

Following [82], an operator splitting approach is used to approximate the coupled thermomechanical Problem 6.1.1 by updating the thermal and mechanical fields sequentially instead of simultaneously. At each time step, three smaller problems are solved instead of one larger one. The first problem, a mechanical one, is solved for a motion field $\boldsymbol{\varphi}_{n+1}^{(\mathrm{pre})}$ and a reference velocity field $\boldsymbol{V}_{n+1}^{(\mathrm{pre})}$ with the temperature field kept fixed at θ_n. The middle problem is a thermal one. It is solved for the updated thermal field θ_{n+1} with the deformation and reference velocity fixed, respectively, as $\boldsymbol{\varphi}_{n+1}^{(\mathrm{pre})}$ and $\boldsymbol{V}_{n+1}^{(\mathrm{pre})}$. The time step is then completed by solving the third problem for the updated motion $\boldsymbol{\varphi}_{n+1}$ and reference velocity $\boldsymbol{V}_{n+1}$ with the thermal field fixed as θ_{n+1}.

The first and third problems, in which the mechanical fields are updated at a fixed temperature, are as follows

Problem 6.2.1. *For each time step $n+1$, given the deformation $\boldsymbol{\varphi}_n$, the reference velocity $\boldsymbol{V}_n$, and the temperature θ_n from the previous time step t_n, assuming the updated temperature remains unchanged (at θ_n in the first mechanical sub-step, and at θ_{n+1} after the thermal sub-step is solved), find the deformation $\boldsymbol{\varphi}_{n+1}^{(\mathrm{pre})}$ and the reference velocity $\boldsymbol{V}_{n+1}^{(\mathrm{pre})}$ such that, for all admissible test functions $\delta\boldsymbol{u}$ defined on $\bigcup_{i=1}^{2}\Omega^{\mathcal{B}}$,*

$$\int_{\Omega^{\mathcal{B}}} \nabla\delta\boldsymbol{u} : \boldsymbol{\tau}_{n+1-\alpha_{\mathrm{f}}}\,\mathrm{d}\Omega + G_{inertial} - \int_{\Omega^{\mathcal{B}}} \delta\boldsymbol{u}\cdot\boldsymbol{f}_{b_{(n+1-\alpha_{\mathrm{f}})}}\,\mathrm{d}\Omega \\ - \int_{\Gamma^{\mathcal{B}}_{N_\mu}} \delta\boldsymbol{u}\cdot\boldsymbol{f}_{s_{(n+1-\alpha_{\mathrm{f}})}}\,J_\Gamma\mathrm{d}\Gamma - \int_{\Gamma_{\mathrm{c}}^{\mathrm{con}}} s^{\mathcal{B}}\delta\boldsymbol{u}\cdot\boldsymbol{f}_{\mathrm{c}_{(n+1-\alpha_{\mathrm{f}})}}\,J_\Gamma\mathrm{d}\Gamma = 0\,, \tag{6.2.1}$$

where the inertial term $G_{inertial} = \int_{\Omega^{\mathcal{B}}} \delta\boldsymbol{u} \cdot \rho_{\mathrm{m}} \boldsymbol{a}_{n+1-\alpha_m} \,\mathrm{d}\Omega$ *is given by*

$$
\begin{aligned}
G_{inertial} = & \int_{\Omega^{\mathcal{B}}} \delta\boldsymbol{u} \cdot \rho_{\mathrm{m}} \left\{ \left(\frac{\partial^2 \boldsymbol{\varphi}}{\partial t^2} \right)_{n+1-\alpha_{\mathrm{m}}} + \left[\boldsymbol{F}_{\mathrm{c}} \left(\frac{\partial \boldsymbol{V}}{\partial t} \right) \right]_{n+1-\alpha_{\mathrm{m}}} \right\} \,\mathrm{d}\Omega \\
& + 2 \int_{\Omega^{\mathcal{B}}} \delta\boldsymbol{u} \cdot \rho_{\mathrm{m}} \left[\left(\frac{\partial \boldsymbol{F}_{\mathrm{c}}}{\partial t} \right) \boldsymbol{V} \right]_{n+1-\alpha_{\mathrm{f}}} \,\mathrm{d}\Omega \qquad (6.2.2) \\
& - \int_{\Omega^{\mathcal{B}}} \delta\boldsymbol{u} \cdot \left[\mathrm{Div}(\rho_{\mathrm{m}} \boldsymbol{V}) \boldsymbol{F}_{\mathrm{c}} \boldsymbol{V} \right]_{n+1-\alpha_{\mathrm{f}}} \,\mathrm{d}\Omega \qquad (6.2.3) \\
& - \int_{\Omega^{\mathcal{B}}} \left((\mathrm{Grad}\ \delta\boldsymbol{u})\, \boldsymbol{V}_{n+1-\alpha_{\mathrm{f}}} \right) \cdot \rho_{\mathrm{m}} \left(\boldsymbol{F}_{\mathrm{c}} \boldsymbol{V} \right)_{n+1-\alpha_{\mathrm{f}}} \,\mathrm{d}\Omega \\
& + \int_{\Gamma^{\mathcal{B}}} \delta\boldsymbol{u} \cdot \left[\rho_{\mathrm{m}} \left(\boldsymbol{F}_{\mathrm{c}} \boldsymbol{V} \right) \left(\boldsymbol{V} \cdot \boldsymbol{N} \right) \right]_{n+1-\alpha_{\mathrm{f}}} \,\mathrm{d}\Gamma \,. \qquad (6.2.4)
\end{aligned}
$$

The second problem, in which the temperature field is updated at fixed deformation and reference velocity fields, is as follows:

Problem 6.2.2. *For each time step* t_{n+1}*, given the deformation* $\boldsymbol{\varphi}_n$*, the reference velocity* $\boldsymbol{V}_n$*, and the temperature* θ_n *from the previous time step* t_n*, and given an updated deformation* $\boldsymbol{\varphi}_{n+1}^{(\mathrm{pre})}$ *and reference velocity* $\boldsymbol{V}_{n+1}^{(\mathrm{pre})}$*, find the temperature* θ_{n+1} *such that, for all admissible test functions* $\delta\vartheta$ *defined on* $\bigcup_{i=1}^{2} \Omega^{\mathcal{B}}$*,*

$$
\begin{aligned}
\int_{\Omega^{\mathcal{B}}} \nabla\delta\vartheta \cdot \boldsymbol{q}_{n+1} \,\mathrm{d}\Omega - & \int_{\Omega^{\mathcal{B}}} \delta\vartheta \left[\mathcal{R}_{b_{(n+1)}} + \mathcal{D}_{\mathrm{mech}_{(n+1)}} - \mathcal{H}_{n+1} \right] \,\mathrm{d}\Omega \\
& + \int_{\Omega^{\mathcal{B}}} \delta\vartheta \; c\dot{\theta}_{n+1} \,\mathrm{d}\Omega - \int_{\Gamma^{\mathcal{B}}_{N_\theta}} \delta\vartheta \; \mathcal{R}_{s_{(n+1)}} \; \frac{J_\Gamma}{J} \,\mathrm{d}\Gamma \\
& - \int_{\Gamma_{\mathrm{c}}^{\mathrm{con}}} \delta\vartheta \; \left(\mathcal{D}_{fric_{(n+1)}} + s^{\mathcal{B}} q_{hc_{(n+1)}} \right) \; \frac{J_\Gamma}{J} \,\mathrm{d}\Gamma = 0 \,. \qquad (6.2.5)
\end{aligned}
$$

6.3 Regularisation and Augmented Lagrangian Iteration

The term involving contact traction in (6.2.1), which is given by $\int_{\Gamma_{\mathrm{c}}^{\mathcal{B}}} \delta\boldsymbol{u} \cdot (\boldsymbol{f}_{\mathrm{c}})_{n+1-\alpha_{\mathrm{f}}} \,\mathrm{d}\Gamma$, must satisfy the complementarity conditions (4.5.1) and (4.5.2). Computing it using the augmented Lagrangian approach, as described in [101], involves iteratively updating an approximate value of the contact force.

The contact force $\boldsymbol{f}_{\mathrm{c}}$ is given by its normal and tangential components, f_N and $\boldsymbol{f}_T$; that is,

$$\boldsymbol{f}_{\mathrm{c}_{(n+1)}} = -f_{N_{(n+1)}}\boldsymbol{n} + \boldsymbol{f}_{T_{(n+1)}}\,, \tag{6.3.1}$$

$$f_{N_{(n+1)}} = -\boldsymbol{f}_{\mathrm{c}_{(n+1)}} \cdot \boldsymbol{n}\,, \tag{6.3.2}$$

$$\boldsymbol{f}_{T_{(n+1)}} = (\mathbf{1} - \boldsymbol{n}\otimes\boldsymbol{n})\boldsymbol{f}_{\mathrm{c}_{(n+1)}}\,. \tag{6.3.3}$$

At each augmented Lagrangian iteration $l+1$, the updated normal contact force is given by

$$f_{N_{(n+1)}}^{(l+1)} = \begin{cases} f_{N_{(n+1)}}^{(l)} + \epsilon_N g & \text{if } g > 0\,, \\ f_{N_{(n+1)}}^{(l)} & \text{otherwise}\,. \end{cases} \tag{6.3.4}$$

The updated tangential contact force is computed by first assuming that contact satisfies the slip condition, and computing a trial value:

$$\boldsymbol{f}_{T_{(n+1)}}^{(l+1),\mathrm{trial}} = \boldsymbol{f}_{T_{(n+1)}}^{(l)} + \epsilon_T \boldsymbol{v}_s\,. \tag{6.3.5}$$

The friction stick limit $\Phi\left(\boldsymbol{f}_T, f_N\right)$ is then evaluated from (4.5.2a), correcting the trial value if necessary:

$$\boldsymbol{f}_{T_{(n+1)}}^{(l+1)} = \begin{cases} \boldsymbol{f}_{T_{(n+1)}}^{(l+1),\mathrm{trial}} & \text{if } \Phi\left(\boldsymbol{f}_{T_{(n+1)}}^{(l+1),\mathrm{trial}}, f_{N_{(n+1)}}^{(l+1)}\right) \leq 0\,, \\ \frac{f_{\mathrm{slip}}}{\|\boldsymbol{v}_s\| + \epsilon_{\mathrm{reg}}}\boldsymbol{v}_{\mathrm{s}} & \text{otherwise}\,. \end{cases} \tag{6.3.6}$$

Here f_{slip} is the stick limit, and ϵ_{reg} is a small positive regularisation factor used to avoid numerical errors at small slip velocities $\|\boldsymbol{v}_s\| \approx 0$.

The augmented Lagrangian iteration is continued until the contact constraints are met, that is, the penetration is smaller than a predefined threshold, $g \leq \varepsilon_{\mathrm{penetration}}$, and the tangential contact constraint is satisfied in that either slip occurs and $\Phi\left(\boldsymbol{f}_{T_{(n+1)}}^{(l+1)}, f_{N_{(n+1)}}^{(l+1)}\right) = 0$; or the slip velocity is smaller than a predefined threshold: $\|\boldsymbol{v}_s\| < \varepsilon_{\mathrm{slip}}$. The approach is summarised in Algorithm 6.3.1.

Algorithm 6.3.1 Augmented Lagrangian algorithm

1: `contact_constraints_are_satisfied` $\leftarrow$ `false`
2: $l \leftarrow 1$
3: $f^{(l)}_{N_{(n+1)}} \leftarrow 0$
4: $\boldsymbol{f}^{(l)}_{T_{(n+1)}} \leftarrow \mathbf{0}$
5: **while** `contact_constraints_are_satisfied` = `false` **do**
6: Solve Problem 6.2.1, where $\boldsymbol{f}_{\mathrm{c}_{(n+1)}} = -f^{(l)}_{N_{(n+1)}}\boldsymbol{n} + \boldsymbol{f}^{(l)}_{T_{(n+1)}}$
7: Update $f^{(l+1)}_{N_{(n+1)}}$ using equation (6.3.4)
8: Update $\boldsymbol{f}^{(l+1)}_{T_{(n+1)}}$ using equations (6.3.5) and (6.3.6)
9: `condition_1` $\leftarrow g \leq 0$
10: `condition_2` $\leftarrow$ either $\Phi\left(\boldsymbol{f}^{(l+1)}_{T_{(n+1)}}, f^{(l+1)}_{N_{(n+1)}}\right) = 0$, or $\|\boldsymbol{v}_s\| < \varepsilon_{\text{slip}}$
11: $k \leftarrow k + 1$
12: `contact_constraints_are_satisfied` $\leftarrow$ `condition_1 AND condition_2`
13: **end while**

6.4 Finite Element Discretisation

The reference domain of each body $\mathcal{B}$ is discretised into a mesh $\Omega^{\mathcal{B}}_h$ of cells $\left\{\Omega^{\mathcal{B},n}_{\mathrm{e}}\right\}_{n=1}^{N^{\mathcal{B}}_{\mathrm{e}}}$, which do not overlap and which completely cover the domain without any gaps:

$$\Omega^{\mathcal{B}} \approx \Omega^{\mathcal{B}}_h = \bigcup_{n=1}^{N^{\mathcal{B}}_{\mathrm{e}}} \Omega^{\mathcal{B},n}_{\mathrm{e}}\,, \tag{6.4.1}$$

where $N^{\mathcal{B}}_{\mathrm{e}}$ is the number of cells in the mesh of body $\mathcal{B}$ in the reference domain.

The approximate solution $\left(\boldsymbol{\varphi}^h, \boldsymbol{V}^h, \theta^h\right)$ is sought in finite dimensional subspaces of the functional spaces on which the exact solution $(\boldsymbol{\varphi}, \boldsymbol{V}, \theta)$ is defined. These finite dimensional subspaces have bases $\{\boldsymbol{\phi}^{\boldsymbol{\varphi}}_i\}_{i=1}^{N_\varphi}$, $\left\{\boldsymbol{\phi}^{\boldsymbol{V}}_i\right\}_{i=1}^{N_V}$, and $\left\{\phi^{\theta}_i\right\}_{i=1}^{N_\theta}$, where $\boldsymbol{\phi}^{\boldsymbol{\varphi}}_i$ and $\boldsymbol{\phi}^{\boldsymbol{V}}_i$ are vector-valued while ϕ^{θ}_i are scalar-valued, and where N_φ, N_V and N_θ are the dimensions of the respective functional subspaces. The discretised motion, reference velocity, and

temperature are then respectively given by coefficients U_i, V_i, and Θ_i as

$$\boldsymbol{\varphi}^h = \sum_{i=1}^{N_\varphi} \boldsymbol{\phi}_i^{\boldsymbol{\varphi}} U_i \,, \tag{6.4.2}$$

$$\boldsymbol{V}^h = \sum_{i=1}^{N_V} \boldsymbol{\phi}_i^{\boldsymbol{V}} V_i \,, \tag{6.4.3}$$

$$\theta^h = \sum_{i=1}^{N_\theta} \phi_i^\theta \Theta_i \,. \tag{6.4.4}$$

A mixed finite element approach is used to discretise the deformation Jacobian and the pressure terms to avoid volumetric locking. The scalar shape functions $\{\phi_i^{\mathrm{p}}\}_{i=1}^{N_{\mathrm{p}}}$, where N_{p} is the total degrees of freedom of the discretisation, are chosen to be discontinuous across element boundaries and to have lower polynomial order than the motion basis functions $\boldsymbol{\phi}_i^{\boldsymbol{\varphi}}$. The lower order discretised deformation Jacobian $\bar{J}^h$ is obtained by least-squares projection of the discretised deformation Jacobian $J^h = \det\left(\operatorname{Grad} \boldsymbol{\varphi}^h\right)$ onto the discrete subspace

$$\bar{J}^h = \phi_i^{\mathrm{p}} \left(\int_\Omega \phi_i^{\mathrm{p}} \, \phi_j^{\mathrm{p}} \, \mathrm{d}\Omega \right)^{-1} \int_\Omega \phi_j^{\mathrm{p}} \, J^h \, \mathrm{d}\Omega \,. \tag{6.4.5}$$

Furthermore, the mixed basis functions ϕ_i^{p} are chosen such that the support of each is completely contained in one cell, such that (6.4.5) can be solved in each cell independently of the rest of the mesh. The pressure is then given, using (4.3.7b), by

$$\bar{p}^h = \phi_i^{\mathrm{p}} \left(\int_\Omega \phi_i^{\mathrm{p}} \, \phi_j^{\mathrm{p}} \, \mathrm{d}\Omega \right)^{-1} \int_\Omega \phi_j^{\mathrm{p}} \, \kappa \left((\bar{J}^h)^2 - 1 \right) \, \mathrm{d}\Omega \,. \tag{6.4.6}$$

The functional spaces from which the test functions are chosen are also discretised. A finite dimensional subspace of admissible test functions is chosen, and the weak formulations are required to hold for any test function therein.

The finite element mechanical problem is as follows.

Problem 6.4.1. *For each time step t_{n+1}, given the deformation $\boldsymbol{\varphi}_n^h$, the reference velocity $\boldsymbol{V}_n^h$, and the temperature θ_n^h from the previous time step t_n, and given an updated*

temperature θ^h_{n+1}, find the deformation $\boldsymbol{\varphi}^h_{n+1}$ and the reference velocity $\boldsymbol{V}^h_{n+1}$ such that, for any test function $\delta\boldsymbol{u}^h$,

$$\begin{aligned}\int_{\Omega^{\mathcal{B}}_h} \nabla\delta\boldsymbol{u}^h \colon (\operatorname{dev}\boldsymbol{\tau}^h_{n+1-\alpha_{\mathrm{f}}} + \bar{p}^h_{n+1-\alpha_{\mathrm{f}}}\,\mathbf{1})\,\mathrm{d}\Omega + G^h_{inertial}\\ - \int_{\Omega^{\mathcal{B}}_h} \delta\boldsymbol{u}^h \cdot \boldsymbol{f}_{\mathrm{b}_{(n+1-\alpha_{\mathrm{f}})}}\,\mathrm{d}\Omega - \int_{\Gamma^{\mathcal{B}}_{hN_\mu}} \delta\boldsymbol{u}^h \cdot \boldsymbol{f}_{\mathrm{s}_{(n+1-\alpha_{\mathrm{f}})}}\,J^h_\Gamma\,\mathrm{d}\Gamma\\ - \int_{\Gamma^{\mathrm{con}}_{hc}} s^{\mathcal{B}}\delta\boldsymbol{u}^h \cdot \boldsymbol{f}^h_{\mathrm{c}_{(n+1-\alpha_{\mathrm{f}})}}\,J^h_\Gamma\,\mathrm{d}\Gamma = 0\,,\end{aligned} \tag{6.4.7}$$

where $\boldsymbol{\tau}^h_{n+1-\alpha_{\mathrm{f}}}$ is the stress computed from the discretised mechanical and thermal fields, and

$$\begin{aligned}G^h_{inertial} = &\int_{\Omega^{\mathcal{B}}_h} \delta\boldsymbol{u}^h \cdot \rho_{\mathrm{m}} \left\{ \left(\frac{\partial^2\boldsymbol{\varphi}^h}{\partial t^2}\right)_{n+1-\alpha_{\mathrm{m}}} + \left[\boldsymbol{F}_{\mathrm{c}}\left(\frac{\partial\boldsymbol{V}^h}{\partial t}\right)\right]_{n+1-\alpha_{\mathrm{m}}} \right\}\mathrm{d}\Omega\\ &+ 2\int_{\Omega^{\mathcal{B}}_h} \delta\boldsymbol{u}^h \cdot \rho_{\mathrm{m}} \left[\left(\frac{\partial\boldsymbol{F}^h_{\mathrm{c}}}{\partial t}\right)\boldsymbol{V}^h\right]_{n+1-\alpha_{\mathrm{f}}}\mathrm{d}\Omega\\ &- \int_{\Omega^{\mathcal{B}}_h} \delta\boldsymbol{u}^h \cdot \left[\mathrm{Div}(\rho_{\mathrm{m}}\boldsymbol{V}^h)\boldsymbol{F}^h_{\mathrm{c}}\boldsymbol{V}^h\right]_{n+1-\alpha_{\mathrm{f}}}\mathrm{d}\Omega\\ &- \int_{\Omega^{\mathcal{B}}_h} \left(\left(\mathrm{Grad}\;\delta\boldsymbol{u}^h\right)\boldsymbol{V}^h_{n+1-\alpha_{\mathrm{f}}}\right)\cdot\rho_{\mathrm{m}}\left(\boldsymbol{F}^h_{\mathrm{c}}\boldsymbol{V}^h\right)_{n+1-\alpha_{\mathrm{f}}}\mathrm{d}\Omega\\ &+ \int_{\Gamma^{\mathcal{B}}_h} \delta\boldsymbol{u}^h \cdot \left[\rho_{\mathrm{m}}\left(\boldsymbol{F}^h_{\mathrm{c}}\boldsymbol{V}^h\right)\left(\boldsymbol{V}^h\cdot\boldsymbol{N}^h\right)\right]_{n+1-\alpha_{\mathrm{f}}}\mathrm{d}\Gamma\,.\end{aligned} \tag{6.4.8}$$

The thermal problem becomes,

Problem 6.4.2. *For each time step t_{n+1}, given the deformation $\boldsymbol{\varphi}^h_n$, the reference velocity $\boldsymbol{V}^h_n$, and the temperature $\theta^h_n = \sum_{i=1}^{N_\theta}\phi^\theta_i\,(\Theta_i)_n$ from the previous time step t_n, and given an updated deformation $\boldsymbol{\varphi}^h_{n+1}$ and reference velocity $\boldsymbol{V}^h_{n+1}$, find the temperature $\theta^h_{n+1} = \sum_{i=1}^{N_\theta}\phi^\theta_i\,(\Theta_i)_{n+1}$ such that, for any test function $\delta\vartheta^h$,*

$$\begin{aligned}\int_{\Omega^{\mathcal{B}}_h} \nabla\delta\vartheta^h\cdot\boldsymbol{q}^h_{n+1}\,\mathrm{d}\Omega - \int_{\Omega^{\mathcal{B}}_h}\delta\vartheta^h\left[\mathcal{R}^h_{b_{(n+1)}} + \mathcal{D}^h_{\mathrm{mech}_{(n+1)}} - \mathcal{H}^h_{n+1}\right]\mathrm{d}\Omega\\ + \int_{\Omega^{\mathcal{B}}_h}\delta\vartheta^h\,c\dot{\theta}^h_{n+1}\,\mathrm{d}\Omega - \int_{\Gamma^{\mathcal{B}}_{hN_\theta}}\delta\vartheta^h\,\mathcal{R}^h_{s_{(n+1)}}\,\frac{J^h_\Gamma}{J^h}\,\mathrm{d}\Gamma\\ - \int_{\Gamma^{\mathrm{con}}_{hc}}\delta\vartheta^h\,\left(\mathcal{D}^h_{fric_{(n+1)}} + s^{\mathcal{B}}q^h_{hc_{(n+1)}}\right)\,\frac{J^h_\Gamma}{J^h}\,\mathrm{d}\Gamma = 0\,,\end{aligned} \tag{6.4.9}$$

where the thermal flux $\boldsymbol{q}^h_{n+1}$ is computed in terms of the discretised thermal field θ^h_{n+1}.

6.5 Linearisation and Consistent Tangent Moduli

The Newton-Raphson method is used to convert each of the nonlinear problems into a sequence of linear problems. The method starts with an estimated solution, and each Newton iteration involves computing an update to that estimate. This is achieved by linearizing the nonlinear problem around the estimated solution, and then solving the resulting linear problem for the update. These steps are repeated until the residual becomes smaller than a predefined threshold.

Linearisation by the Newton-Raphson method is described in the following Problem by using the Gateaux derivatives, defined for a function $\square = \square(\boldsymbol{\varphi}^h, \boldsymbol{V}^h, \theta^h)$ by

$$\mathrm{D}_{\boldsymbol{\varphi}} \square \left(\boldsymbol{\varphi}^h, \boldsymbol{V}^h, \theta^h; \boldsymbol{\phi}_i^{\boldsymbol{\varphi}}\right) = \left[\frac{\mathrm{d}}{\mathrm{d}\epsilon} \square(\boldsymbol{\varphi}^h + \epsilon \boldsymbol{\phi}_i^{\boldsymbol{\varphi}}, \boldsymbol{V}^h, \theta^h)\right]_{\epsilon=0}, \tag{6.5.1a}$$

$$\mathrm{D}_{\boldsymbol{V}} \square \left(\boldsymbol{\varphi}^h, \boldsymbol{V}^h, \theta^h; \boldsymbol{\phi}_i^{\boldsymbol{V}}\right) = \left[\frac{\mathrm{d}}{\mathrm{d}\epsilon} \square(\boldsymbol{\varphi}^h, \boldsymbol{V}^h + \epsilon \boldsymbol{\phi}_i^{\boldsymbol{V}}, \theta^h)\right]_{\epsilon=0}, \tag{6.5.1b}$$

$$\mathrm{D}_{\theta} \square \left(\boldsymbol{\varphi}^h, \boldsymbol{V}^h, \theta^h; \phi_i^{\theta})\right) = \left[\frac{\mathrm{d}}{\mathrm{d}\epsilon} \square(\boldsymbol{\varphi}^h, \boldsymbol{V}^h, \theta^h + \epsilon \phi_i^{\theta})\right]_{\epsilon=0}. \tag{6.5.1c}$$

Problem 6.5.1. *At a time step t_{n+1}, let the deformation $\boldsymbol{\varphi}_n^h$, the reference velocity $\boldsymbol{V}_n^h$, the elastic strain $(\boldsymbol{B}_h^e)_n$, the plastic strain α_n^h, the temperature θ_n^h from the previous time step t_n, and the updated temperature θ_{n+1}^h be given. At an augmented Lagrangian step $l+1$, let the normal and tangential contact tractions from the previous augmented Lagrangian step l, respectively $(f_N^h)_{n+1}^{(l)}$ and $(f_T^h)_{n+1}^{(l)}$ be given. At a Newton step $k+1$, let an estimated deformation $\left(\boldsymbol{\varphi}_{n+1}^h\right)_k = \sum_{i=1}^{N_\varphi} \boldsymbol{\phi}_i^{\boldsymbol{\varphi}} (U_i)_{n+1}^k$ and reference velocity $\left(\boldsymbol{V}_{n+1}^h\right)_k = \sum_{i=1}^{N_V} \boldsymbol{\phi}_i^{\boldsymbol{V}} (V_i)_{n+1}^k$ be given. Find the updates $\Delta^{k+1} U_i$ and $\Delta^{k+1} V_i$, which give the updated deformation*

$$\left(\boldsymbol{\varphi}_{n+1}^h\right)_{k+1} = \left(\boldsymbol{\varphi}_{n+1}^h\right)_k + \sum_{i=1}^{N_\varphi} \boldsymbol{\phi}_i^{\boldsymbol{\varphi}} \Delta^{k+1} U_i \,,$$

and the updated reference velocity

$$\left(\boldsymbol{V}_{n+1}^h\right)_{k+1} = \left(\boldsymbol{V}_{n+1}^h\right)_k + \sum_{i=1}^{N_V} \boldsymbol{\phi}_i^{\boldsymbol{V}} \Delta^{k+1} V_i \,,$$

such that for any test function $\delta\boldsymbol{u}^h$,

$$R_{\mathrm{m}}^{k+1}\left(\delta\boldsymbol{u}^h;\boldsymbol{\varphi}^h,\boldsymbol{V}^h,\theta^h\right)+\sum_{i=1}^{N_\varphi}\left[\mathrm{D}_{\boldsymbol{\varphi}}\,R_{\mathrm{m}}^{k+1}\left(\delta\boldsymbol{u}^h;\boldsymbol{\varphi}^h,\boldsymbol{V}^h,\theta^h;\boldsymbol{\phi}_i^{\boldsymbol{\varphi}}\right)\right]\Delta^{k+1}U_i + \sum_{i=1}^{N_V}\left[\mathrm{D}_{\boldsymbol{V}}\,R_{\mathrm{m}}^{k+1}\left(\delta\boldsymbol{u}^h;\boldsymbol{\varphi}^h,\boldsymbol{V}^h,\theta^h;\boldsymbol{\phi}_i^{\boldsymbol{V}}\right)\right]\Delta^{k+1}V_i=0\,, \tag{6.5.2}$$

where the mechanical residual R_{m}^{k+1} *is*

$$\begin{aligned}R_{\mathrm{m}}^{k+1}\left(\delta\boldsymbol{u}^h;\boldsymbol{\varphi}^h,\boldsymbol{V}^h,\theta^h\right)=&\int_{\Omega_h^{\mathcal{B}}}\nabla\delta\boldsymbol{u}^h\colon\left(\operatorname{dev}\boldsymbol{\tau}^h_{n+1-\alpha_{\mathrm{f}}}+\bar{p}^h_{n+1-\alpha_{\mathrm{f}}}\,\mathbf{1}\right)\mathrm{d}\Omega+G^h_{inertial}\\&-\int_{\Omega_h^{\mathcal{B}}}\delta\boldsymbol{u}^h\cdot\boldsymbol{f}_{\mathrm{b}_{(n+1-\alpha_{\mathrm{f}})}}\,\mathrm{d}\Omega\\&-\int_{\Gamma^{\mathcal{B}}_{hN_\mu}}\delta\boldsymbol{u}^h\cdot\boldsymbol{f}_{\mathrm{s}_{(n+1-\alpha_{\mathrm{f}})}}\,J^h_\Gamma\,\mathrm{d}\Gamma\\&-\int_{\Gamma^{\mathrm{con}}_{hc}}s^{\mathcal{B}}\delta\boldsymbol{u}^h\cdot\boldsymbol{f}^h_{\mathrm{c}_{(n+1-\alpha_{\mathrm{f}})}}\,J^h_\Gamma\,\mathrm{d}\Gamma\,.\end{aligned} \tag{6.5.3}$$

The linearised thermal step is similarly described as follows:

Problem 6.5.2. *At time step* t_{n+1}*, given the deformation* $\boldsymbol{\varphi}^h_n$*, the reference velocity* $\boldsymbol{V}^h_n$*, and the temperature* θ^h_n *from the previous time step* t_n*, and given an updated deformation* $\boldsymbol{\varphi}^h_{n+1}$ *and reference velocity* $\boldsymbol{V}^h_{n+1}$*, at a Newton step* $k{+}1$*, given the estimated temperature* $\left(\theta^h_{n+1}\right)_k=\sum_{i=1}^{N_\theta}\phi_i^\theta(\Theta_i)^k_{n+1}$ *from the previous time step* k*, find the updates* $\Delta^{k+1}\Theta_i$*, which give the updated temperature*

$$\left(\theta^h_{n+1}\right)_{k+1}=\left(\theta^h_{n+1}\right)_k+\sum_{i=1}^{N_\theta}\boldsymbol{\phi}_i^\theta\Delta^{k+1}\Theta_i\,,$$

such that for any test function $\delta\vartheta^h$,

$$R_\theta^{k+1}\left(\delta\vartheta^h;\boldsymbol{\varphi}^h,\boldsymbol{V}^h,\theta^h\right)+\sum_{i=1}^{N_\theta}\left[\mathrm{D}_\theta\,R_\theta^{k+1}\left(\delta\vartheta^h;\boldsymbol{\varphi}^h,\boldsymbol{V}^h,\theta^h;\phi_i^\theta\right)\right]\Delta^{k+1}\Theta_i=0\,, \tag{6.5.4}$$

where the thermal residual R_θ^{k+1} *is*

$$\begin{aligned} R_\theta^{k+1}\left(\delta\vartheta^h;\boldsymbol{\varphi}^h,\boldsymbol{V}^h,\theta^h\right) = &\int_{\Omega^{\mathcal{B}}} \nabla\delta\vartheta^h\cdot\boldsymbol{q}_{n+1}^h\,\mathrm{d}\Omega + \int_{\Omega^{\mathcal{B}}}\delta\vartheta^h\,c\dot{\theta}_{n+1}^h\,\mathrm{d}\Omega \\ &- \int_{\Omega_h^{\mathcal{B}}}\delta\vartheta^h\left[\mathcal{R}^h_{b_{(n+1)}} + \mathcal{D}^h_{\mathrm{mech}_{(n+1)}} - \mathcal{H}^h_{n+1}\right]\mathrm{d}\Omega \\ &- \int_{\Gamma_{hc}^{\mathrm{con}}}\delta\vartheta^h\,\left(\mathcal{D}^h_{fric_{(n+1)}} + s^{\mathcal{B}}q^h_{hc_{(n+1)}}\right)\,\frac{J^h_\Gamma}{J^h}\,\mathrm{d}\Gamma \\ &- \int_{\Gamma^{\mathcal{B}}_{hN_\theta}}\delta\vartheta^h\,\mathcal{R}^h_{s_{(n+1)}}\,\frac{J^h_\Gamma}{J^h}\,\mathrm{d}\Gamma\,. \end{aligned} \tag{6.5.5}$$

6.5.1 Consistent Tangent Moduli

The Gateaux derivatives of the fields involved in the residuals (6.5.3) and (6.5.5) are needed for their linearisation at each Newton-Raphson iteration. These Gateaux derivatives are derived in this subsection.

The Gateaux derivatives of the deformation, reference velocity, and the temperature are given, by definitions (6.5.1), by

$$\mathrm{D}_{\boldsymbol{\varphi}}\,\boldsymbol{\varphi} = \boldsymbol{\phi}^{\boldsymbol{\varphi}}\,, \tag{6.5.6}$$

$$\mathrm{D}_{\boldsymbol{V}}\,\boldsymbol{V} = \boldsymbol{\phi}^{\boldsymbol{V}}\,, \tag{6.5.7}$$

$$\mathrm{D}_{\theta}\,\theta = \phi^{\theta}\,. \tag{6.5.8}$$

The Gateaux derivative of the reference deformation gradient is given by

$$\begin{aligned} \mathrm{D}_{\boldsymbol{\varphi}}\,\boldsymbol{F}_{\mathrm{c}} &= \mathrm{D}_{\boldsymbol{\varphi}}\left[\mathrm{Grad}\,\boldsymbol{\varphi}\right] \\ &= \mathrm{Grad}\left[\mathrm{D}_{\boldsymbol{\varphi}}\,\boldsymbol{\varphi}\right] \\ &= \mathrm{Grad}\,\boldsymbol{\phi}^{\boldsymbol{\varphi}}\,. \end{aligned} \tag{6.5.9}$$

The Gateaux derivative of the Jacobian is given by Jacobi's formula as

$$\begin{aligned} \mathrm{D}_{\boldsymbol{\varphi}}\,J &= J\,\mathrm{tr}\left[\left(\mathrm{D}_{\boldsymbol{\varphi}}\,\boldsymbol{F}_{\mathrm{c}}\right)\boldsymbol{F}_{\mathrm{c}}^{-1}\right] \\ &= J\,\mathrm{tr}\left[\left(\mathrm{Grad}\,\boldsymbol{\phi}^{\boldsymbol{\varphi}}\right)\boldsymbol{F}_{\mathrm{c}}^{-1}\right] \\ &= J\,\mathrm{tr}\left(\nabla\boldsymbol{\phi}^{\boldsymbol{\varphi}}\right). \end{aligned} \tag{6.5.10}$$

From (4.1.15), we have

$$\boldsymbol{n} = \frac{\boldsymbol{F}_{\mathrm{c}}^{-\mathrm{t}} \boldsymbol{N}}{\left\| \boldsymbol{F}_{\mathrm{c}}^{-\mathrm{t}} \boldsymbol{N} \right\|} . \tag{6.5.11}$$

Furthermore, the Gateaux derivative of $\boldsymbol{F}_{\mathrm{c}}^{-1}$ is obtained, by following the same steps as (3.3.37), as

$$\begin{aligned} \mathrm{D}_{\boldsymbol{\varphi}} \boldsymbol{F}_{\mathrm{c}}^{-1} &= -\boldsymbol{F}_{\mathrm{c}}^{-1} \left(\mathrm{D}_{\boldsymbol{\varphi}} \boldsymbol{F}_{\mathrm{c}} \right) \boldsymbol{F}_{\mathrm{c}}^{-1} \\ &= -\boldsymbol{F}_{\mathrm{c}}^{-1} \left(\operatorname{Grad} \boldsymbol{\phi}^{\boldsymbol{\varphi}} \right) \boldsymbol{F}_{\mathrm{c}}^{-1} \\ &= -\boldsymbol{F}_{\mathrm{c}}^{-1} \left(\nabla \boldsymbol{\phi}^{\boldsymbol{\varphi}} \right) . \end{aligned} \tag{6.5.12}$$

Thus, the Gateaux derivative of J_Γ defined in (5.2.5) is given by

$$\begin{aligned} \mathrm{D}_{\boldsymbol{\varphi}} J_\Gamma &= \mathrm{D}_{\boldsymbol{\varphi}} \left[J \left\| \boldsymbol{F}_{\mathrm{c}}^{-\mathrm{t}} \boldsymbol{N} \right\| \right] \\ &= \left(\mathrm{D}_{\boldsymbol{\varphi}} J \right) \left\| \boldsymbol{F}_{\mathrm{c}}^{-\mathrm{t}} \boldsymbol{N} \right\| + J \, \mathrm{D}_{\boldsymbol{\varphi}} \left\| \boldsymbol{F}_{\mathrm{c}}^{-\mathrm{t}} \boldsymbol{N} \right\| \\ &= J \operatorname{tr} \left(\nabla \boldsymbol{\phi}^{\boldsymbol{\varphi}} \right) \left\| \boldsymbol{F}_{\mathrm{c}}^{-\mathrm{t}} \boldsymbol{N} \right\| + J \frac{\boldsymbol{F}_{\mathrm{c}}^{-\mathrm{t}} \boldsymbol{N}}{\left\| \boldsymbol{F}_{\mathrm{c}}^{-\mathrm{t}} \boldsymbol{N} \right\|} \cdot \mathrm{D}_{\boldsymbol{\varphi}} \left[\boldsymbol{F}_{\mathrm{c}}^{-\mathrm{t}} \boldsymbol{N} \right] \\ &= J_\Gamma \operatorname{tr} \left(\nabla \boldsymbol{\phi}^{\boldsymbol{\varphi}} \right) - J \frac{\boldsymbol{F}_{\mathrm{c}}^{-\mathrm{t}} \boldsymbol{N}}{\left\| \boldsymbol{F}_{\mathrm{c}}^{-\mathrm{t}} \boldsymbol{N} \right\|} \cdot \left[\boldsymbol{F}_{\mathrm{c}}^{-1} \left(\nabla \boldsymbol{\phi}^{\boldsymbol{\varphi}} \right) \right]^{\mathrm{t}} \boldsymbol{N} \\ &= J_\Gamma \operatorname{tr} \left(\nabla \boldsymbol{\phi}^{\boldsymbol{\varphi}} \right) - J \frac{\boldsymbol{F}_{\mathrm{c}}^{-\mathrm{t}} \boldsymbol{N}}{\left\| \boldsymbol{F}_{\mathrm{c}}^{-\mathrm{t}} \boldsymbol{N} \right\|} \cdot \left(\nabla \boldsymbol{\phi}^{\boldsymbol{\varphi}} \right)^{\mathrm{t}} \boldsymbol{F}_{\mathrm{c}}^{-\mathrm{t}} \boldsymbol{N} \\ &= J_\Gamma \operatorname{tr} \left(\nabla \boldsymbol{\phi}^{\boldsymbol{\varphi}} \right) - J \left\| \boldsymbol{F}_{\mathrm{c}}^{-\mathrm{t}} \boldsymbol{N} \right\| \frac{\boldsymbol{F}_{\mathrm{c}}^{-\mathrm{t}} \boldsymbol{N}}{\left\| \boldsymbol{F}_{\mathrm{c}}^{-\mathrm{t}} \boldsymbol{N} \right\|} \cdot \left(\nabla \boldsymbol{\phi}^{\boldsymbol{\varphi}} \right)^{\mathrm{t}} \frac{\boldsymbol{F}_{\mathrm{c}}^{-\mathrm{t}} \boldsymbol{N}}{\left\| \boldsymbol{F}_{\mathrm{c}}^{-\mathrm{t}} \boldsymbol{N} \right\|} \\ &= J_\Gamma \operatorname{tr} \left(\nabla \boldsymbol{\phi}^{\boldsymbol{\varphi}} \right) - J_\Gamma \, \boldsymbol{n} \cdot \left(\nabla \boldsymbol{\phi}^{\boldsymbol{\varphi}} \right)^{\mathrm{t}} \boldsymbol{n} \\ &= J_\Gamma \left[\operatorname{tr} \left(\nabla \boldsymbol{\phi}^{\boldsymbol{\varphi}} \right) - \left(\nabla \boldsymbol{\phi}^{\boldsymbol{\varphi}} \right) \boldsymbol{n} \cdot \boldsymbol{n} \right] . \end{aligned} \tag{6.5.13}$$

Linearisation of contact terms

We consider a fixed contactor point in the reference configuration $\boldsymbol{X} \in \Gamma_{hc}^{\mathrm{con}}$, and a corresponding target point given in the reference configuration by $\boldsymbol{Y}_{n+1} = \boldsymbol{\eta} \left(\boldsymbol{X}; \boldsymbol{\varphi}_{n+1}^{h,\mathrm{con}}, \boldsymbol{\varphi}_{n+1}^{h,\mathrm{tar}} \right)$. They are respectively given in the current configuration at a time step $n+1$ by $\boldsymbol{x}_{n+1} =$

$\boldsymbol{\varphi}_{n+1}^{h,\mathrm{con}}(\boldsymbol{X})$ and $\boldsymbol{y}_{n+1} = \boldsymbol{\varphi}_{n+1}^{h,\mathrm{tar}}(\boldsymbol{Y}_{n+1})$. The Gateaux derivative (6.5.1a) for a function $\square\left(\boldsymbol{X}; \boldsymbol{\varphi}_{n+1}^{h,\mathrm{con}}, \boldsymbol{\varphi}_{n+1}^{h,\mathrm{tar}}\right)$ is then

$$\begin{aligned}\mathrm{D}_{\boldsymbol{\varphi}}\,\square\left(\boldsymbol{X}; \boldsymbol{\varphi}_{n+1}^{h,\mathrm{con}}, \boldsymbol{\varphi}_{n+1}^{h,\mathrm{tar}}; \boldsymbol{\phi}_{i}^{\boldsymbol{\varphi},\mathrm{con}}, \boldsymbol{\phi}_{i}^{\boldsymbol{\varphi},\mathrm{tar}}\right)\\ = \left[\frac{\mathrm{d}}{\mathrm{d}\epsilon}\square\left(\boldsymbol{X}; \boldsymbol{\varphi}_{n+1}^{h,\mathrm{con}} + \epsilon\boldsymbol{\phi}_{i}^{\boldsymbol{\varphi},\mathrm{con}}, \boldsymbol{\varphi}_{n+1}^{h,\mathrm{tar}} + \epsilon\boldsymbol{\phi}_{i}^{\boldsymbol{\varphi},\mathrm{tar}}\right)\right]_{\epsilon=0}.\end{aligned} \tag{6.5.14}$$

The Gateaux derivative of the target surface unit normal is given, following the same steps as (3.3.40), by

$$\mathrm{D}_{\boldsymbol{\varphi}}\,\boldsymbol{n} = -\boldsymbol{G}\left[\boldsymbol{G}^{\mathrm{t}}\boldsymbol{G}\right]^{-1}\left[\mathrm{D}_{\boldsymbol{\varphi}}\,\boldsymbol{G}^{\mathrm{t}}\right]\boldsymbol{n}\,, \tag{6.5.15}$$

where, similar to (3.3.15),

$$\begin{aligned}\mathrm{D}_{\boldsymbol{\varphi}}\,G_{ij} &= \mathrm{D}_{\boldsymbol{\varphi}}\left[\varphi_{i,k}^{\mathrm{tar}}\,\Xi_{kj}\right]\\ &= \phi_{i,k}^{\boldsymbol{\varphi},\mathrm{tar}}\,\Xi_{kj} + \left(\varphi_{i,km}^{\mathrm{tar}}\,\Xi_{kj}\Xi_{ml} + \varphi_{i,k}^{\mathrm{tar}}\,\hat{\eta}_{k,jl}\right)\left(\mathrm{D}_{\boldsymbol{\varphi}}\,\hat{Y}_{l}\right)\\ &= \phi_{i,k}^{\boldsymbol{\varphi},\mathrm{tar}}\,\Xi_{kj} + \frac{\partial G_{ij}}{\partial\hat{Y}_{l}}\left(\mathrm{D}_{\boldsymbol{\varphi}}\,\hat{Y}_{l}\right).\end{aligned} \tag{6.5.16}$$

Here, the Gateaux derivative of $\hat{\boldsymbol{Y}}$ is similarly given by following the same steps as (3.3.18) by

$$\mathrm{D}_{\boldsymbol{\varphi}}\,\hat{Y}_{i} = \mathcal{A}_{ji}^{-1}\,\mathcal{W}_{j}\,, \tag{6.5.17}$$

where

$$\mathcal{A}_{ji} = G_{kj}G_{ki} - (x_k - y_k)\left(\varphi_{k,lm}^{\mathrm{tar}}\,\Xi_{lj}\Xi_{mi} + \varphi_{k,l}^{\mathrm{tar}}\,\hat{\eta}_{l,ji}\right), \tag{6.5.18}$$

$$\mathcal{W}_{j} = \left[\phi_{i}^{\boldsymbol{\varphi},\mathrm{con}} - \phi_{i}^{\boldsymbol{\varphi},\mathrm{tar}}\right]G_{ij} + (x_i - y_i)\left(\phi_{i,k}^{\boldsymbol{\varphi},\mathrm{tar}}\right)\left(\varphi_{l,k}^{\mathrm{tar}}\right)^{-1}G_{lj}\,. \tag{6.5.19}$$

The Gateaux derivative of g defined in (3.3.33) is given by

$$\begin{aligned}\mathrm{D}_{\boldsymbol{\varphi}}\,g &= \mathrm{D}_{\boldsymbol{\varphi}}\left[\left(\boldsymbol{\varphi}^{\mathrm{con}} - \boldsymbol{\varphi}^{\mathrm{tar}}\right)\cdot\boldsymbol{n}\right]\\ &= \left(\phi^{\boldsymbol{\varphi},\mathrm{con}} - \phi^{\boldsymbol{\varphi},\mathrm{tar}} - \boldsymbol{G}\,\mathrm{D}_{\boldsymbol{\varphi}}\,\boldsymbol{\eta}\right)\cdot\boldsymbol{n} + \left(\boldsymbol{\varphi}^{\mathrm{con}} - \boldsymbol{\varphi}^{\mathrm{tar}}\right)\cdot\mathrm{D}_{\boldsymbol{\varphi}}\,\boldsymbol{n}\\ &= \left(\phi^{\boldsymbol{\varphi},\mathrm{con}} - \phi^{\boldsymbol{\varphi},\mathrm{tar}} - \boldsymbol{G}\,\mathrm{D}_{\boldsymbol{\varphi}}\,\boldsymbol{\eta}\right)\cdot\boldsymbol{n} + g\boldsymbol{n}\cdot\boldsymbol{G}\left[\boldsymbol{G}^{\mathrm{t}}\boldsymbol{G}\right]^{-1}\left[\mathrm{D}_{\boldsymbol{\varphi}}\,\boldsymbol{G}^{\mathrm{t}}\right]\boldsymbol{n}\\ &= \left(\phi^{\boldsymbol{\varphi},\mathrm{con}} - \phi^{\boldsymbol{\varphi},\mathrm{tar}}\right)\cdot\boldsymbol{n} + \left\{-\mathrm{D}_{\boldsymbol{\varphi}}\,\boldsymbol{\eta} + g\left[\boldsymbol{G}^{\mathrm{t}}\boldsymbol{G}\right]^{-1}\left[\mathrm{D}_{\boldsymbol{\varphi}}\,\boldsymbol{G}^{\mathrm{t}}\right]\boldsymbol{n}\right\}\cdot\boldsymbol{G}^{\mathrm{t}}\boldsymbol{n}\\ &= \left(\phi^{\boldsymbol{\varphi},\mathrm{con}} - \phi^{\boldsymbol{\varphi},\mathrm{tar}}\right)\cdot\boldsymbol{n}\,,\end{aligned} \tag{6.5.20}$$

where the second term on the right-hand side vanishes due to (3.3.27).

The Gateaux derivative of $\frac{\partial \hat{\boldsymbol{Y}}}{\partial t}$ is given from (3.3.18) using (3.3.37) as

$$\begin{aligned}
\mathrm{D}_{\boldsymbol{\varphi}} \frac{\partial \hat{Y}_k}{\partial t} &= \mathrm{D}_{\boldsymbol{\varphi}} \left[\mathcal{A}^{-1}_{jk} \mathcal{V}_j \right] \\
&= -\mathcal{A}^{-1}_{mk} \left[\mathrm{D}_{\boldsymbol{\varphi}} \mathcal{A}_{ml} \right] \mathcal{A}^{-1}_{jl} \mathcal{V}_j + \mathcal{A}^{-1}_{jk} \left[\mathrm{D}_{\boldsymbol{\varphi}} \mathcal{V}_j \right] \\
&= \mathcal{A}^{-1}_{mk} \left\{ - \left[\mathrm{D}_{\boldsymbol{\varphi}} \mathcal{A}_{ml} \right] \mathcal{A}^{-1}_{jl} \mathcal{V}_j + \mathrm{D}_{\boldsymbol{\varphi}} \mathcal{V}_m \right\} \\
&= \mathcal{A}^{-1}_{mk} \left\{ - \left[\mathrm{D}_{\boldsymbol{\varphi}} \mathcal{A}_{ml} \right] \frac{\partial \hat{Y}_l}{\partial t} + \mathrm{D}_{\boldsymbol{\varphi}} \mathcal{V}_m \right\} .
\end{aligned} \tag{6.5.21}$$

Here,

$$\begin{aligned}
\mathrm{D}_{\boldsymbol{\varphi}} \mathcal{A}_{jk} = \; & \mathrm{D}_{\boldsymbol{\varphi}} \left[G_{ij} \, G_{ik} - (x_i - y_i) \frac{\partial G_{ij}}{\partial \hat{Y}_k} \right] \\
= \; & \left[\mathrm{D}_{\boldsymbol{\varphi}} G_{ij} \right] \, G_{ik} + G_{ij} \left[\mathrm{D}_{\boldsymbol{\varphi}} G_{ik} \right] \\
& - \left[\phi^{\boldsymbol{\varphi},\mathrm{con}}_i - \phi^{\boldsymbol{\varphi},\mathrm{tar}}_i - G_{im} \, \mathrm{D}_{\boldsymbol{\varphi}} \hat{Y}_m \right] \frac{\partial G_{ij}}{\partial \hat{Y}_k} \\
& - \left[x_i - y_i \right] \left[\mathrm{D}_{\boldsymbol{\varphi}} \frac{\partial G_{ij}}{\partial \hat{Y}_k} \right] \\
& - \left[x_i - y_i \right] \frac{\partial^2 G_{ij}}{\partial \hat{Y}_k \partial \hat{Y}_m} \, \mathrm{D}_{\boldsymbol{\varphi}} \hat{Y}_m \, ,
\end{aligned} \tag{6.5.22}$$

where, from (3.3.16),

$$\frac{\partial G_{ij}}{\partial \hat{Y}_k} = \varphi^{\mathrm{tar}}_{i,lm} \, \Xi_{mk} \, \Xi_{lj} + \varphi^{\mathrm{tar}}_{i,l} \; \hat{\eta}_{l,jk} \, , \tag{6.5.23}$$

which gives

$$\begin{aligned}
\frac{\partial^2 G_{ij}}{\partial \hat{Y}_k \partial \hat{Y}_m} &= \frac{\partial}{\partial \hat{Y}_m} \left[\varphi^{\mathrm{tar}}_{i,ln} \, \Xi_{nk} \, \Xi_{lj} + \varphi^{\mathrm{tar}}_{i,l} \; \hat{\eta}_{l,jk} \right] \\
&= \varphi^{\mathrm{tar}}_{i,lnp} \, \Xi_{nk} \, \Xi_{lj} \, \Xi_{pm} + \varphi^{\mathrm{tar}}_{i,ln} \, \hat{\eta}_{n,km} \, \Xi_{lj} + \varphi^{\mathrm{tar}}_{i,ln} \, \Xi_{nk} \, \hat{\eta}_{l,jm} \\
&\quad + \varphi^{\mathrm{tar}}_{i,ln} \, \Xi_{nm} \, \hat{\eta}_{l,jk} + \varphi^{\mathrm{tar}}_{i,l} \; \hat{\eta}_{l,jkm} \, ,
\end{aligned} \tag{6.5.24}$$

and

$$\begin{aligned}
\mathrm{D}_{\boldsymbol{\varphi}} \frac{\partial G_{ij}}{\partial \hat{Y}_k} &= \phi^{\boldsymbol{\varphi},\mathrm{tar}}_{i,ln} \, \Xi_{nk} \, \Xi_{lj} + \phi^{\boldsymbol{\varphi},\mathrm{tar}}_{i,l} \; \hat{\eta}_{l,jk} \\
&\quad + \frac{\partial^2 G_{ij}}{\partial \hat{Y}_k \partial \hat{Y}_m} \, \mathrm{D}_{\boldsymbol{\varphi}} \hat{Y}_m \, .
\end{aligned} \tag{6.5.25}$$

Substitution of (6.5.16) and (6.5.25) into (6.5.22) gives

$$\begin{aligned}
\mathrm{D}_{\boldsymbol{\varphi}}\,\mathcal{A}_{jk} = {} & \left[\phi_{i,l}^{\boldsymbol{\varphi},\mathrm{tar}}\Xi_{lj}\right]\, G_{ik} + G_{ij}\left[\phi_{i,l}^{\boldsymbol{\varphi},\mathrm{tar}}\Xi_{lk}\right] \\
& + \left[\frac{\partial G_{ij}}{\partial \hat{Y}_m}G_{ik} + G_{ij}\frac{\partial G_{ik}}{\partial \hat{Y}_m} + G_{im}\frac{\partial G_{ij}}{\partial \hat{Y}_k}\right]\mathrm{D}_{\boldsymbol{\varphi}}\,\hat{Y}_m \\
& - \left[\phi_i^{\boldsymbol{\varphi},\mathrm{con}} - \phi_i^{\boldsymbol{\varphi},\mathrm{tar}}\right]\frac{\partial G_{ij}}{\partial \hat{Y}_k} \\
& - \left[x_i - y_i\right]\left[\phi_{i,ln}^{\boldsymbol{\varphi},\mathrm{tar}}\,\Xi_{nk}\,\Xi_{lj} + \phi_{i,l}^{\boldsymbol{\varphi},\mathrm{tar}}\;\hat{\eta}_{l,jk}\right] \\
& - 2\left[x_i - y_i\right]\frac{\partial^2 G_{ij}}{\partial \hat{Y}_k \partial \hat{Y}_m}\,\mathrm{D}_{\boldsymbol{\varphi}}\,\hat{Y}_m\,, \qquad (6.5.26)
\end{aligned}$$

Similarly, from (3.3.20),

$$\begin{aligned}
\mathrm{D}_{\boldsymbol{\varphi}}\,\mathcal{V}_m &= \mathrm{D}_{\boldsymbol{\varphi}}\left[(x_i - y_i)\left(\frac{\partial \varphi_{i,k}^{\mathrm{tar}}}{\partial t}\bigg|_{\boldsymbol{Y}}\right)\Xi_{km} + \left(\frac{\partial \varphi_i^{\mathrm{con}}}{\partial t} - \frac{\partial \varphi_i^{\mathrm{tar}}}{\partial t}\bigg|_{\boldsymbol{Y}}\right)G_{im}\right] \\
&= \left(\phi_i^{\boldsymbol{\varphi},\mathrm{con}} - \phi_i^{\boldsymbol{\varphi},\mathrm{tar}} - G_{ij}\,\mathrm{D}_{\boldsymbol{\varphi}}\,\hat{Y}_j\right)\left(\frac{\partial \varphi_{i,k}^{\mathrm{tar}}}{\partial t}\bigg|_{\boldsymbol{Y}}\right)\Xi_{km} \\
&\quad + (x_i - y_i)\left(\frac{\partial \phi_{i,k}^{\boldsymbol{\varphi},\mathrm{tar}}}{\partial t}\bigg|_{\boldsymbol{Y}} + \frac{\partial \varphi_{i,kl}^{\mathrm{tar}}}{\partial t}\bigg|_{\boldsymbol{Y}}\Xi_{lj}\,\mathrm{D}_{\boldsymbol{\varphi}}\,\hat{Y}_j\right)\Xi_{km} \\
&\quad + (x_i - y_i)\left(\frac{\partial \varphi_{i,k}^{\mathrm{tar}}}{\partial t}\bigg|_{\boldsymbol{Y}}\right)\hat{\eta}_{k,mj}\,\mathrm{D}_{\boldsymbol{\varphi}}\,\hat{Y}_j \\
&\quad + \left(\frac{\partial \phi_i^{\boldsymbol{\varphi},\mathrm{con}}}{\partial t} - \frac{\partial \phi_i^{\boldsymbol{\varphi},\mathrm{tar}}}{\partial t}\bigg|_{\boldsymbol{Y}} - \frac{\partial \varphi_{i,k}^{\mathrm{tar}}}{\partial t}\bigg|_{\boldsymbol{Y}}\Xi_{kj}\,\mathrm{D}_{\boldsymbol{\varphi}}\,\hat{Y}_j\right)G_{im} \\
&\quad + \left(\frac{\partial \varphi_i^{\mathrm{con}}}{\partial t} - \frac{\partial \varphi_i^{\mathrm{tar}}}{\partial t}\bigg|_{\boldsymbol{Y}}\right)\mathrm{D}_{\boldsymbol{\varphi}}\,G_{im} \\
&= \left(\phi_i^{\boldsymbol{\varphi},\mathrm{con}} - \phi_i^{\boldsymbol{\varphi},\mathrm{tar}}\right)\left(\frac{\partial \varphi_{i,k}^{\mathrm{tar}}}{\partial t}\bigg|_{\boldsymbol{Y}}\right)\Xi_{km} + (x_i - y_i)\left(\frac{\partial \phi_{i,k}^{\boldsymbol{\varphi},\mathrm{tar}}}{\partial t}\bigg|_{\boldsymbol{Y}}\right)\Xi_{km} \\
&\quad + (x_i - y_i)\left(\frac{\partial \varphi_{i,kl}^{\mathrm{tar}}}{\partial t}\bigg|_{\boldsymbol{Y}}\Xi_{lj}\,\mathrm{D}_{\boldsymbol{\varphi}}\,\hat{Y}_j\right)\Xi_{km} + (x_i - y_i)\left(\frac{\partial \varphi_{i,k}^{\mathrm{tar}}}{\partial t}\bigg|_{\boldsymbol{Y}}\right)\hat{\eta}_{k,mj}\,\mathrm{D}_{\boldsymbol{\varphi}}\,\hat{Y}_j \\
&\quad - G_{ij}\,\mathrm{D}_{\boldsymbol{\varphi}}\,\hat{Y}_j\left(\frac{\partial \varphi_{i,k}^{\mathrm{tar}}}{\partial t}\bigg|_{\boldsymbol{Y}}\right)\Xi_{km} - \left(\frac{\partial \varphi_{i,k}^{\mathrm{tar}}}{\partial t}\bigg|_{\boldsymbol{Y}}\Xi_{kj}\,\mathrm{D}_{\boldsymbol{\varphi}}\,\hat{Y}_j\right)G_{im} \\
&\quad + \left(\frac{\partial \phi_i^{\boldsymbol{\varphi},\mathrm{con}}}{\partial t} - \frac{\partial \phi_i^{\boldsymbol{\varphi},\mathrm{tar}}}{\partial t}\bigg|_{\boldsymbol{Y}}\right)G_{im} + \left(\frac{\partial \varphi_i^{\mathrm{con}}}{\partial t} - \frac{\partial \varphi_i^{\mathrm{tar}}}{\partial t}\bigg|_{\boldsymbol{Y}}\right)\mathrm{D}_{\boldsymbol{\varphi}}\,G_{im}\,, \qquad (6.5.27)
\end{aligned}$$

which simplifies to

$$\begin{aligned}
\mathrm{D}_{\boldsymbol{\varphi}}\,\mathcal{V}_m = {} & \left(\phi_i^{\boldsymbol{\varphi},\mathrm{con}} - \phi_i^{\boldsymbol{\varphi},\mathrm{tar}}\right)\left(\left.\frac{\partial \varphi_{i,k}^{\mathrm{tar}}}{\partial t}\right|_{\boldsymbol{Y}}\right)\Xi_{km} + \left(\frac{\partial \varphi_i^{\mathrm{con}}}{\partial t} - \left.\frac{\partial \varphi_i^{\mathrm{tar}}}{\partial t}\right|_{\boldsymbol{Y}}\right)\left(\phi_{i,k}^{\boldsymbol{\varphi},\mathrm{tar}}\,\Xi_{km}\right) \\
& + \left(\frac{\partial \phi_i^{\boldsymbol{\varphi},\mathrm{con}}}{\partial t} - \left.\frac{\partial \phi_i^{\boldsymbol{\varphi},\mathrm{tar}}}{\partial t}\right|_{\boldsymbol{Y}}\right) G_{im} + (x_i - y_i)\left(\left.\frac{\partial \phi_{i,k}^{\boldsymbol{\varphi},\mathrm{tar}}}{\partial t}\right|_{\boldsymbol{Y}}\right)\Xi_{km} \\
& + (x_i - y_i)\left(\left.\frac{\partial \varphi_{i,kl}^{\mathrm{tar}}}{\partial t}\right|_{\boldsymbol{Y}}\Xi_{lj}\Xi_{km} + \left.\frac{\partial \varphi_{i,k}^{\mathrm{tar}}}{\partial t}\right|_{\boldsymbol{Y}}\hat{\eta}_{k,mj}\right)\mathrm{D}_{\boldsymbol{\varphi}}\,\hat{Y}_j \\
& - G_{ij}\left(\left.\frac{\partial \varphi_{i,k}^{\mathrm{tar}}}{\partial t}\right|_{\boldsymbol{Y}}\Xi_{km}\right)\mathrm{D}_{\boldsymbol{\varphi}}\,\hat{Y}_j - \left(\left.\frac{\partial \varphi_{i,k}^{\mathrm{tar}}}{\partial t}\right|_{\boldsymbol{Y}}\Xi_{kj}\right) G_{im}\,\mathrm{D}_{\boldsymbol{\varphi}}\,\hat{Y}_j \\
& + \left(\frac{\partial \varphi_i^{\mathrm{con}}}{\partial t} - \left.\frac{\partial \varphi_i^{\mathrm{tar}}}{\partial t}\right|_{\boldsymbol{Y}}\right)\frac{\partial G_{im}}{\partial \hat{Y}_j}\,\mathrm{D}_{\boldsymbol{\varphi}}\,\hat{Y}_j\,. \qquad (6.5.28)
\end{aligned}$$

Substitution of (6.5.26) and (6.5.28) into (6.5.21) gives

$$\begin{aligned}
\mathrm{D}_{\boldsymbol{\varphi}}\,\frac{\partial \hat{Y}_l}{\partial t} = \mathcal{A}_{ml}^{-1}\Bigg\{ & \left(\phi_i^{\boldsymbol{\varphi},\mathrm{con}} - \phi_i^{\boldsymbol{\varphi},\mathrm{tar}}\right)\left(\left.\frac{\partial \varphi_{i,k}^{\mathrm{tar}}}{\partial t}\right|_{\boldsymbol{Y}}\right)\Xi_{km} + \left(\frac{\partial \varphi_i^{\mathrm{con}}}{\partial t} - \left.\frac{\partial \varphi_i^{\mathrm{tar}}}{\partial t}\right|_{\boldsymbol{Y}}\right)\left(\phi_{i,k}^{\boldsymbol{\varphi},\mathrm{tar}}\,\Xi_{km}\right) \\
& + \left(\frac{\partial \phi_i^{\boldsymbol{\varphi},\mathrm{con}}}{\partial t} - \left.\frac{\partial \phi_i^{\boldsymbol{\varphi},\mathrm{tar}}}{\partial t}\right|_{\boldsymbol{Y}}\right) G_{im} + (x_i - y_i)\left(\left.\frac{\partial \phi_{i,k}^{\boldsymbol{\varphi},\mathrm{tar}}}{\partial t}\right|_{\boldsymbol{Y}}\right)\Xi_{km} \\
& + (x_i - y_i)\left(\left.\frac{\partial \varphi_{i,kl}^{\mathrm{tar}}}{\partial t}\right|_{\boldsymbol{Y}}\Xi_{lj}\Xi_{km} + \left.\frac{\partial \varphi_{i,k}^{\mathrm{tar}}}{\partial t}\right|_{\boldsymbol{Y}}\hat{\eta}_{k,mj}\right)\mathrm{D}_{\boldsymbol{\varphi}}\,\hat{Y}_j \\
& + (x_i - y_i)\left(\phi_{i,kl}^{\boldsymbol{\varphi},\mathrm{tar}}\,\Xi_{lj}\,\Xi_{km} + \phi_{i,k}^{\boldsymbol{\varphi},\mathrm{tar}}\,\hat{\eta}_{k,mj}\right)\frac{\partial \hat{Y}_j}{\partial t} \\
& - G_{ij}\left[\left.\frac{\partial \varphi_{i,k}^{\mathrm{tar}}}{\partial t}\right|_{\boldsymbol{Y}}\Xi_{km}\right]\mathrm{D}_{\boldsymbol{\varphi}}\,\hat{Y}_j - \left[\left.\frac{\partial \varphi_{i,k}^{\mathrm{tar}}}{\partial t}\right|_{\boldsymbol{Y}}\Xi_{kj}\right] G_{im}\,\mathrm{D}_{\boldsymbol{\varphi}}\,\hat{Y}_j \\
& - G_{ij}\left[\phi_{i,k}^{\boldsymbol{\varphi},\mathrm{tar}}\Xi_{km}\right]\frac{\partial \hat{Y}_j}{\partial t} - \left[\phi_{i,k}^{\boldsymbol{\varphi},\mathrm{tar}}\Xi_{kj}\right]\,G_{im}\frac{\partial \hat{Y}_j}{\partial t} \\
& + \left[\frac{\partial \varphi_i^{\mathrm{con}}}{\partial t} - \left.\frac{\partial \varphi_i^{\mathrm{tar}}}{\partial t}\right|_{\boldsymbol{Y}}\right]\frac{\partial G_{im}}{\partial \hat{Y}_j}\,\mathrm{D}_{\boldsymbol{\varphi}}\,\hat{Y}_j + \left[\phi_i^{\boldsymbol{\varphi},\mathrm{con}} - \phi_i^{\boldsymbol{\varphi},\mathrm{tar}}\right]\frac{\partial G_{im}}{\partial \hat{Y}_j}\frac{\partial \hat{Y}_j}{\partial t} \\
& - \left[\frac{\partial G_{im}}{\partial \hat{Y}_k}G_{ij} + G_{im}\frac{\partial G_{ij}}{\partial \hat{Y}_k} + G_{ik}\frac{\partial G_{im}}{\partial \hat{Y}_j}\right]\frac{\partial \hat{Y}_j}{\partial t}\,\mathrm{D}_{\boldsymbol{\varphi}}\,\hat{Y}_k \\
& + 2\,[x_i - y_i]\left[\frac{\partial^2 G_{im}}{\partial \hat{Y}_j \partial \hat{Y}_k}\right]\frac{\partial \hat{Y}_j}{\partial t}\,\mathrm{D}_{\boldsymbol{\varphi}}\,\hat{Y}_k\Bigg\}\,. \qquad (6.5.29)
\end{aligned}$$

The Gateaux derivatives of the contactor and target reference velocities are

$$\mathrm{D}_{\boldsymbol{V}}\, \boldsymbol{V}^{\mathrm{con}} = \boldsymbol{\phi}^{\boldsymbol{V},\mathrm{con}}\,, \tag{6.5.30}$$

$$\mathrm{D}_{\boldsymbol{V}}\, \boldsymbol{V}^{\mathrm{tar}} = \boldsymbol{\phi}^{\boldsymbol{V},\mathrm{tar}}\,, \tag{6.5.31}$$

$$\mathrm{D}_{\boldsymbol{\varphi}}\, \boldsymbol{V}^{\mathrm{tar}} = \left(\mathrm{Grad}\, \boldsymbol{V}^{\mathrm{tar}}\right) \mathrm{D}_{\boldsymbol{\varphi}}\, \boldsymbol{\eta}\,, \tag{6.5.32}$$

$$\tag{6.5.33}$$

where

$$\boldsymbol{\phi}^{\boldsymbol{V},\mathrm{con}} = \boldsymbol{\phi}^{\boldsymbol{V}}\big|_{\Gamma_{\mathrm{c}}^{\mathrm{con}}}\,, \tag{6.5.34}$$

$$\boldsymbol{\phi}^{\boldsymbol{V},\mathrm{tar}} = \boldsymbol{\phi}^{\boldsymbol{V}}\big|_{\Gamma_{\mathrm{c}}^{\mathrm{tar}}}\,, \tag{6.5.35}$$

$$\mathrm{D}_{\boldsymbol{\varphi}}\, \boldsymbol{\eta} = \boldsymbol{\Xi}\, \mathrm{D}_{\boldsymbol{\varphi}}\, \hat{\boldsymbol{Y}}\,. \tag{6.5.36}$$

7 Solver Implementation

This Chapter describes the implementation of a solver based on the discretisation steps described in the previous Chapter. The implementation was programmed in C++ making use of the deal.II finite element library [19].

In Section 7.1, the finite element discretisation is described and the thermomechanical fields and material state variables which describe the solution are detailed. Section 7.2 describes the high-level structure of the solver and the solution procedure. Section 7.3 describes computation of the in-plane component of the reference motion and its incorporation into the material remapping of the nodal fields and quadrature point variables. Section 7.4 gives an overview of solution for the mechanical fields, which is then described in detail in Sections 7.5 through 7.7. Solution for the thermal fields is described in Section 7.8.

7.1 Finite Element Discretisation

The domains of the contacting bodies in the reference configuration are discretised into axisymmetric meshes of quadrilateral elements. To make use of distributed-memory parallel computing resources, the mesh of each body is divided into subdomains. The distributed-memory parallel program is run as multiple processes, each process running independently and coordinating with the other processes through message passing. Each

of the meshed subdomains is assigned to one process. A cell and its faces are said to be owned by the process that is assigned the subdomain which contains the cell.

7.1.1 Rotational Symmetry

The implemented solver makes use of the rotational symmetry so that a three-dimensional problem is converted into a two-dimensional axisymmetric one. A point in the reference configuration $\boldsymbol{X} = \sum_{i=1}^{3} X_i \hat{\boldsymbol{e}}_i$, where $\hat{\boldsymbol{e}}_i$ are the unit vectors along the three Cartesian axes, has the cylindrical coordinates (R, Θ, Z) such that

$$X_1 = R\cos\Theta\,, \tag{7.1.1a}$$

$$X_2 = R\sin\Theta\,, \tag{7.1.1b}$$

$$X_3 = Z\,. \tag{7.1.1c}$$

The ALE formulation is implemented by representing motion at each time step $n+1$ in terms of both the incremental reference motion as well as the deformation from the reference configuration. For a point $\boldsymbol{X}$ in the reference configuration, the incremental reference motion is given by the remapped position $\hat{\boldsymbol{X}}_{n+1}$ given by (6.1.62) as

$$\hat{\boldsymbol{X}}_{n+1} \coloneqq \mathcal{M}_{t_n}^{t_{n+1}}\{\boldsymbol{X}\} = \boldsymbol{X} - \int_{t_n}^{t_{n+1}} \mathcal{M}_{\tau}^{t_{n+1}}\{\boldsymbol{V}\}\ \mathrm{d}\tau\,. \tag{7.1.2}$$

The remapped position $\hat{\boldsymbol{X}}_{n+1} = \sum_{i=1}^{3} \hat{X}_{i,n+1}\hat{\boldsymbol{e}}_i$ has the cylindrical coordinates $(\hat{R}, \hat{\Theta}, \hat{Z})$ such that

$$\hat{X}_{1,n+1} = \hat{R}_{n+1}\cos\hat{\Theta}_{n+1}\,, \tag{7.1.3a}$$

$$\hat{X}_{2,n+1} = \hat{R}_{n+1}\sin\hat{\Theta}_{n+1}\,, \tag{7.1.3b}$$

$$\hat{X}_{3,n+1} = \hat{Z}_{n+1}\,, \tag{7.1.3c}$$

where

$$\hat{R}_{n+1} = R - \Delta R_{n+1}\,, \tag{7.1.4a}$$

$$\hat{Z}_{n+1} = Z - \Delta Z_{n+1}\,, \tag{7.1.4b}$$

$$\hat{\Theta}_{n+1} = \Theta - \Delta\Theta_{n+1}\,, \tag{7.1.4c}$$

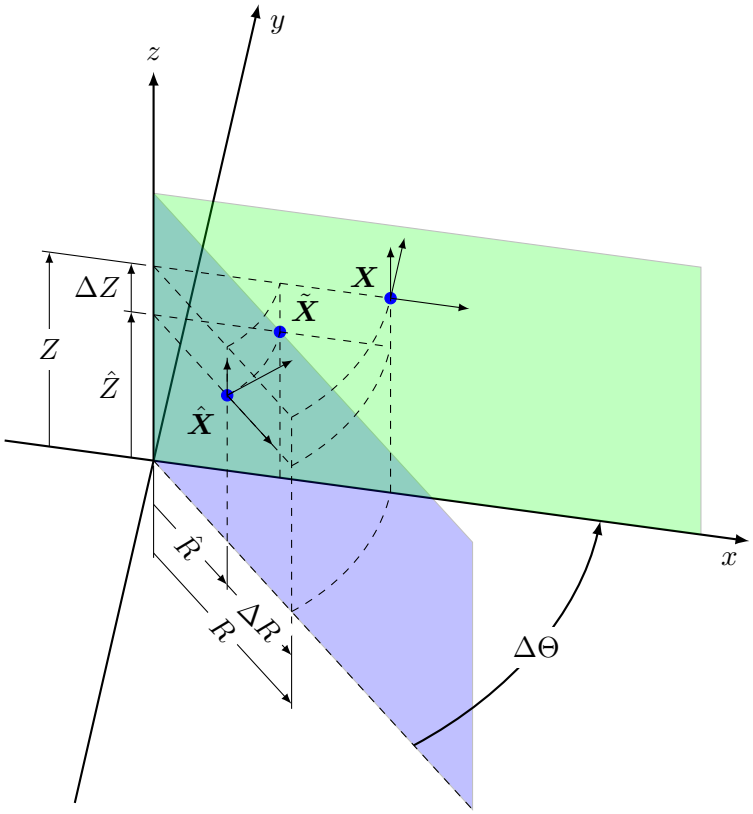

Figure 7.1: Incremental reference motion representation in cylindrical coordinates

and $\Delta R_{n+1} = \Delta R_{n+1}(R, Z)$, $\Delta\Theta_{n+1} = \Delta\Theta_{n+1}(R, Z)$ and $\Delta Z_{n+1} = \Delta Z_{n+1}(R, Z)$ vary only with R and Z at any fixed time step $n + 1$.

The incremental reference motion is decomposed into an in-plane component and a circumferential component. The in-plane component at $\boldsymbol{X}$ is represented by the point $\tilde{\boldsymbol{X}}$ that has the cylindrical coordinates $(\hat{R}, \Theta, \hat{Z})$, and the circumferential component is represented by the angular increment $\Delta\Theta$. Representation of the incremental reference motion in cylindrical coordinates is depicted in Figure 7.1.

Deformation from the reference configuration is represented, at any given time step $n+1$, by position in the current configuration $\boldsymbol{x}_{n+1} = \boldsymbol{\varphi}(\boldsymbol{X}, t_{n+1}) = \sum_{i=1}^{3} x_{i,n+1}\hat{\boldsymbol{e}}_i$, which has

the cylindrical coordinates $(R + r_{n+1}, \Theta, Z + z_{n+1})$ such that

$$x_{1,n+1} = (R + r_{n+1}) \cos \Theta \,, \tag{7.1.5a}$$

$$x_{2,n+1} = (R + r_{n+1}) \sin \Theta \,, \tag{7.1.5b}$$

$$x_{3,n+1} = Z + z_{n+1} \,, \tag{7.1.5c}$$

where $r_{n+1} = r_{n+1}(R, Z)$ and $z_{n+1} = z_{n+1}(R, Z)$ vary only with R and Z.

In this representation, deformation between the reference configuration and the current configuration (7.1.5) leaves planes containing the axisymmetry axis unchanged, and the circumferential component of the motion is completely captured by the reference velocity given in terms of the incremental reference motion (7.1.3). This choice does not limit the range of the motion that can be represented, but rather it is a constraint on its composition between the Eulerian and Lagrangian parts of the representation. This way, both in-plane and torsional effects are well accounted for, and the reference and current configuration meshes remain entirely on the axisymmetry plane.

7.1.2 Cell Shape Functions and Local Degrees of Freedom

The finite element discretisation also includes the definition of shape functions for the mechanical, thermal, and reference motion fields. From a programming perspective, a number of `FiniteElement` [1] objects are defined which encapsulate these sets of shape functions. These objects are named `mech_fe`, `therm_fe`, `vol_var_fe` and `ref_motion_fe`. The `mech_fe` object encapsulates the shape functions for the deformation from the reference configuration, along with the circumferential component of the reference motion. The `therm_fe` one encapsulates the shape functions for the temperature. The `vol_var_fe` object encapsulates the element-wise continuous shape functions used to discretise the

[1] As a convention, we use `CamelCase` for `class` and `struct` names such as `FiniteElement`, and we use `snake_case` for the names of objects and member variables and functions such as `mech_fe`.

pressure and deformation Jacobian terms. The `ref_motion_fe` object encapsulates the shape functions for the in-plane components of the reference motion.

The `FiniteElement` objects also provide a mapping between the shape functions and the local cell degrees of freedom. The `mech_fe` object includes a total of `mech_dofs_per_cell` local degrees of freedom, such that each degree of freedom i is mapped to a pair of shape functions $\left(\boldsymbol{\phi}_i^{\boldsymbol{\varphi}}, \phi_i^{\mathrm{ref},\Theta}\right)$. The shape functions $\{\boldsymbol{\phi}_i^{\boldsymbol{\varphi}}\}_{i=1}^{\texttt{mech\_dofs\_per\_cell}}$, which are vector functions, form a basis for the deformation, while the shape functions $\{\phi_i^{\mathrm{ref},\Theta}\}_{i=1}^{\texttt{mech\_dofs\_per\_cell}}$, which are scalar functions, form a basis for the circumferential component of the reference motion.

Similarly, the `therm_fe` object includes a total of `therm_dofs_per_cell` local cell degrees of freedom, such that each degree of freedom i is mapped to a shape function ϕ_i^{θ}. These scalar shape functions $\left\{\phi_i^{\theta}\right\}_{i=1}^{\texttt{therm\_dofs\_per\_cell}}$ form a basis for the thermal field.

Furthermore, the `vol_var_fe` object includes a total of `vol_dofs_per_cell` degrees of freedom, which are mapped to the shape functions $\{\phi_i^{\mathrm{p}}\}_{i=1}^{\texttt{vol\_dofs\_per\_cell}}$ that form a basis of subspace onto which the pressure and deformation Jacobian fields are projected by (6.4.5) and (6.4.6). The shape functions $\{\boldsymbol{\phi}_i^{\boldsymbol{\varphi}}\}$, $\{\phi_i^{\mathrm{ref},\Theta}\}$, and $\{\phi_i^{\mathrm{p}}\}$ are chosen to form continuous biquadratic-discontinuous linear mixed elements, which are stable and convergent, such that the discretised deformation and reference motion fields are biquadratic, and the projected deformation Jacobian and pressure fields are cell-wise continuous linear. As represented in Figure 7.2, a biquadratic-linear quadrilateral element has two sets of degrees of freedom. The first is the set of nine degrees of freedom of a continuous cell-wise biquadratic field, whose local support points comprise four nodes at the corners of the quadrilateral, four nodes at the centres of its edges, and one node at its centre. These degrees of freedom are used to construct the components of $\{\boldsymbol{\phi}_i^{\boldsymbol{\varphi}}\}$ and $\{\phi_i^{\mathrm{ref},\Theta}\}$. The second set of degrees of freedom corresponds to the cell-wise discontinuous linear field, which are the local degrees of freedom of $\{\phi_i^{\mathrm{p}}\}$. The support points of these sets of degrees of freedom are represented, respectively, by the black and white circles in Figure 7.2.

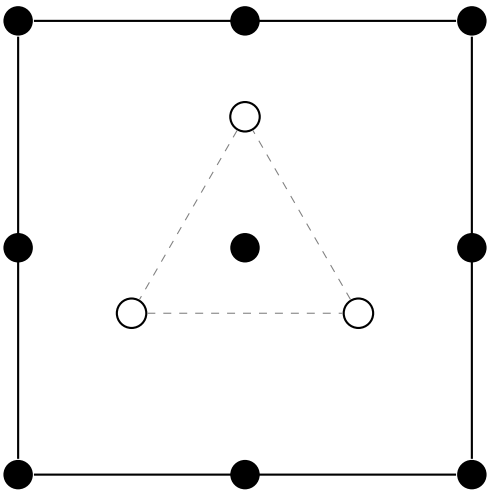

Figure 7.2: Nodes and degrees of freedom in a biquadratic-linear element. The black nodes are support points for the continuous cell-wise biquadratic field. The white circles represent the degrees of freedom of the discontinuous linear field

The `ref_motion_fe` object includes `ref_motion_dofs_per_cell` degrees of freedom. These are mapped to the shape functions $\{\boldsymbol{\phi}_i^{\mathrm{ref,P}}\}_{i=1}^{\texttt{ref\_motion\_dofs\_per\_cell}}$, which form a basis for the in-plane component of the reference motion.

The shape functions correspond to nodal support points, such that any shape function that is not identically zero vanishes at all support points except one. Furthermore, each scalar shape function, such as ϕ^θ, has unit value at its corresponding support point. Similarly, each tensor shape function, such as $\boldsymbol{\phi}^\varphi$, has unit norm at its corresponding support point. Moreover, the inner product of any two distinct tensor shape functions at any support point vanishes. Furthermore, the components of the tensor shape functions satisfy the Kronecker relation at the support points, i.e. exactly one component has a unit value and all other components vanish.

7.1.3 Thermomechanical Fields

The thermomechanical state and the formulation and solution of the linear system at a Newton step are represented by objects of type `NewtonStepLinearSystem`.

Each such object includes a matrix `Newton_step_matrix`, and the vectors `Newton_step_residual` and `Newton_step_solution`, which represent the formulation and solution of the linear system. Each `NewtonStepLinearSystem` also includes the vectors `previous_value`, `previous_time_rate`, `previous_second_time_rate` and `current_increment`. The variables contained in a `NewtonStepLinearSystem` object are represented in the class diagram in Figure 7.3. Three such `NewtonStepLinearSystem` objects are defined for each of the contacting bodies: `mech_step_system`, `therm_step_system` and `reference_motion_step_system`, as summarised in Figure 7.4. Each of `contactor_mech_step_system` and `target_mech_step_system` represents the deformation from the reference configuration and the circumferential component of the reference motion fields for the respective contacting body. Similarly, `contactor_therm_step_system` and `target_therm_step_system` represent the respective thermal fields, and `contactor_reference_motion_step_system` and `contactor_reference_motion_step_system` represent the in-plane components of the reference motion.

NewtonStepLinearSystem
Newton_step_matrix : SparseMatrix
Newton_step_residual: Vector
Newton_step_solution: Vector
previous_value: Vector
previous_time_rate: Vector
previous_second_time_rate: Vector
current_increment: Vector

Figure 7.3: Attributes of a `NewtonStepLinearSystem` object

The components of the global vectors and matrices encapsulated in the `NewtonStepLinearSystem` objects correspond to global degrees of freedom. These are linked to the local degrees of freedom described in the previous section in that the shape function of each global degree of freedom is defined on several adjacent cells in terms

NonlinearFields
contactor_mech_step_system: NewtonStepLinearSystem
target_mech_step_system: NewtonStepLinearSystem
contactor_therm_step_system: NewtonStepLinearSystem
target_therm_step_system: NewtonStepLinearSystem
contactor_reference_motion_step_system: NewtonStepLinearSystem
target_reference_motion_step_system: NewtonStepLinearSystem

Figure 7.4: Objects of type `NewtonStepLinearSystem`

of the local shape functions on those cells. Specifically, the shape functions are defined in terms of nodal support points, which have a one-to-one mapping with the degrees of freedom. Thus, a local nodal support point at an internal cell boundary is shared among the neighbouring cells which share that boundary, such that the local degrees of freedom which correspond to that shared support point map to the same global degrees of freedom.

In addition to the global vectors, the material state variables are stored as data at each quadrature point. These are the elastic deformation tensor from the previous time step $\boldsymbol{B}_n^{\mathrm{e}}$, the equivalent plastic strain α_n, and the reference motion Jacobian $J_{\mathrm{r},n}$. Updates to these quadrature point-stored values are also unknowns to be solved for at each time step.

7.2 Solution Procedure

The solution progresses through time steps. Each time step starts with determination of the in-plane component of the reference motion, followed by determination of the remaining thermomechanical fields using the split-step procedure by Simo and Miehe [82]. The procedure followed at each time step is shown at a high level in Figure 7.5. First, the in-plane component of the reference motion is determined, and it is used to remap the

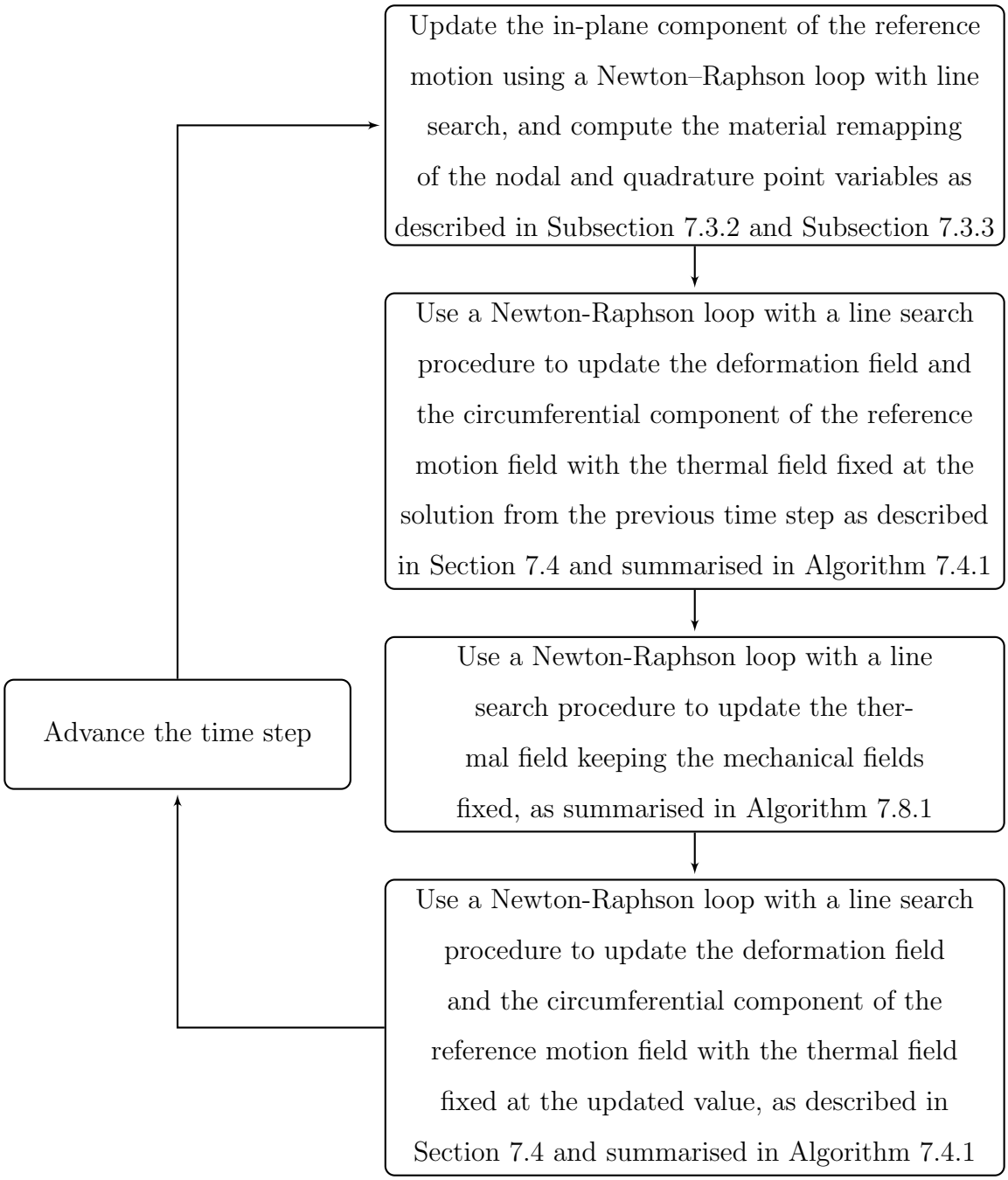

Figure 7.5: Mechanical and thermal operator-split time step

nodal and quadrature point fields account for the incremental material motion. Then, the mechanical variables are updated at a fixed thermal field. The thermal field is then updated with the mechanical fields fixed at the updated mechanical solution. Finally, the updated thermal field is kept fixed and the mechanical fields are updated again, which completes the time step. Following such a staggered approach has several advantages. Not only is computational expense lowered by reducing the sizes of the problems to be solved without a significant loss of accuracy, but this approach also results in a set of symmetric problems and enables exact linearisation in both the mechanical and thermal steps [82].

At each mechanical sub-step, an augmented Lagrangian procedure is used to satisfy the contact constraints. In each augmented Lagrangian iteration, the mechanical system is assembled with the contact residual given by the sum of a fixed augmented Lagrangian term accumulated from previous augmented Lagrangian iterations, and a penalty term computed from the penetration and slip velocity in the current iteration. The resulting nonlinear problem is solved using a Newton Raphson method.

Each Newton-Raphson iteration consists of assembly and solution of a linear problem (6.5.2) given by bulk and contact residual vectors and tangent matrices, followed by one or more line search steps.

Implementation of the thermal sub-steps is structured similarly, except that augmented Lagrangian iteration is not required because no inequality constraints are involved. Each thermal sub-step consists of a Newton-Raphson loop to solve a linearised problem (6.5.4).

7.3 In-Plane Component of Reference Motion

Mechanical motion is described in the ALE formulation in terms of both the reference motion $\boldsymbol{\Upsilon}_0$ as well as the motion from the reference configuration $\boldsymbol{\varphi}_\mathrm{c}$. The reference

motion is represented incrementally by (6.1.62), so that each point $\boldsymbol{X}$ in the reference configuration, which has the cylindrical coordinates (R, Θ, Z), is mapped to a point $\hat{\boldsymbol{X}}$ with cylindrical coordinates $(\hat{R}, \hat{\Theta}, \hat{Z})$. The angular (circumferential) component $\hat{\Theta} = \Theta - \Delta\Theta$ of the reference motion increment is solved simultaneously with the deformation from the reference configuration in each mechanical sub-step. The in-plane component of the reference motion, which is represented by the point $\tilde{\boldsymbol{X}}$ that has the cylindrical coordinates $(\hat{R}, \Theta, \hat{Z})$, is computed separately at the start of each time step with the goal of controlling mesh distortion. The values of the mechanical and thermal fields and the material state variables at $\tilde{\boldsymbol{X}}$ are then computed. These values are needed to compute the material remapping of these fields, i.e. their values at $\hat{\boldsymbol{X}}$.

7.3.1 Reference Motion Increment Determination

The reference motion increment is defined by the nodal field $\hat{\boldsymbol{X}}_{n+1}$, which is related to the reference velocity by (6.1.61). Its in-plane component, which is given by the nodal field $\tilde{\boldsymbol{X}}_{n+1}$, is determined at the start of the time step. This is done with the objective of reducing distortion of the deformed configuration mesh. We approximate the mesh distortion using the deformation measure

$$\boldsymbol{F}^{\text{mesh}}_{n+1} = \boldsymbol{F}_{\text{c},n} \operatorname{Grad} \tilde{\boldsymbol{X}}_{n+1} \,. \tag{7.3.1}$$

Thus, the in-plane component of the mesh motion, $\tilde{\boldsymbol{X}}_{n+1}$, is determined by definition of a mesh distortion stress $\boldsymbol{\tau}^{\text{mesh}}_{n+1}$ and numerical solution of the corresponding momentum

balance equation

$$\operatorname{div} \boldsymbol{\tau}_{n+1}^{\text{mesh}} = \mathbf{0}\,, \tag{7.3.2}$$

$$\boldsymbol{\tau}_{n+1}^{\text{mesh}} = \operatorname{dev} \boldsymbol{\tau}_{n+1}^{\text{mesh}} + p_{n+1}^{\text{mesh}} \mathbf{1}\,, \tag{7.3.3}$$

$$\operatorname{dev} \boldsymbol{\tau}_{n+1}^{\text{mesh}} = \mu^{\text{mesh}} \operatorname{dev} \bar{\boldsymbol{b}}_{n+1}^{\text{mesh}}\,, \tag{7.3.4}$$

$$p_{n+1}^{\text{mesh}} = \kappa^{\text{mesh}} \left(J^{\text{mesh}} + \frac{1}{J^{\text{mesh}}} \right)\,, \tag{7.3.5}$$

$$\bar{\boldsymbol{b}}_{n+1}^{\text{mesh}} = \left[J_{n+1}^{\text{mesh}} \right]^{-2/3} \boldsymbol{b}_{n+1}^{\text{mesh}}\,, \tag{7.3.6}$$

$$\boldsymbol{b}_{n+1}^{\text{mesh}} = \left(\boldsymbol{F}_{n+1}^{\text{mesh}} \right) \left(\boldsymbol{F}_{n+1}^{\text{mesh}} \right)^{\text{t}}\,, \tag{7.3.7}$$

$$J_{n+1}^{\text{mesh}} = \sqrt{\det \boldsymbol{b}_{n+1}^{\text{mesh}}}\,. \tag{7.3.8}$$

A Newton-Raphson loop with a line search procedure is used to solve for $\tilde{\boldsymbol{X}}_{n+1}$, where the residual vector and tangent matrix are assembled in a procedure analogous to that of the mechanical problem.

7.3.2 Material Mapping of Nodal Mechanical and Thermal Fields

The material remapped values of the discrete mechanical and thermal fields are needed in the formulation and solution of the thermomechanical problems in each time step. Computation of these values is now described.

Since the deformation and thermal fields do not vary with the angular coordinate of position in the reference configuration Θ, they are determined using the in-plane component of the incremental reference motion, which is computed at the start of each time step. As an example, for the temperature field we have $\theta_n = \theta_n(R, Z)$, so that

$$\mathcal{M}_n^{n+1}\theta \coloneqq \theta_n|_{\hat{\boldsymbol{X}}_{n+1}} = \theta_n(\hat{R}, \hat{Z}) = \theta_n|_{\tilde{\boldsymbol{X}}_{n+1}}\,. \tag{7.3.9}$$

Material remapping is computed as follows for a field $\square$ that is given on a cell c in terms of shape functions $\{\phi_i^{\square}\}_{i=1}^{\square\_\texttt{dofs\_per\_cell}}$ that correspond to nodal support points $\{\boldsymbol{X}_{c:i}^{\square}\}_{i=1}^{\square\_\texttt{support\_pts\_per\_cell}}$. The fields for which this computation is carried out are the

deformation and temperature, as well as the first and second time derivatives of the deformation.

First, the in-plane component of the incremental reference motion is applied to each of the support points to obtain $\{\tilde{\boldsymbol{X}}^{\square}_{c:i}\}_{i=1}^{\square\_\texttt{support\_pts\_per\_cell}}$. Then, the field $\square_n$ is evaluated at these new nodal support points. In general, not all of the new support points remain within the same cell c. Rather, they may be contained in different cells, which may be owned by different processes from that which owns c. As a result, evaluation of the field $\square_n$ at each of the new nodal support points $\{\tilde{\boldsymbol{X}}^{\square}_{c:i}\}_{i=1}^{\square\_\texttt{support\_pts\_per\_cell}}$ is carried out by sending the new positions to the processes that own the cells in which they are contained, followed by carrying out the evaluation and sending the result back to the process that owns the cell c. Material remapping is then completed by populating these values into the global vectors at the global degrees of freedom of the respective nodal support points.

7.3.3 Material Mapping of Quadrature Point Variables

Material remapped values of the fields represented by values at the quadrature points are also needed at each time step. These fields are the equivalent plastic strain α_n, the tensor field $\boldsymbol{B}^{\mathrm{e}}_n$, and the reference motion deformation determinant Jacobian $J_{\mathrm{r},n}$.

Material remapping of these fields is performed in a procedure similar to that applied to the nodal fields. First, at each cell c, each quadrature point $\{\boldsymbol{X}^{\mathrm{qp}}_{c:i}\}_{i=1}^{\texttt{q\_points\_per\_cell}}$ is transformed by the in-plane component of the reference motion to obtain $\{\tilde{\boldsymbol{X}}^{\mathrm{qp}}_{c:i}\}_{i=1}^{\texttt{q\_points\_per\_cell}}$. The values of the fields at this remapped position are then computed by projection from the known values of the quadrature points $\{\boldsymbol{X}^{\mathrm{qp}}_{\tilde{c}:i}\}_{i=1}^{\texttt{q\_points\_per\_cell}}$ in the cell $\tilde{c}$ which contains $\tilde{\boldsymbol{X}}^{\mathrm{qp}}_{c:i}$. Projection is carried out onto a function space defined in terms of a set of shape functions $\{\phi^{\mathrm{q}}_i\}_{i=1}^{\texttt{projection\_dim}}$. For a field $\square$, this is given by

$$\square|_{\tilde{\boldsymbol{X}}^{\mathrm{qp}}_{c:i}} = \phi^{\mathrm{q}}_j(\tilde{\boldsymbol{X}}^{\mathrm{qp}}_{c:i}) \left[\sum_l \phi^{\mathrm{q}}_j(\boldsymbol{X}^{\mathrm{qp}}_{\tilde{c}:l})\phi^{\mathrm{q}}_k(\boldsymbol{X}^{\mathrm{qp}}_{\tilde{c}:l})\right]^{-1} \left[\sum_l \phi^{\mathrm{q}}_k(\boldsymbol{X}^{\mathrm{qp}}_{\tilde{c}:l})\square(\boldsymbol{X}^{\mathrm{qp}}_{\tilde{c}:l})\right], \tag{7.3.10}$$

where the summations are over the quadrature point indices $l = (1, ..., \texttt{q\_points\_per\_cell})$.

In order to preserve the isochoric property of the plastic deformation, remapping of the volume preserving part, $\bar{\boldsymbol{B}}^{\mathrm{e}} = J_{\mathrm{r}}^{-2/3}\boldsymbol{B}^{\mathrm{e}}$, of the tensor $\boldsymbol{B}^{\mathrm{e}}$ is done after a pre-transformation, and is followed by a post transformation as follows:

$$\bar{\boldsymbol{B}}^{\mathrm{e}}_n\big|_{\tilde{\boldsymbol{X}}^{\mathrm{qp}}_{c:i}} = \left[\bar{\boldsymbol{F}}^{-1}_{\mathrm{c},n} \exp\left(\log \bar{\boldsymbol{b}}^{\mathrm{e}}_n\right) \bar{\boldsymbol{F}}^{-\mathrm{t}}_{\mathrm{c},n}\right]_{\tilde{\boldsymbol{X}}^{\mathrm{qp}}_{c:i}}, \tag{7.3.11}$$

$$\bar{\boldsymbol{F}}_{\mathrm{c},n} = J_{\mathrm{c},n}^{-1/3}\boldsymbol{F}_{\mathrm{c},n}\,, \tag{7.3.12}$$

$$\log \bar{\boldsymbol{b}}^{\mathrm{e}}_n\big|_{\tilde{\boldsymbol{X}}^{\mathrm{qp}}_{c:i}} = \phi^{\mathrm{q}}_j\big|_{\tilde{\boldsymbol{X}}^{\mathrm{qp}}_{c:i}} \left[\sum_l \left[\phi^{\mathrm{q}}_j \phi^{\mathrm{q}}_k\right]_{\boldsymbol{X}^{\mathrm{qp}}_{\tilde{c}:l}}\right]^{-1} \left[\sum_l \left[\phi^{\mathrm{q}}_k \log\left(\bar{\boldsymbol{F}}_{\mathrm{c},n}\bar{\boldsymbol{B}}^{\mathrm{e}}_n\bar{\boldsymbol{F}}^{\mathrm{t}}_{\mathrm{c},n}\right)\right]_{\boldsymbol{X}^{\mathrm{qp}}_{\tilde{c}:l}}\right]. \tag{7.3.13}$$

First, an interpolation is computed of $\log \bar{\boldsymbol{b}}^{\mathrm{e}}_n = \log\left(\bar{\boldsymbol{F}}_{\mathrm{c},n}\bar{\boldsymbol{B}}^{\mathrm{e}}_n\bar{\boldsymbol{F}}^{\mathrm{t}}_{\mathrm{c},n}\right)$, which is a deviatoric tensor by (3.1.40), since it is the natural logarithm of a tensor with a unit determinant. The resulting interpolated tensor $\log \bar{\boldsymbol{b}}^{\mathrm{e}}_n\big|_{\tilde{\boldsymbol{X}}^{\mathrm{qp}}_{c:i}}$ is also deviatoric since it is a linear combination of deviatoric tensors. This interpolated value is then used to complete the computation as $\bar{\boldsymbol{B}}^{\mathrm{e}}_n = \bar{\boldsymbol{F}}^{-1}_{\mathrm{c},n} \exp\left(\log \bar{\boldsymbol{b}}^{\mathrm{e}}_n\right) \bar{\boldsymbol{F}}^{-\mathrm{t}}_{\mathrm{c},n}$, which has unit determinant due to (3.1.40). This ensures that the plastic deformation remains volume preserving since, by (4.3.16),

$$\begin{aligned}\det \boldsymbol{G}^{\mathrm{p}} &= J_{\mathrm{r}}^{-2/3} \det \boldsymbol{B}^{\mathrm{e}} \\ &= \det \bar{\boldsymbol{B}}^{\mathrm{e}} \\ &= 1\,.\end{aligned} \tag{7.3.14}$$

This is similar to the procedure described in [18], where the natural logarithm of the right Cauchy-Green plastic tensor $\boldsymbol{G}^{\mathrm{p}}$ is interpolated with the cell shape functions, and the exponential of the resulting value is taken. The difference is that here, we interpolate the logarithm of the elastic tensor $\boldsymbol{b}^{\mathrm{e}}$, and take the exponential of the resulting value, which removes dependence on the material configuration.

7.4 Mechanical Fields Solution

Each of the two mechanical parts of a time step, in which the deformation field and the circumferential-component of the reference motion field are updated with the thermal field fixed, is completed by an augmented Lagrangian loop. At each iteration, a thermo-mechanical problem is solved in which the thermal field is fixed and the contact forces are given by the sum of an augmented Lagrangian term and a penalty term. This solution is completed in a sequence of Newton-Raphson steps. Each Newton step consists of assembly and solution of a linear system followed by a line search procedure to compute an update to the approximate solution. The high-level structure of the mechanical parts of the time step is given in Algorithm (7.4.1).

Assembly of the residual vectors and tangent matrices forms a major part of the implementation. It is completed in three main stages, which are represented in Figure 7.6. First, the bulk parts of the residual vectors and tangent matrices are assembled, as detailed in Section 7.5. Then, as detailed in Section 7.6, the contact geometry mappings are prepared by finding for each contactor point the corresponding target point. Finally, the contact residual vectors and tangent matrices are assembled, as detailed in Section 7.7.

7.4.1 Linear System Block Structure

The finite element assembly procedures yield a block linear system to be solved for the optimal increments with which to update the approximate solutions of the mechanical and thermal problems. The block structure of the stiffness matrix and the residual and solution vectors is due to the choice of the finite element shape functions. The shape functions $\boldsymbol{\phi}_i^{\boldsymbol{\varphi}}$, $\boldsymbol{\phi}_i^{\mathrm{ref},\Theta}$, and ϕ_i^{θ}, with which the mechanical and thermal solution fields are discretised, are such that the support of each function is completely contained within one body. That is to say if a shape function is nonzero anywhere on the contactor then it is

zero everywhere on the target. For any $\boldsymbol{X} \in \Omega^{\text{con}}$, if $\boldsymbol{\phi}_i^{\varphi}(\boldsymbol{X}) \neq 0$, then for all $\boldsymbol{Y} \in \Omega^{\text{tar}}$, $\boldsymbol{\phi}_i^{\varphi}(\boldsymbol{Y}) = 0$; and vice versa. The analogous statements also hold for $\boldsymbol{\phi}_i^{\text{ref},\Theta}$, and ϕ_i^{θ}. This choice arises naturally as the contactor and target meshes are generated independently and the shape functions are constructed from piecewise polynomials on the cells of those meshes. A consequence of this choice is that the increment vector can be divided into two blocks, one corresponding to the target and the other to the contactor.

Each element of the mechanical residual vector and its corresponding row in the mechanical stiffness matrix are given by one instance of the linearised residual (6.5.2) with a concrete choice of the test function $\delta\boldsymbol{u}^h$. Similarly, each instance of the linearised thermal residual (6.5.4) with a concrete choice of the thermal test function $\delta\vartheta^h$ gives one element of the thermal residual vector and the corresponding row in the thermal stiffness matrix. As a result, by ordering the test functions in a fashion similar to that of the shape functions, the residual vector can be divided into two blocks corresponding to the contactor and the target.

Thus, the block structure of the linear system is as follows

$$\left[\begin{array}{c|c} \boldsymbol{K}^{\text{con}}_{\text{bulk}} + \boldsymbol{K}^{\text{con}}_{\text{auto}} & \boldsymbol{K}^{\text{con}}_{\text{cross}} \\ \hdashline \boldsymbol{K}^{\text{tar}}_{\text{cross}} & \boldsymbol{K}^{\text{tar}}_{\text{bulk}} + \boldsymbol{K}^{\text{tar}}_{\text{auto}} \end{array}\right] \left[\begin{array}{c} \boldsymbol{U}^{\text{con}} \\ \hdashline \boldsymbol{U}^{\text{tar}} \end{array}\right] = \left[\begin{array}{c} \boldsymbol{r}^{\text{con}}_{\text{bulk}} + \boldsymbol{r}^{\text{con}}_{\text{contact}} \\ \hdashline \boldsymbol{r}^{\text{tar}}_{\text{bulk}} + \boldsymbol{r}^{\text{tar}}_{\text{contact}} \end{array}\right]. \tag{7.4.1}$$

Here, $\boldsymbol{r}^{\text{con}}_{\text{bulk}}$ and $\boldsymbol{r}^{\text{con}}_{\text{contact}}$ are respectively the bulk and contact components of the residual vector (6.5.3), whose entries correspond to the contactor test functions $\delta\boldsymbol{u}_i^{\text{h,con}}$, i.e. the elements of the chosen basis of the functional space of the contactor test functions. Similarly, $\boldsymbol{r}^{\text{tar}}_{\text{bulk}}$ and $\boldsymbol{r}^{\text{tar}}_{\text{contact}}$ are the bulk and contact residuals corresponding to the target test functions $\delta\boldsymbol{u}_i^{\text{h,tar}}$. The increment vector blocks $\boldsymbol{U}^{\text{con}}$ and $\boldsymbol{U}^{\text{tar}}$ correspond respectively to degrees of freedom on the contactor and target discretisations. The bulk components $\boldsymbol{K}^{\text{con}}_{\text{bulk}}$ and $\boldsymbol{K}^{\text{tar}}_{\text{bulk}}$ of the diagonal blocks of the stiffness matrix correspond to the Gateaux derivatives of the contactor and target bulk residual vectors, respectively. The contact components of the stiffness matrix blocks are split into auto-interaction and cross-interaction blocks. The contactor auto-interaction stiffness matrix $\boldsymbol{K}^{\text{con}}_{\text{auto}}$ is assembled from the Gateaux derivatives of the contactor contact residual vector with respect

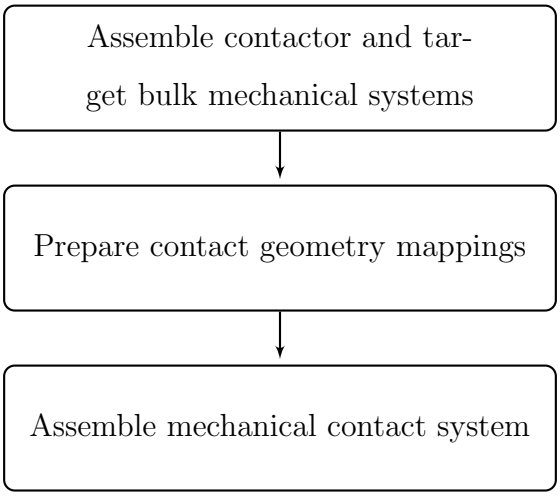

Figure 7.6: Assembly of mechanical linear system

to degrees of freedom on the contactor surface discretisation. This is in contrast to the contactor cross-interaction stiffness matrix $\boldsymbol{K}^{\text{con}}_{\text{cross}}$, which is assembled from the Gateaux derivatives with respect to degrees of freedom on the target surface discretisation. Similarly, the target auto- and cross-interaction stiffness matrix blocks $\boldsymbol{K}^{\text{tar}}_{\text{auto}}$ and $\boldsymbol{K}^{\text{tar}}_{\text{cross}}$ are assembled from the Gateaux derivatives of the target contact residual components with respect to degrees of freedom on the target and contactor surface discretisations, respectively.

7.5 Bulk Mechanical System Assembly

Assembly of the bulk part of the residual vectors and tangent matrices is performed by iteration over the cells. At each cell, a local cell residual $\boldsymbol{r}^{\text{e}}_{\text{bulk}}$ and tangent matrix $\boldsymbol{K}^{\text{e}}_{\text{bulk}}$ are computed, and these are assembled into the global system bulk residual and tangent matrix blocks.

At each cell, two loops over the quadrature points are completed. In the first loop over the quadrature points, the coefficients $\int_{\Omega^{\text{e}}} \phi^{\text{p}}_j \, J^h \, \mathrm{d}\Omega$ are computed, which are used

Algorithm 7.4.1 Solving mechanical step

1: `contact_constraints_are_satisfied` $\leftarrow$ `false`

2: **while** `contact_constraints_are_satisfied` $=$ `false` **do**

3: Assemble mechanical bulk and contact systems to update residuals $\boldsymbol{r}^{\mathrm{con}}_{\mathrm{contact}}$, $\boldsymbol{r}^{\mathrm{con}}_{\mathrm{bulk}}$,$\boldsymbol{r}^{\mathrm{tar}}_{\mathrm{contact}}$, $\boldsymbol{r}^{\mathrm{tar}}_{\mathrm{bulk}}$ and tangents $\boldsymbol{K}^{\mathrm{con}}_{\mathrm{bulk}}$, $\boldsymbol{K}^{\mathrm{tar}}_{\mathrm{bulk}}$, $\boldsymbol{K}^{\mathrm{con}}_{\mathrm{auto}}$, $\boldsymbol{K}^{\mathrm{con}}_{\mathrm{cross}}$, $\boldsymbol{K}^{\mathrm{tar}}_{\mathrm{auto}}$, $\boldsymbol{K}^{\mathrm{tar}}_{\mathrm{cross}}$

4: **while** $\sqrt{\left(\boldsymbol{r}^{\mathrm{con}}_{\mathrm{bulk}} + \boldsymbol{r}^{\mathrm{con}}_{\mathrm{contact}}\right)^2 + \left(\boldsymbol{r}^{\mathrm{tar}}_{\mathrm{bulk}} + \boldsymbol{r}^{\mathrm{tar}}_{\mathrm{contact}}\right)^2} \geq \epsilon_{\mathrm{mech}}$ **do**

5: Solve mechanical linear system for full updates $\Delta\boldsymbol{U}^{\mathrm{con}}$ and $\Delta\boldsymbol{U}^{\mathrm{tar}}$

6: Set line search step size $\alpha_{\mathrm{L}} \leftarrow 1$

7: **while** `line_search_condition_is_met` $=$ `false` **do**

8: Update mechanical fields $\boldsymbol{U}^{\mathcal{B}} \leftarrow \boldsymbol{U}^{\mathcal{B}} + \alpha_{\mathrm{L}}\Delta\boldsymbol{U}^{\mathcal{B}}$, $\mathcal{B} \in \{\mathrm{con}, \mathrm{tar}\}$

9: Assemble mechanical bulk and contact systems to update the residuals

10: Update line search step size $\alpha_{\mathrm{L}} \leftarrow \frac{1}{2}\alpha_{\mathrm{L}}$

11: Update `line_search_condition_is_met`

12: **end while**

13: Assemble mechanical bulk and contact systems to update residuals and tangents

14: **end while**

15: Assemble mechanical contact system to update augmented Lagrangian contact forces $\boldsymbol{f}^{(l+1)}_{\mathrm{T}}$, $\boldsymbol{f}^{(l+1)}_{\mathrm{N}}$ and residuals $\boldsymbol{r}^{\mathrm{con}}_{\mathrm{AL}}$, $\boldsymbol{r}^{\mathrm{tar}}_{\mathrm{AL}}$ and to re-evaluate whether `contact_constraints_are_satisfied`

16: **end while**

to compute value and tangent of the projection of the deformation Jacobian onto the subspace spanned by $\{\phi_j^{\mathrm{p}}\}$. The second loop over the quadrature points computes the integrals to assemble the cell residual vector and tangent matrix. This requires the stress deviator $\operatorname{dev}\boldsymbol{\tau}_{n+1}$, which is computed in terms of a trial left Cauchy-Green elastic tensor $\boldsymbol{b}_{n+1}^{\mathrm{e,trial}}$ using a predictor-corrector approach as described in Subsection 6.1.1. This part of the implementation is described next.

Algorithm 7.5.1 Assembly of Mechanical Bulk System

1: Loop over quadrature points to compute coefficients of projection of the following fields onto the subspace spanned by $\{\phi_i^{\mathrm{p}}\}_{i=1}^{N_{\mathrm{DoF}}^{\mathrm{p}}}$:
   a: The deformation Jacobian J and the temperature θ
   b: For each mechanical DoF j: $\operatorname{tr}\left[\left(\operatorname{Grad}\boldsymbol{\phi}_j^{\boldsymbol{\varphi}}\right)\boldsymbol{F}_c^{-1}\right]$ and $J\operatorname{tr}\left[\left(\operatorname{Grad}\boldsymbol{\phi}_j^{\boldsymbol{\varphi}}\right)\boldsymbol{F}_c^{-1}\right]$
   c: For each pair of mechanical DoF's j and k: $\operatorname{tr}\left[\left(\operatorname{Grad}\boldsymbol{\phi}_j^{\boldsymbol{\varphi}}\right)\boldsymbol{F}_c^{-1}\left(\operatorname{Grad}\boldsymbol{\phi}_k^{\boldsymbol{\varphi}}\right)\boldsymbol{F}_c^{-1}\right]$
2: **for** quadrature point $\boldsymbol{X}_q$, $1 \leq q \leq N^{\mathrm{QP}}$ **do**
3: From the coefficients computed in Step 1, compute the projected Jacobian $\bar{J}$ and temperature $\bar{\theta}$ using (6.4.5)
4: Compute $\boldsymbol{X}'$ from the increment $\Delta\boldsymbol{X}_{n+1} \coloneqq \int_{t_n}^{t_{n+1}} \mathcal{M}_\tau^{t_{n+1}}\{\boldsymbol{V}\}\,\mathrm{d}\tau$ using (6.1.62)
5: Using (6.1.61) compute $\boldsymbol{B}_{n+1}^{\mathrm{e,trial}}$, and compute $\boldsymbol{b}_{n+1}^{\mathrm{e,trial}}$ from (6.1.59)
6: From $\boldsymbol{b}_{n+1}^{\mathrm{e,trial}}$, $\mathcal{M}_{t_n}^{t_{n+1}}\{\alpha\}$ and θ_{n+1}, compute the stress deviator $\operatorname{dev}\boldsymbol{\tau}_{n+1}^h$ using the return mapping algorithm described in Subsection 7.5.2
7: From the projected Jacobian $\bar{J}_{n+1}$ and the projected temperature $\bar{\theta}_{n+1}$, compute the pressure $\bar{p}_{n+1}^{\mathrm{h}}$
8: Compute the inertial component of the residual from (6.4.8)
9: Update the cell residual $\boldsymbol{r}_{\mathrm{bulk}}^{\mathrm{e}}$ and tangent matrix $\boldsymbol{K}_{\mathrm{bulk}}^{\mathrm{e}}$
10: **end for**
11: Accumulate the local residual vector and tangent matrix onto their global counterparts

7.5.1 Trial Elastic Deformation Tensor

The trial left Cauchy-Green elastic tensor $\boldsymbol{b}_{n+1}^{\mathrm{e,trial}}$ is given by (6.1.59) and (6.1.61) in terms of the deformation gradient $\boldsymbol{F}_{\mathrm{c},n+1}$ and the reference motion increment gradient $\operatorname{Grad}\hat{\boldsymbol{X}}_{n+1}$, and in terms of $\boldsymbol{B}_n^{\mathrm{e}}|_{\hat{\boldsymbol{X}}_{n+1}}$. The deformation gradient $\boldsymbol{F}_{\mathrm{c}} = \frac{\partial \boldsymbol{x}}{\partial \boldsymbol{X}}$ is obtained by differentiation of both the current and reference positions with respect to the cylindrical coordinates. Due to the axisymmetry assumption, it is only needed on the plane with $\Theta = 0$, where it is given by

$$\boldsymbol{F}_{\mathrm{c}}|_{\Theta=0} = \begin{bmatrix} 1+\frac{\partial r}{\partial R} & 0 & \frac{\partial r}{\partial Z} \\ 0 & 1+\frac{r}{R} & 0 \\ \frac{\partial z}{\partial R} & 0 & 1+\frac{\partial z}{\partial Z} \end{bmatrix} . \tag{7.5.1}$$

Similarly, the incremental material motion gradient $\operatorname{Grad}\boldsymbol{X}'$ is given for $\Theta = 0$ by

$$\operatorname{Grad}\hat{\boldsymbol{X}}\Big|_{\Theta=0} = \begin{bmatrix} \frac{\partial \hat{R}}{\partial R}\cos\hat{\Theta} - \hat{R}\frac{\partial \hat{\Theta}}{\partial R}\sin\hat{\Theta} & -\frac{\hat{R}}{R}\sin\hat{\Theta} & \frac{\partial \hat{R}}{\partial Z}\cos\hat{\Theta} - \hat{R}\frac{\partial \hat{\Theta}}{\partial Z}\sin\hat{\Theta} \\ \frac{\partial \hat{R}}{\partial R}\sin\hat{\Theta} + \hat{R}\frac{\partial \hat{\Theta}}{\partial R}\cos\hat{\Theta} & \frac{\hat{R}}{R}\cos\hat{\Theta} & \frac{\partial \hat{R}}{\partial Z}\sin\hat{\Theta} + \hat{R}\frac{\partial \hat{\Theta}}{\partial Z}\cos\hat{\Theta} \\ \frac{\partial \hat{Z}}{\partial R} & 0 & \frac{\partial \hat{Z}}{\partial Z} \end{bmatrix} . \tag{7.5.2}$$

The tensor $\boldsymbol{B}_n^{\mathrm{e}}|_{\hat{\boldsymbol{X}}_{n+1}}$ at $\hat{\boldsymbol{X}}_{n+1}$, which has the cylindrical coordinates $(\hat{R}, \hat{\Theta}, \hat{Z})$, is also needed for computing the trial left Cauchy-Green elastic tensor $\boldsymbol{b}_{n+1}^{\mathrm{e,trial}}$ through (6.1.61). Available from the remapping process carried out at the start of each time step $n+1$ is $\boldsymbol{B}_n^{\mathrm{e}}|_{\tilde{\boldsymbol{X}}_{n+1}}$ at $\tilde{\boldsymbol{X}}_{n+1}$, which has the cylindrical coordinates $(\hat{R}, 0, \hat{Z})$. The values of $\boldsymbol{B}_n^{\mathrm{e}}$ at the two points are related by the rotational symmetry assumption. We consider any two vectors $\boldsymbol{v} = v_i\hat{\boldsymbol{e}}_i$ and $\boldsymbol{w} = w_i\hat{\boldsymbol{e}}_i$ and their rotated counterparts

$$\boldsymbol{v}_{\mathrm{rot}} = v_1\hat{\boldsymbol{e}}_R + v_2\hat{\boldsymbol{e}}_\Theta + v_3\hat{\boldsymbol{e}}_Z \,, \tag{7.5.3}$$

$$\boldsymbol{w}_{\mathrm{rot}} = w_1\hat{\boldsymbol{e}}_R + w_2\hat{\boldsymbol{e}}_\Theta + w_3\hat{\boldsymbol{e}}_Z \,, \tag{7.5.4}$$

where the unit vectors of the cylindrical coordinate frame are given in terms of the

Cartesian unit vectors by

$$\hat{\boldsymbol{e}}_R = \hat{\boldsymbol{e}}_1 \cos\hat{\Theta} + \hat{\boldsymbol{e}}_2 \sin\hat{\Theta}\,, \tag{7.5.5a}$$

$$\hat{\boldsymbol{e}}_\Theta = -\hat{\boldsymbol{e}}_1 \sin\hat{\Theta} + \hat{\boldsymbol{e}}_2 \cos\hat{\Theta}\,, \tag{7.5.5b}$$

$$\hat{\boldsymbol{e}}_Z = \hat{\boldsymbol{e}}_3\,. \tag{7.5.5c}$$

Substitution of (7.5.5) into (7.5.3) and using $v_i = \hat{\boldsymbol{e}}_i \cdot \boldsymbol{v}$ gives

$$\begin{aligned}
\boldsymbol{v}_{\text{rot}} =& v_1 \left(\hat{\boldsymbol{e}}_1 \cos\hat{\Theta} + \hat{\boldsymbol{e}}_2 \sin\hat{\Theta}\right) + v_2 \left(-\hat{\boldsymbol{e}}_1 \sin\hat{\Theta} + \hat{\boldsymbol{e}}_2 \cos\hat{\Theta}\right) + v_3 \hat{\boldsymbol{e}}_3 \\
=& \left(\hat{\boldsymbol{e}}_1 \cdot \boldsymbol{v}\right) \left(\hat{\boldsymbol{e}}_1 \cos\hat{\Theta} + \hat{\boldsymbol{e}}_2 \sin\hat{\Theta}\right) \\
&+ \left(\hat{\boldsymbol{e}}_2 \cdot \boldsymbol{v}\right) \left(-\hat{\boldsymbol{e}}_1 \sin\hat{\Theta} + \hat{\boldsymbol{e}}_2 \cos\hat{\Theta}\right) \\
&+ \left(\hat{\boldsymbol{e}}_3 \cdot \boldsymbol{v}\right) \hat{\boldsymbol{e}}_3 \\
=& \cos\hat{\Theta} \left(\hat{\boldsymbol{e}}_1 \otimes \hat{\boldsymbol{e}}_1\right) \boldsymbol{v} + \sin\hat{\Theta} \left(\hat{\boldsymbol{e}}_1 \otimes \hat{\boldsymbol{e}}_2\right) \boldsymbol{v} \\
&- \sin\hat{\Theta} \left(\hat{\boldsymbol{e}}_2 \otimes \hat{\boldsymbol{e}}_1\right) \boldsymbol{v} + \cos\hat{\Theta} \left(\hat{\boldsymbol{e}}_2 \otimes \hat{\boldsymbol{e}}_2\right) \boldsymbol{v} \\
&+ \left(\hat{\boldsymbol{e}}_3 \otimes \hat{\boldsymbol{e}}_3\right) \boldsymbol{v} \\
=& \boldsymbol{R}_{\hat{\Theta}} \boldsymbol{v}\,,
\end{aligned} \tag{7.5.6}$$

where

$$\begin{aligned}
\boldsymbol{R}_{\hat{\Theta}} =& \cos\hat{\Theta} \left(\hat{\boldsymbol{e}}_1 \otimes \hat{\boldsymbol{e}}_1\right) + \sin\hat{\Theta} \left(\hat{\boldsymbol{e}}_1 \otimes \hat{\boldsymbol{e}}_2\right) \\
&- \sin\hat{\Theta} \left(\hat{\boldsymbol{e}}_2 \otimes \hat{\boldsymbol{e}}_1\right) + \cos\hat{\Theta} \left(\hat{\boldsymbol{e}}_2 \otimes \hat{\boldsymbol{e}}_2\right) \\
&+ \left(\hat{\boldsymbol{e}}_3 \otimes \hat{\boldsymbol{e}}_3\right)\,.
\end{aligned} \tag{7.5.7}$$

This rotation tensor $\boldsymbol{R}_{\hat{\Theta}}$ is given in component form in the Cartesian coordinates as

$$\boldsymbol{R}_{\hat{\Theta}} = \begin{bmatrix} \cos\hat{\Theta} & -\sin\hat{\Theta} & 0 \\ \sin\hat{\Theta} & \cos\hat{\Theta} & 0 \\ 0 & 0 & 1 \end{bmatrix}\,. \tag{7.5.8}$$

Similarly, $\boldsymbol{w}_{\text{rot}} = \boldsymbol{R}_{\hat{\Theta}} \boldsymbol{w}$.

By rotational symmetry,

$$\boldsymbol{v}^{\text{t}} (\boldsymbol{B}_n^{\text{e}}|_{\tilde{\boldsymbol{X}}_{n+1}}) \boldsymbol{w} = \boldsymbol{v}_{\text{rot}}^{\text{t}} (\boldsymbol{B}_n^{\text{e}}|_{\hat{\boldsymbol{X}}_{n+1}}) \boldsymbol{w}_{\text{rot}}\,, \tag{7.5.9}$$

which by substitution of $\boldsymbol{v}_{\mathrm{rot}} = \boldsymbol{R}_{\hat{\Theta}}\boldsymbol{v}$ and $\boldsymbol{w}_{\mathrm{rot}} = \boldsymbol{R}_{\hat{\Theta}}\boldsymbol{w}$ gives

$$\boldsymbol{B}^{\mathrm{e}}_{n}|_{\hat{\boldsymbol{X}}_{n+1}} = \boldsymbol{R}_{\Theta}\left(\boldsymbol{B}^{\mathrm{e}}_{n}|_{\tilde{\boldsymbol{X}}_{n+1}}\right)\boldsymbol{R}^{\mathrm{t}}_{\Theta}\,. \tag{7.5.10}$$

7.5.2 Return Mapping

The elasto-viscoplastic stress is computed using a predictor-corrector approach as described in Subsection 6.1.1 with a viscoplastic yield criterion that is a function of the stress deviator, the equivalent plastic strain and its time rate, and the temperature. The stress deviator predictor value $\operatorname{dev}\boldsymbol{\tau}^{\mathrm{h,trial}}_{n+1}$ is computed from the trial elastic deformation tensor $\boldsymbol{b}^{\mathrm{e,trial}}_{n+1}$ by (6.1.34). This value is then used to compute the trial yield criterion (6.1.25e) as

$$\begin{aligned}\phi^{\mathrm{trial}}_{n+1} &= \left\|\operatorname{dev}\boldsymbol{\tau}^{\mathrm{h,trial}}_{n+1}\right\| - \sqrt{\frac{2}{3}}\sigma^{y}(\alpha^{\mathrm{trial}}_{n+1}, \dot{\alpha}^{\mathrm{trial}}_{n+1}, \theta^{\mathrm{h}}_{n+1}) \\ &= \left\|\operatorname{dev}\boldsymbol{\tau}^{\mathrm{h,trial}}_{n+1}\right\| - \sqrt{\frac{2}{3}}\sigma^{y}(\alpha_{n}, 0, \theta^{\mathrm{h}}_{n+1})\,,\end{aligned} \tag{7.5.11}$$

where the equivalent plastic strain is assumed to remain unchanged from the previous time step: $\alpha^{\mathrm{trial}}_{n+1} = \alpha_n$, and its time rate $\dot{\alpha}^{\mathrm{trial}}_{n+1}$ is assumed to vanish.

If the trial yield criterion is within the admissible range $\phi^{\mathrm{trial}}_{n+1} \leq 0$, then the trial stress deviator is accepted: $\operatorname{dev}\boldsymbol{\tau}^{\mathrm{h}}_{n+1} = \operatorname{dev}\boldsymbol{\tau}^{\mathrm{h,trial}}_{n+1}$. Otherwise, a corrector step is carried out by solving (6.1.37) for $\Delta\lambda$, such that the corrected stress deviator is obtained from (6.1.33) as

$$\operatorname{dev}\boldsymbol{\tau}^{\mathrm{h}}_{n+1} = \operatorname{dev}\boldsymbol{\tau}^{\mathrm{h,trial}}_{n+1} - 2\mu\Delta\lambda\,\frac{\operatorname{dev}\boldsymbol{\tau}^{\mathrm{h,trial}}_{n+1}}{\left\|\operatorname{dev}\boldsymbol{\tau}^{\mathrm{h,trial}}_{n+1}\right\|}\,. \tag{7.5.12}$$

Implementation of a thermo-viscoplasticity constitutive model consists of four functions. Given the equivalent plastic strain α, its time rate $\dot{\alpha}$, and the temperature θ, the first function computes the yield stress $\sigma^{\mathrm{y}} = \sigma^{\mathrm{y}}(\alpha, \dot{\alpha}, \theta)$. The remaining three functions give the partial derivatives of the yield stress with respect to its three parameters: $\frac{\partial\sigma^{\mathrm{y}}}{\partial\alpha}$, $\frac{\partial\sigma^{\mathrm{y}}}{\partial\dot{\alpha}}$, and $\frac{\partial\sigma^{\mathrm{y}}}{\partial\theta}$.

Solution for $\Delta\lambda$ is performed by applying Newton's method to equation (6.1.37). The residual is defined as

$$r(\Delta\lambda) = \left\|\operatorname{dev}\boldsymbol{\tau}_{n+1}^{\text{trial}}\right\| - 2\mu\Delta\lambda - \sqrt{\frac{2}{3}}\sigma_{n+1}^{y}\,, \tag{7.5.13}$$

where

$$\sigma_{n+1}^{y} = \sigma^{y}\left(\alpha_{n+1}, \dot{\alpha}_{n+1}, \theta_{n+1}\right)\,, \tag{7.5.14}$$

$$\alpha_{n+1} = \alpha_n + \sqrt{\frac{2}{3}}\Delta\lambda\,, \tag{7.5.15}$$

$$\dot{\alpha}_{n+1} = \sqrt{\frac{2}{3}}\frac{\Delta\lambda}{\Delta t}\,. \tag{7.5.16}$$

The derivative of the residual is

$$\begin{aligned} r'(\Delta\lambda) &= -2\mu - \sqrt{\frac{2}{3}}\frac{\partial\sigma^{\mathrm{y}}}{\partial\alpha}\frac{\partial\alpha}{\partial\Delta\lambda} - \sqrt{\frac{2}{3}}\frac{\partial\sigma^{\mathrm{y}}}{\partial\dot{\alpha}}\frac{\partial\dot{\alpha}}{\partial\Delta\lambda} \\ &= -2\mu - \frac{2}{3}\frac{\partial\sigma^{\mathrm{y}}}{\partial\alpha} - \frac{1}{\Delta t}\frac{2}{3}\frac{\partial\sigma^{\mathrm{y}}}{\partial\dot{\alpha}}\,. \end{aligned} \tag{7.5.17}$$

Solution for $\Delta\lambda$ is then done by iteratively updating it to

$$\Delta\lambda \leftarrow \Delta\lambda - \frac{r(\Delta\lambda)}{r'(\Delta\lambda)}\,, \tag{7.5.18}$$

until the residual $r(\Delta\lambda)$ is smaller than a predefined threshold.

7.6 Contact Geometry Preparation

The bodies at the two ends of a contact surface are designated as a contactor and a target, and the integrals for the weak form of the contact conditions are evaluated on the contactor surface. Thus, the contact residual vectors and tangent matrices are computed by accumulating values at the quadrature points on cell faces on the contactor surface. To this end, the mapping between the contactor points, which are the quadrature points on the contactor surface, and their corresponding target points is first constructed.

The quadrature points on the contactor surface are designated as the contactor points. Their positions in the reference configuration remain fixed throughout the simulation. At each time step $n+1$, based on the deformations of the contactor and target surfaces $\boldsymbol{\varphi}^{\mathrm{con}}_{n+1}$ and $\boldsymbol{\varphi}^{\mathrm{tar}}_{n+1}$, each contactor point $\boldsymbol{X}$ is assigned a target point $\boldsymbol{Y}^{\mathrm{tar}}_{n+1} \coloneqq \boldsymbol{\eta}_{n+1}(\boldsymbol{X})$. This is done by an iterative search on each of the candidate cell faces on the target. Each iteration is a Newton step, where an increment to $\boldsymbol{Y}^{\mathrm{tar}}_{n+1}$ is computed by linearizing the surface using its tangent plane.

The domains of the contactor and the target are split into subsets that are computed by separate parallel computing processes. Therefore, a contactor point and its corresponding target point may be owned by separate processes.

To compute the target point $\boldsymbol{Y}_{n+1} \coloneqq \boldsymbol{\eta}_{n+1}(\boldsymbol{X})$ corresponding to a given contactor point $\boldsymbol{X}$, the position in the current configuration $\boldsymbol{x}_{n+1} \coloneqq \boldsymbol{\varphi}^{\mathrm{con}}_{n+1}(\boldsymbol{X})$ of the contactor point is sent to all the processes. For each process that owns any target surface faces, a search is carried out within the subset of the target surface that is owned by the process for the nearest point in the current configuration to $\boldsymbol{x}_{n+1}$. In each such process, a candidate target point is thus computed, and these candidate target points are sent to the contactor owning process. The contactor owning process then selects from the received candidate target points the one that is nearest to $\boldsymbol{x}_{n+1}$, and thus forms a contactor-target point pair and adds it to the geometric mapping. The contactor owning process also sends a message to the process that owns the chosen target point so that the target-contactor point pair is added to the contact geometry mapping there.

The resulting mapping has the form of two arrays in each process: one array of contactor points and another of target points. Either or both of these arrays may be empty, or they may be of arbitrary lengths, but the sums of their lengths over all the processes equal the total number of contactor points, that is the total number of quadrature points on the contactor surface.

Each entry in the array of contactor points stores data about the contactor point, includ-

ing its positions in the reference and current configurations, and identifiers pointing to the mesh cell and cell face to which it belongs. In addition, each entry in the contactor point array also contains two indices that point to the corresponding target point. These are the index of the target owning process, and the index of the target point entry in the target point array. Similarly, each entry in the array of target points stores data about the target point as well as indices that point to the corresponding contactor point.

7.7 Contact Mechanical System Assembly

The contact terms of the residual vectors and tangent matrix blocks are assembled by accumulating the local residual vectors and tangent matrices at the contactor and target points. At each contactor point, a local residual vector is computed to be assembled into the relevant degrees of freedom of the contactor contact residual vector $\boldsymbol{r}^{\text{con}}_{\text{contact}}$, and two local tangent matrices are computed to be assembled into the contactor contact auto- and cross-interaction matrices $\boldsymbol{K}^{\text{con}}_{\text{auto}}$ and $\boldsymbol{K}^{\text{con}}_{\text{cross}}$. Similarly, at each target point, a local residual vector and local auto- and cross- interaction tangent matrices are computed to be assembled respectively into $\boldsymbol{r}^{\text{tar}}_{\text{contact}}$, $\boldsymbol{K}^{\text{tar}}_{\text{auto}}$ and $\boldsymbol{K}^{\text{tar}}_{\text{cross}}$.

The distributed memory parallel implementation means that the contactor point and its corresponding target point may be owned by different processes. It is therefore necessary to exchange information between the two owning processes to construct the components of the residual vector and the stiffness matrix.

The assembly procedure, which is described in Algorithm 7.7.1 is implemented as two loops over the contactor and target points. In the first loop, the relevant variables are sent from each contactor point to the corresponding target owning process, and from each target point to the corresponding contactor owning process. In the second loop, the local variables are used along with the received variables to compute the local residual vectors and tangent matrices.

Algorithm 7.7.1 Assembly of Mechanical Contact System at Time Step $n+1$ at Augmented Lagrangian Step $l+1$

1: loop over `contactor_points` and `target_points` to exchange information necessary for computing of contact forces and their tangents
2: **for** `contactor_point` in `contactor_points` **do**
3: From the `contactor_point` position $\boldsymbol{x} = \boldsymbol{\varphi}_{n+1}^{\mathrm{con}}\big|_{\boldsymbol{X}}$ and the `target_point` position $\boldsymbol{y} = \boldsymbol{\varphi}_{n+1}^{\mathrm{tar}}\big|_{\boldsymbol{Y}}$ compute the penetration $\boldsymbol{g} = \boldsymbol{x} - \boldsymbol{y}$
4: Compute the augmented Lagrangian contact normal force $\boldsymbol{f}_{\mathrm{N}}^{\mathrm{c}(l+1)} = \boldsymbol{f}_{\mathrm{N}}^{\mathrm{c}(l)} + \mu_{\mathrm{N}} \langle \boldsymbol{g} \rangle$
5: From the contactor material velocity (3.3.42) and the target material velocity (3.3.43), compute the slip velocity $\boldsymbol{v}_{\mathrm{s}} = (\mathbf{1} - \boldsymbol{n} \otimes \boldsymbol{n}) (\boldsymbol{v}^{\mathrm{con}} - \boldsymbol{v}^{\mathrm{tar}})$
6: Compute the augmented Lagrangian tangential contact friction force from the slip velocity $\boldsymbol{v}_{\mathrm{s}}$ and (6.3.6).
7: loop over the local degrees of freedom to accumulate contributions to the local residual vector, and over pairs of degrees of freedom to accumulate contributions to the local auto- and cross-interaction tangent matrices
8: Accumulate the local residual vector and auto- and cross-interaction tangent matrices onto their global counterparts
9: **end for**

7.8 Thermal Field Solution

The thermal part of a time step, in which the temperature field is updated with the motion and reference velocity kept fixed, is completed by a sequence of Newton-Raphson steps. Each Newton step consists of assembly and solution of a linear system followed by a line search procedure to compute an update to the approximate solution. The high-level structure of the thermal part of the time step is given in Algorithm (7.8.1).

The contact geometry mapping constructed in the mechanical part of a time step is also used in assembling the thermal contact residual vectors and tangent matrices.

10: **for** `target_point` in `target_points` **do**

11: From the `contactor_point` position $\boldsymbol{x} = \boldsymbol{\varphi}_{n+1}^{\mathrm{con}}\big|_{\boldsymbol{X}}$ and the `target_point` position $\boldsymbol{y} = \boldsymbol{\varphi}_{n+1}^{\mathrm{tar}}\big|_{\boldsymbol{Y}}$ compute the penetration $\boldsymbol{g} = \boldsymbol{x} - \boldsymbol{y}$

12: Compute the augmented Lagrangian contact normal force $\boldsymbol{f}_{\mathrm{N}}^{\mathrm{c}(l+1)} = \boldsymbol{f}_{\mathrm{N}}^{\mathrm{c}(l)} + \mu_{\mathrm{N}} \langle \boldsymbol{g} \rangle$

13: From the contactor material velocity (3.3.42) and the target material velocity (3.3.43), compute the slip velocity $\boldsymbol{v}_{\mathrm{s}} = (\mathbf{1} - \boldsymbol{n} \otimes \boldsymbol{n}) (\boldsymbol{v}^{\mathrm{con}} - \boldsymbol{v}^{\mathrm{tar}})$

14: Compute the augmented Lagrangian tangential contact friction force from the slip velocity $\boldsymbol{v}_{\mathrm{s}}$ and (6.3.6).

15: loop over the local degrees of freedom to accumulate contributions to the local residual vector, and over pairs of degrees of freedom to accumulate contributions to the local auto- and cross-interaction tangent matrices

16: Accumulate the local residual vector and auto- and cross-interaction tangent matrices onto their global counterparts

17: **end for**

Algorithm 7.8.1 Solving thermal step

1: **while** $\sqrt{(\boldsymbol{r}_{\mathrm{bulk}}^{\mathrm{con}} + \boldsymbol{r}_{\mathrm{contact}}^{\mathrm{con}})^2 + (\boldsymbol{r}_{\mathrm{bulk}}^{\mathrm{tar}} + \boldsymbol{r}_{\mathrm{contact}}^{\mathrm{tar}})^2} \geq \epsilon_{\mathrm{therm}}$ **do**

2: Solve thermal linear system for full updates $\Delta\boldsymbol{\Theta}^{\mathrm{con}}$ and $\Delta\boldsymbol{\Theta}^{\mathrm{tar}}$

3: Set line search step size $\alpha_{\mathrm{L}} \leftarrow 1$

4: **while** `line_search_condition_is_met` = `false` **do**

5: Update thermal fields $\boldsymbol{\Theta}^{\mathcal{B}} \leftarrow \boldsymbol{\Theta}^{\mathcal{B}} + \alpha_{\mathrm{L}} \Delta\boldsymbol{\Theta}^{\mathcal{B}}$, $\mathcal{B} \in \{\mathrm{con}, \mathrm{tar}\}$

6: Assemble thermal bulk and contact systems to update the residuals

7: Update line search step size $\alpha_{\mathrm{L}} \leftarrow \frac{1}{2}\alpha_{\mathrm{L}}$

8: Update `line_search_condition_is_met`

9: **end while**

10: Assemble thermal bulk and contact systems to update residuals and tangents

11: **end while**

Part IV

Benchmark and Application Simulations

8 Benchmark Problems

In this Chapter, the implemented solver is validated using benchmark problems. These are chosen to validate the relevant features of the solver: solution of coupled thermo-mechanical problems, solution of frictional and frictionless contact and contact heat generation and transfer, and the ALE formulation. The benchmark problems used are thermally-triggered necking of a circular bar (Section 8.1), dynamic impact of a circular bar (Section 8.2), and interference fit insertion of a cylinder into a tapered hole (Section 8.3).

8.1 Thermally-Triggered Necking of a Circular Bar

This benchmark problem is used to test finite strain elastoplasticity solvers [139] and coupled finite strain thermoplasticity solvers [82, 140–142]. A tensile test on a circular bar with a radius of 6.4 mm and a height of 106.7 mm is simulated. The bar is elongated by 16 mm. A thermal convection boundary condition is applied to the boundaries with an ambient temperature of 293 K and a convection coefficient of $17.5 \times 10^{-6}\,\mathrm{J/mm^2 \cdot s \cdot K}$. The thermal initial condition is a homogeneous temperature of 293 K. The material parameters used are specified in Table 8.1, where the dissipation factor χ is an empirical quantity that represents mechanical dissipation as a proportion of the total plastic power [82].

parameter	value	unit
Bulk modulus	164 206	$\mathrm{N{\cdot}mm^{-2}}$
Shear modulus	801 938	$\mathrm{N{\cdot}mm^{-2}}$
Flow stress	450	$\mathrm{N{\cdot}mm^{-2}}$
Linear hardening	129.24	$\mathrm{N{\cdot}mm^{-2}}$
Saturation hardening	715	$\mathrm{N{\cdot}mm^{-2}}$
Hardening exponent	16.93	
Density	7.8×10^{-9}	$\mathrm{N{\cdot}mm^{-4}{\cdot}s^{2}}$
Thermal expansion coefficient	1×10^{-5}	$\mathrm{K^{-1}}$
Thermal conductivity	4.5×10^{-2}	$\mathrm{J{\cdot}mm^{-1}{\cdot}s^{-1}{\cdot}K^{-1}}$
Volumetric heat capacity	3.588×10^{-3}	$\mathrm{J{\cdot}mm^{-3}{\cdot}K^{-1}}$
Dissipation factor	0.9	
Flow stress softening	0.002	$\mathrm{K^{-1}}$
Hardening softening	0.002	$\mathrm{K^{-1}}$

Table 8.1: Material parameters for thermally triggered necking benchmark

Rotational symmetry is used to reduce the problem to an axisymmetric one. Mirror symmetry is used to further reduce the problem so that it is only necessary to simulate one quadrant of the bar.

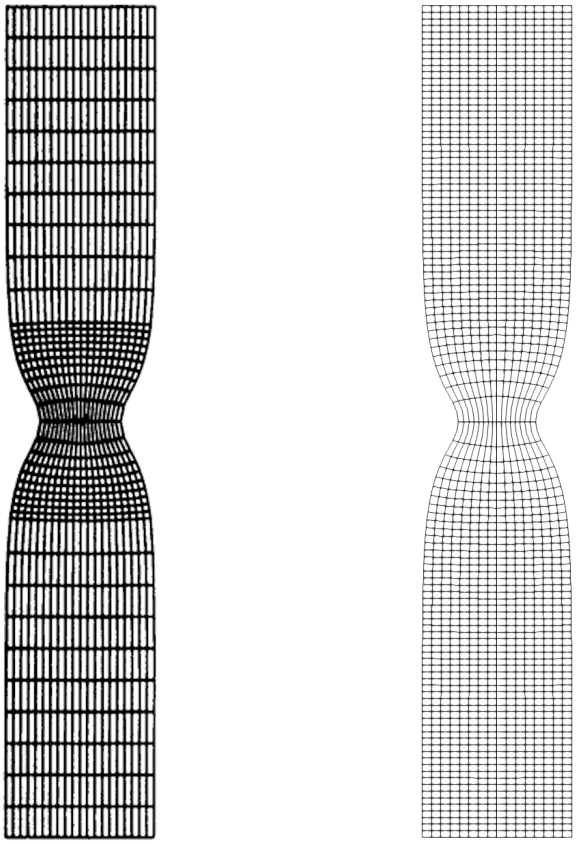

(a) From [82] (b) From current work

Figure 8.1: Thermally triggered necking of a circular bar: Elongation of 14.08 mm

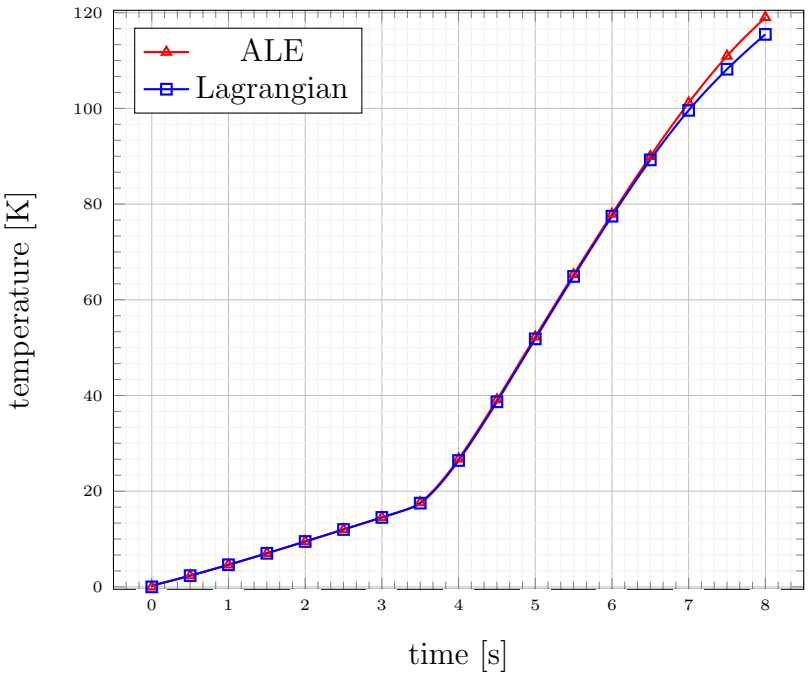

(a) Results from current work

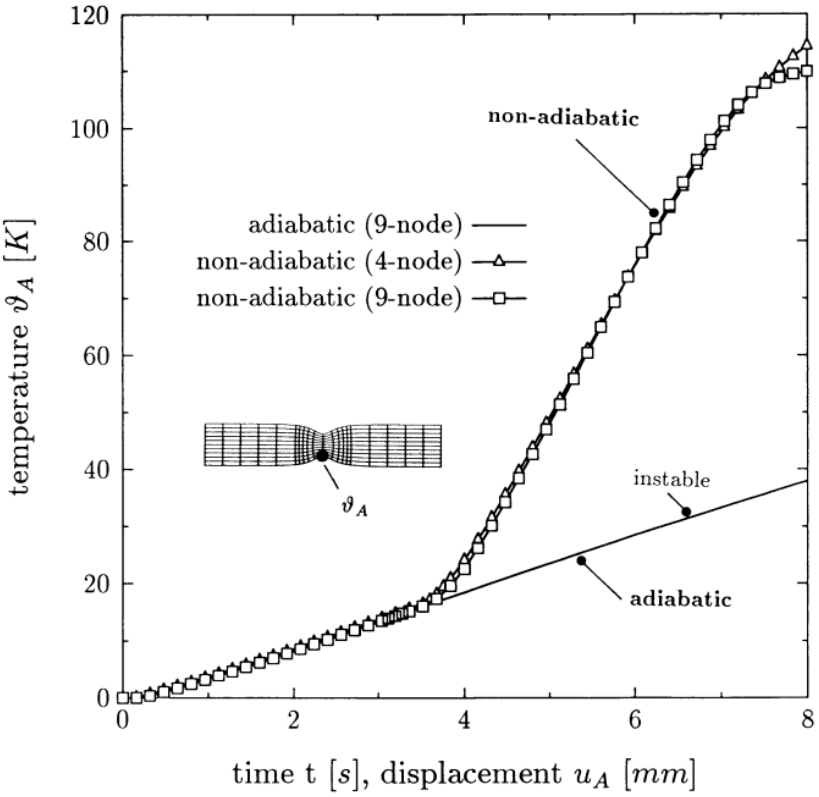

(b) Results from [82]

Figure 8.2: Thermally-triggered necking of a circular bar: Surface temperature increase at the midpoint

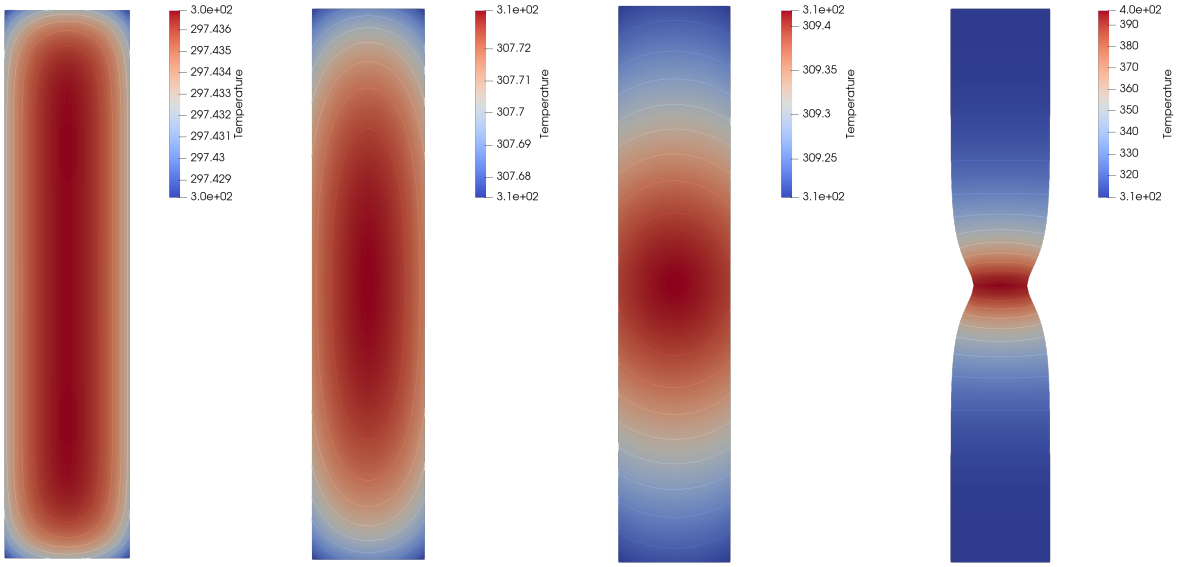

(a) 1.92 mm (b) 6.08 mm (c) 6.72 mm (d) 14.08 mm

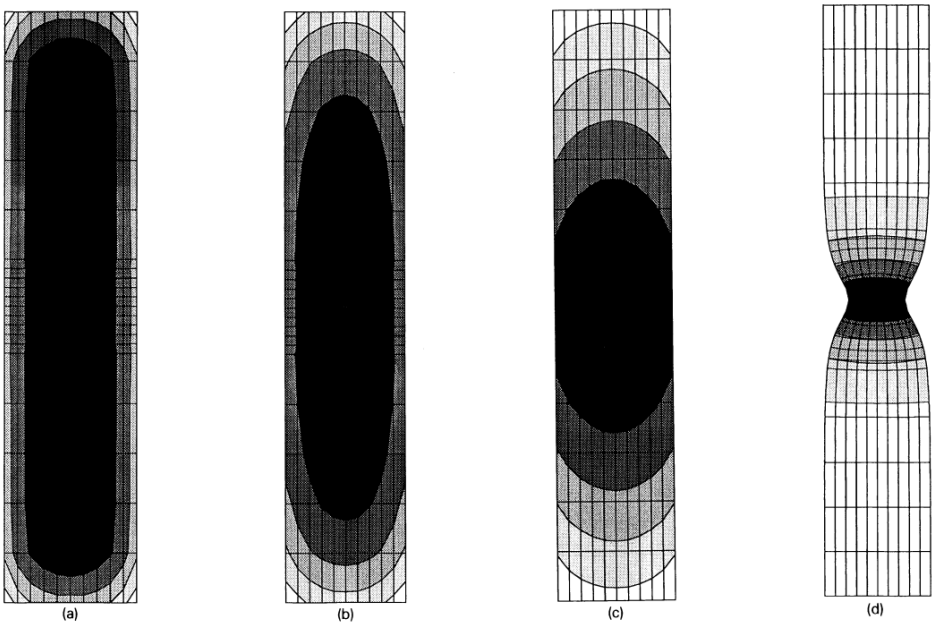

(e) Results at the same elongation values from [82]

Figure 8.3: Thermally triggered necking of a circular bar: Temperature distribution at four elongation values

The outline of the deformed body after elongation by 14.08 mm is shown in Figure 8.1 in comparison to results from [82]. Figure 8.2 shows the increase in surface temperature

at the midpoint from the current work (Figure 8.2a), along with the results reported in [82] (Figure 8.2b). The temperature distribution at different elongation values is shown in Figure 8.3. The deformed configuration, the temperature distributions, and the elongation at the onset of necking are all in good agreement with the benchmark results [82, 142].

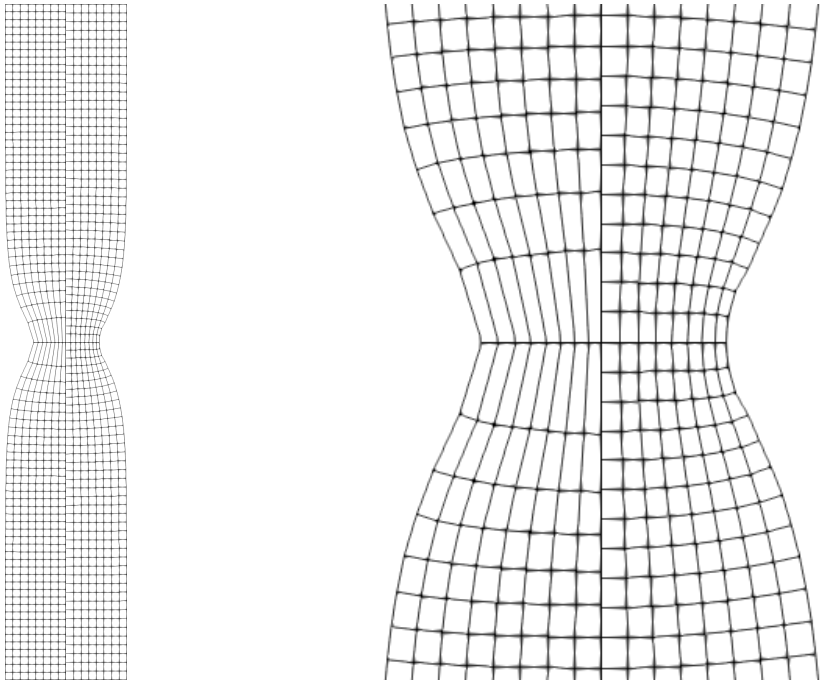

(a) View of entire length (b) View of necking region

Figure 8.4: Thermally triggered necking of a circular bar: Elongation of 14.08 mm. Lagrangian (left of midline) vs ALE (right of midline) formulations.

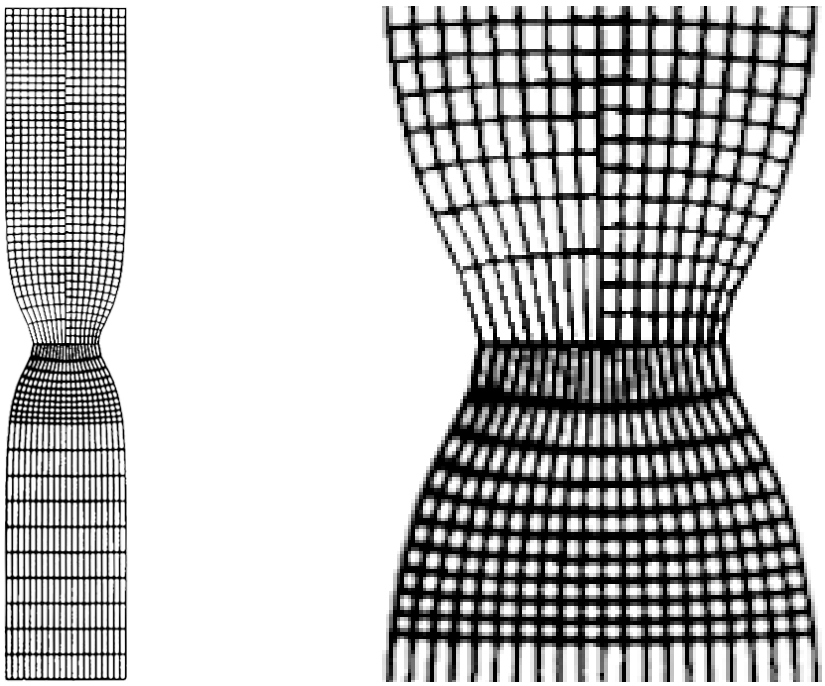

(a) View of entire length (b) View of necking region

Figure 8.5: Thermally triggered necking of a circular bar: Elongation of 14.08 mm. Lagrangian (top-left quarter) and ALE (top-right quarter) formulations compared to results from [82] (bottom half).

This benchmark problem was also used to test the developed ALE formulation. The mesh of the deformed configuration that results when the ALE formulation is employed is compared to that which results when a fully Lagrangian formulation is used. The resulting deformed meshes at an elongation of 14.08 mm are shown on either side of the symmetry axis in Figure 8.4, and are shown in Figure 8.5 alongside the deformed configuration from [82] at the same elongation. In the fully Lagrangian simulation, the cells at the necking region of the current configuration mesh undergo large elongations. In the ALE simulation, in contrast, the current configuration mesh quality at the necking region remains high throughout the weld. Figures 8.6g and 8.6h show the equivalent plastic strain α at the same elongation in the ALE and Lagrangian results, respectively, compared to the results of a simulation run with a fine Lagrangian mesh. Figures 8.6a

and 8.6b show a similar comparison of the temperature distribution. Similarly, comparisons of the pressure and von Mises stress results are shown in Figures 8.6c, 8.6d, 8.6e and 8.6f. In all these comparisons, the ALE simulation produces more accurate results than the Lagrangian simulation with the same initial mesh, where accuracy is evaluated against the results of the simulation run with a fine mesh.

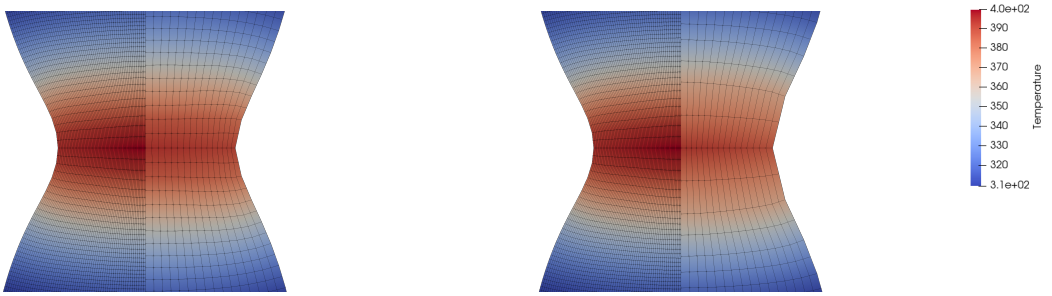

(a) Temperature: ALE formulation

(b) Temperature: Lagrangian

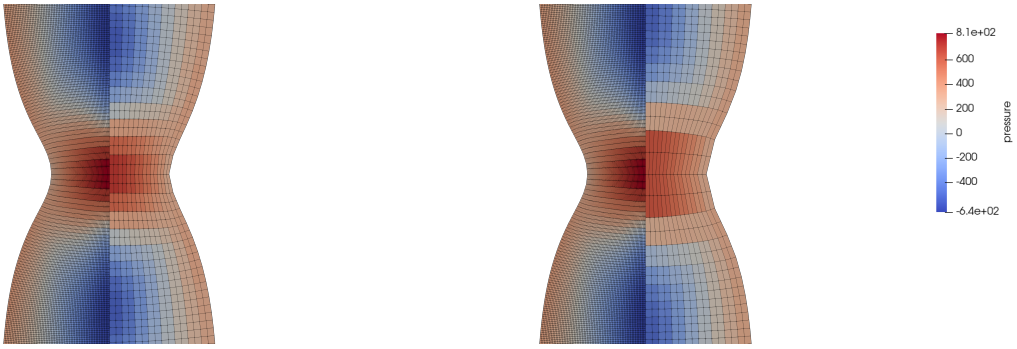

(c) Pressure: ALE Formulation

(d) Pressure: Lagrangian

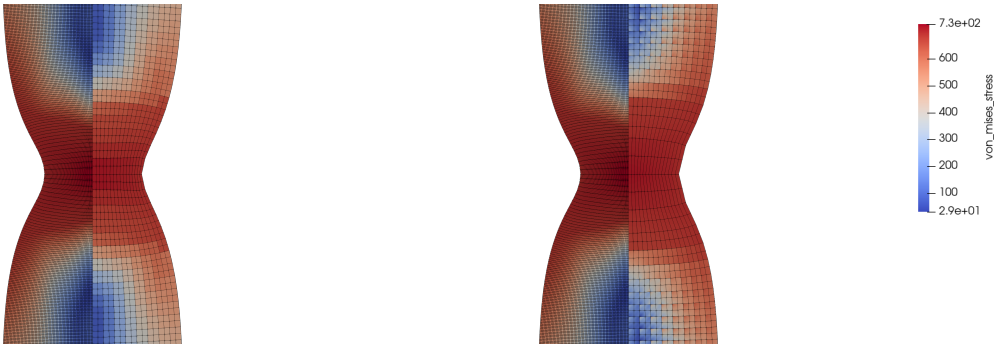

(e) Von Mises stress: ALE formulation

(f) Von Mises stress: Lagrangian

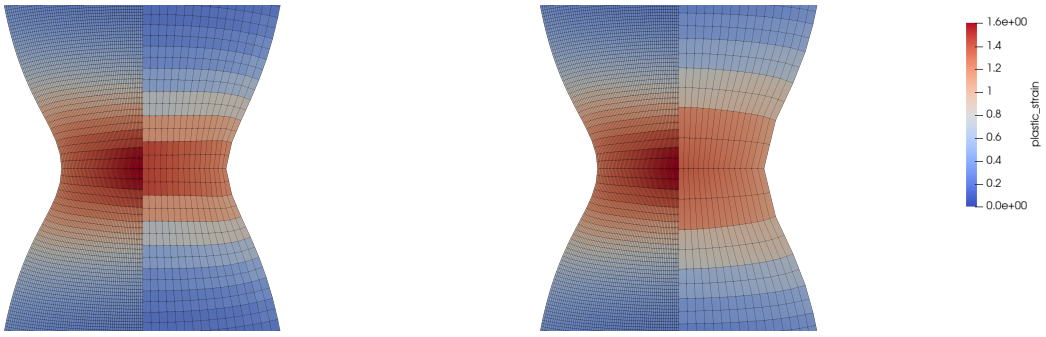

(g) Plastic strain: ALE formulation

(h) Plastic strain: Lagrangian

Figure 8.6: Thermally triggered necking of a circular bar at elongation of 14.08 mm: Comparison of ALE and Lagrangian formulations with fine mesh results

8.1.1 Performance Comparison between ALE and Lagrangian Solvers

Of the total computation time to complete the ALE solution of this benchmark problem, 34.2% was spent on the solution of the mesh motion and remapping of the nodal and quadrature point fields, 61.6% was spent on the solution of the mechanical sub-steps, and 4.2% was spent on the thermal sub-step. The total computation time of the ALE solver was 60% longer than that of the entirely Lagrangian solver, in which 93.9% of the total computation time was spent on the mechanical sub-steps and 6.1% was spent on the thermal sub-steps. As shown in Figure 8.7, there is no significant difference in the number of Newton steps required to solve the mechanical sub-steps when the ALE solution is compared to the entirely Lagrangian solution of this benchmark problem.

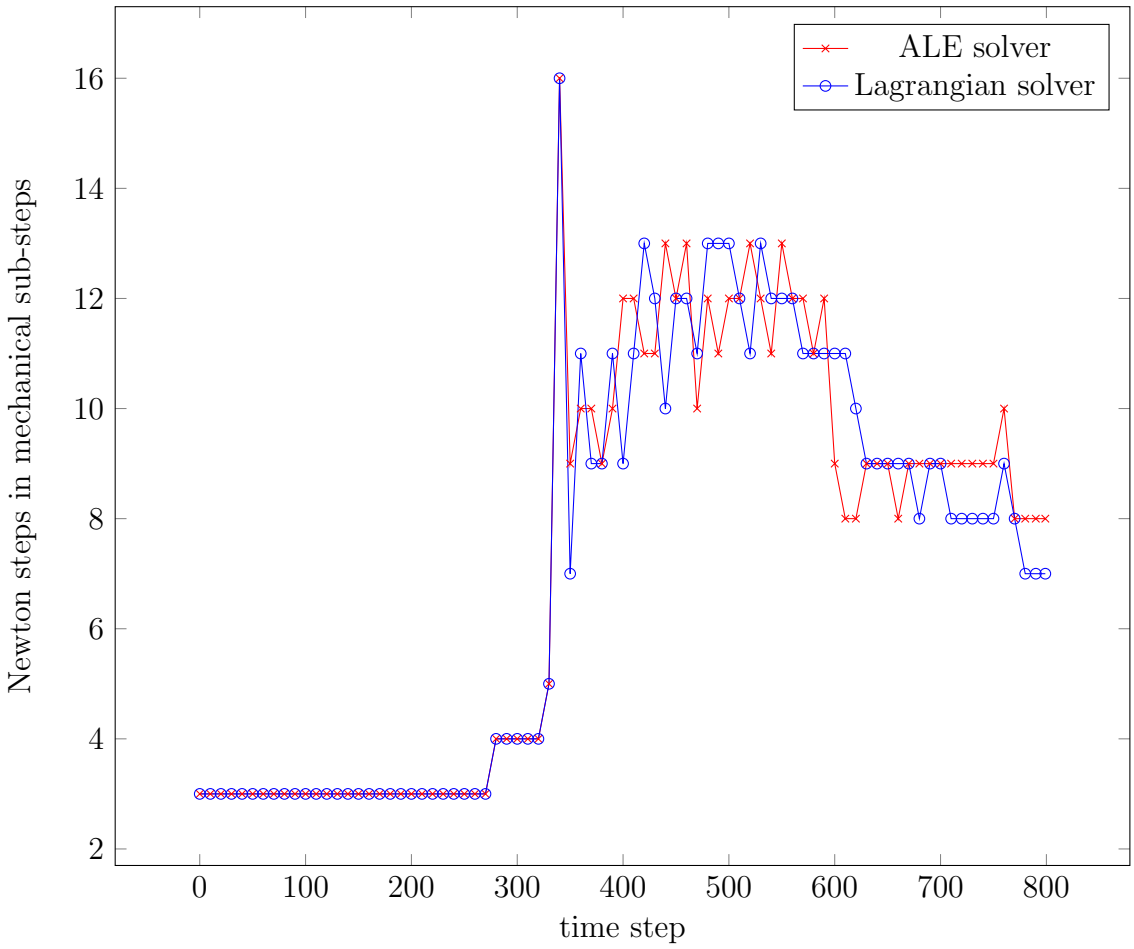

Figure 8.7: Comparison of Newton step counts in ALE vs Lagrangian solutions of mechanical sub-steps in the necking benchmark problem

8.2 Dynamic Impact of a Circular Bar

The Taylor anvil on rod impact test [143] is commonly used for characterisation of dynamic behaviour of metals at elevated temperatures and high strain rates. It is also a useful test in evaluation of dynamic solvers and hydrocodes. Lacy, Novascone, Richins *et al.* [144], for instance, used it as part of a method for software selection for analysis of dynamic events.

parameter	value	unit
Bulk modulus	103 300	$\mathrm{N{\cdot}mm^{-2}}$
Shear modulus	47 690	$\mathrm{N{\cdot}mm^{-2}}$
Johnson-Cook A	89.7	$\mathrm{N{\cdot}mm^{-2}}$
Johnson-Cook B	291.87	$\mathrm{N{\cdot}mm^{-2}}$
Johnson-Cook C	0.025	
Johnson-Cook m	1.09	
Johnson-Cook n	0.31	
Melting temperature	1356	K
Reference strain rate	1	$\mathrm{s^{-1}}$
Density	8.96×10^{-9}	$\mathrm{N{\cdot}mm^{-4}{\cdot}s^{2}}$
Thermal expansion coefficient	1×10^{-5}	$\mathrm{K^{-1}}$
Thermal conductivity	4.5×10^{-2}	$\mathrm{J{\cdot}mm^{-1}{\cdot}s^{-1}{\cdot}K^{-1}}$
Volumetric heat capacity	3.588×10^{-3}	$\mathrm{J{\cdot}mm^{-3}{\cdot}K^{-1}}$
Dissipation factor	0.9	

Table 8.2: Material parameters for dynamic impact of a circular bar

The analysis involves a cylindrical rod with a radius of 3.81 mm and a height of 25.4 mm which is subjected to an impact load by collision with a rigid obstacle at an initial velocity of 1.9×10^5 mm/s. The convective boundary condition at the surface is omitted in this problem, as the duration of the impact is so short that convection heat transfer is negligible. The Johnson-Cook model is used to describe the rod material, with the material parameters listed in Table 8.2.

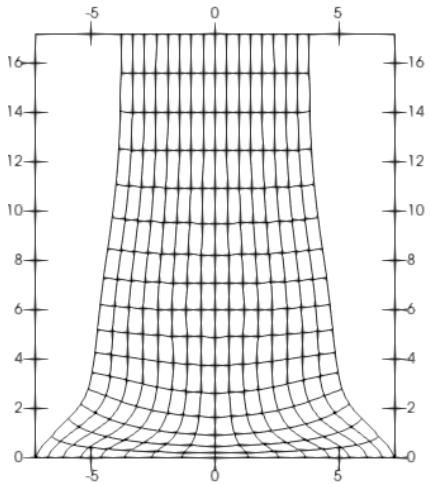

(a) Deformed mesh

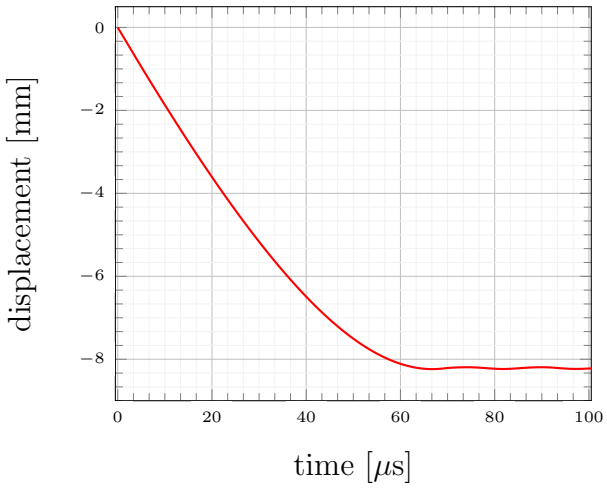

(b) Top displacement

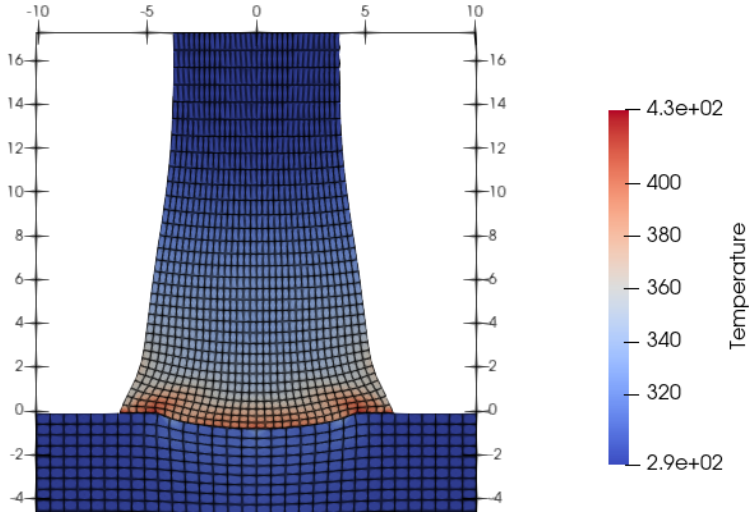

(c) Contact with a deformable obstacle

Figure 8.8: Dynamic impact of a circular bar

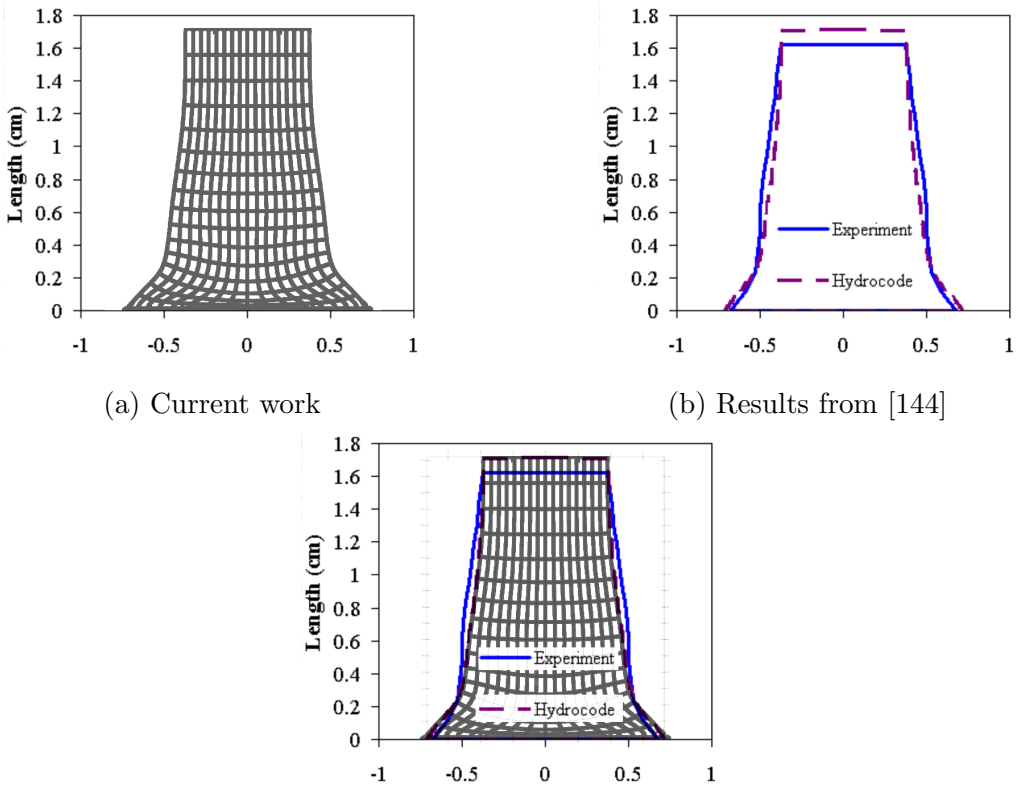

(a) Current work

(b) Results from [144]

(c) Comparison

Figure 8.9: Taylor impact: Final deformation in comparison to experimental and numerical results reported in [144]

The deformed body at the end of the simulation is depicted in Figure 8.8a. In addition, Figure 8.8b shows the vertical position measured at the centre of the upper surface as a function of time. As shown in Figure 8.9c, the final deformation is nearly identical to those produced by ALEGRA, ABAQUS, LS-DYNA and CTH as reported in [144].

In addition to the standard benchmark simulation, which considers impact with a rigid obstacle, the simulation was also carried out with a deformable obstacle that has the same material properties as the rod. This additional test case serves as a test of the capability to resolve contact at high strain rates. The resulting deformed cylindrical rod and obstacle at the end of the simulation are shown in Figure 8.8c.

Finally, the Taylor impact benchmark was used as a test of the ALE formulation in a dynamic problem. Figure 8.10 shows, on either side of the midline, the final deformed configuration meshes that result when the simulation is run with or without the ALE steps, as well as the temperature distribution, the pressure, and the von Mises stress. As expected, the current configuration mesh distortion near the impact region is higher in the Lagrangian simulation than the ALE one. The results of the Lagrangian and ALE simulations of the problem are otherwise closely similar.

Of the total computation time to complete the ALE solution of this benchmark problem, 35.0% was spent on the solution of the mesh motion and remapping of the nodal and quadrature point fields, 46.5% was spent on the solution of the mechanical sub-steps, and 18.5% was spent on the thermal sub-steps. The total computation time of the ALE solver was 79.2% longer than that of the entirely Lagrangian solver, in which 72.3% of the total computation time was spent on the mechanical sub-steps and 27.7% was spent on the thermal sub-steps. Like the thermally triggered necking benchmark, there was no significant difference in the number of required Newton steps to solve the mechanical substeps when comparing the ALE and Lagrangian solvers. All time steps required between 4 and 6 Newton steps to complete the mechanical sub-steps. At each time step, the total number of line search steps varied between 13 and 16.

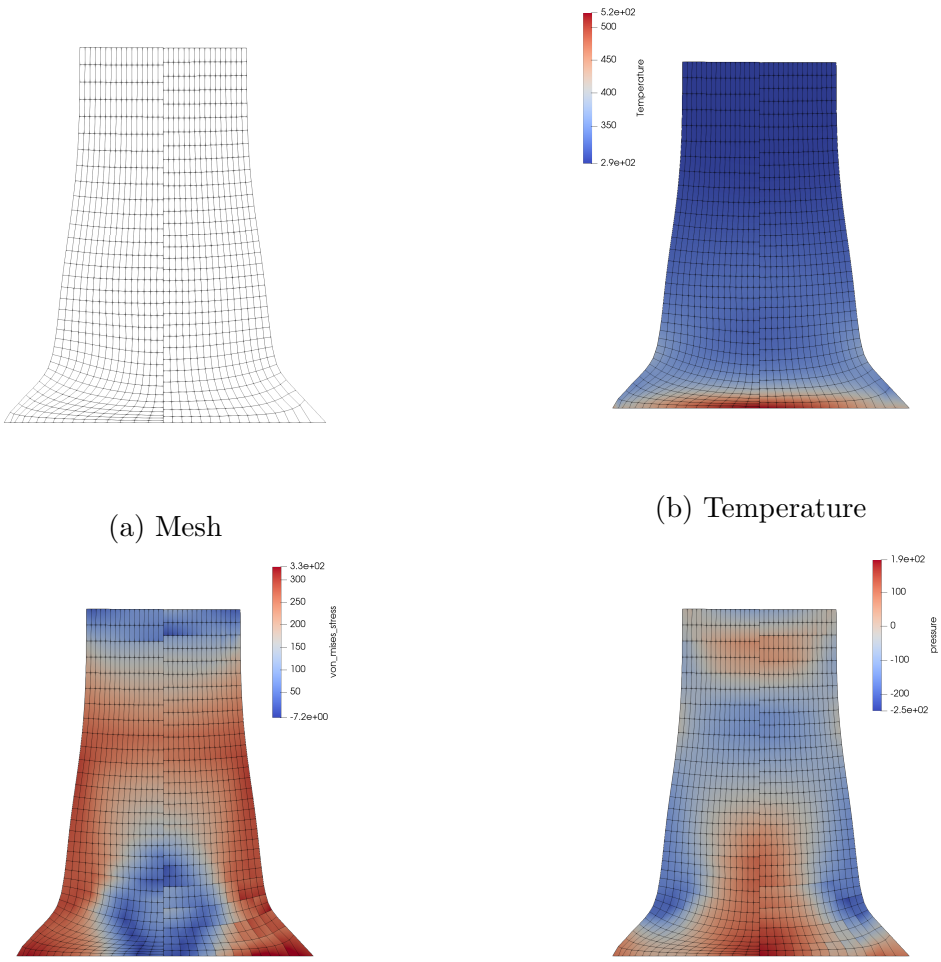

(a) Mesh

(b) Temperature

(c) von Mises stress

(d) Pressure

Figure 8.10: Taylor anvil results comparison between ALE (right of midline) and Lagrangian (left of midline) formulations

8.3 Interference Fit Insertion of a Cylinder into a Tapered Hole

This benchmark problem, which was presented by Laursen and Simo [100], involves simulation of interference fit insertion of a cylinder into a tapered hole in a block. The

cylinder has a radius of 40 mm and a length of 300 mm. The block has an outer radius of 300 mm and a height of 600 mm. The tapered hole has a radius of 40 mm at the surface and it linearly transitions to a radius of 35 mm at a depth of 150 mm. It remains at that reduced radius for the remaining depth. The initial setup of this benchmark problem is shown in Figure 8.11. The cylinder is pressed into the hole with a fixed vertical speed of 1 mm/s until it moves by a distance equal to its initial length. A thermal convection boundary condition is applied to the surfaces of both the cylinder and the block, with a convection coefficient of $17.5 \times 10^{-6}\,\mathrm{J/mm^2 \cdot s \cdot K}$. No external heat sources were added, so that any temperature change is entirely due to elastic heating, mechanical dissipation, and frictional heat generation.

Both the cylinder and the block are modelled as elastoplastic materials with linear hardening. The material properties used are listed in Table 8.3.

parameter	value	unit
Bulk modulus	63 840	$\mathrm{N{\cdot}mm^{-2}}$
Shear modulus	26 120	$\mathrm{N{\cdot}mm^{-2}}$
Flow stress	31	$\mathrm{N{\cdot}mm^{-2}}$
Linear hardening	261.20	$\mathrm{N{\cdot}mm^{-2}}$
Density	7.8×10^{-9}	$\mathrm{N{\cdot}mm^{-4}{\cdot}s^2}$
Thermal expansion coefficient	1×10^{-5}	$\mathrm{K^{-1}}$
Thermal conductivity	4.5×10^{-2}	$\mathrm{J{\cdot}mm^{-1}{\cdot}s^{-1}{\cdot}K^{-1}}$
Volumetric heat capacity	3.588×10^{-3}	$\mathrm{J{\cdot}mm^{-3}{\cdot}K^{-1}}$
Dissipation factor	0.9	
Flow stress softening	0.002	$\mathrm{K^{-1}}$
Hardening softening	0.002	$\mathrm{K^{-1}}$

Table 8.3: Material parameters for interference fit benchmark

The final deformed configuration that results when the simulation is run with a friction coefficient of 0.2 is shown in Figure 8.12a. When run without friction, the simulation

produces the final deformed configuration shown in Figure 8.12b. As expected [100], the presence of frictional forces causes more deformation in the block and upwelling of material around the hole. Figures 8.13c and 8.14c show comparisons of the final deformation with the results in [100] for the smooth contact and frictional contact cases, respectively. Both these Figures show the results are in very good agreement with the benchmark.

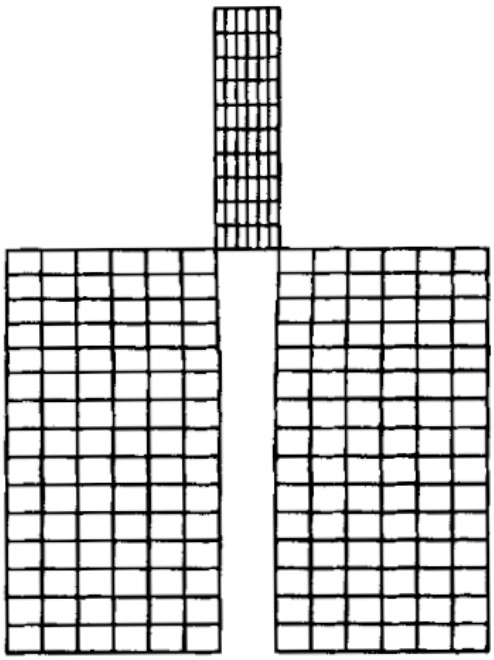

Figure 8.11: Interference fit benchmark: Initial setup [100]

In addition, the problem was also run with the top surface of the cylinder constrained to rotate around the axisymmetry axis with a constant angular velocity of 0.2 radians per second. The friction coefficient was set to 0.2. Results of this case are shown in Figure 8.12c. As expected, the bodies deform less than the test case with friction and no spinning, but more than the frictionless test case, and more heat is generated than both test cases due to the slipping against frictional forces.

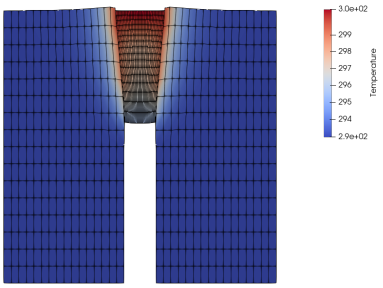

(a) With friction, without rotation

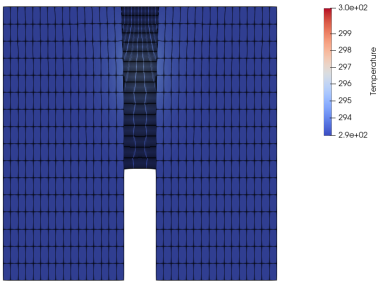

(b) Without friction, without rotation

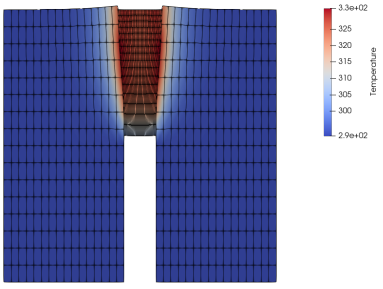

(c) With friction and rotation

Figure 8.12: Interference fit benchmark

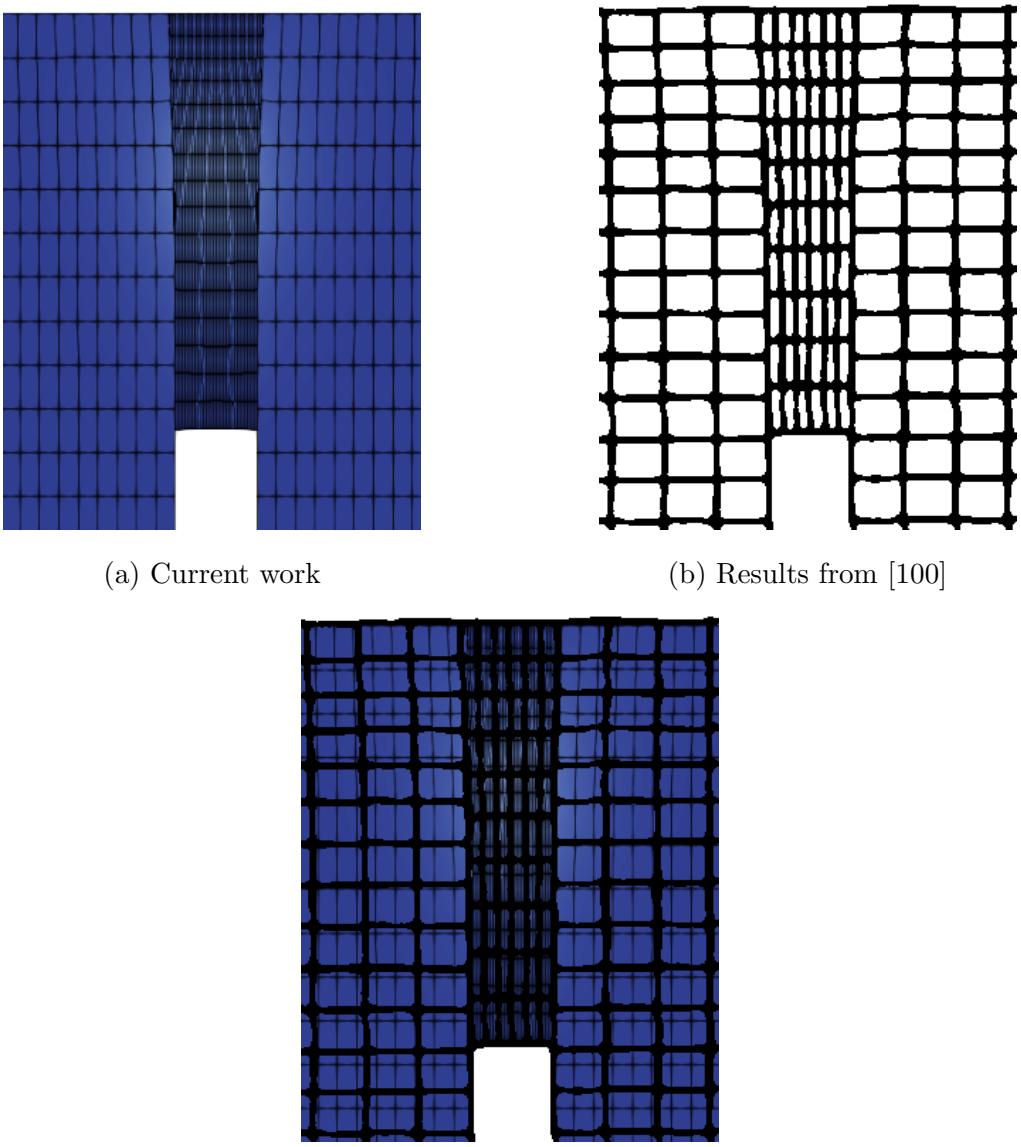

(a) Current work

(b) Results from [100]

(c) Comparison

Figure 8.13: Frictionless interference fit: Final deformation in comparison to results from [100]

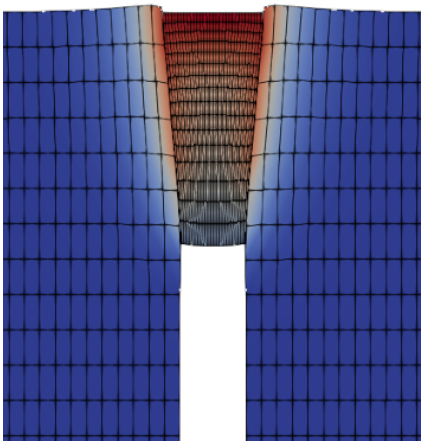

(a) Current work

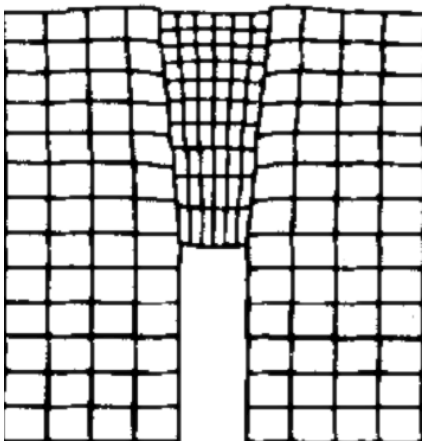

(b) Results from [100]

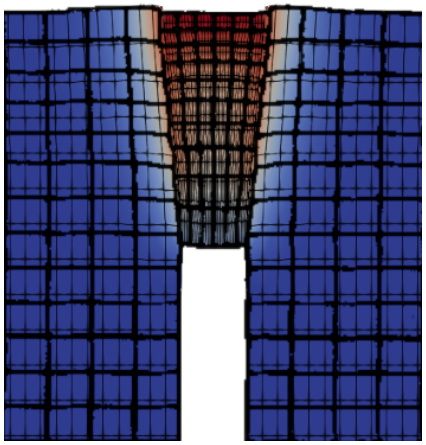

(c) Comparison

Figure 8.14: Interference fit with friction: Final deformation in comparison to results from [100]

9 Friction Welding Simulations

In this Chapter, the implemented and validated solver is used to simulate a friction welding process. Sections 9.1 and 9.2 detail the weld stages and introduce an adaptive time stepping procedure. Section 9.3 contains a description of a direct-drive friction weld simulation using the solver.

9.1 Weld Stages

A Direct Drive Friction Weld is a solid state process that consists of three stages: the conditioning (or heating) stage, the burn-off stage, and the forging stage. In both the conditioning and burn-off stages, the two workpieces are pressed against each other, and one of them is spun at a constant angular speed. During the conditioning stage, the temperature at the weld interface increases due to frictional heat generation, and the mechanical deformation that takes place is limited. In contrast, the majority of the viscoplastic deformation during the weld occurs during the burn-off stage. In the forging stage, rotation is stopped and a forging force is maintained. The weld joint is formed as the plasticised material in the thermomechanically affected zone cools down in the presence of the compressive stresses due to the forging force.

9.2 Adaptive Time Stepping

During the burn-off stage of the weld, where viscoplastic deformation takes place with high strain rates, the time increment required to accurately resolve the material response is orders of magnitude smaller than that required during the conditioning stage, where the deformation is primarily elastic. For this reason, the adaptive time stepping procedure summarised in Algorithm 9.2.1 was implemented. In this procedure, the time increment size in increased by a small percentage at every time step up to a predetermined maximum value. However, whenever a convergence failure is detected, the time increment size is halved and computation of that time step is restarted. This way, computational time is saved during the early stages of the weld by using a larger time increment value, and a sufficiently small time increment value is used later in the weld when it is necessary.

Algorithm 9.2.1 Adaptive Time Stepping

```
time_increment ← min(max_time_increment, 1.1 * time_increment)
successfully_converged ← false
while successfully_converged = false do
    Solve split-step thermomechanical problem
    if Solution completed with no convergence issues then
        successfully_converged ← true
    else
        time_increment ← 0.5 * time_increment
    end if
end while
```

9.3 Direct Drive Friction Weld of a Hollow Bar

This section describes the simulation of a direct drive friction weld between two similar hollow bars with an outer diameter of 50 mm and an inner diameter of 25 mm. The workpiece geometry and weld process parameters are based on the weld presented by Schmicker, Naumenko and Strackeljan [75]. Figure 9.1 shows the initial geometry of the weld.

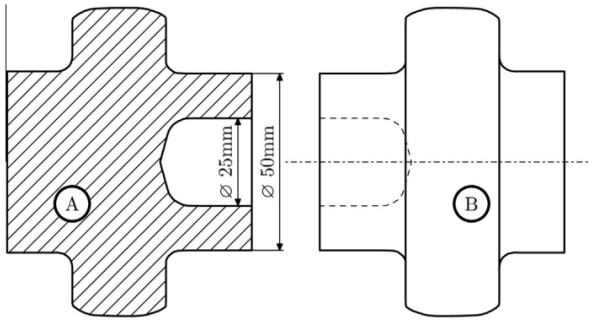

Figure 9.1: Direct drive friction weld of a hollow bar: Initial geometry [75]

9.3.1 Boundary Conditions

Based on the weld process parameters [75], the mechanical boundary conditions are a constant rotational speed of 800 rpm and a constant downward pressure of $40\,\mathrm{N{\cdot}mm^{-2}}$ throughout the weld. The friction coefficient is set to 0.3.

The only thermal boundary condition imposed is a convection boundary condition with a convection coefficient of $20 \times 10^{-6}\,\mathrm{J/mm^2 \cdot s \cdot K}$ on the boundaries of the two workpieces and an ambient temperature of 293 K, which is also the constant temperature used as the thermal initial condition.

Unidirectional Spring Boundary Condition

During the weld simulation, the downward force is primarily balanced by the normal contact force. As described in Section 6.3, the normal contact force at each augmented Lagrangian step is made up of two components: the penalty component and the accumulated augmented Lagrangian component from the previous steps. The penalty component, in turn, is modified at each Newton step according to the penetration and the normal contact penalty factor ϵ_{N}. Naturally, if the contact penalty factor is sufficiently large, then the magnitude of the total normal contact force may overshoot that of the applied downward force in some intermediate iterations of the Newton-Raphson loop. If the resulting incremental displacement is such that the gap between the contactor and target surfaces is positive, then the Newton-Raphson method may fail to converge, because the force balance would require, at least as an intermediate measure, the application of a tensile contact force, which would violate the normal contact constraints.

This scenario has been observed during the friction weld simulations carried out in this work, and it caused severe reduction of the adaptive time increment which prohibitively increased the simulation time. Attempting to circumvent this issue by lowering the normal contact penalty factor caused a large increase in the required number of augmented Lagrangian iterations at each time step.

The solution implemented in this simulation that avoided this scenario without a large change in the number of augmented Lagrangian steps or the time increment is the application of a unidirectional spring boundary condition in combination with the downward force boundary condition. At each point on the upper surface of the contactor, if the displacement is in the opposite direction of the applied downward force, then a small downward force proportional to the displacement is added. If the displacement is in the same direction as the downward force, then no additional force is applied.

While this boundary condition is numerical in nature, it provides a reasonable model

of real friction welding machines, in which the downward force is applied by hydraulics where unidirectional valves are used that restrict motion in the direction opposite to that of the applied force.

9.3.2 Material Constitutive Law

The elasto-thermo-viscoplastic behaviour of the material is modelled by adapting the constitutive law described in [75] to the formulation described in Subsection 6.1.1 and implemented as detailed in Subsection 7.5.2. Specifically, the constitutive law is modified so that strain rate dependence only takes effect when the strain rate exceeds a temperature-dependent minimum value $\dot{\varepsilon}_{\min}$ given by

$$\dot{\varepsilon}_{\min} = \left(1 - \left(\frac{\theta - \theta_{\mathrm{R}}}{\theta_{\mathrm{M}} - \theta_{\mathrm{R}}}\right)^{m}\right) \dot{\varepsilon}_0 \,, \tag{9.3.1}$$

where the Johnson-Cook reference strain rate parameter $\dot{\varepsilon}_0$ and temperature dependence form are used. The strain rate value used in the constitutive law is then taken to be the highest of the two values: the equivalent plastic strain rate $\dot{\alpha}$ and this minimum value $\dot{\varepsilon}_{\min}$.

$$\dot{\varepsilon} = \max(\dot{\alpha}, \dot{\varepsilon}_{\min}) \,, \tag{9.3.2}$$

where the equivalent plastic strain rate $\dot{\alpha}$ is obtained from the return-mapping computation using (7.5.16).

The flow stress is given as a function of a strain-rate independent yield strength $\sigma_{\mathrm{s}}^{\mathrm{y}}$ and the modified strain rate $\dot{\varepsilon}$ as

$$\sigma^{\mathrm{y}} = 3 \left\{ \left[1 + \left(\left(\frac{\sigma_{\mathrm{s}}^{\mathrm{y}}}{3\dot{\varepsilon}_0 \mu_0} \right)^{\frac{1}{C-1}} \frac{\dot{\varepsilon}}{\dot{\varepsilon}_0} \right)^2 \right]^{\frac{C-1}{2}} (\mu_0 - \mu_\infty) + \mu_\infty \right\} \dot{\varepsilon} \,, \tag{9.3.3}$$

$$\sigma_{\mathrm{s}}^{\mathrm{y}} = (A + B\alpha^n) \left(1 - \left(\frac{\theta - \theta_{\mathrm{R}}}{\theta_{\mathrm{M}} - \theta_{\mathrm{R}}}\right)^{m}\right) . \tag{9.3.4}$$

In [75], the material is modelled as a perfectly viscoplastic solid, with the stress vanishing as the strain rate approaches zero. In that work, the elastic behaviour of the material

parameter	value	unit
Bulk modulus	158 700	$\mathrm{N{\cdot}mm^{-2}}$
Shear modulus	77 520	$\mathrm{N{\cdot}mm^{-2}}$
Johnson-Cook A	235	$\mathrm{N{\cdot}mm^{-2}}$
Johnson-Cook B	0	$\mathrm{N{\cdot}mm^{-2}}$
Johnson-Cook C	0.2	
Johnson-Cook m	1.5	
Johnson-Cook n	1	
Melting temperature θ_M	1693.15	K
Reference temperature θ_R	293.15	K
Reference strain rate $\dot{\varepsilon}_0$	1.0	$\mathrm{s^{-1}}$
Density	7.87×10^{-9}	$\mathrm{N{\cdot}mm^{-4}{\cdot}s^2}$
Thermal expansion coefficient	1×10^{-5}	$\mathrm{K^{-1}}$
Thermal conductivity	3.5×10^{-2}	$\mathrm{J{\cdot}mm^{-1}{\cdot}s^{-1}{\cdot}K^{-1}}$
Volumetric heat capacity	6.445×10^{-3}	$\mathrm{J{\cdot}mm^{-3}{\cdot}K^{-1}}$
Dissipation factor	0.9	
Upper saturation viscosity μ_0	1×10^{22}	$\mathrm{N{\cdot}mm^{-2}{\cdot}s}$
Lower saturation viscosity μ_∞	1×10^{-4}	$\mathrm{N{\cdot}mm^{-2}{\cdot}s}$

Table 9.1: Material parameters for direct drive welding of hollow bars

is approximated by using a very large viscosity value in the stress range below the yield strength. In contrast, in the return-mapping approach employed in this work, the material remains elastic when the stress is below the yield strength of the material. With this modification, the flow rule only applies at stresses above the yield strength.

The material parameter values used are listed in Table 9.1.

9.3.3 Simulation Results

The deformation and temperature distributions at the end of the burn-off stage of the weld are shown in Figure 9.2. A comparison between the deformation at the end of the weld to the experimental and numerical results from [75] are shown in Figure 9.3. Figure 9.4 shows the deformed workpieces at different times during the weld simulation. A comparison of the temperature distribution at the end of the weld is shown in Figure 9.5. It shows a good qualitative agreement at the weld interface, with the temperature in both simulations approaching the melting temperature (1420 °C or 1693 K) but not reaching it. Furthermore, a comparison of the upset curves, i.e. the vertical displacement of the top surface over time, is shown in Figure 9.6. The equivalent plastic strain distribution is shown in Figure 9.7.

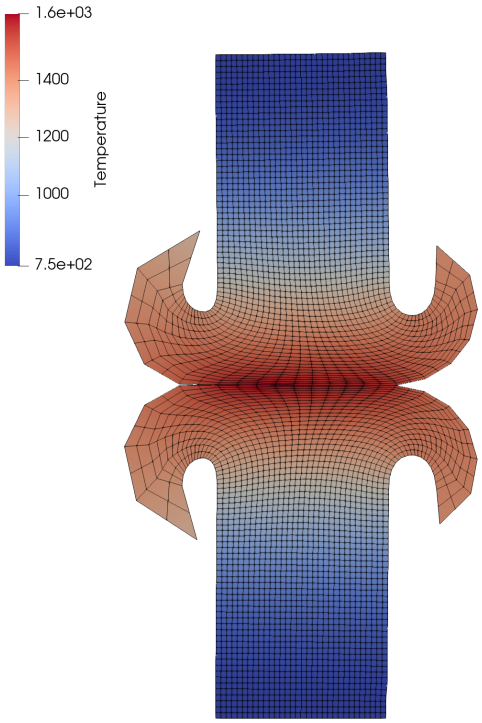

Figure 9.2: Simulation result: Deformation and absolute temperature distributions after burn-off stage in a direct drive friction weld of hollow bars

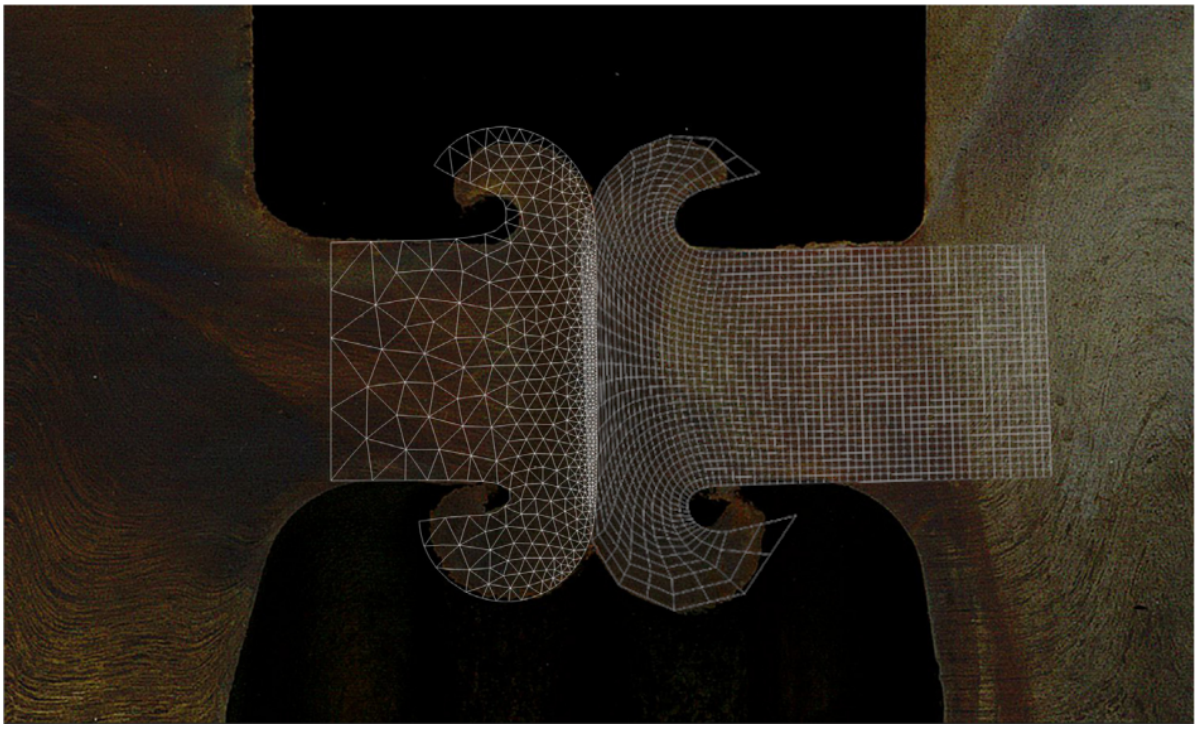

Figure 9.3: Simulation result is compared to experimental weld. The weld photograph and simulation on the left are from [75]

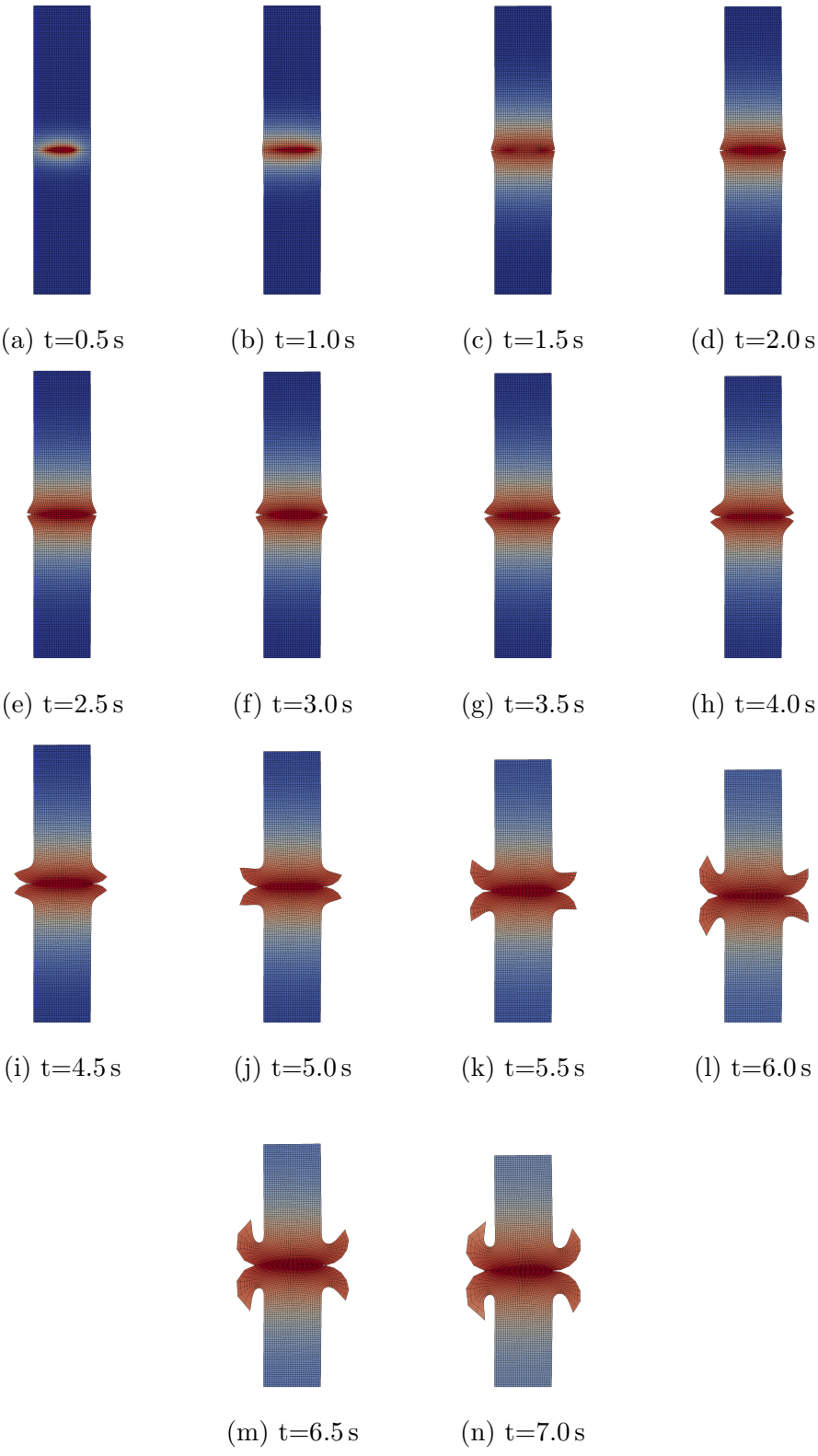

(a) t=0.5 s (b) t=1.0 s (c) t=1.5 s (d) t=2.0 s

(e) t=2.5 s (f) t=3.0 s (g) t=3.5 s (h) t=4.0 s

(i) t=4.5 s (j) t=5.0 s (k) t=5.5 s (l) t=6.0 s

(m) t=6.5 s (n) t=7.0 s

Figure 9.4: Weld progress

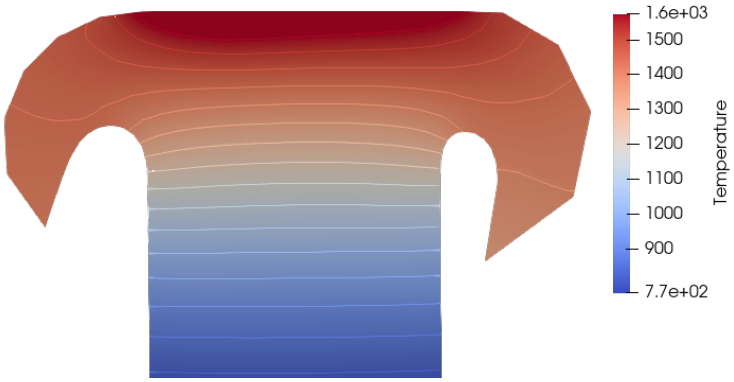

(a) Temperature distribution from current simulation (in Kelvin)

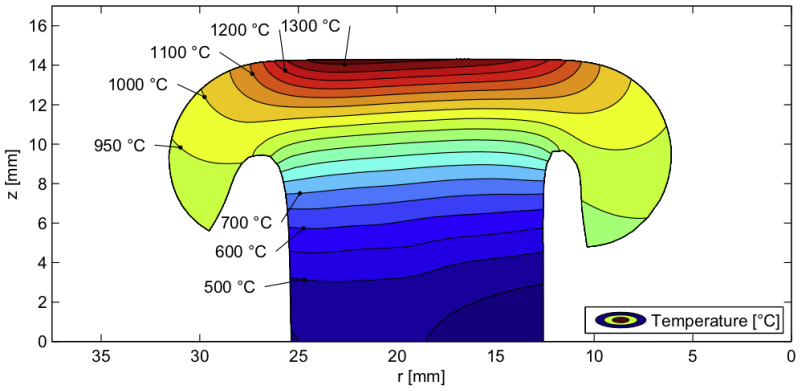

(b) Temperature distribution from [75]

Figure 9.5: Temperature distribution at the end of the weld in comparison with [75]

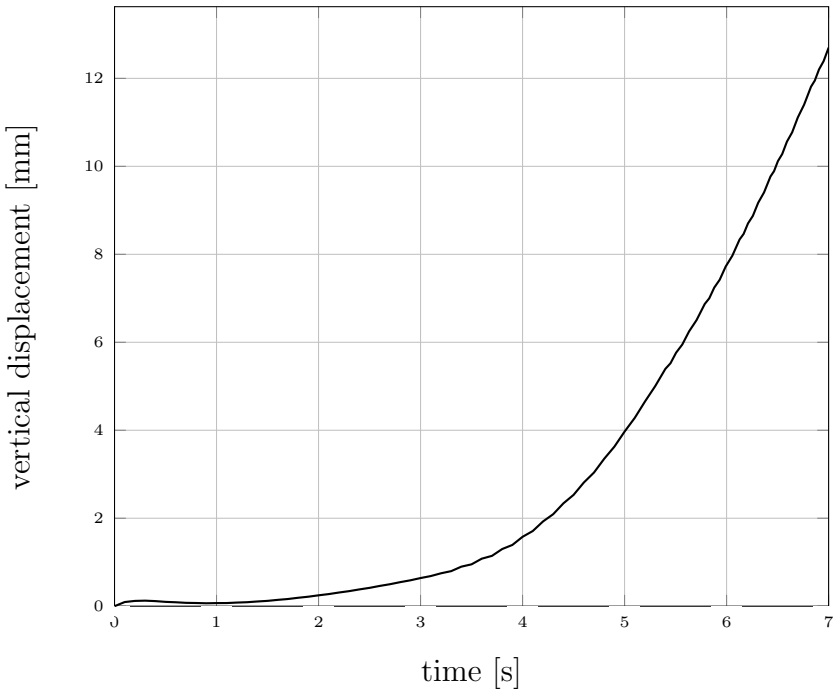

(a) Results from current work

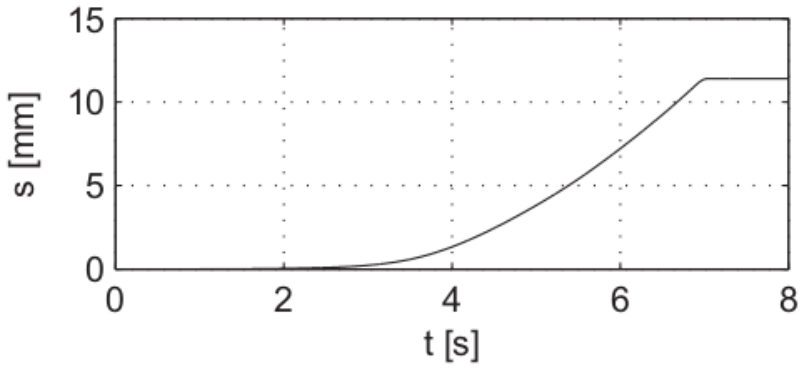

(b) Results from [75]

Figure 9.6: Vertical displacement of top surface (upset) over weld time

Figure 9.7: Equivalent plastic strain distribution

Necessity of ALE Formulation

A fully Lagrangian simulation of the weld was tested, and it resulted in severe mesh distortion around the weld interface, which caused large deviations from the experimentally observed results, followed by failure in convergence of the solution steps. Figure 9.8 shows a comparison between the Lagrangian and ALE simulations at different stages of the weld, and Figure 9.9 shows the same comparison at an enlarged view of the weld interface region, which shows the differences in mesh distortion more clearly. Early in the simulation, the differences between the Lagrangian and ALE simulations are small. As the mesh distortion in the Lagrangian simulation increases, however, the results deviate considerably. Since the ALE results correlate well with the experimental and numerical results from [75] as shown in Figure 9.5, this deviation confirms that excessive distortions limit the reliability of a fully Lagrangian formulation in simulation of friction welding processes, and shows the ALE formulation is effective in addressing this limitation.

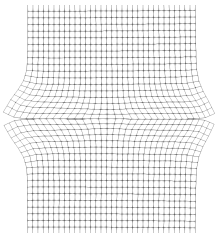

(a) Lagrangian t=2.0 s

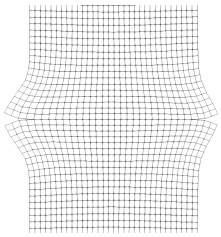

(b) ALE t=2.0 s

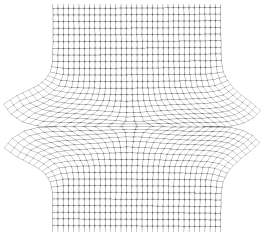

(c) Lagrangian t=2.8 s

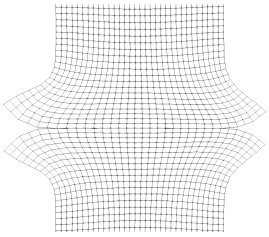

(d) ALE t=2.8 s

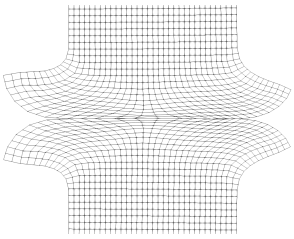

(e) Lagrangian t=3.5 s

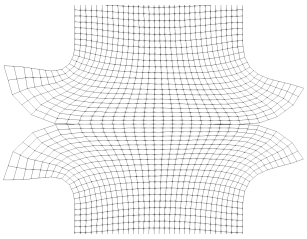

(f) ALE t=3.5 s

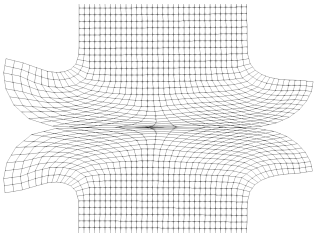

(g) Lagrangian t=4.2 s

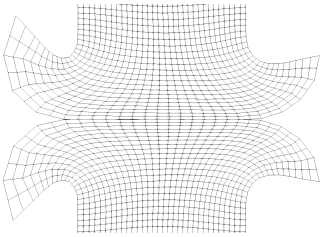

(h) ALE t=4.2 s

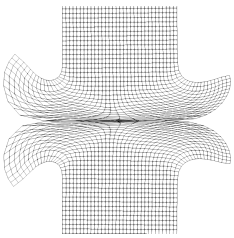

(i) Lagrangian t=7.0 s

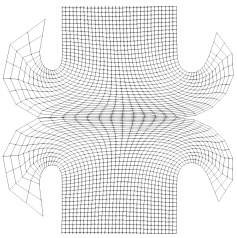

(j) ALE t=7.0 s

Figure 9.8: Comparison between ALE and fully Lagrangian weld simulations

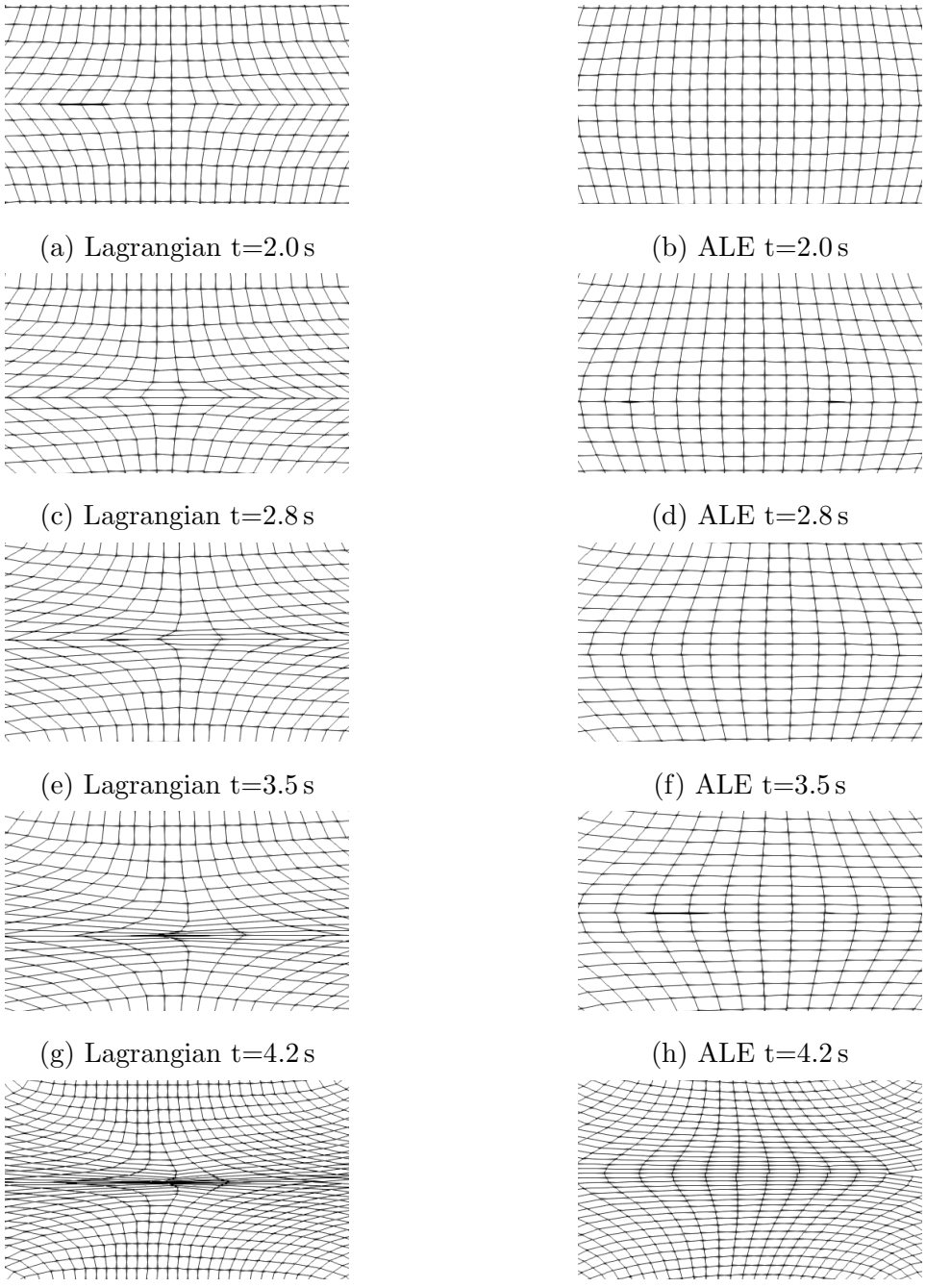

(a) Lagrangian t=2.0 s (b) ALE t=2.0 s

(c) Lagrangian t=2.8 s (d) ALE t=2.8 s

(e) Lagrangian t=3.5 s (f) ALE t=3.5 s

(g) Lagrangian t=4.2 s (h) ALE t=4.2 s

(i) Lagrangian t=7.0 s (j) ALE t=7.0 s

Figure 9.9: Comparison between ALE and fully Lagrangian weld simulations: Enlarged view of weld interface

10 Discussion and Conclusions

This thesis describes the development and implementation of a finite strain thermo-elastoviscoplasticity solver with thermomechanical friction contact for numerical simulation of friction welding processes. Though several works on numerical simulation of friction welding have been published, there have been no studies published which simulate friction welding using the model for associative coupled thermoplasticity at finite strain. The utility of this model is that it accounts for the elastic as well as the viscoplastic effects and is suitable for the large deformations characteristic of friction welding processes. To make this possible, a novel Arbitrary Lagrangian-Eulerian formulation for coupled finite strain thermoplasticity with thermomechanical friction contact was developed and incorporated into the solver, which was implemented using the deal.II library. The implementation of the solver and ALE formulation was validated with benchmark problems and it was used to simulate a friction welding process.

The novelty of the developed ALE formulation lies in that the deformation gradient between the current and material configurations is not required; motion of the material configuration is represented only incrementally in terms of the reference velocity. The finite strain thermoplasticity and the thermomechanical friction contact formulations were extended by including the contribution of the reference velocity field.

The ALE formulation that was developed and implemented in this work improves on the state of the art of ALE approaches for finite strain plasticity as presented in the works of [18] and [17]. Unlike [18], there is no need to keep track of the material configuration

mesh, which enables simulation of more severe deformations, such as those that arise in friction welding applications, because there is no requirement to limit distortions in the material configuration mesh. Also, unlike [17], it is not necessary to use a Godunov-like technique for convection of the left Cauchy-Green deformation tensor $\boldsymbol{b}^{\mathrm{e}}$, the equivalent plastic strain α and the deformation Jacobian. Rather, those are evaluated directly at the quadrature point positions before the incremental mesh motion. This alleviates convection accuracy considerations when choosing mesh motion step size. This also makes it possible to use the developed remapping procedure unchanged for adaptive mesh refinement and coarsening or for remeshing.

The implemented solver made use of the rotational symmetry in rotary friction welding processes. The reference motion was therefore decomposed into an in-plane component and a circumferential component. While the in-plane component of the reference motion was updated in a split-step approach, the circumferential component was updated simultaneously with the deformation field.

The implementation of the solver and the ALE formulation using the deal.II library was programmed for a distributed memory parallel computing architecture. This drastically reduces the simulation run times, and it enables running simulations with larger meshes than would fit on one computer. In such a parallel implementation, additional inter-process communications are required for the contact and ALE computations. These communications were implemented and described in this thesis. Furthermore, as part of this work, the deal.II library was extended by incrementing the highest order of shape function derivatives available in the library to enable computation of the consistent tangent moduli of the tangential contact terms.

Open problems and possible extensions of current work

The solver implemented in the current work can be extended in a number of ways in order to simulate other friction welding processes and general metal working scenarios. First,

the rotational symmetry assumption that applies to direct-drive and inertia friction welding processes is not suitable for friction stir welding and linear friction welding simulations, and a three-dimensional implementation would need to be completed and validated. Another possible extension is modelling, implementation and validation of self-contact, which is also relevant in some rotational friction welding applications.

Prediction of solid bonding in numerical simulation of friction welding processes remains an open problem [12]. The use of an associative coupled thermoplasticity model with thermomechanical friction contact in simulation of friction welding processes as enabled by the current work makes it possible to model solid bonding to predict when the behaviour at the welding interface transitions from contact between two bodies to deformation of one bonded body. This is achievable by modelling the bonding criterion as an internal variable at the contactor-target pairs and using it as a parameter in computing the normal and tangential forces acting across the contact surface.

Bibliography

[1] Thomas W., Nicholas E., Needham J., Murch M., Temple-Smith P., and Dawes C. Friction stir welding, international patent application, 1991. GB Patent Application PCT/GB92/02203.

[2] Maurya R. R. and Kauzlarich J. J. Reciprocating friction bonding apparatus, 1969. US Patent 3,420,428.

[3] Crossland B. Friction welding. *Contemporary Physics*, 12(6):559–574, 1971.

[4] Vill V. I. *Friction Welding of Metals*, volume 1. American Welding Society; Trade Distributor: Reinhold Pub. Co., 1962.

[5] Li W., Shi S., Wang F., Zhang Z., Ma T., and Li J. Numerical simulation of friction welding processes based on ABAQUS environment. *Journal of Engineering Science and Technology Review*, 5(3):10–19, 2012.

[6] Li W., Wang F., Shi S., and Ma T. Numerical simulation of linear friction welding based on ABAQUS environment: Challenges and perspectives. *Journal of Materials Engineering and Performance*, 23(2):384–390, 2014.

[7] Kallee S. W., Thomas W. M., and Dave Nicholas E. Friction stir welding of lightweight materials. In Kainer K. U., editor, *Magnesium Alloys and their Applications*, pages 173–190. Wiley-VCH, 2000.

[8] He X., Gu F., and Ball A. A review of numerical analysis of friction stir welding. *Progress in Materials Science*, 65(3):1–66, 2014.

[9] Neto D. M. and Neto P. Numerical modeling of friction stir welding process: a literature review. *The International Journal of Advanced Manufacturing Technology*, 65(1–4):115–126, 2013.

[10] Vairis A. and Frost M. Modelling the linear friction welding of titanium blocks. *Materials Science and Engineering: A*, 292(1):8–17, 2000.

[11] Frigaard Ø., Grong Ø., and Midling O. T. A process model for friction stir welding of age hardening aluminum alloys. *Metallurgical and Materials Transactions A*, 32(5):1189–1200, 2001.

[12] Buffa G. and Fratini L. Strategies for numerical simulation of linear friction welding of metals: a review. *Production Engineering*, 11(3):221–235, 2017.

[13] Li W., Vairis A., Preuss M., and Ma T. Linear and rotary friction welding review. *International Materials Reviews*, 61(2):71–100, 2016.

[14] McAndrew A. R., Colegrove P. A., Bühr C., Flipo B. C., and Vairis A. A literature review of Ti–6Al–4V linear friction welding. *Progress in Materials Science*, 92:225–257, 2018.

[15] Ouyang J., Yarrapareddy E., and Kovacevic R. Microstructural evolution in the friction stir welded 6061 aluminum alloy (T6-temper condition) to copper. *Journal of Materials Processing Technology*, 172(1):110–122, 2006.

[16] Sarvghad-Moghaddam M., Parvizi R., Davoodi A., Haddad-Sabzevar M., and Imani A. Establishing a correlation between interfacial microstructures and corrosion initiation sites in Al/Cu joints by SEM–EDS and AFM–SKPFM. *Corrosion Science*, 79:148–158, 2014.

[17] Rodríguez-Ferran A., Pérez-Foguet A., and Huerta A. Arbitrary Lagrangian–Eulerian (ALE) formulation for hyperelastoplasticity. *International Journal for Numerical Methods in Engineering*, 53(8):1831–1851, 2002.

[18] Armero F. and Love E. An arbitrary Lagrangian–Eulerian finite element method for finite strain plasticity. *International Journal for Numerical Methods in Engineering*, 57(4):471–508, 2003.

[19] Bangerth W., Hartmann R., and Kanschat G. deal.II – a general purpose object oriented finite element library. *ACM Transactions on Mathematical Software*, 33(4):24/1–24/27, 2007.

[20] Bangerth W., Davydov D., Heister T., Heltai L., Kanschat G., Kronbichler M., Maier M., Turcksin B., and Wells D. The deal.II library, version 8.4. *Journal of Numerical Mathematics*, 24(3):135–141, 2016.

[21] Wang K. and Lin W. Flywheel friction welding research. *Welding Journal*, 53(6):233s–241s, 1974.

[22] Maalekian M. Friction welding–critical assessment of literature. *Science and Technology of Welding and Joining*, 12(8):738–759, 2007.

[23] Uday M. B., Fauzi M. N. A., Zuhailawati H., and Ismail A. B. Advances in friction welding process: a review. *Science and Technology of Welding and Joining*, 15(7):534–558, 2010.

[24] Bhamji I., Preuss M., Threadgill P. L., and Addison A. Solid state joining of metals by linear friction welding: a literature review. *Materials Science and Technology*, 27(1):2–12, 2011.

[25] Mishra R. S. and Ma Z. Friction stir welding and processing. *Materials Science and Engineering: R: Reports*, 50(1-2):1–78, 2005.

[26] Nandan R., DebRoy T., and Bhadeshia H. Recent advances in friction-stir welding – process, weldment structure and properties. *Progress in Materials Science*, 53(6):980–1023, 2008.

[27] Zhang Y., Cao X., Larose S., and Wanjara P. Review of tools for friction stir welding and processing. *Canadian Metallurgical Quarterly*, 51(3):250–261, 2012.

[28] Sassani F. and Neelam J. Friction welding of incompatible materials. *Welding Journal*, 67(11):264–270, 1988.

[29] Sahin A. Z., Yibaş B. S., Ahmed M., and Nickel J. Analysis of the friction welding process in relation to the welding of copper and steel bars. *Journal of Materials Processing Technology*, 82(1-3):127–136, 1998.

[30] Vairis A. and Frost M. High frequency linear friction welding of a titanium alloy. *Wear*, 217(1):117–131, 1998.

[31] Shinoda T., Endo S., and Kato Y. Friction welding of cast iron and stainless steels. *Welding International*, 13(2):89–95, 1999.

[32] Fuji A. Friction welding of Al–Mg–Si alloy to Ni–Cr–Mo low alloy steel. *Science and Technology of Welding and Joining*, 9(1):83–89, 2004.

[33] Satyanarayana V., Madhusudhan Reddy G., and Mohandas T. Continuous drive friction welding studies on AISI 304 austenitic stainless steel welds. *Materials and Manufacturing Processes*, 19(3):487–505, 2004.

[34] Satyanarayana V., Reddy G. M., and Mohandas T. Dissimilar metal friction welding of austenitic–ferritic stainless steels. *Journal of Materials Processing Technology*, 160(2):128–137, 2005.

[35] Sahin M. Joining with friction welding of high-speed steel and medium-carbon steel. *Journal of Materials Processing Technology*, 168(2):202–210, 2005.

[36] Maalekian M. *Friction welding of high carbon steel in large cross-section.* PhD thesis, 2007.

[37] Threadgill P., Leonard A., Shercliff H., and Withers P. Friction stir welding of aluminium alloys. *International Materials Reviews*, 54(2):49–93, 2009.

[38] Ananthapadmanaban D., Rao V. S., Abraham N., and Rao K. P. A study of mechanical properties of friction welded mild steel to stainless steel joints. *Materials & Design*, 30(7):2642–2646, 2009.

[39] Wang F., Li W., Li J., and Vairis A. Process parameter analysis of inertia friction welding nickel-based superalloy. *The International Journal of Advanced Manufacturing Technology*, 71(9-12):1909–1918, 2014.

[40] Leśniewski J. and Ambroziak A. Modelling the friction welding of titanium and tungsten pseudoalloy. *Archives of Civil and Mechanical Engineering*, 15(1):142–150, 2015.

[41] Galvão I., Loureiro A., and Rodrigues D. Critical review on friction stir welding of aluminium to copper. *Science and Technology of Welding and Joining*, 21(7):523–546, 2016.

[42] Midling O. and Grong Ø. A process model for friction welding of Al–Mg–Si alloys and Al–SiC metal matrix composites–II. HAZ microstructure and strength evolution. *Acta Metallurgica et Materialia*, 42(5):1611–1622, 1994.

[43] Baeslack III W., Broderick T., Juhas M., and Fraser H. Characterization of solid-phase welds between Ti–6A1–2Sn–4Zr–2Mo–0.1Si and Ti–13.5A1–21.5Nb titanium aluminide. *Materials Characterization*, 33(4):357–367, 1994.

[44] Preuss M., Withers P., Pang J., and Baxter G. Inertia welding nickel-based superalloy: Part I. metallurgical characterization. *Metallurgical and Materials Transactions A*, 33(10):3215–3225, 2002.

[45] Lee W. B., Yeon Y., Kim D., and Jung S. Effect of friction welding parameters on mechanical and metallurgical properties of aluminium alloy 5052–A36 steel joint. *Materials Science and Technology*, 19(6):773–778, 2003.

[46] Wanjara P. and Jahazi M. Linear friction welding of Ti–6Al–4V: Processing, microstructure, and mechanical-property inter-relationships. *Metallurgical and Materials Transactions A*, 36(8):2149–2164, 2005.

[47] Kimura M., Choji M., Kusaka M., Seo K., and Fuji A. Effect of friction welding conditions and aging treatment on mechanical properties of A7075–T6 aluminium alloy friction joints. *Science and Technology of Welding and Joining*, 10(4):406–412, 2005.

[48] Kimura M., Nakamura S., Kusaka M., Seo K., and Fuji A. Mechanical properties of friction welded joint between Ti–6Al–4V alloy and Al–Mg alloy (AA5052). *Science and Technology of Welding and Joining*, 10(6):666–672, 2005.

[49] Kimura M., Choji M., Kusaka M., Seo K., and Fuji A. Effect of friction welding conditions on mechanical properties of A5052 aluminium alloy friction welded joint. *Science and Technology of Welding and Joining*, 11(2):209–215, 2006.

[50] Kanan L. F., Vicharapu B., Bueno A. F. B., Clarke T., and De A. Friction hydro-pillar processing of a high carbon steel: joint structure and properties. *Metallurgical and Materials Transactions B*, 49(2):699–708, 2018.

[51] Craine R. and Francis A. Frictional heat generated in the early stages of an orbital friction welding process. *Wear*, 114(3):355–365, 1987.

[52] Służalec A. Thermal effects in friction welding. *International Journal of Mechanical Sciences*, 32(6):467–478, 1990.

[53] Dave V., Cola M., and Hussen G. Heat generation in the inertia welding of dissimilar tubes. *Welding Journal (New York)*, 80(10):246S–246S, 2001.

[54] Maalekian M., Kozeschnik E., Brantner H. P., and Cerjak H. Comparative analysis of heat generation in friction welding of steel bars. *Acta Materialia*, 56(12):2843–2855, 2008.

[55] Yang Y. C., Chen W. L., and Lee H.-L. A nonlinear inverse problem in estimating the heat generation in rotary friction welding. *Numerical Heat Transfer, Part A: Applications*, 59(2):130–149, 2011.

[56] Xiong J., Li J., Wei Y., Zhang F., and Huang W. An analytical model of steady-state continuous drive friction welding. *Acta Materialia*, 61(5):1662–1675, 2013.

[57] Słżalec A. and Służalec A. Solutions of thermal problems in friction welding—comparative study. *International Journal of Heat and Mass Transfer*, 36(6):1583–1587, 1993.

[58] Midling O. and Grong Ø. A process model for friction welding of Al–Mg–Si alloys and Al–SiC metal matrix composites–I. HAZ temperature and strain rate distribution. *Acta Metallurgica et Materialia*, 42(5):1595–1609, 1994.

[59] Nguyen T. and Weckman D. A thermal and microstructure evolution model of direct-drive friction welding of plain carbon steel. *Metallurgical and Materials Transactions B*, 37(2):275–292, 2006.

[60] Zhang L., Pei J., Zhang Q., Liu C., Zhu W., Qu S., and Wang J. The coupled FEM analysis of the transient temperature field during inertia friction welding of GH4169 alloy. *Acta Metallurgica Sinica (English Letters)*, 20(4):301–306, 2007.

[61] Łukaszewicz A. Nonlinear numerical model of friction heating during rotary friction welding. *Journal of Friction and Wear*, 39(6):476–482, 2018.

[62] Balasubramanian V., Li Y., Stotler T., Crompton J., Soboyejo A., Katsube N., and Soboyejo W. A new friction law for the modelling of continuous drive friction welding: applications to 1045 steel welds. *Materials and Manufacturing Processes*, 14(6):845–860, 1999.

[63] Francis A. and Craine R. On a model for frictioning stage in friction welding of thin tubes. *International Journal of Heat and Mass Transfer*, 28(9):1747–1755, 1985.

[64] Yin Y., Yang X., Cui L., Wang F., and Li S. Material flow influence on the weld formation and mechanical performance in underwater friction taper plug welds for pipeline steel. *Materials & Design*, 88:990–998, 2015.

[65] Liu X., Zhao S., Chen K., and Ni J. Material flow visualization of dissimilar friction stir welding process using nano-computed tomography. *Journal of Manufacturing Science and Engineering*, 140(11), 2018.

[66] Duffin F. and Bahrani A. Frictional behaviour of mild steel in friction welding. *Wear*, 26(1):53–74, 1973.

[67] Hasegawa M. and Ieda T. Effects of friction welding conditions on initial joining phenomena. *Welding International*, 13(9):701–711, 1999.

[68] Li P., Li J., Li X., Xiong J., Zhang F., and Liang L. A study of the mechanisms involved in initial friction process of continuous drive friction welding. *Journal of Adhesion Science and Technology*, 29(12):1246–1257, 2015.

[69] Ananthapadmanaban D. Mechanisms of friction and their correlation to bond strength of friction welded Ti-6Al-4V similar welds, low carbon steel-stainless steel and aluminium-copper dissimilar welds. *International Journal of Innovations in Engineering and Technology*, 9(3):014–020, 2018.

[70] Wang G., Li J., Xiong J., Wang W., Ma P., and Zhang F. Study on the friction interface evolution during rotary friction welding of tube. *Journal of Adhesion Science and Technology*, 33(10):1033–1046, 2019.

[71] Moal A. and Massoni E. Finite element simulation of the inertia welding of two similar parts. *Engineering Computations*, 12(6):497–512, 1995.

[72] Bendzsak G., North T., and Li Z. Numerical model for steady-state flow in friction welding. *Acta Materialia*, 45(4):1735–1745, 1997.

[73] D'Alvise L., Massoni E., and Walløe S. J. Finite element modelling of the inertia friction welding process between dissimilar materials. *Journal of Materials Processing Technology*, 125(1):387–391, 2002.

[74] Zhang Q., Zhang L., Liu W., Zhang X., Zhu W., and Qu S. 3D rigid viscoplastic fe modelling of continuous drive friction welding process. *Science and Technology of Welding and Joining*, 11(6):737–743, 2006.

[75] Schmicker D., Naumenko K., and Strackeljan J. A robust simulation of direct drive friction welding with a modified carreau fluid constitutive model. *Computer Methods in Applied Mechanics and Engineering*, 265(1):186–194, 2013.

[76] Fu L., Duan L., and Du S. Numerical simulation of inertia friction welding process by finite element method. *Welding Journal*, 82(3):65S–70S, 2003.

[77] Xu Y., Jing H., Han Y., and Xu L. Numerical simulation of the effects of various stud and hole configurations on friction hydro-pillar processing. *International Journal of Mechanical Sciences*, 90:44–52, 2015.

[78] Landell R., Kanan L. F., Buzzatti D., Vicharapu B., De A., and Clarke T. Material flow during friction hydro-pillar processing. *Science and Technology of Welding and Joining*, 25(3):228–234, 2020.

[79] Dillon Jr O. W. Coupled thermoplasticity. *Journal of the Mechanics and Physics of Solids*, 11(1):21–33, 1963.

[80] Coleman B. D. and Owen D. R. On the thermodynamics of elastic-plastic materials with temperature-dependent moduli and yield stresses. *Archive for Rational Mechanics and Analysis*, 70(4):339–354, 1979.

[81] Lee E. H. Elastic-plastic deformation at finite strains. *Journal of Applied Mechanics*, 36(1):1–6, 1969.

[82] Simo J. and Miehe C. Associative coupled thermoplasticity at finite strains: Formulation, numerical analysis and implementation. *Computer Methods in Applied Mechanics and Engineering*, 98(1):41–104, 1992.

[83] Adam L. and Ponthot J. P. A coupled formulation for thermo-viscoplasticity at finite strains: Application to hot metal forming. In Murakami S. and Ohno N., editors, *IUTAM Symposium on Creep in Structures*, pages 197–206. Springer, 2001.

[84] Vaz Jr M., Muñoz-Rojas P., and Lange M. Damage evolution and thermal coupled effects in inelastic solids. *International Journal of Mechanical Sciences*, 53(5):387–398, 2011.

[85] Chabrand P. Contact models and numerical methods for metal forming processes. *Revue Européenne des Eléments*, 14(2-3):323–337, 2005.

[86] Böhlke T., Risy G., and Bertram A. Finite element simulation of metal forming operations with texture based material models. *Modelling and Simulation in Materials Science and Engineering*, 14(3):365–387, mar 2006.

[87] Oñate E., Franci A., and Carbonell J. M. A particle finite element method for analysis of industrial forming processes. *Computational Mechanics*, 54(1):85–107, 2014.

[88] Sanz M. A., Nguyen K., Latorre M., Rodríguez M., and Montáns F. J. Sheet metal forming analysis using a large strain anisotropic multiplicative plasticity formulation, based on elastic correctors, which preserves the structure of the infinitesimal theory. *Finite Elements in Analysis and Design*, 164:1–17, 2019.

[89] Mediavilla J., Peerlings R., and Geers M. An integrated continuous–discontinuous approach towards damage engineering in sheet metal forming processes. *Engineering Fracture Mechanics*, 73(7):895–916, 2006.

[90] Böhlke T., Risy G., and Bertram A. Finite element simulation of metal form-

ing operations with texture based material models. *Modelling and Simulation in Materials Science and Engineering*, 14(3):365, 2006.

[91] Martinet F. and Chabrand P. Application of ALE finite elements method to a lubricated friction model in sheet metal forming. *International Journal of Solids and Structures*, 37(29):4005–4031, 2000.

[92] Hallberg H., Ryttberg K., and Ristinmaa M. Model describing material-dependent deformation behavior in high-velocity metal forming processes. *Journal of Engineering Mechanics*, 135(4):345–357, 2009.

[93] Shutov A., Silbermann C., and Ihlemann J. Ductile damage model for metal forming simulations including refined description of void nucleation. *International Journal of Plasticity*, 71:195–217, 2015.

[94] Cardiff P., Tuković Ž., Jaeger P. D., Clancy M., and Ivanković A. A Lagrangian cell-centred finite volume method for metal forming simulation. *International Journal for Numerical Methods in Engineering*, 109(13):1777–1803, 2017.

[95] Adam L. and Ponthot J. P. Numerical simulation of viscoplastic and frictional heating during finite deformation of metal. part I: Theory. *Journal of Engineering Mechanics*, 128(11):1215–1221, 2002.

[96] Brännberg N. and Mackerle J. Finite element methods and material processing technology. *Engineering Computations*, 11(5):413–455, 1994.

[97] Armero F. and Simo J. A priori stability estimates and unconditionally stable product formula algorithms for nonlinear coupled thermoplasticity. *International Journal of Plasticity*, 9(6):749–782, 1993.

[98] Simo J. and Armero F. Recent advances in the numerical analysis and simulation of thermoplasticity at finite strains. In Besdo D. and Stein E., editors, *Finite Inelastic Deformations—Theory and Applications*, pages 259–272. Springer-Verlag, 1992.

[99] Wriggers P., Van T. V., and Stein E. Finite element formulation of large deformation impact-contact problems with friction. *Computers & Structures*, 37(3):319–331, 1990.

[100] Laursen T. and Simo J. A continuum-based finite element formulation for the implicit solution of multibody, large deformation-frictional contact problems. *International Journal for Numerical Methods in Engineering*, 36(20):3451–3485, 1993.

[101] Simo J. and Laursen T. An augmented Lagrangian treatment of contact problems involving friction. *Computers & Structures*, 42(1):97–116, 1992.

[102] Laursen T. and Simo J. Algorithmic symmetrization of coulomb frictional problems using augmented Lagrangians. *Computer Methods in Applied Mechanics and Engineering*, 108(1-2):133–146, 1993.

[103] Wriggers P. and Miehe C. Contact constraints within coupled thermomechanical analysis–a finite element model. *Computer Methods in Applied Mechanics and Engineering*, 113(3-4):301–319, 1994.

[104] Pantuso D., Bathe K.-J., and Bouzinov P. A. A finite element procedure for the analysis of thermomechanical solids in contact. *Computers & Structures*, 75(6):551–573, 2000.

[105] Hirt C. W., Amsden A. A., and Cook J. An arbitrary Lagrangian-Eulerian computing method for all flow speeds. *Journal of Computational Physics*, 14(3):227–253, 1974.

[106] Donea J., Giuliani S., and Halleux J. P. An arbitrary Lagrangian-Eulerian finite element method for transient dynamic fluid-structure interactions. *Computer Methods in Applied Mechanics and Engineering*, 33(1-3):689–723, 1982.

[107] Hughes T. J., Liu W. K., and Zimmermann T. K. Lagrangian-Eulerian finite element formulation for incompressible viscous flows. *Computer Methods in Applied Mechanics and Engineering*, 29(3):329–349, 1981.

[108] Liu W. K., Belytschko T., and Chang H. An arbitrary Lagrangian-Eulerian finite element method for path-dependent materials. *Computer Methods in Applied Mechanics and Engineering*, 58(2):227–245, 1986.

[109] Kam L. W., Chang H., Chen J.-S., and Belytschko T. Arbitrary Lagrangian-Eulerian Petrov-Galerkin finite elements for nonlinear continua. *Computer Methods in Applied Mechanics and Engineering*, 68(3):259–310, 1988.

[110] Nobile F. and Formaggia L. A stability analysis for the arbitrary Lagrangian Eulerian formulation with finite elements. *East-West Journal of Numerical Mathematics*, 7(2):105–132, 1999.

[111] Hu H. H., Patankar N. A., and Zhu M. Direct numerical simulations of fluid–solid systems using the arbitrary Lagrangian–Eulerian technique. *Journal of Computational Physics*, 169(2):427–462, 2001.

[112] Souli M. and Zolesio J. Arbitrary Lagrangian–Eulerian and free surface methods in fluid mechanics. *Computer Methods in Applied Mechanics and Engineering*, 191(3-5):451–466, 2001.

[113] Movahhedy M., Gadala M., and Altintas Y. Simulation of the orthogonal metal cutting process using an arbitrary Lagrangian–Eulerian finite-element method. *Journal of Materials Processing Technology*, 103(2):267–275, 2000.

[114] Sarrate J., Huerta A., and Donea J. Arbitrary Lagrangian–Eulerian formulation for fluid–rigid body interaction. *Computer Methods in Applied Mechanics and Engineering*, 190(24-25):3171–3188, 2001.

[115] Kuhl E., Hulshoff S., and De Borst R. An arbitrary Lagrangian-Eulerian finite-element approach for fluid–structure interaction phenomena. *International Journal for Numerical Methods in Engineering*, 57(1):117–142, 2003.

[116] Duarte F., Gormaz R., and Natesan S. Arbitrary Lagrangian–Eulerian method for

Navier–Stokes equations with moving boundaries. *Computer Methods in Applied Mechanics and Engineering*, 193(45-47):4819–4836, 2004.

[117] Yamada T. and Kikuchi F. An arbitrary Lagrangian-Eulerian finite element method for incompressible hyperelasticity. *Computer Methods in Applied Mechanics and Engineering*, 102(2):149–177, 1993.

[118] Gadala M. and Wang J. ALE formulation and its application in solid mechanics. *Computer Methods in Applied Mechanics and Engineering*, 167(1-2):33–55, 1998.

[119] Ghosh S. and Kikuchi N. An arbitrary Lagrangian-Eulerian finite element method for large deformation analysis of elastic-viscoplastic solids. *Computer Methods in Applied Mechanics and Engineering*, 86(2):127–188, 1991.

[120] Bonet J. and Wood R. D. *Nonlinear Continuum Mechanics for Finite Element Analysis*. Cambridge University Press, Cambridge, 2008.

[121] Başar Y. and Weichert D. *Nonlinear Continuum Mechanics of Solids: Fundamental Mathematical and Physical Concepts*. Springer Science & Business Media, 2000.

[122] Coleman B. D. and Noll W. The thermodynamics of elastic materials with heat conduction and viscosity. In Noll W., editor, *The Foundations of Mechanics and Thermodynamics*, pages 145–156. Springer, 1974.

[123] Simo J. and Hughes T. *Computational Inelasticity*, volume 7. Springer-Verlag, New York, 1998.

[124] Zhang H., Zhang Z., and Chen J. 3D modeling of material flow in friction stir welding under different process parameters. *Journal of Materials Processing Technology*, 183(1):62–70, 2007.

[125] Buffa G., Hua J., Shivpuri R., and Fratini L. A continuum based FEM model for friction stir welding - Model development. *Materials Science and Engineering A*, 419(1-2):389–396, 2006.

[126] Heurtier P., Jones M., Desrayaud C., Driver J., Montheillet F., and Allehaux D. Mechanical and thermal modelling of friction stir welding. *Journal of Materials Processing Technology*, 171(3):348–357, 2006.

[127] Johnson G. and Cook W. A constitutive model and data for metals subjected to large strains, high strain rates and high temperatures. In *Proceedings of the Seventh International Symposium on Ballistics*, The Hague, The Netherlands, 1983.

[128] Schmidt H. and Hattel J. A local model for the thermomechanical conditions in friction stir welding. *Modelling and Simulation in Materials Science and Engineering*, 13(1):77–93, 2005.

[129] Grujicic M., Arakere G., Pandurangan B., Ochterbeck J. M., Yen C. F., Cheeseman B. A., Reynolds A. P., and Sutton M. A. Computational analysis of material flow during friction stir welding of AA5059 aluminum alloys. *Journal of Materials Engineering and Performance*, 21(9):1824–1840, 2011.

[130] Veljic D., Rakin M., Perovic M., Medjo B., Radakovic Z., Todorovic P., and Pavisic M. Heat generation during plunge stage in friction stir welding. *Thermal Science*, 17(2):489–496, 2013.

[131] Nandan R., Roy G. G., and Debroy T. Numerical simulation of three-dimensional heat transfer and plastic flow during friction stir welding. *Metallurgical and Materials Transactions A*, 37(4):1247–1259, 2006.

[132] Kuykendall K., Nelson T., and Sorensen C. On the selection of constitutive laws used in modeling friction stir welding. *International Journal of Machine Tools and Manufacture*, 74:74–85, 2013.

[133] Ulysse P. Three-dimensional modeling of the friction stir-welding process. *International Journal of Machine Tools and Manufacture*, 42(14):1549–1557, 2002.

[134] Colegrove P. and Shercliff H. 3-Dimensional CFD modelling of flow round a

threaded friction stir welding tool profile. *Journal of Materials Processing Technology*, 169(2):320–327, 2005.

[135] Sheppard T. and Wright D. Determination of flow stress: Part 1 constitutive equation for aluminium alloys at elevated temperatures. *Metals Technology*, 6(1):215–223, 1979.

[136] Simo J. C. and Laursen T. A. An augmented Lagrangian treatment of contact problems involving friction. *Computers & Structures*, 42(1):97–116, 1992.

[137] Agelet de Saracibar C. Numerical analysis of coupled thermomechanical frictional contact problems. computational model and applications. *Archives of Computational Methods in Engineering*, 5(3):243–301, 1998.

[138] Chung J. and Hulbert G. M. A time integration algorithm for structural dynamics with improved numerical dissipation: the generalized-α method. *Journal of Applied Mechanics*, 60(2), 1993.

[139] Argyris J. and Doltsinis J. S. On the large strain inelastic analysis in natural formulation part I: Quasistatic problems. *Computer Methods in Applied Mechanics and Engineering*, 20(2):213–251, 1979.

[140] Needleman A. A numerical study of necking in circular cylindrical bar. *Journal of the Mechanics and Physics of Solids*, 20(2):111–127, 1972.

[141] Wriggers P., Miehe C., Kleiber M., and Simo J. On the coupled thermomechanical treatment of necking problems via finite element methods. *International Journal for Numerical Methods in Engineering*, 33(4):869–883, 1992.

[142] Lehmann T. and Blix U. On the coupled thermo-mechanical process in the necking problem. *International Journal of Plasticity*, 1(2):175–188, 1985.

[143] Taylor G. I. The use of flat-ended projectiles for determining dynamic yield stress I. theoretical considerations. *Proceedings of the Royal Society of London. Series A. Mathematical and Physical Sciences*, 194(1038):289–299, 1948.

[144] Lacy J., Novascone S., Richins W., and Larson T. A method for selecting software for dynamic event analysis: II—the Taylor anvil and dynamic Brazilian tests. In *Proceedings of the 16th International Conference on Nuclear Engineering*, volume 48175, pages 261–270, 2008.